The geysers geothermal area, California: tomographic images of the depleted steam reservoir and non-double-couple earthquakes

Ross, Alwyn C.

The Geysers Geothermal Area, California: Tomographic Images of the Depleted Steam Reservoir and Non-Double-Couple Earthquakes

Alwyn C. Ross

A thesis submitted in partial fulfilment of the requirements for the degree of Doctor of Philosophy

Department of Geological Sciences

University of Durham

November 1996

The Geysers Geothermal Area, California: Tomographic Images of the Depleted Steam Reservoir and Non-Double-Couple Earthquakes

Alwyn C. Ross

Abstract

The Geysers geothermal area, California is the world's largest and most intensively exploited steam field, providing about 6% of California's electrical power. The geothermal area is very active seismically, generating about 140 earthquakes per month with $M_D \geq 1.2$. Non-DC earthquakes have been routinely detected in other geothermal and volcanic areas such as the Hengill-Grensdalur volcanic complex, Iceland but previously went undetected at The Geysers. The steam field is, however, a likely source of non-DC earthquakes because large volumes of steam are extracted and condensate injected during the course of commercial exploitation which might cause cracks or fractures to open and close.

Maps of seismic activity through time show conclusively that earthquakes initiate at the onset of production, continue through it and stop when production ceases. Furthermore the volume of steam extracted and/or condensate injected may directly control the rate of seismicity within the geothermal area.

A temporary field experiment in April, 1991 recorded about 4000 high-quality earthquakes on three-component digital sensors. Three-dimensional tomographic models of v_P and, for the first time at The Geysers, v_P/v_S were determined using 3906 *P*-wave and 944 *S*-wave arrival times from 185 earthquakes. Variations in lithology, temperature and the pore-fluid phase probably produce the variations in v_P. A strong low in the v_P/v_S model defines fluid-deficient areas in the steam reservoir and is surrounded by a "halo" of high-v_P/v_S anomalies. v_P/v_S can remotely monitor temporal depletion of liquid reserves in the steam reservoir.

Well-constrained moment tensor solutions for 30 earthquakes were determined by inverting the polarities and amplitude ratios of *P*- and *S*-wave arrivals. Strong evidence for the existence of non-DC earthquakes at The Geysers geothermal area was found. Explosive and implosive events occur in equal numbers and probably reflect source processes involving opening and closing cracks or cavities. The events form a symmetric pattern on source-type plots extending from the postive dipole-to-negative dipole loci, passing through the DC locus. The association with dipole loci rather than crack loci suggests the source process must also involve a compensating flow of fluids, liquid or steam.

Declaration

I declare that this thesis, which I submit for the degree of Doctor of Philosophy at the University of Durham, UK is my own work and is not substantially the same as any which has previously been submitted for a degree at this or any other university.

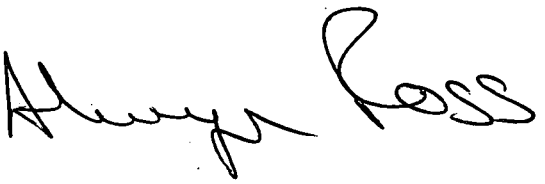

Alwyn Campbell Ross
University of Durham
November 1996

Dedicated to my

wife Maureen

Acknowledgements

Thanks are due to:

My supervisors Gill Foulger and Bruce Julian who collected the data which made all this possible and for providing invaluable advice, guidance, support and encouragement throught out my Ph.D.

Al Lindh and Walter Mooney, Branch Chiefs at the US Geological Survey, Menlo Park, California for hosting my visits there.

Angus Miller for his generous assistance and constructive discussions on a subject new to us both.

Scientists at the US Geological Survey for their help, advice and hospitality throughout my stay, in particular, John Evans and Greg Allen.

M. Stark, S. Davis and many others from UNOCAL Corporation for assistance. F. Palmieri, the Abril trusts, C.Chapman, E. Frandsen, the Gauer Estate Vineyard, J. Aidlin, G. and M. Gouvea, and the Coldwater Creek Operator Corporation gave permission to operate instruments on their lands. This work was supported by a G. K. Gilbert Fellowship from USGS, a NERC Grant and equipment Loan, and a loan of IRIS/PASSCAL equipment.

A special thanks to Grant, Lynn, Kathleen, Tim, Brian, Johnny, Rich, Pete and Diane for introducing me to the joys of life in California and for extending much more than a warm welcome.

Fellow Durham students, especially Ziad, Wayne and Alun, not forgetting Gradsoc A.F.C. (still on course for global domination) who made my stay in Durham such good fun.

Staff in the Department of Geological Sciences, University of Durham

Financial funding for this project was provided by the Department of Education for Northern Ireland.

My parents for all their interest, encouragement and support.

Finally (but by no means least) my wife Maureen, whose support, encouragement and understanding during both the highs and lows of the last 3 years have made the experience worthwhile, thank-you.

And to close–

"If we knew what it was we were doing, it would not be called research, would it?"

Albert Einstein.

List of contents

List of figures

List of tables

List of additional material

Copies of the following papers are contained in a pocket at the back of this thesis:

Evans, J. R., B. R. Julian, G. R. Foulger and A. Ross, Shear-wave splitting from local earthquakes at The Geysers Geothermal Field, California, *Geophys. Res. Lett.*, **22**, 501-504, 1995

Foulger, G. R., C. C. Grant, B. R. Julian and A. Ross, Changes in structure at an exploited geothermal reservoir, California, in press *Geophys. Res. Lett.*, 1996

Julian, B. R., A. Ross, G. R. Foulger and J. R. Evans, Three-dimensional seismic image of a geothermal reservoir: The Geysers, California, *Geophysical Res. Lett.*, **23**, 685-688, 1996

Ross, A., G. R. Foulger, and B. R. Julian, Non-double-couple earthquake mechanisms at The Geysers geothermal area, California, *Geophysical Res. Lett.*, **23**, 877-880, 1996

Chapter 1

Introduction

1.1 Overview

The Geysers geothermal area, located about 120 km north of San Francisco, northern California, is the largest commercially-exploited steam field in the world, presently supplying about 6% of California's electrical power. The area is also one of the most seismically active in California providing a rich source of continuous, low-magnitude earthquakes. Seismicity is restricted almost exclusively to the steam production area and results largely from ongoing commercial exploitation activities.

Vapour-dominated geothermal systems such as The Geysers have a finite life span, effectively becoming extinct when liquid reserves are exhausted and the reservoir "boils dry". Preliminary forecasts of a limitless supply of steam at The Geysers were overly optimistic. A pressure decline initiated in some parts of the steam field in the 1960's. This became significant by 1987, accelerated by intense commercial exploitation. The wealth of seismic and other data accumulated during commercial development of the resource and the unique opportunity of studying a vapour-dominated geothermal system approaching the end of its commercial development provides the impetus for the research presented in this thesis. The project aims to improve understanding of pore-fluid variations, structure and processes within the geothermal reservoir by applying relatively new techniques in three-dimensional tomographic modelling and earthquake source mechanisms.

1.2 Tectonic setting of northern California

The San Andreas fault system and Mendocino Triple Junction (MTJ) dominate the tectonics of northern California. The MTJ is a trench-transform-transform type triple junction which formed at about 30 Ma when the north American continental plate came into contact with the Pacific and Gorda oceanic plates (Figure 1.1) (*Furlong*, 1993). The triple junction then migrated north from southern California reaching Monterey at ~10 Ma and The Geysers-Clear Lake area by ~3.3 Ma (Figure 1.1) (*Atwater,* 1970; *McLaughlin*, 1981; *Furlong*, 1993). The present rate of migration is about 5 cm/yr and is controlled by the oblique northeast motion of the southwest edge of the subducting Gorda plate relative to North America. Hypothetically as the triple junction passes a point, subduction of the Gorda plate stops, leaving a void termed the "slabless window" (Figure 1.2). Geodynamic processes primarily associated with thermal and rheological evolution of this window initiated a broad lateral shear zone (the San Andreas fault zone) southeast of the propagating transform front.

North of the MTJ oblique subduction of the Gorda plate under northern California continues, characterised by a fold and thrust belt 90-100 km wide (Figure 1.3) reflecting compressional deformation within the southern fore-arc margin of the Cascadia subduction zone (*Clarke*, 1992). Structural features include accretionary folds and a range of low- to high-angle reverse faults trending northwest-southeast. Gravity and seismic studies define the geometry of the Gorda plate as it subducts under North America (*Jachens and Griscom,* 1983; *Walter*, 1986; *Benz et al.*, 1992; *Cockerham*, 1984). At the MTJ the Gorda plate is about 7-8 km below sea level (bsl) and dips at about 9° to the southeast (*Jachens and Griscom,* 1983). East of the Bartlett Springs fault the plate is 20 km bsl and the dip is 20°-30° (Figure 1.3). The deepest section of the subducted slab imaged is at depths of 100-150 km under Mt. Shasta and Lassen Peak (Figure 1.1) (*Benz et al.*, 1992). The southwest edge of the subducting slab is marked by large gradients in the gravity field. From the MTJ area southeast to the Bartlett Springs fault area the strike of the subducted slab is parallel to the present-day motion of the Pacific and Gorda plates (Figure 1.3). Southeast of the Bartlett Springs fault area the strike changes, reflecting the dominant plate motion at about 3.5 Ma which was to the east.

The San Andreas fault formed at ~30 Ma and represents the boundary between the Pacific and North American plates. It is continually increasing in length and changing as transform motion replaces subduction when the triple junction passes (*Furlong*, 1993). The tectonic stress regime undergoes a similar transition from subduction- to shear-dominated. Great (M>8) earthquakes along the main branch of the fault accommodate most of the relative plate motion (*Hill et al.,* 1990). The San Andreas shear system immediately south of the MTJ is the youngest part of the system, and extends over a zone

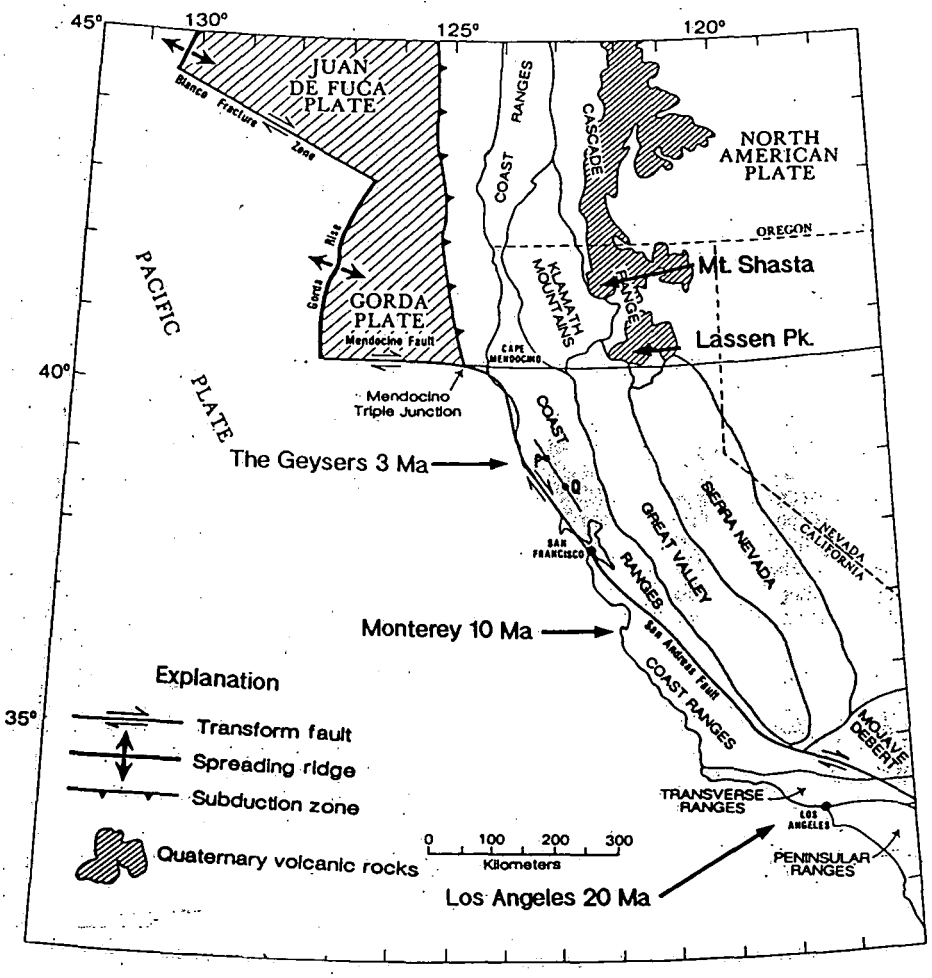

Figure 1.1. Plate tectonic setting of northern California, detailing the interaction and relative motion of the Pacific, Gorda and north American plates which form the Mendocino Triple Junction (from *Jachens and Griscom*, 1983). Estimates of the position of the triple junction as it migrates northwards are indicated.

>100 km wide (Figure 1.3). Components include the Maacama, Healdsburg, Rogers Creek, Green Valley and Bartlett Springs faults. The Hayward and Calaveras faults are thought to be collinear branches of these fault zones with the connection obscured by an aseismic zone in San Francisco bay. Plate motion is restricted to the San Andreas fault near to the MTJ. In the latitude range 36.5-39° N, motion is distributed among several faults (Figure 1.3). Deformation is again accommodated principally by the San Andreas fault south of the San Francisco bay area at 36.5° N.

The development of the San Andreas fault is a fundamental change in plate boundary structure *(Furlong,* 1993). The slabless window filled with asthenosphere which rose to shallower levels in the crust producing a complex, three-dimensional plate boundary geometry (Figure 1.4a). Three-dimensional thermo-mechanical modelling of the San Andreas fault system suggests that the Pacific-North American plate boundary at the

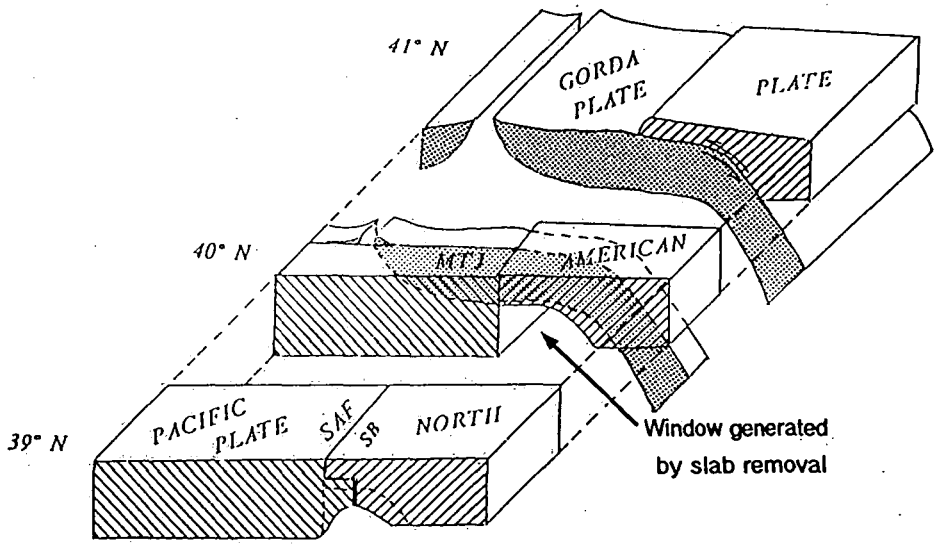

Figure 1.2. Schematic representation of plate interaction in the vicinity of the Mendocino Triple Junction MTJ, from *Furlong et al.* (1989). North of the triple junction (41° N) the Gorda plate is subducted under north America. South of the triple junction (40° N) subduction is terminated and the Gorda slab removed to form a slabless window. SB; Sebastopol Block; SAF, San Andreas fault.

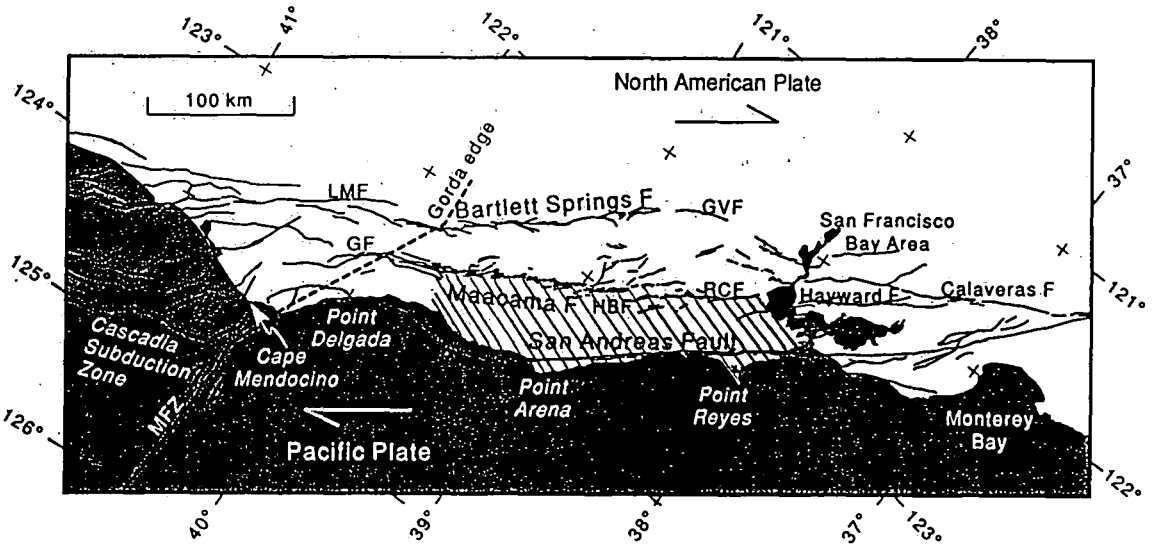

Figure 1.3. Tectonic map of northern California showing the main Holocene and Quaternary faults, from *Castillo and Ellsworth* (1993). The bold dashed line is the surface projection of the southeast edge of the Gorda plate. The relative motions between the Pacific and north American plates are indicated. CF, Calaveras fault; GF, Garberville Fault; GVF, Green Valley fault; HBF, Healdsburg fault; HF, Hayward fault; LMF, Lake Mountain fault; MFZ, Mendocino fracture zone; RCF, Rogers Creek fault. The hatched area encloses the Sebastopol block.

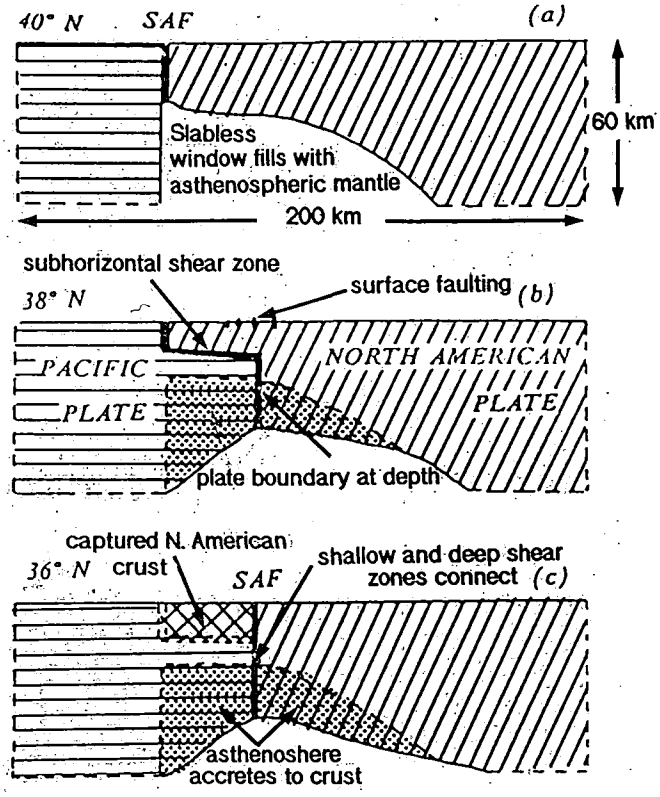

Figure 1.4. Schematic representation of North American-Pacific plate boundary evolution following the passage of the Mendocino triple junction, from *Furlong et al.* (1989) (a) Subducting slab is removed to form a "slabless window" which fills with upwelling asthenospheric mantle. SAF: San Andreas fault. (b) The system cools and part of the asthenospheric mantle accretes to the base of the Pacific and north American plate (dotted section). The plate boundary at depth is offset to the east by 30-40 km and connected to the shallower plate boundary by a horizontal detachment zone. Newly formed faults sit above the deeper part of the plate boundary. This is the present configuration in the San Francisco bay area. (c) The fault system configuration in central California. The deeper shear zone connects with surface faults and the Pacific plate captures part of the North American crust (stippled section).

MTJ is restricted to the thickness of the lithosphere (15-20 km) (Figure 1.4a) (*Furlong et al.*, 1989). Immediately south of the MTJ the surface trace of the plate boundary occupies the previous western edge of the north American plate. The deeper lithospheric plate boundary is 30-40 km east of the surface trace of the San Andreas fault and is thought to be connected by a sub-horizontal shear/detachment surface 10-15 km deep beneath the Sebastapol block (Figure 1.4b) (*Furlong et al.*, 1989). Based on evidence from older segments of the San Andreas fault south of 36° N, the shallow plate boundary near the MTJ might in the future migrate eastwards relative to the surface expression of the San Andreas fault until it sits over and connects with the deeper plate boundary. Deformation

is accommodated along the horizontal detachment zone (Figure 1.4c) (*Furlong et al.*, 1989). The Hayward and Calaveras faults and their northern continuations (Healdsburg-Rogers Creek-Maacama faults and Green Valley-Bartlett Springs faults), presently overly the deeper plate boundary and these may represent surface expressions of this future plate boundary (Figures 1.3 and 1.4b).

The distribution of seismicity in northern California maps out the active tectonic faults (Figure 1.5). Although the San Andreas is the principal fault it has been relatively aseismic in northern California since the 1906 earthquake. The Sebastapol block between the San Andreas and Maacama fault zones appears to act as a semi-rigid block (Figures 1.3 and 1.5). The Maacama fault zone has been moderately active and the Bartlett Springs fault has been characterised by more discrete areas of seismic activity (*Castillo and Ellsworth*, 1993). Fault-plane solutions for earthquakes along these faults indicate right-lateral motion on faults dipping northeast at 50-75°. They are thought to have formed initially as reverse faults in the Cascadia subduction environment but are now under the influence of a transform-shear regime (*Castillo and Ellsworth*, 1993). The Maacama-Garberville, and the Bartlett Springs-Lake Mountain fault zones are thought to form fault pairs based on strike and dip geometries (Figure 1.5). Transform slip along the northern end of the San Andreas is therefore thought to occur along pre-existing structures.

1.3 The Geysers area

1.3.1 Geology

The Geysers area consists of two Jurassic-Cretaceous units assigned to the Franciscan and the Great Valley sequences. These are partially capped by Quaternary volcanics and intruded by a composite batholith called the "felsite". Slices of ancient oceanic crust have also been identified.

The Franciscan assemblage is divided in to three thrust-fault-bounded structural slabs which young progressively to the west and range from late Jurassic to Miocene in age (Figure 1.6). These units, the Eastern (Yolla Bolly) belt, the Central belt and the Coastal belt, consist of a heterogeneous assemblage of intensely-deformed, mildly-to-moderately metamorphosed sedimentary and mafic igneous rocks with minor metamorphic mineral constituents. They are interpreted to have been deposited in a trench environment over an easterly-dipping subduction zone. The mafic igneous rocks and chert have an oceanic affinity but the sandstone units (arkosic and some volcanic-lithic) may be derived from a terrestrial (island-arc or continental) source.

The Eastern (Yolla Bolly) belt is the oldest within the Franciscan and is composed of metamorphosed sandstone with minor interbedded chert and layers of metamorphosed

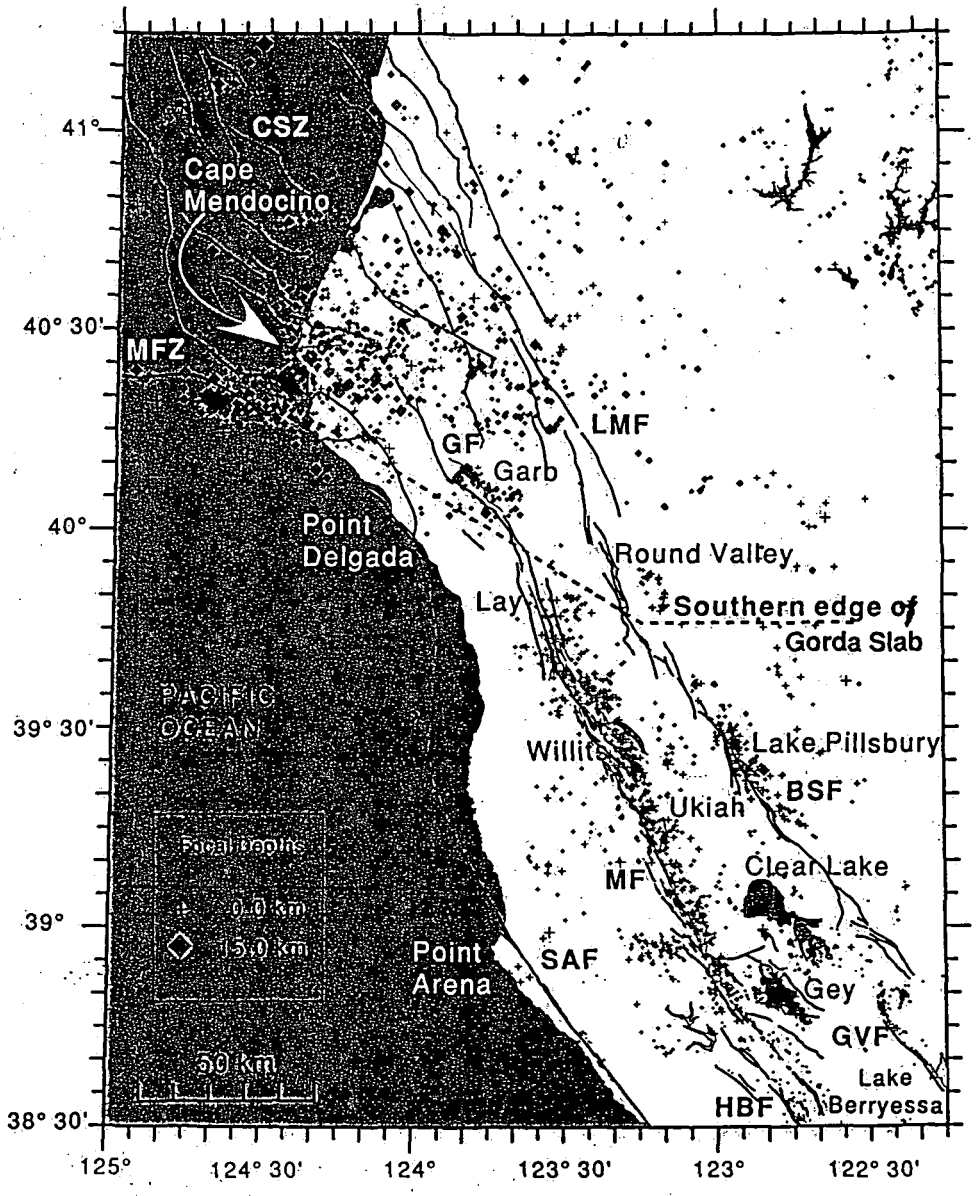

Figure 1.5. Seismicity of northern California 1980-1991 for earthquakes with M>1.5, from *Castillo and Ellsworth* (1993). Events shallower than 15 km are plotted as crosses and events deeper than 15 km are plotted as diamonds. Abbreviations GF, GVF, HBF, LMF and MFZ are the same as for Figure 1.3. CSZ: Cascadia subduction zone; BSF: Bartlett Springs fault; Garb: Garberville fault; Gey, The Geysers; Lay: Laytonville; MF: Maacama fault; SAF: San Andreas fault.

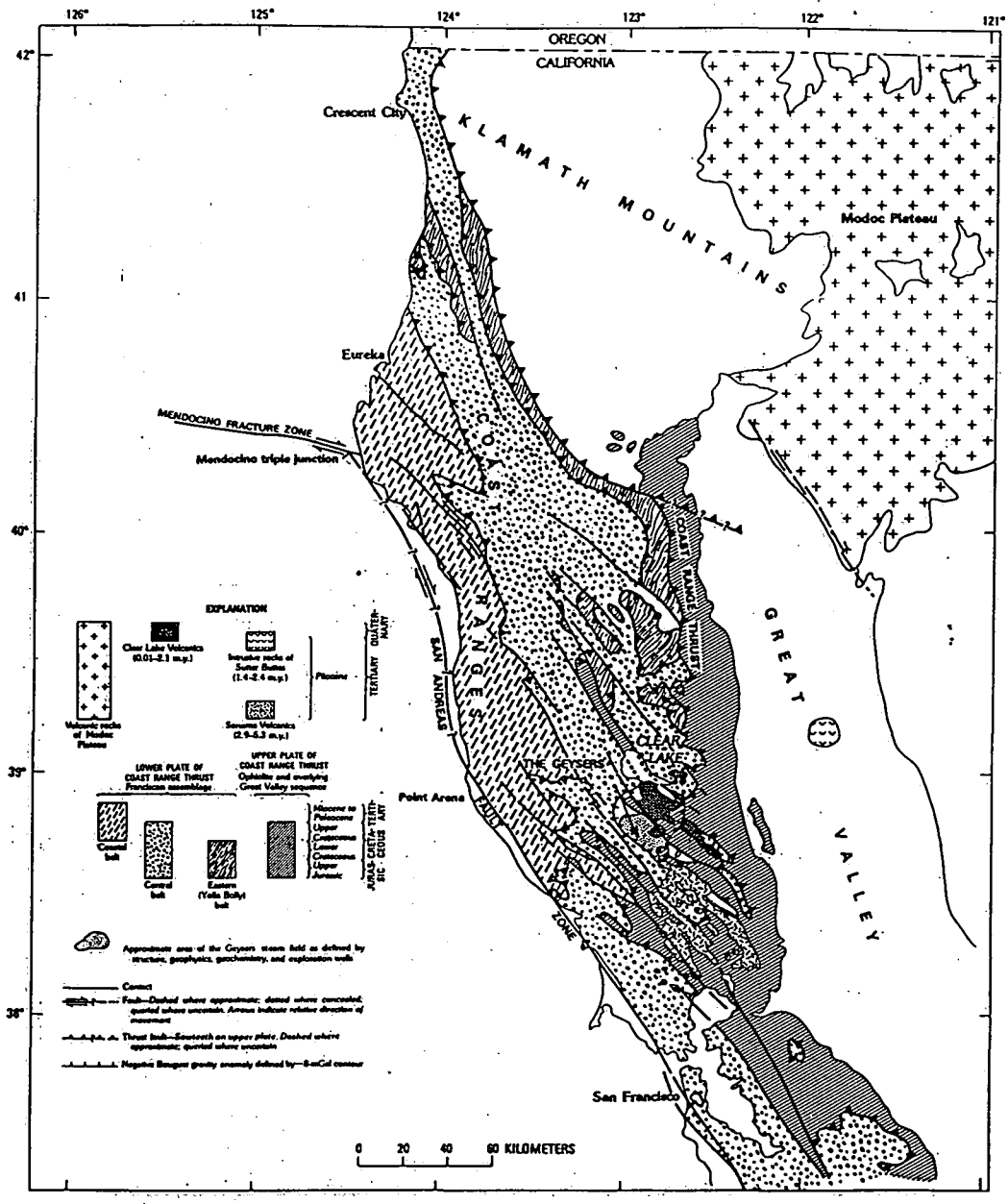

Figure 1.6. Generalised regional geologic map of northern California, with particular reference to The Geysers-Clear Lake area, from *McLaughlin* (1981).

igneous rocks. The Central belt consists of slightly younger metamorphosed sandstone and argillite, basaltic igneous rocks and chert of late Jurassic to late Cretaceous age, subdivided depending on whether they occur within extensive melange sequences or broken formations. Rocks in the western Coastal belt are weakly-metamorphosed arkosic-sandstones and shale. These are the youngest rocks in the Franciscan assemblage ranging in age from late Cretaceous to Miocene.

The Great Valley sequence, east of the Franciscan, consists of moderately-deformed conglomerate mudstone and sandstones ranging in age from late Jurassic to late Cretaceous (Figure 1.6). These rocks were deposited in a series of submarine fans within an arc-trench gap or fore-arc basin environment. The Great Valley sequence overlies late Jurassic fragmented ophiolite, called the Coast Range ophiolite, thought to represent ancient oceanic crust.

The Clear Lake volcanic field was extruded onto Franciscan assemblage and Great Valley sequence rocks east and northeast of The Geysers, and covers an area of about 400 km^2 (Figure 1.7). Extrusive igneous rocks within the Clear Lake volcanics include basalt, basaltic andesite, andesite, dacite, rhyodacite and rhyolite. These represent the eruptive products of mantle heating, crystal fractionation and assimilation of rocks from the Franciscan assemblage, Great Valley sequence and lower crust. Silicic lavas (dacite and rhyolite) are estimated to have twice the volume of the mafic lavas (basalt, basaltic andesite, and andesite) with dacite the most abundant and basalt the rarest volcanic rock type. Basalt, basaltic andesite, and andesite occur as flows, cinder cones and volcanic vent deposits (*Hearn et al.*, 1981).

Volcanic activity commenced around 2 Ma and ended about 10,000 years ago. Within this period four distinct episodes of volcanic activity are identified (Table 1.1). The rock types and the estimated volumes extruded during each episode are presented in Figure 1.8. *K/Ar* age dates indicate the volcanic rocks young progressively to the north within the volcanic field. This mirrors a regional trend in northern California with the Clear Lake Volcanics being the youngest of several volcanic fields which become young to the north *i.e.*, the Sonoma, Tolay, Berkeley Hills, Leona, Quien Sabe and Neenach-Pinnacles fields (Figure 1.9). Their formation may relate to the northeast migration of the triple junction, possibly aided by the development of a "slab window", or the passage of the North American continental plate over a stationary hot spot in the mantle (*McLaughlin*, 1981; *Furlong et al.*, 1989; *Hearn et al.*, 1981).

The "felsite" batholith intruded into Franciscan assemblage under The Geysers geothermal field is the only well-documented intrusive igneous rock in The Geysers region (Section 1.4.1) (*Hulen and Nielson*, 1993). The batholith forms a composite intrusion consisting of rhyolite porphyry, granite and granodiorite. The close temporal (about 1 Ma) and geochemical similarities between the granidiorite (felsite) and dacite

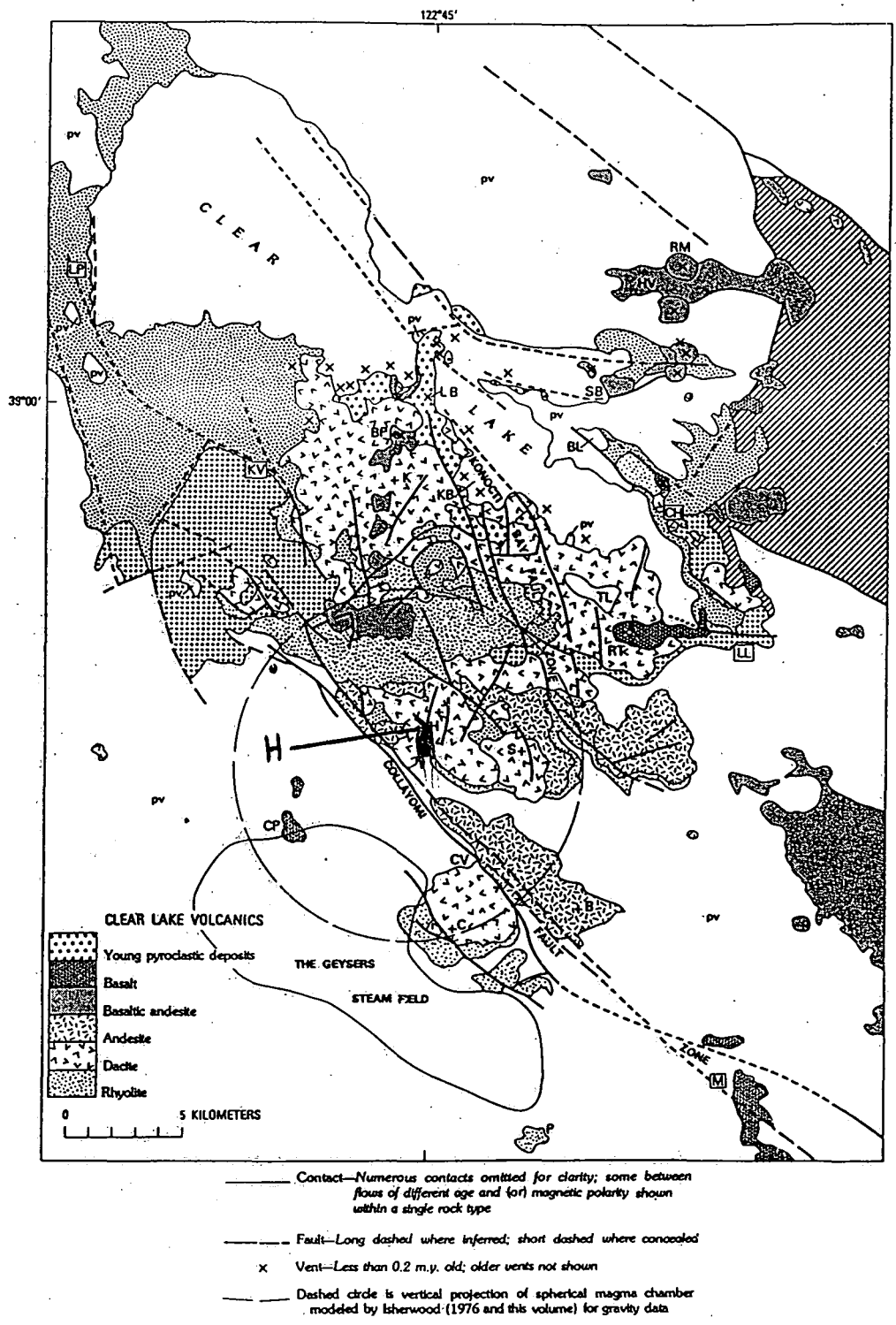

Figure 1.7. Geology of The Geysers-Clear Lake area showing volcanic rocks of the Clear Lake volcanic field, from *Hearn et al.* (1981). +: mountain summit; C: Cobb Mountain; H: Mount Hannah; HV: High Valley; K: Mount Konocti; S: Seigler Mountain; BP: Buckingham Peak; KB: Konocti Bay; CP: Caldwell Pines; CV: Cobb Valley; SB: Sulphur Bank; BL: Borax Lake; LB: Little Borax Lake; Tl: Thurston Lake; CH: Clear Lake Highlands; KV: Kelseyville; LL: Lower Lake; LP: Lakeport; M: Middleton; P: Pine Mountain; RM: Round Mountain; RT: Roundtop Mountain.

Table 1.1. Periods of volcanic activity associated with the Clear Lake volcanic field

Group no	Period of Volcanism (Ma)
1	0.01-0.20
2	0.30-0.65
3	0.80-1.10
4	1.30-2.10

outcropping on Cobb mountain and other localities within the Clear Lake volcanic field suggest the two may be equivalents (*Hulen and Nielson*, 1993). The rhyolite porphyry and granite intrusives are geochemically similar to granites in the Clear Lake volcanic field but different ages preclude them from being equivalents (1.3 vs. 1.07 Ma respectively).

1.3.2 Geophysics

Geophysical surveys in The Geysers-Clear Lake region have been designed largely to locate, define and improve understanding of the geothermal system and heat source. Gravity surveys indicate a large negative (–25 mGal) anomaly centred over Mt. Hannah (*Chapman*, 1966). The circular shape of the gravity anomaly precludes it from being caused by density contrasts between structural blocks within the northwest-southeast structural fabric (*Hearn et al.*, 1976). With additional gravity data the anomaly was divided into three component parts consisting of a depressed regional field, a –30 mGal gravity low centred on Mt. Hannah and a negative anomaly over the geothermal production area (see Section 1.4.3) (Figure 1.10a) (*Isherwood*, 1975).

Aeromagnetic surveys found two negative magnetic anomalies of –120 nT and –60 nT 10 km south of The Geysers production area and 10 km northeast of Mt. Hannah (the Clear Lake low) respectively, separated by a 60 nT positive anomaly centred on the Collayomi fault zone (Figure 1.10b) (*Chapman*, 1975). The anomalies are thought to result from ultramafic rocks (serpentinite) and some Clear Lake volcanic rocks in the upper 6.5 km of the crust. Magnetic anomalies do not coincide with the gravity anomalies.

Early interpretations of both gravity and magnetic anomalies suggested a low-density, spherical magma chamber, centred at about 13.5 km bsl and extending upwards to about 7 km below The Geysers-Clear Lake area (*Isherwood*, 1975). Recent gravity and magnetic modelling studies have adopted a more complex upper crustal geometry which assumes a body of partial melt centred at depths of 15-20 km (*Blakely and Stanley*, 1993). The calculated gravity field agrees closely with the observed field (Figure 1.11a). One can assume that the poor correlation of the gravity anomaly calculated by *Isherwood* (1976) provides evidence for a more complex upper crustal structure in The Geysers-Clear Lake

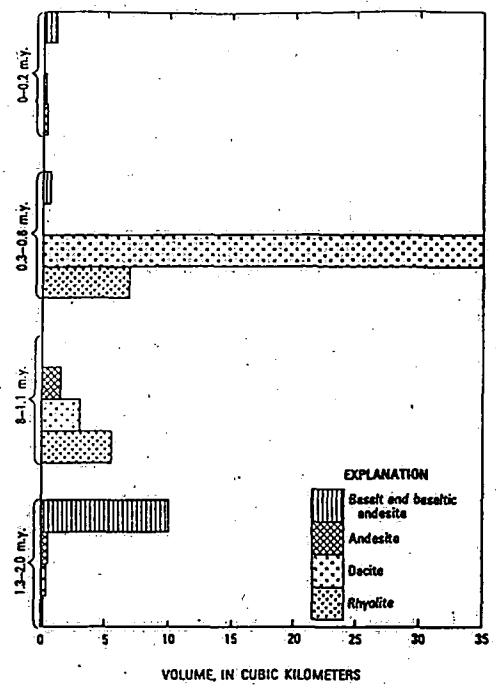

Figure 1.8. Estimated volumes of igneous rock extruded during the four episodes of volcanic activity in the Clear Lake volcanic field, from *Donnelly-Nolan et al.* (1981).

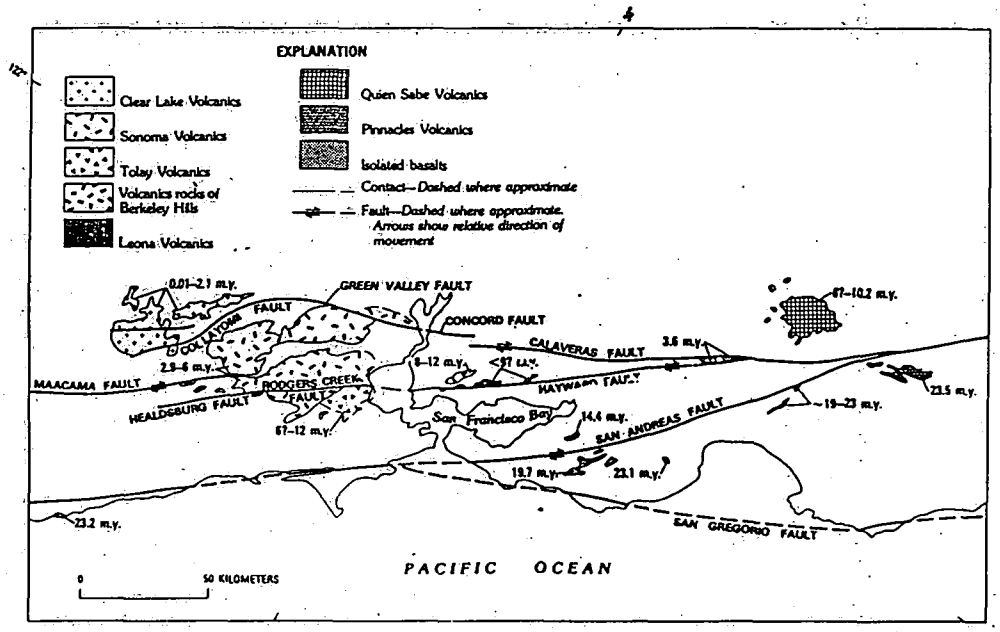

Figure 1.9. Map of the seven volcanic centres and principal faults within the central Coast Ranges, after *Hearn et al.* (1981). Rocks within the each volcanic centre become progressively younger to the north. This same pattern is reflected in relative age relationships between each volcanic centre which become progressively younger to the north. The Clear Lake volcanic field formed most recently.

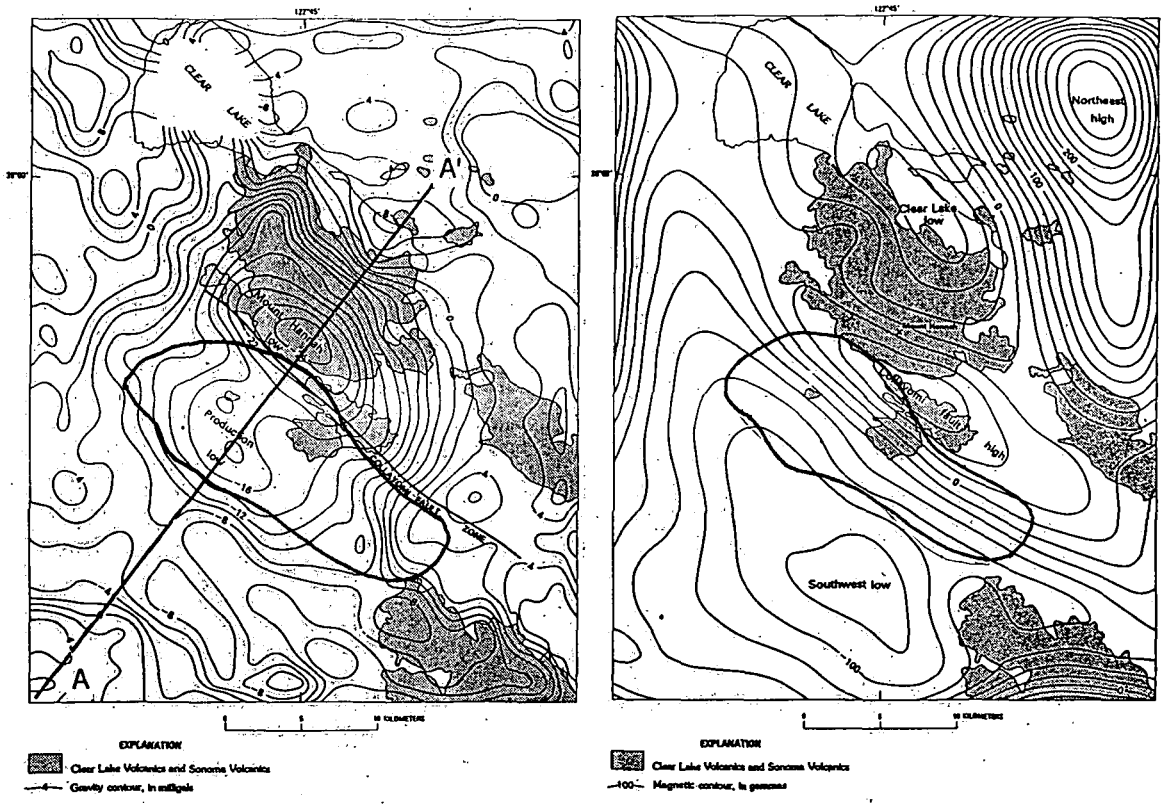

(a) (b)

Figure 1.10. (a) Residual gravity map of The Geysers-Clear Lake area, from *Isherwood* (1981). Gravity lows are centred over Mount Hannah and the geothermal production area. The line A-A' refers to the line of section used by *Blakely and Stanley* (1993) in gravity and magnetic field modelling (Figure 1.11). (b) Magnetic-field intensity map of The Geysers-Clear Lake area, from *Isherwood* (1981). Positive and negative anomalies alternate from northeast to southwest. The magnetic and gravity anomalies do not correlate directly with one another.

area. The long-wavelength component was interpreted as a body of low-density partial melt at depths of 15-20 km (*Blakely and Stanley*, 1993). An easterly-dipping serpentinte body juxtaposed along the Collayomi fault zone extends to a depth of about 5 km where it may connect with the Coast Range ophiolite. The Northeast High positive anomaly is thought to be produced by the Coast Range ophiolite (Figure 1.11b).

The lithosphere under The Geysers-Clear Lake area has been investigated using teleseismic *P*-waves (*Iyer et al.*, 1981; *Oppenheimer and Herkenhoff*, 1981; *Benz et al.*, 1992). All three studies found evidence of a low-velocity zone consistent with silicic partial melt. *P*-wave arrival-time studies found delays of 1 s under the steam field, and 0.9 s under Siegler Mtn. and Mt. Hannah which represent regional velocity decreases of 15% and decreases of up to 25% under both Mt. Hannah and The Geysers production area

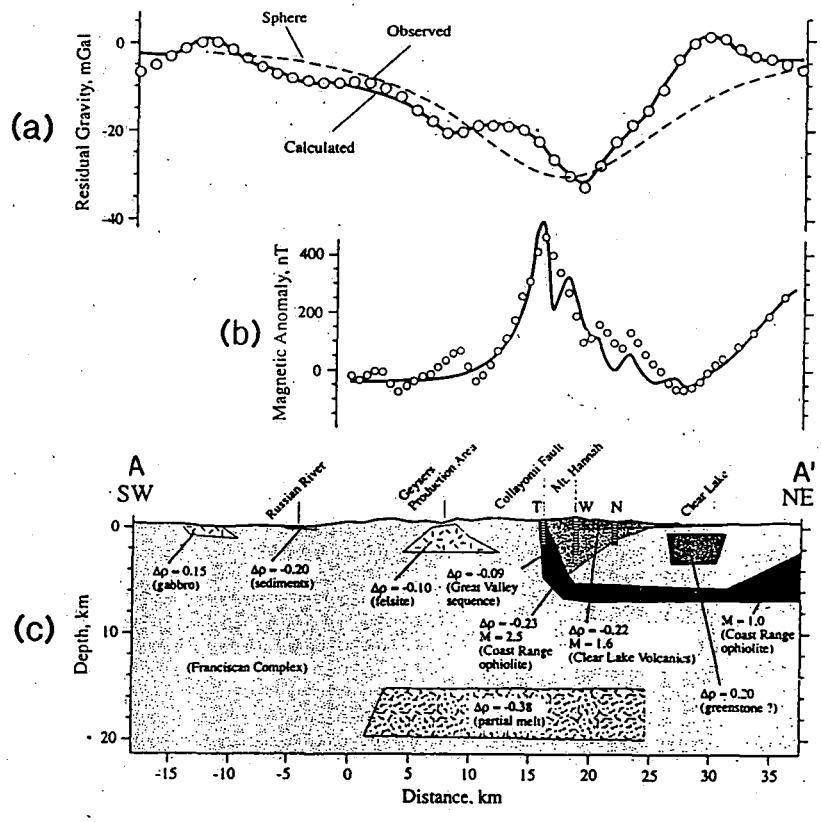

Figure 1.11. Gravity and magnetic field modelling for a southwest-northeast profile (see Figure 1.10 for location) at The Geysers-Clear Lake area, from *Blakely and Stanley* (1993). (a) Calculated and observed gravity fields, along with the gravity field calculated for a spherical body centred at 13.5 km depth (*Blakely and Stanley*, 1993; *Isherwood*, 1975b). (b) Calculated and observed magnetic fields along the same profile. (c) Crustal model derived from gravity and magnetic modelling.

(*Iyer et al.*, 1981). Three-dimensional compressional velocity structure determined by inverting *P*-wave arrival-times found regional velocity decreases of about 8-12% in the top 30 km of the lithosphere (*Oppenheimer and Herkenhoff*, 1981; *Benz et al.*, 1992). Combined interpretations of teleseismic, seismic-tomography and gravity data are consistent with a zone of partial melt at depth in lithosphere (*Oppenheimer and Herkenhoff*, 1981). Upper crustal properties such as anisotropy, frequency-dependent attenuation, elevated temperatures and high pore pressures (beneath Mt. Hannah) could contribute to *P*-wave delays (*Stanley and Blakely*, 1993).

Electrical surveys of The Geysers-Clear Lake region were designed to map the geology and structure, and provide information which might constrain earlier models derived from gravity and *P*-wave delay data suggesting the existence of a silicic magma

chamber at depth. A well-defined low resistivity anomaly with regional (northwest-southeast) elongation correlates with the gravity low centred on Mt. Hannah (Figure 1.12) (*Stanley et al.* 1973). The thin (<500 m) Clear Lake volcanic rocks have high resistivity (25-1000 ohm-m) values. Low resistivity values result from the combined effects of hot saline pore fluids in the underlying shales of the Great Valley sequence or carbonaceous shales of the Franciscan assemblage and a silicic magma chamber at depth (*Hearn et al.*, 1976b).

1.3.3 Tectonics

The Geysers-Clear Lake region has a complex history of deformation reflecting the transition from a subduction to a shear regime during the Cretaceous and early Tertiary (Section 1.2). Franciscan-assemblage rocks accumulated in a subduction-type environment while rocks of the Great Valley sequence formed in a fore-arc basin (Section 1.4.1). Both units were deformed and probably underwent significant strike-slip motion during the Cretaceous and early Tertiary before being uplifted during the Tertiary to their present position in the Coast Ranges. Franciscan (lower plate) and Great Valley sequence (upper plate) rocks are separated by the Coast Range thrust which dips to the northeast. Crustal thickness in The Geysers area is about 24 km (*Oppenheimer and Eaton*, 1984).

Franciscan rocks in The Geysers geothermal area record the early tectonic history of the area. Typically, old high-angle faults within thrust packets are truncated by individual thrusts bounding these thrust packets. These in turn are truncated by young, high-angle faults of the San Andreas system (*Thompson,* 1992). The thrust packets formed because of compressional deformation in a subduction regime. The structural relationship between thrust packets indicates repeated episodes of low- and high-angle faulting (*Thompson*, 1992). Young normal and strike-slip faults overprint subduction-related structures without significant displacement of the thrust packets.

Major fault zones in The Geysers-Clear Lake area trend northwest-southeast following the regional trend, and include the Maacama, Mercuryville and Collayomi fault zones (Figure 1.13). Faults within these fracture zones show complicated displacement histories on high-angle and northeasterly-dipping surfaces reflecting periods of thrusting or reverse-slip, normal faulting and predominant right-lateral strike-slip faulting (*Hearn et al.*, 1981; *McLaughlin*, 1981). The right-lateral motion on northeast-dipping faults in the Maacama fault zone, reflects displacement along a pre-existing compressional tectonic fabric formed within the Cascadia fore-arc region (*Castillo and Ellsworth,* 1993). Fault zones adjacent to the Maacama fault zone in The Geysers-Clear Lake region are thought to undergo similar strike-slip motion. Numerous high-angle faults occur between these major fault zones. Their structural trend varies from northeast, north-northwest and

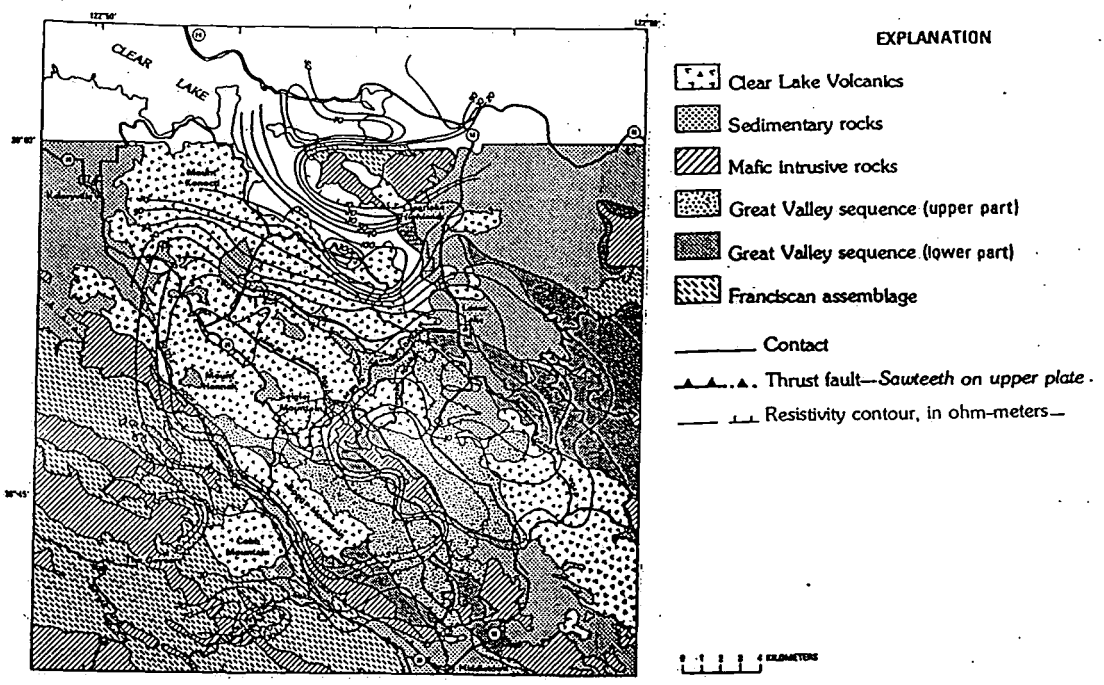

Figure 1.12. Resistivity contour map of The Geysers-Clear Lake area superimposed on the generalised geology, from *Isherwood* (1981).

northwest oriented normal faults, and northwest-trending strike-slip faults (*Hearn et al.*, 1976).

1.4 The steam reservoir

1.4.1 Geology

The Geysers steam field occupies the northwest limb of a complexly faulted antiform that plunges to the southeast (*McLaughlin*, 1981). Host rocks to the steam reservoir are primarily Mesozoic metagreywacke of the central belt of the Franciscan assemblage and upper portions of the felsite batholith (Figure 1.13). Thrust packets consisting of Franciscan melange form reservoir cap rock and the underlying steam reservoir extends to unknown depths. The steam field is bounded to the northeast and southwest by the Collayomi and Mercuryville fault zones respectively, with poorly defined field limits to the northwest and southeast (Figure 1.13) (*McLaughlin*, 1981).

Franciscan rocks in The Geysers reservoir area are divided into several fault-bounded, slab-like units based on lithology and metamorphic grade (*McLaughlin*, 1981). Franciscan units forming host rocks to the steam reservoir include structural units 1 and portions of structural unit 2 (referred to as the massive or main greywacke) with the more intensely-metamorphosed and deformed rocks of units 2 and 3 forming impermeable

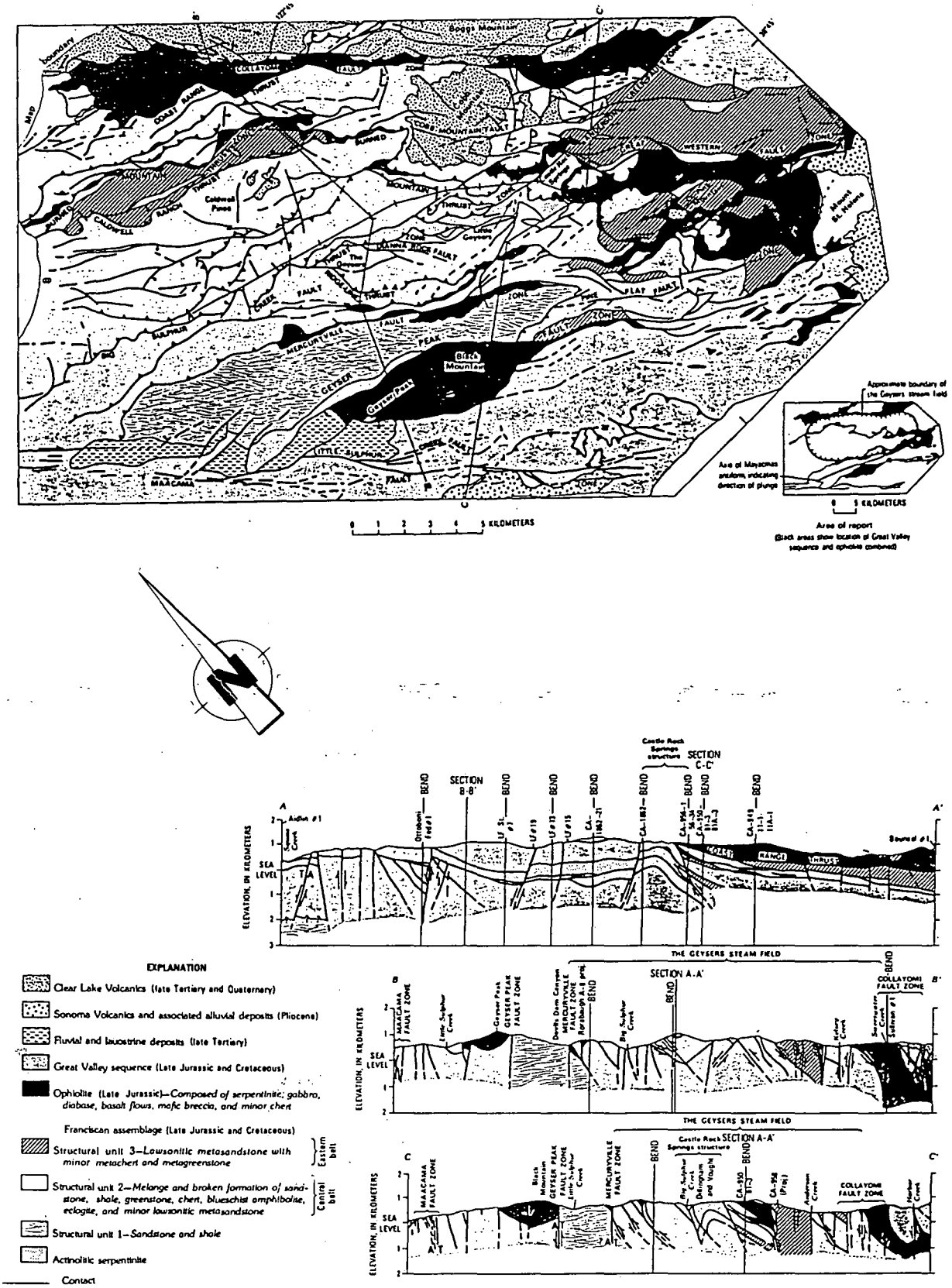

Figure 1.13. Generalised geology map and geological cross section of The Geysers steam-field.

reservoir cap rock (*Thompson*, 1992). The structurally lowest unit 1 consists of weakly metamorphosed greywacke with minor occurrences of shale. The rocks are well fractured and show penetrative shearing. They outcrop at the surface between the Mercuryville and Geyser Peak fault zones, and may extend into the reservoir. The reservoir host rocks of unit 2 consist of large fractured slabs of conglomeratic and lithic greywacke interrupted by melange sequences containing blocks of blueschist, amphibolite and eclogite along with chert, basalt and greywacke. Rocks in the highest structural sequence, unit 3, consist of extensively-recrystallised metagreywacke with penetrative schistosity making this rock a poorer reservoir rock than the structurally lower, more metamorphosed equivalents. Minor amounts of metachert and metavolanic rocks also exist within this unit. Late Cretaceous and Tertiary imbricate thrusts have juxtaposed melange blocks of Franciscan structural units 2 and 3.

Fault identification within the main reservoir greywacke is difficult since the unit is relatively homogeneous and lacks internal marker horizons. Thrust packets within structural units 2 and 3 are stratigraphically continuous with one lithology dominant (*Thompson,* 1992).

Upper portions of the hypabyssal felsic intrusive complex (the felsite batholith) also serve as host rocks to the steam reservoir (Figures 1.14, 1.15 and 1.16). This composite intrusion was emplaced into the Franciscan greywacke assemblage during the Pleistocene with reported age ranges of 0.9-2.4 Ma (*Schriener and Suemnicht,* 1980; unpublished age dates). Borehole evidence suggests that the pluton has an areal extent of at least 75 km^2 at about 2 km bsl (*Hulen and Nielson,* 1993). In plan view, the batholith is elongate with its principal axis trending northwest to southeast, roughly coincident with the axis of the steam reservoir (Figure 1.14). In cross-section, the intrusion deepens from about sea level in the southeast to about 2 km bsl in the northwest (Figure 1.15). Perpendicular to the principal axis the intrusive body has an antiformal shape with asymmetric flanks dipping at 30-40^{o} to the southwest with gentler dips to the northeast (*Gunderson*, 1992).

At least three distinct episodes of silicic magma emplacement produced the felsite batholith. The pluton is composed of three major intrusive rock types (1) biotite rhyolite porphyry, (2) orthopyroxene-biotite granite, and (3) horneblende-pyroxene-biotite granodiorite (*Hulen and Nielson*, 1993). The relationships between each of these igneous rock types, derived from borehole data, is presented in Figure 1.16. The rhyolite porphyry occupies the central and southeast parts of the batholith, forming an upward-extending boss. The rhyolite porphyry appears to grade into the orthopyroxene-biotite granite which occupies most of the northwestern part of the pluton. The biotite-granodiorite is restricted to the eastern part of the felsite. The rhyolite porphyry and granite, although geochemically similar to the overlying extrusive Clear Lake rhyolites, are too old (1.3 vs. 1.07 Ma) to be contemporaneous. The granodiorite is thought to be the magmatic

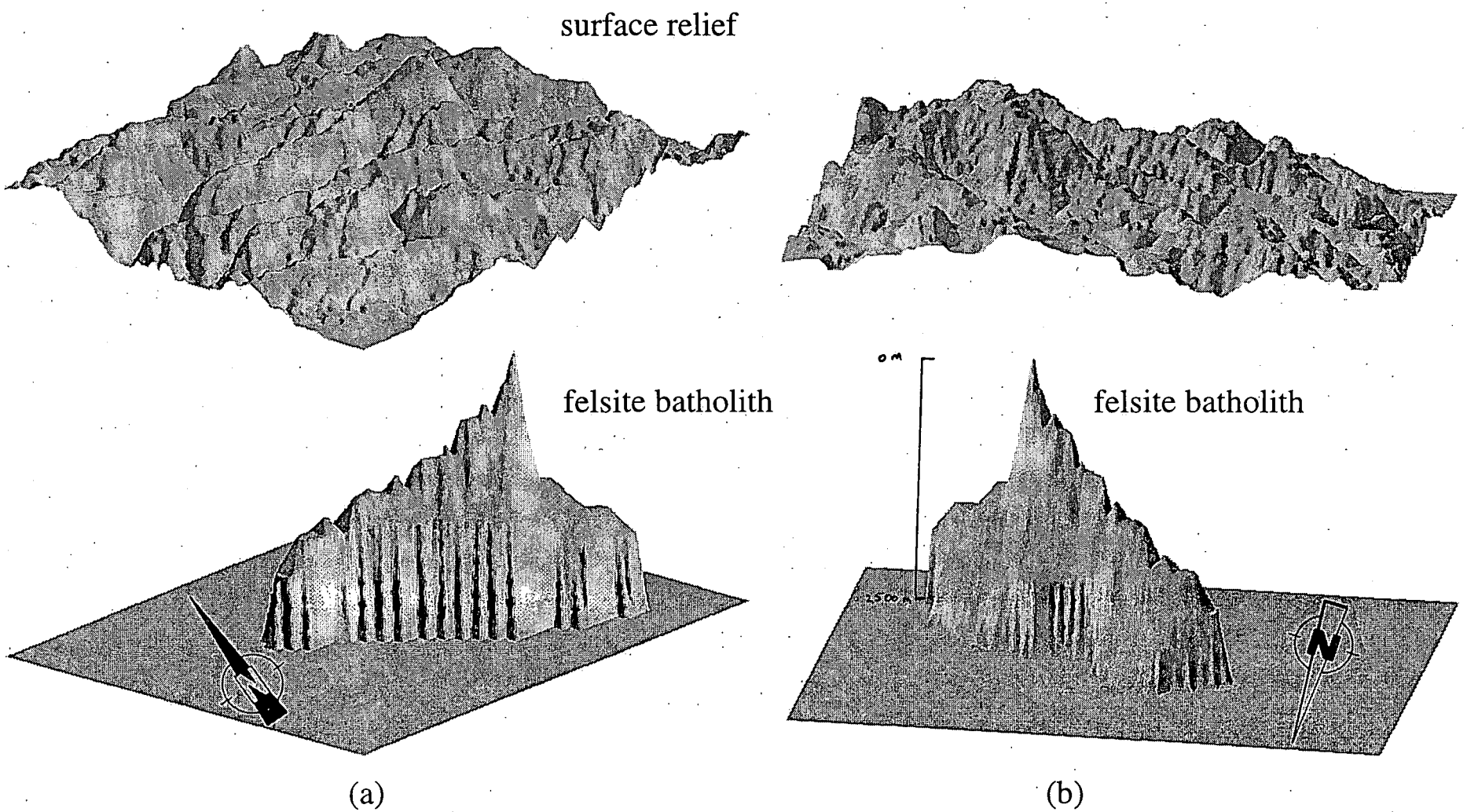

Figure 1.14. Three-dimensional perspective plots of the felsite batholith at The Geysers. Topography is exaggerated by a factor of 7. Three-dimensional images of the batholith are generated from two-dimensional contour plots (Stone, 1992). (a) The felsite batholith viewed from an azimuth of 230° and an elevation angle of 20°. (b) The felsite batholith viewed from an azimuth of 350° and an elevation angle of 20°.

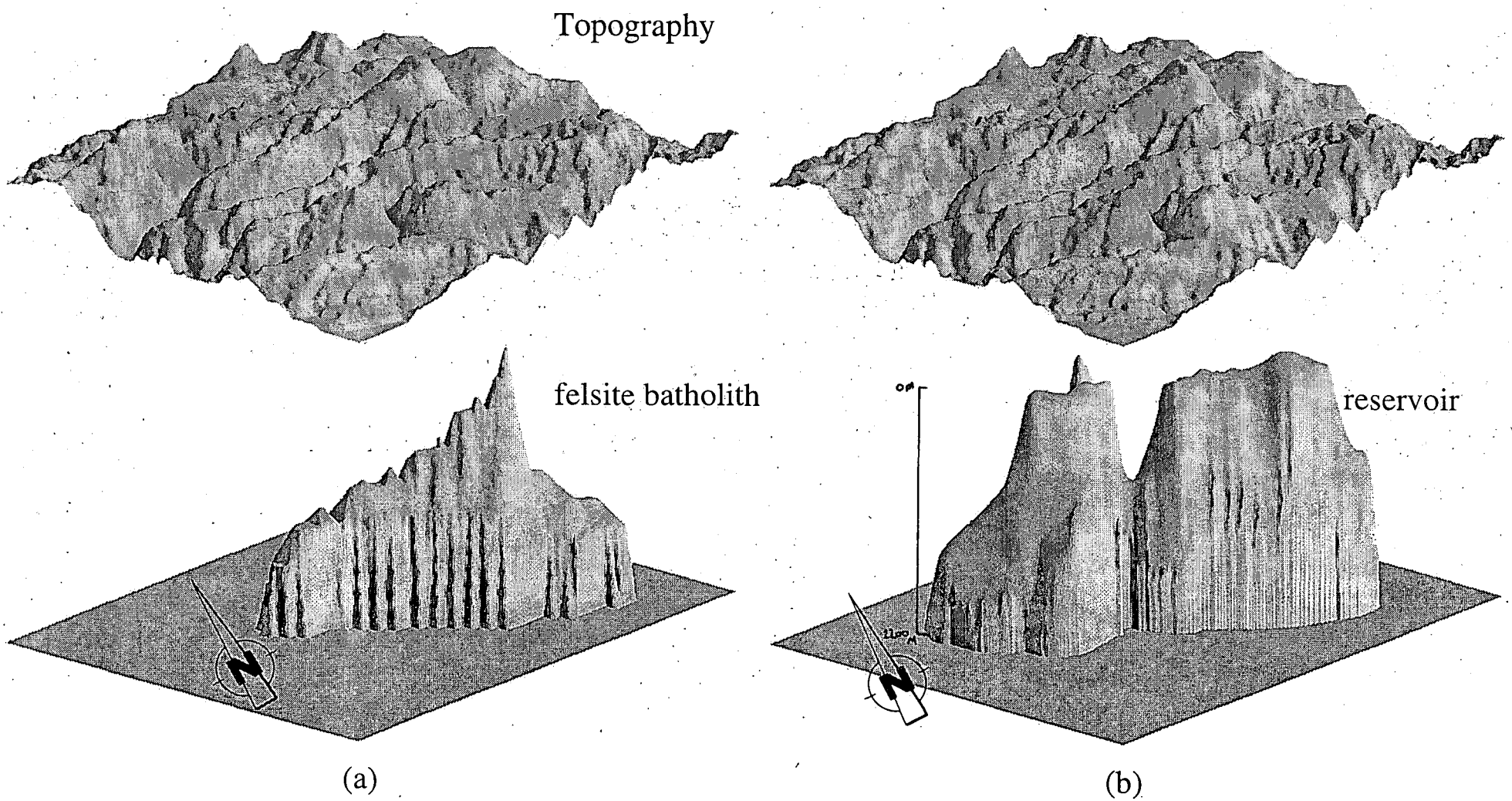

Figure 1.15. Three-dimensional perspective plots of (a) the felsite batholith, and (b) the steam reservoir, veiwed from an azimuth of 230° and an elevation angle of 20°. These images were generated from two-dimensional contour plots of the felsite batolith and steam reservoir (Stone, 1992). Topography is exaggerated by a factor of 7.

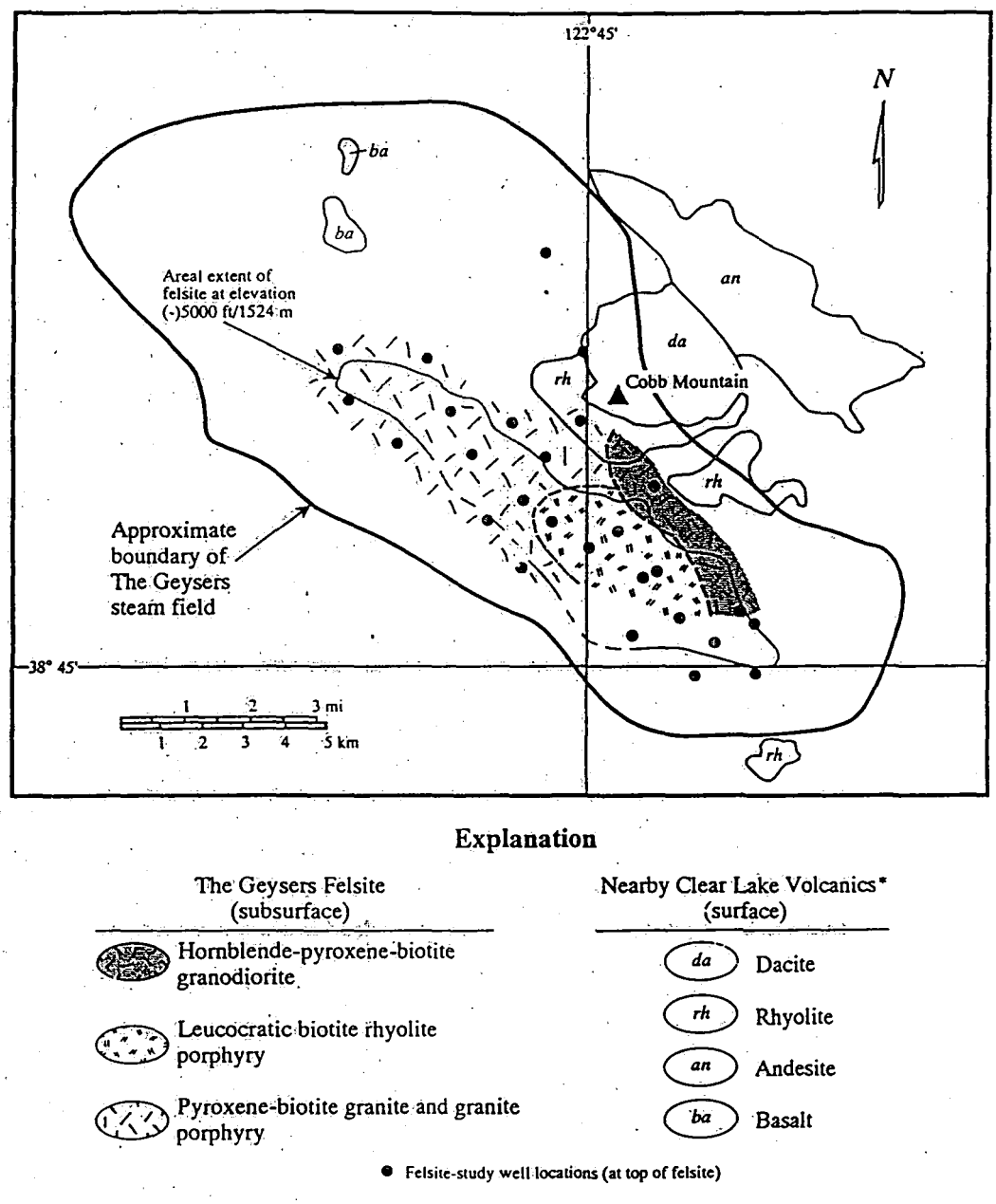

Figure 1.16. Map of The Geysers geothermal area showing the position of the subsurface felsite batholith relative to the producing area (for 1992) of the steam field. The type and distribution of igneous rocks within the intrusive body area are shown together with rocks from the Clear Lake volcanic field, from *Hulen and Nielson* (1993).

equivalent of the overlying extrusive Clear Lake dacite.

1.4.2 Formation and evolution

The Geysers steam reservoir has hosted at least three distinct hydrothermal systems:

1. An ancient regional-metamorphic system at 170-200° C heated in response to rapid burial in the presence of a normal geothermal gradient.
2. A hot-water system at 175-350° C, heated by a magmatic heat source.
3. The present, vapour-dominated reservoir, which evolved from the earlier hot-water system, with temperatures ranging between 235-342° C (*Walters et al.*, 1992).

The felsite batholith displays a close spatial relationship with the steam reservoir although it is too old to be the heat source of the present geothermal system (Figure 1.14). Heat energy is probably derived from a shallow (7-10 km bsl), cooling magma body about 0.1 Ma old (*Truesdale et al.*, 1993). The felsite was of primary importance in the development of fluid-flow characteristics in the reservoir host rocks. The vertical and horizontal fracture network within the overlying Franciscan was enhanced and intensified by repeated episodes of intrusion (*Truesdale et al.*, 1993). Processes contributing to fracture enhancement include tensional fracturing accompanying forceful intrusion, subsequent cooling of the pluton, hydrothermal fracturing and brecciation due to overpressured magma and meteoric-hydrothermal fluids heated by, or expelled from the cooling pluton, and dissolution of carbonates and other rocks within the Franciscan greywacke by circulating hydrothermal fluids. The porosity of felsite-related greywacke is greater (average 2.3%) than its felsite-free counterparts outside the reservoir (average 1.6%) (Figure 1.17) (*Gunderson,* 1992). Upper portions of the felsite, which form part of the reservoir, have an average porosity of about 2%.

The reservoir can be divided into two distinct parts (Figure 1.18):

1. A field-wide "normal" reservoir with steam temperatures of about 235° C
2. A high-temperature reservoir (HTR) with temperatures of up to 342° C. This reservoir is restricted to the northwest area of the steam field where it underlies the normal reservoir.

Depth to the top of the reservoir is larger, and the caprock is thicker (3300 m), in the northwest than in the southeast (shallowest 1100m). The normal reservoir is thin, between 600-1000 m thick, in the northwest with the first steam entries occurring at 760-1370 m bsl. Reservoir thickness increases to at least 1500 m and possibly to 5000 m in central and southeastern areas with the first steam entries at shallower depths (610-760 m bsl) than in the northwest (*Eberhart-Phillips and Oppenheimer*, 1984). The HTR and normal reservoir in the northwest are vertically separated, with a temperature difference of

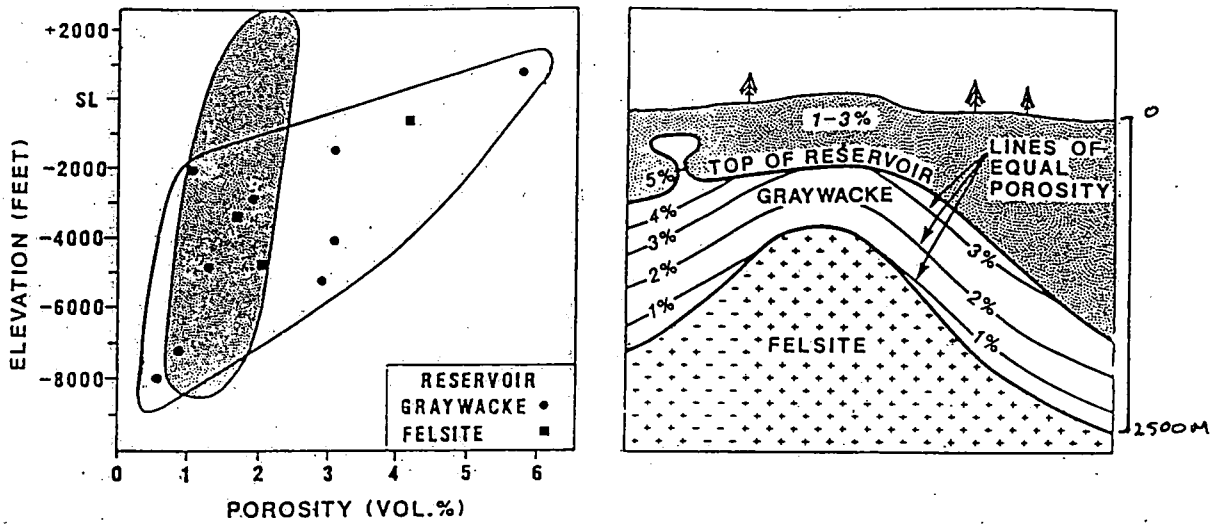

Figure 1.17. (a) Distribution of porosity with depth for felsite-free greywacke (outside the reservoir), reservoir greywacke (felsite related) and felsite. The shaded region gives porosity distribution for felsite-free greywacke. The region enclosed without fill is the combined distribution of porosity for reservoir felsite and greywacke. Square symbols are porosity measurements for the felsite and solid circles greywacke porosity measurements. (b) Schematic diagram showing the variation of porosity above the felsite. Both figures from *Gunderson* (1992).

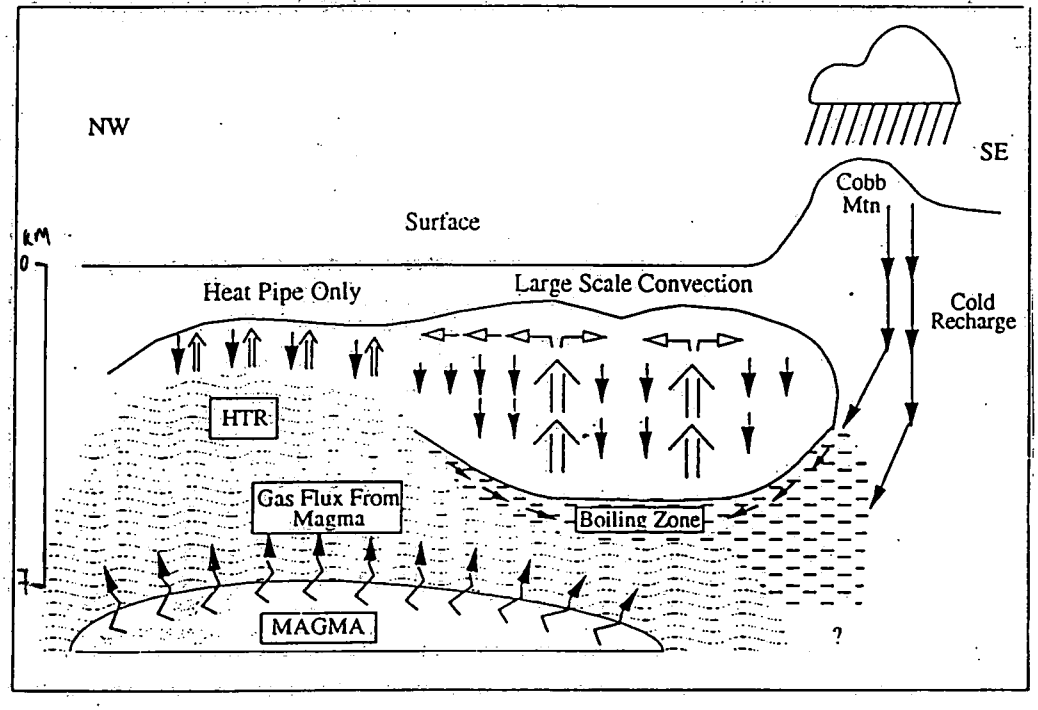

Figure 1.18. Conceptual model of the perceived processes operating within the steam reservoir, from *Truesdale et al.* (1992). The figure shows a northwest-southeast cross-section through the reservoir. A thin, "normal" reservoir sits above the high temperature reservoir (HTR) in the northwest, with the HTR absent in central and southeast areas. Open arrows: flow of steam; solid arrows: condensation and recharge. Cobb Mountain to the east provides conduits for meteoric water to recharge the reservoir. Heat is transferred by conduction from an unknown, but probably magmatic, heat source at depth.

100° C occurring over a 100-200 m depth interval (*Truesdale et al.*, 1993). This results from more efficient heat transfer in the normal reservoir compared to the conductive heat transfer in the HTR. Steam pressure is the same in both, suggesting that the reservoirs are connected and a low-permeability zone is absent. The rock type, and secondary mineralogy are also non-diagnostic of the HTR. The boundary between the HTR and normal reservoir is described as a transient thermodynamic zone (*Walters et al.*, 1992). A causal relationship is inferred between the high concentrations of hydrogen chloride, carbon dioxide and methane gas in steam from the northwest Geysers and the paucity of surface geothermal manifestations in this area. This contrasts with the central and southeast Geysers.

Three boiling centres instead of a continuous zone of boiling brine are thought to exist in the central and southeast areas (*Truesdale et al.* 1993; *White et al.*, 1971). Water flashes to steam in the boiling zones, flows upwards and condenses at the top of the reservoir before returning to boiling centre (Figure 1.18). Both the high heat-flow produced by condensing steam and low mass flow out of the system resulting from this process describe the "heat-pipe" effect (*Truesdale et al.* 1992). Heat is transferred from the condensation zone to the surface by conduction. Large-scale convection that is present in the central and southeast areas is absent in the northeast.

Several models have been developed to explain the formation of the normal and HTR at The Geysers. Shallow emplacement of the felsite body in the central and southeast Geysers produced a fracture system which reached the Earth's surface in these areas (*Walters et al.*, 1992). This allowed venting and decompression of the liquid-dominated geothermal system and initiated boiling in the central and southeast Geysers to form the normal reservoir. The reservoir lost most of its original gas and was flushed by meteoric water. In contrast, the fracture system associated with emplacement of the felsite body in the northwest is deeper and did not reach the surface. The reservoir in this area may have evolved more slowly, venting at the surface along tectonic faults and through fracture communication with the normal reservoir in the central Geysers. Venting was enhanced artificially by extensive commercial steam extraction in the central areas of the field, though the poorer surface connection in the northwest ensured that less non-condensable gas was vented and dilution by meteoric water was less important.

The HTR may also be a fossil of an earlier liquid-dominated system that is still cooling, with the result that temperatures in the two reservoirs have not been able to reach equilibrium as quickly as pressure (*Walters et al.*, 1992). Alternatively the liquid saturation zone in the HTR is absent and water supplied from the normal reservoir above is evaporated on the hot dry rocks in the HTR, heated by conduction from a deeper magmatic source (*Truesdale et al.*, 1993). Noble gas isotope studies found that a portion of the high gas concentrations in the HTR is caused by active degassing of an underlying

magma body and *Kennedy and Truesdale* (1994) suggested the HTR was formed by rapid heating and boiling of the existing reservoir liquid caused by magma injection.

1.4.3 Geophysics

Most workers agree that the enclosed negative gravity anomalies (Section 1.3.2) are probably produced (in part or totally) by a partially-molten silicic magma chamber at mid-to-deep crustal levels (*Isherwood,* 1981; *Blakely and Stanley,* 1993). What is less certain is the contribution of low-density bodies in the upper crust. Some (*Isherwood,* 1981) suggest density contrasts in the upper 2-3 km of the crust are insufficient to contribute to the anomaly while others disagree (*Blakely and Stanley,* 1993).

A wide range of seismic techniques applied to The Geysers geothermal reservoir aimed to improve understanding of both reservoir structure and geothermal processes. Three-dimensional local earthquake tomography modelling techniques utilise the continuous, low-magnitude seismic activity within The Geysers geothermal area (Section 4.4). Reflection and refraction seismic surveying techniques have rarely been used within the geothermal area because of the structural complexity and heterogeneity of the geology and because of rough surface terrain. Reflection profiles in the southeast Geysers imaged an anticlinal trap feature. A deeper reflecting horizon (<4 km) was interpreted as a tectonic boundary within the Franciscan assemblage (*Denlinger and Kovach,* 1981). Refraction profiles revealed anomalously high *P*-and *S*-wave velocities and low attenuation compared to regional values at shallow depths (<3 km) in the production zone (*Majer and McEvilly*, 1979). Controlled-source vertical seismic profiling measured 11% shear-wave anisotropy attributed to fractures (*Majer et al.*, 1988). Shear-wave splitting from local earthquakes recorded in The Geysers geothermal field shows seismic anisotropy is distributed in a complex geographic pattern, averaging 4% in the upper 1.5 km (*Evans et al.*, 1995).

Geodetic studies indicate horizontal compression and vertical subsidence related to the extraction of liquid from the reservoir (*Lofgren*, 1981). A maximum subsidence rate of about 3 cm/year and horizontal contraction rate of 2 cm/year correlate with the most intensely-exploited part of the steam field. The pre-1980 steam production rate was about 50% less than post-1980 production rate so following this study the rates of contraction and vertical subsidence probably increased significantly.

Resistivity surveys (unpublished data, *Stanley and Jackson,* 1973; see *Stanley and Blakely*, 1995) within the production area show that rocks associated with the Franciscan melange have highly variable resistivity values compared to the conductive Great Valley sequence in the Mt. Hannah region (Figure 1.19). Low-resistivity values correlate with altered, unmetamorphosed greywacke and high values are attributed to greenstone and

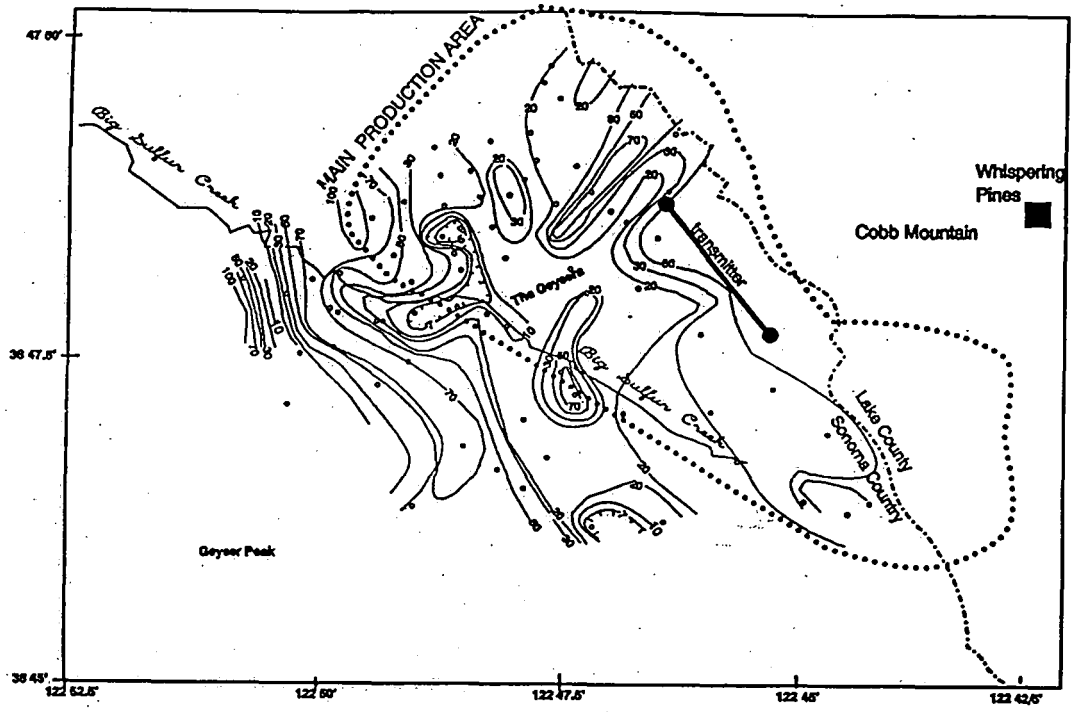

Figure 1.19. Resistivity map of The Geysers production area, from *Stanley and Blakely* (1993). Contours in ohm-m.

metagreywacke. The felsite batholith could not be defined since the maximum depth of penetration was 2 km.

1.4.4 The heat source

The Geysers steam field derives heat from a source at depth which could be solidified magma or magma chambers and fluids. Heat is transferred by convection within the reservoir and through the overlying caprock by conduction. The felsite batholith is the most obvious candidate for this heat source but it is too old (>1.0 Ma). Its presence does suggest that partial melts or magma bodies may exist nearby. Early geophysical surveys using gravity and seismic methods (Section 1.3.2) suggested that a body of partial melt dipping to the west exists at depth under The Geysers-Clear Lake region (*Oppenheimer and Herkenhoff*, 1981). Recent studies provide the most complete upper-crustal model detailing the heat source and its connectivity with the surface (*Stimac et al.*, 1992; *Stanley and Blakely*, 1993). A geological sketch combining geophysical interpretations with a model of the magmatic system in the area developed using petrologic evidence proposes that basalt dykes fed a mafic magmatic system in the lower to middle crust, initiated by

upwelling in the asthenosphere after the passage of the MTJ at about 3 Ma (Figure 1.20) (*Stanley and Blakely,* 1993; *Stimac et al.*, 1992). Differentiation within the primary mafic zones produced an upper layer of silicic crystal mush separated from the lower mafic magma by a hybrid zone.

1.4.5 Commercial exploitation

The name The Geysers is misleading, because no erupting hot springs exist. In 1847 the explorer William Bell Elliot first discovered the area and reported that he thought he had come upon "the gates of hell". Although plumes of steam leaking from fumaroles in the ground were misinterpreted as geysers, the area retains the name The Geysers.

The Geysers geothermal area has undergone varying degrees of commercial exploitation over the past 140 years. In the 1860's a resort hotel south of Big Sulphur Creek (Figure 1.13) took advantage of the numerous fumaroles and hot water springs. Steam was first used in electrical power production to supply the resort as early as the 1922. Wells drilled north of Big Sulphur Creek supplied steam to a steam-engine-driven generator which generated about one kilowatt. The project was abandoned around 1940 because the abrasive and corrosive nature of the steam destroyed pipes carrying the steam and the steam turbines themselves.

The most recent large scale development presently supports the largest complex of geothermal electricity generating plants in the world, supplying 6% of California's power and accounting for 75% of all installed geothermal generating capacity in the United States (*Kerr,* 1991). The concept of exploiting natural geothermal systems such as The Geysers to generate electricity is a relatively simple one (Figure 1.21). Water trapped in the rocks, fractures and pores is heated by a deep magmatic source. An impermeable caprock retains the majority of steam within the reservoir. Production wells drilled through the caprock and into the reservoir allow steam to flow into turbines at the surface, thereby generating electricity. Spent steam cools in a condenser. Commercial development of The Geysers appealed to both developers and environmentalists with its offer of unlimited, cheap, pollution-free power production. However, poor resource management during the commercial development phase resulted in a (currently) irreversible decline in steam production. Liquid reserves are converted to steam at a much faster rate than the reservoir can replenish them. In effect the reservoir is boiling dry. The maximum installed generating capacity of the field in 1989 was 2043 MW. Present steam production can support only about two-thirds of the 1989 capacity. Field developers now concentrate their efforts on attempting to slow the field-wide steam pressure decline.

The present large-scale commercial exploitation of the geothermal field commenced in the mid 1950's (Figure 1.22). The development of new stainless steel alloys

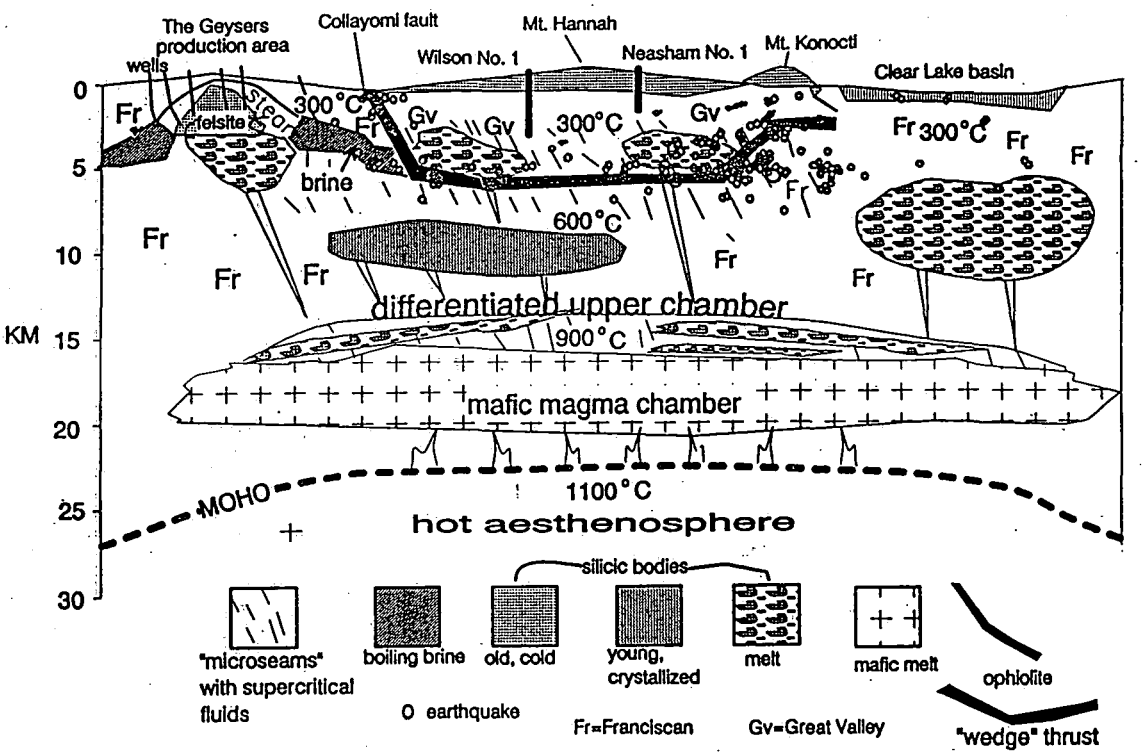

Figure 1.20. Schematic diagram showing the perceived distribution and relationship of magma bodies and igneous intrusions in the lithosphere below The Geysers-Clear Lake area which supply heat to the geothermal system, from *Stanley and Blakely* (1993).

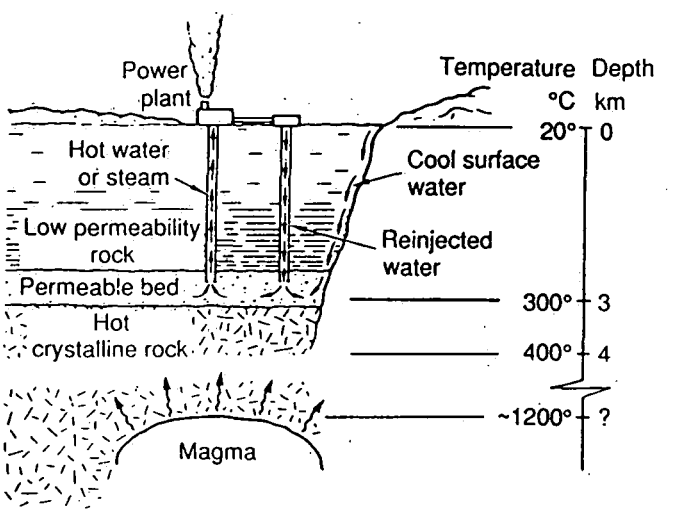

Figure 1.21. Schematic diagram showing how water heated to boiling point by a deep magmatic source is extracted in the form of steam and used to generate electrical power.

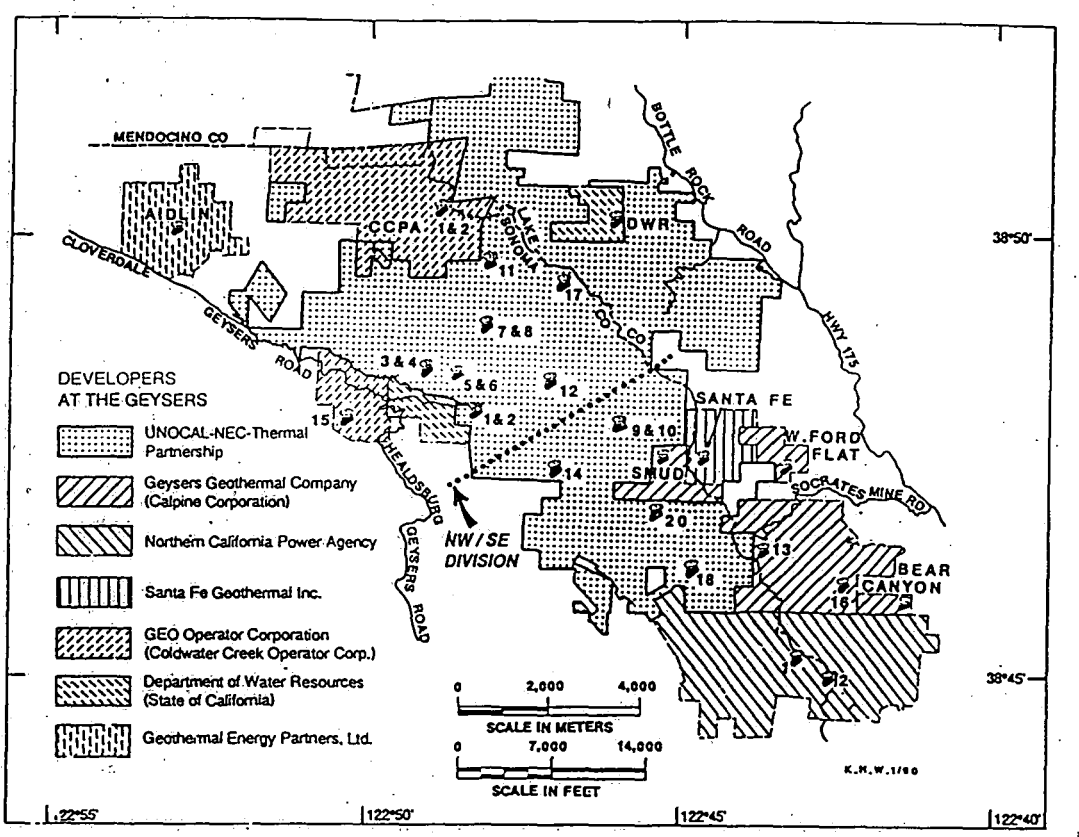

Figure 1.22. Map of The Geysers production area detailing the area operated by each of the steam field developers, from *Barker et al.* (1992). The location of power generating units is indicated by the symbol with associated number. Information on the generating units is contained in Table 1.3.

that could withstand the corrosion overcame many of the earlier production problems. A drilling program initiated in 1955 had, by 1958, sufficient wells to supply steam to a small electrical power generating unit. The first Pacific Gas and Electricity (PGE) Utility (Unit 1, a 12 MW power unit) went into commercial production in September 1960, using steam supplied by a consortium of field developers. The growth of generating capacity at The Geysers from this first unit did not follow a predetermined program but can generally be divided into three phases (Table 1.2). The locations of power stations and of areas leased by the field developers who supply the steam are shown in Figure 1.22. Details of their generating capacity and installation histories are presented in Table 1.3. Growth in generating capacity was modest throughout the 1960's (phase 1) with steam production increasing from a rate of 0.1×10^6 kg/hr in 1960 to 0.726×10^6 kg/hr in 1968, and remaining constant at this level through mid-1970. The arrival of the UNOCAL Corporation in 1971 marked the beginning of a sustained period of growth in electrical power production during phase 2. From 1971-81 twelve power plants were installed,

increasing average generating capacity at a rate of 67 MW/yr to an installed generating capacity of 943 MW. Mass steam withdrawal mirrored increases in power production, with the average withdrawal rate increasing by 0.53×10^6 kg/hr/yr to about 6.58×10^6 kg/hr by 1981. In 1982, electrical power generation entered its third phase of development, with fourteen power plants installed between 1982-89, representing an average power production increase of 150 MW/yr to a total installed capacity of 2043 MW. Steam production during the third phase doubled, increasing at a rate of 1.16×10^6 kg/hr/yr and peaking at 13.61×10^6 kg/hr in mid-1987.

Table 1.2. History of commercial development at The Geysers geothermal area (from *Barker et al.*, 1992)

Development phase	Generating capacity installed, MW	Period	Yearly increase in power generation, MW
1	82	1960-1968	10
2	861	1969-1981	67
3	1100	1982-1989	150

A decline in steam-flow rates in some wells was the first indication that power production at The Geysers could not be sustained indefinitely. Initially local reductions in steam pressure took time to spread across the reservoir, with the result that new power units were installed up until 1989. Since 1987 steam production decline rates for UNOCAL-NEC-Thermal (UNT) leases averaged 15%/yr in the southeast and 7%/yr in the northwest with a field-wide decline averaging about 11%/yr. The variation in decline rates results from the large-scale expansion in production in the southeast throughout the 1980's. The steam pressure has decreased dramatically in certain parts of the field from pre-production levels, *e.g.*, >3.5 MPa to <1.38 MPa by 1988 (*Barker et al.*, 1992). Power production is presently less than 1500 MW and five of the older units have been decommissioned (Table 1.3).

Field operators have been forced to develop new strategies, aimed at extending the life of the field, which amounts to slowing the decline in steam production. No new wells are to be drilled on UNT leases, due to their prohibitive cost ($1.5 million each) for perhaps only a marginal gain in steam production and total recovery. Heat within the reservoir is largely stored in the rock, rather than in water, and depletion is therefore largely a consequence of loss of liquid. One of the most practical and successful solutions to slowing the steam pressure decline has been to replace the liquid mass withdrawn from the reservoir. An important consideration with this process is that injection must proceed

Table 1.3. Power generating units operating at The Geysers (from *Barker et al.*, 1992).

Power generating unit	On-line for commercial operation	Steam supplier	Gross capacity (MW)	Cumulative capacity (MW)
PGE-1	09-1960	Retired 1991	12	12
PGE-2	03-1963	Retired 1992	14	26
PGE-3	04-1967	Retired 1992	28	54
PGE-4	11-1968	Retired 1992	28	82
PGE-5	12-1971	UNT	55	137
PGE-6	12-1971	UNT	55	192
PGE-7	11-1972	UNT	55	247
PGE-8	11-1972	UNT	55	302
PGE-9	11-1973	UNT	55	357
PGE-10	11-1973	UNT	55	412
PGE-11	05-1975	UNT	110	522
PGE-12	03-1979	UNT	110	632
PGE-15	06-1979	Retired 1989	62	692
PGE-13	05-1980	Calpine-SRGC	138	829
PGE-14	09-1980	UNT	114	943
PGE-17	12-1982	UNT	117	1062
NCPA-1	01-1983	NCPA	110	1172
PGE-18	02-1983	UNT	119	1291
SMUDGEO-1	10-1983	GGC	72	1363
Santa Fe	04-1984	SFI	80	1443
DWR-Bottle rock	03-1985	DWR	55	1498
PGE-16	10-1985	Calpine-SRGC	119	1617
PGE-20	10-1985	UNT	119	1736
NCPA-2	11-1985	NCPA	110	1846
CCPA-1	05-1988	GEO	65	1911
Bear Canyon	09-1988	GGC	20	1931
CCPA-2	10-1988	GEO	65	1996
West Ford Flat	12-1988	GGC	27	2023
Aidlin	06-1989	GEP	20	2043

Explanation of abbreviations: CCPA: Central California Power Agency; DWR: California Department of Water Resources; GEO: Geothermal Energy Operator; GEP: Geothermal Energy Partners; GGC: Geysers Geothermal Corp.; NCPA: Northern California Power Agency; PGE: Pacific Gas and Electricity; SFI: Santa Fe International, SMUD: Sacramento Municipal Utility District; UNT: UNOCAL-NEC-Thermal.

in such a way as to avoid extensive chilling of rock surfaces in the vicinity of the injection well. Otherwise this could lower short-term production. Steam condensate had been "injected" into the reservoir as early as 1969 to meet environmental regulation regarding disposal of corrosive condensate (*Goyal,* 1995). The reservoir pressure at The Geysers is actually lower than hydrostatic pressure, so injection simply means pouring water down non-producing boreholes. A condensate reinjection program initiated in the 1980's has been returning about 25% of extracted steam and fresh water from Big Sulphur Creek back to the reservoir. More recently a pipeline has been constructed to carry treated sewage from local sources to the southeast Geysers for reinjection, however, this will not become operational until Spring, 1997. Field operators have had both successes and failures with injection. Success depends on fracture distribution, rock permeability, temperature, steam pressure, rock type and liquid saturation. In some cases steam recovery has increased by up to 7%, while in others operators have found water rather than steam, reaching the base of their production wells (*Barker et al.*, 1992). The benefits associated with water injection are in general moderate but long-term.

1.5 Other vapour-dominated geothermal systems

Only a few systems in the world, such as Lardarello-Travale, Italy, Matsukawa, Japan, and Kawah Kamojang, Indonesia produce saturated or slightly superheated steam with temperatures similar to The Geysers (~240° C). Very little literature exists on these areas. The Larderello-Travale geothermal area, situated about 100 km south of Florence, is exploited for commercial power production in much the same way as The Geysers (*Batini et al.*, 1985). It lies within the structurally-complex Apennines which are characterised by overlapping folds. Host rocks to the steam reservoir are Triassic evaporate deposits where permeability has been enhanced by strong fracturing during the compressive phases of the Alpine orogeny. The present tectonic regime has a component of northwest-southeast extension and northeast-southwest compression. The steam field has an installed generating capacity about 20% (430 MW) of that at The Geysers. The geothermal area has characteristic continuous, low-magnitude seismic activity (M <4). Events are shallower than 8 km bsl. Some of events are induced by reinjection of condensate into the reservoir. Declining steam pressure is accelerated by production-related activities. The Larderello-Travale geothermal area therefore displays essentially similar characteristics to The Geysers geothermal area.

1.6 Summary

The tectonics of northern California is dominated by the interaction of three

tectonic plates which meet at the MTJ. The Gorda oceanic plate subducts obliquely under North America north of the MTJ, with the Pacific oceanic plate sliding dextrally past the North American plate south of this junction. The latter plate boundary is the San Andreas fault zone.

The Geysers geothermal area lies within the San Andreas shear zone in northern California. Franciscan metagreywacke (Jurassic-Cretaceous in age) and upper portions of a Quaternary felsic pluton host the vapour-dominated reservoir with thrust-packets of Franciscan melange forming impermeable caprock. Geophysical and petrological evidence suggests that The Geysers is heated by a magmatic system in the lower to middle crust. The steam reservoir can be divided into a field-wide normal reservoir (at ~235° C) and a HTR (at ~342° C) restricted to the northwest Geysers where it underlies the normal reservoir.

Large-scale commercial development of The Geysers commenced in the 1950's and presently supplies 6% of California's electrical energy requirements. Resource over-development accelerated significant declines in steam pressure about 1987. Efforts to mitigate the decline by reinjecting condensate have been partially successful and have slowed down the decline but not reversed it. The steam field presently produces about 66% of its installed generating capacity of 2043 MW.

The Larderello geothermal area, Italy is one of the few other commercially exploited steam fields in the world. Although the commercial operation produces only about 20% of the electrical power generated at The Geysers, in many ways the two areas are similar.

Chapter 2

Seismicity

2.1 Regional seismicity around The Geysers geothermal area

California, and particularly the San Andreas fault system, experiences great earthquakes capable of enormous damage and loss of life. The last great fault rupture in northern California triggered the 1906 San Francisco earthquake (M=8.3) which devastated the San Francisco bay area and killed over 2,000 citizens. In its role as a U.S. government agency responsible for earthquake hazards, the U.S. Geological Survey (USGS) sought to improve understanding of large earthquakes and the complex fault systems generating them by initiating a program of seismic station installation in 1969 that would continually monitor and catalogue seismic activity in California. By 1979, California Network (CALNET) had reached its present-day configuration of upwards of 550 stations covering all of California. The USGS has catalogued all earthquakes $M_D \geq 1.0$ occurring in California over the last 25 years (M_D: magnitude determined by coda duration). This monitoring has proved invaluable in understanding the structure and evolution of fault systems in California.

The distribution of seismic activity in northern California is controlled by the present tectonic stress regime associated with the northward migration of the MTJ (Section 1.2). The patterns of seismicity north and south of the junction are considerably different. Earthquakes associated with the Wadati-Benioff zone to the north delineate the Gorda plate, subducting obliquely under the North American plate (*Cockerham*, 1984; *Walter*, 1986; *Castillo and Ellsworth*, 1993; *Hill et al.*, 1990) (Figure 2.1). Hypocentres

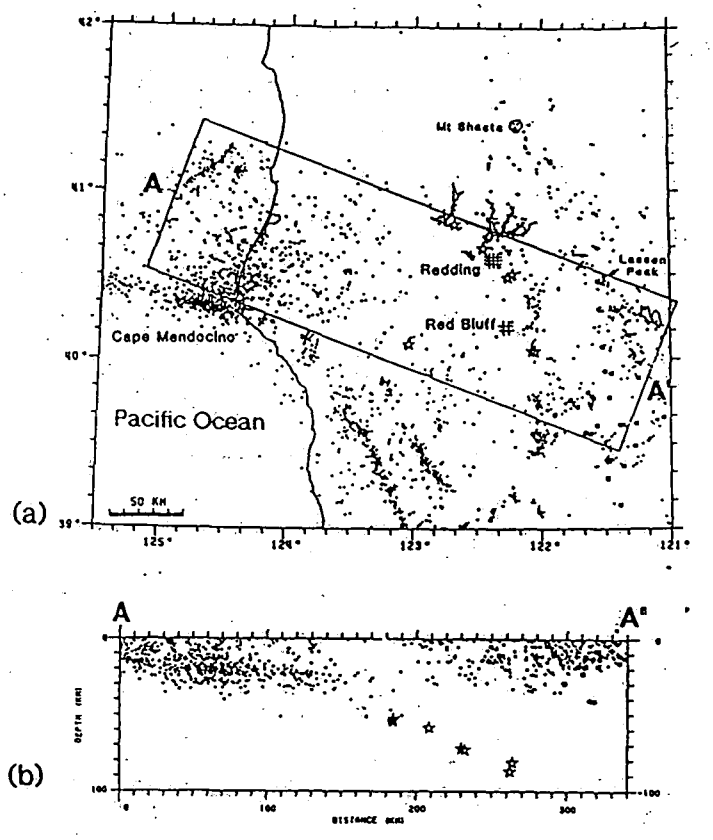

Figure 2.1. (a) CALNET epicentres $M_D \geq 1.5$ at the Mendocino Triple Junction, northern California recorded over a two year period from 1980. Shallow earthquakes are indicated by dots and intermediate-focus events with a star. The box defines the area in which hypocentres are projected onto the cross-section A-A'. From *Cockerham* (1984) and *Walter* (1986). (b) Northwest-southeast cross-section A-A' showing hypocentre distribution with depth.

progressively deepen to the east-southeast, reaching a maximum depth of 87 km, and are distinct from shallow earthquakes in the North American plate that are related to compression in a subduction environment. Epicentres cluster in the vicinity of the triple junction, becoming more diffuse to the north, east and southeast (*Hill et al.*, 1990).

South of the triple junction the San Andreas fault and its associated right-lateral shear system, which is over 100 km wide, dominates (Figure 2.2). Most of the relative plate motion is accommodated in great (M>8) earthquakes which recur at intervals of the order of a century. In the intervening time periods smaller-magnitude seismicity dominates and tends to occur along minor faults within the San Andreas shear system. For example, since the 1906 San Francisco earthquake, the San Andreas fault in northern California has been relatively aseismic with most activity restricted to faults to the east. Recent earthquake studies in the northern Coast Ranges (*Hill et al.*, 1990; *Castillo and Ellsworth*, 1993) suggest that epicentres generally define lineations east of, and sub-parallel to, the

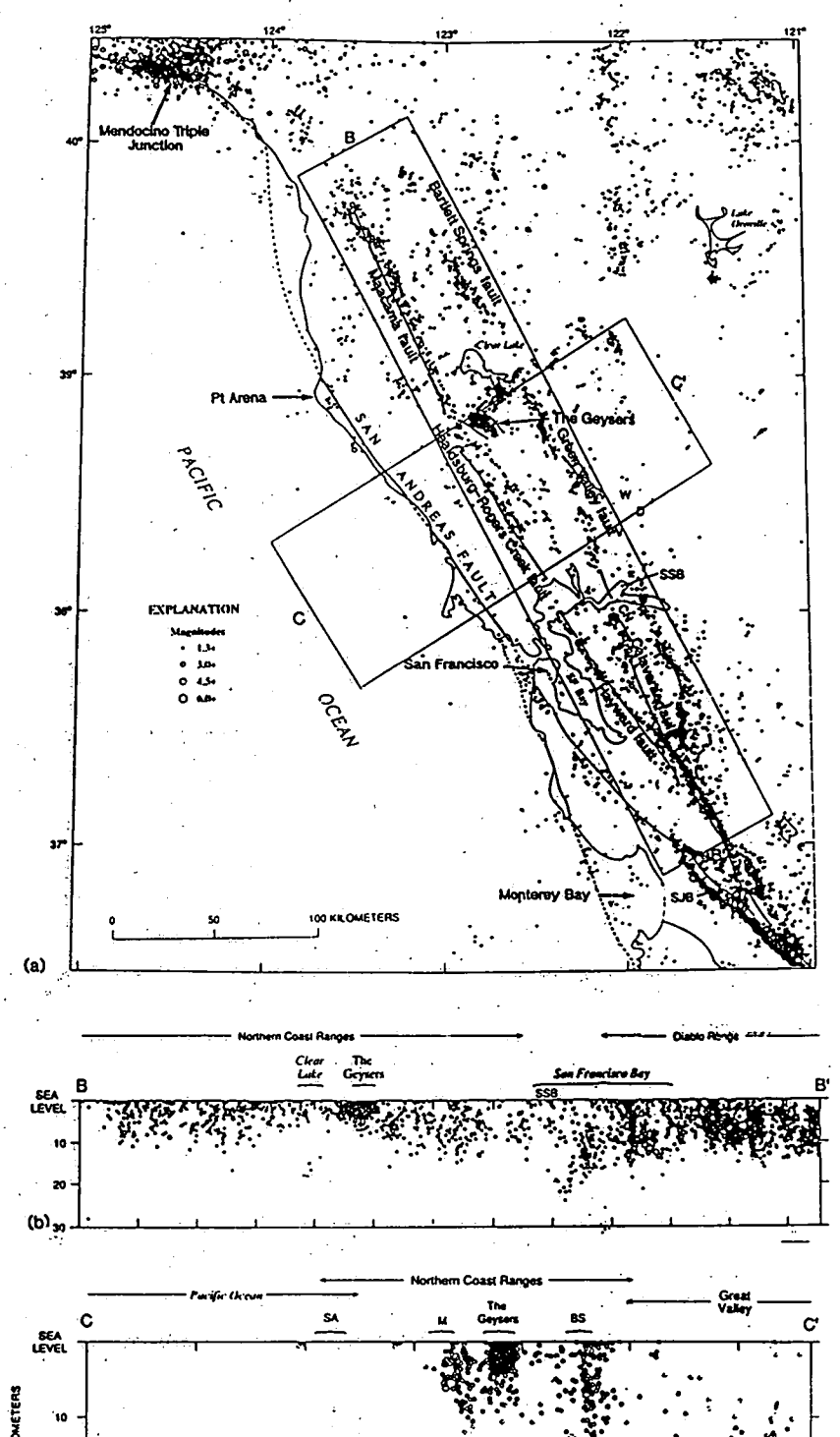

Figure 2.2. (a) CALNET epicentres $M_D \geq 1.5$ in northern California 1980-86, modified from *Hill et al.* (1990). Faults are shown as lines, dotted where concealed. The boxes define areas in which earthquakes are projected onto cross-sections B-B' and C-C'. (b) Northwest-southeast cross section showing hypocentre distribution in the northern Coast Ranges. (c) Southwest-northeast cross section of hypocentre distribution which incorporates The Geysers-Clear Lake area.

San Andreas fault (Figure 2.2). The lineations indicate faults of the San Andreas system (*e.g.*, the Maacama, Healdsberg, Rogers-Creek and Hayward faults, and the Bartlett Springs, Green Valley and Calaveras fault zones) each of which consists of sub-parallel faults in zones 2-3 km across.

Northwest-southeast longitudinal cross-sections of hypocentres along the northern Coast Ranges for the period 1980-86 indicate continuous levels of seismic activity and an undulating seismogenic base which is shallowest under The Geysers, and increases to about 10 km in the northwest and 12-13 km to the southeast (*e.g.*, Figure 2.2b) (*Hill et al.*, 1990). A complementary transverse depth section shows that seismicity constrains both the Maacama and Bartlett Springs faults but fails to delineate the San Andreas fault zone (Figure 2.2c). Hypocentres generally deepen between these two branches of the San Andreas shear zone with earthquakes to the east extending to 10-25 km depth beneath the Great Valley. The region between the San Andreas and the western branch of the San Andreas shear zone is virtually aseismic and relates to the rigid Sebastapol block. The landward extension of the Mendocino Fracture Zone (MFZ) has a clear seismic signature marked by an abrupt shallowing in seismic activity that reflects transition to a thin, slab-deficient seismogenic crust from north to south (*Hill et al.*, 1990).

Regional seismicity studies in northern California show that The Geysers geothermal area has anomalously abundant earthquake activity, the distribution of which differs from the regional pattern (Figure 2.2) (*Hill et al.*, 1990; *Eberhart-Phillips and Oppenheimer*, 1984; *Castillo and Ellsworth*, 1993). The rate of seismicity at The Geysers is estimated to be at least 45 times the regional value, based on the CALNET catalogue (Section 2.2) (*Ludwin et al.*, 1982).

The geothermal field is bounded by tectonic faults to the northeast and southwest but seismic activity is largely restricted to the intervening, shallow (<5 km bsl) seismogenic volume (Figure 2.3). The pattern of anomalously shallow seismicity at The Geysers compared to the regional trend probably reflects the elevated temperatures associated with The Geysers-Clear Lake area producing a transition from brittle to ductile deformation at much shallower depths. There is no apparent correlation between earthquakes and major through-going faults with the distribution, at first glance, appearing diffuse and random (Section 2.4).

2.2 Seismic Monitoring at The Geysers geothermal area

Prior to 1975 monitoring of seismicity at The Geysers was restricted to temporary networks of seismometers deployed in short-duration experiments. Installation of seismometer stations forming part of CALNET in The Geysers-Clear Lake area in 1975 provided the first opportunity to monitor continuous seismic activity within the geothermal

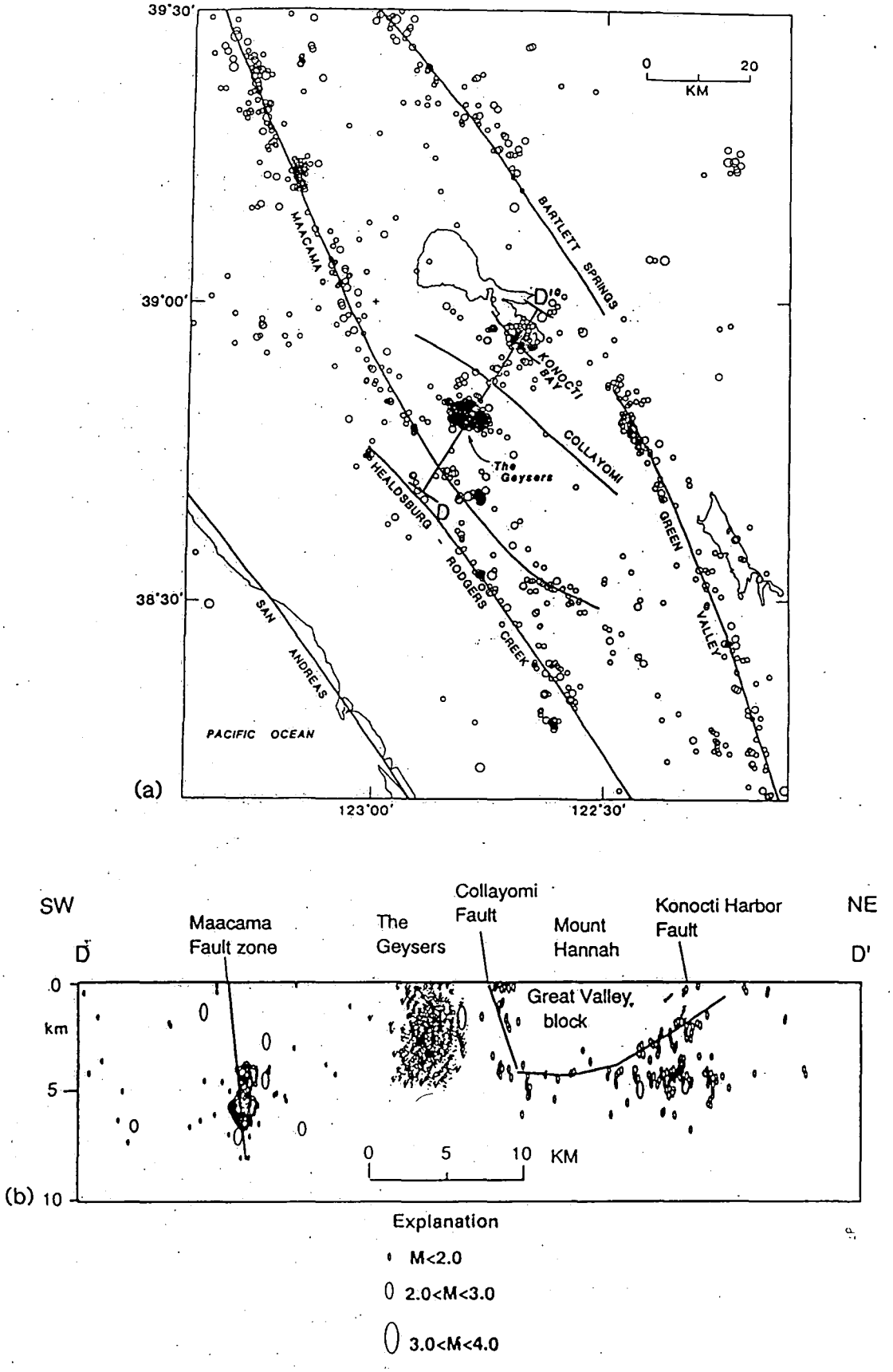

Figure 2.3. CALNET epicentres $M_D \geq 1.5$ in The Geysers-Clear Lake area 1975-81. Principal faults are indicated by black lines. D-D' is the line of cross-section used in Figure b. From *Eberhart-Phillips and Oppenheimer* (1984) and *Stanley and Blakely* (1995). (b) Southwest-northeast cross section showing the distribution of hypocentres with depth, from *Stanley and Blakely* (1995).

field (*Marks et al.*, 1978). It became clear that many more events occurred at The Geysers than could be detected by the sparse regional seismometer network. To address this problem the UNT partnership installed a dense network of stations in 1985 dedicated to monitoring microearthquakes within the steam field (microearthquake is defined by the USGS in California as having $M_D \leq 2.0$). Small, dense permanent networks in the northwest and southeast parts of the area have operated intermittently since 1988 and 1992 respectively. These networks have been supplemented periodically by temporary deployments of sensors.

Seismic monitoring first commenced at The Geysers in 1968 with the deployment of six temporary, vertical-component seismometers in an array located in the southeast Geysers (*Lange and Westphal*, 1969). The network operated for 120 hours. Two further temporary networks have been operated within the central Geysers. Seven vertical-component sensors (1 Hz) were deployed for a three-week recording period in 1971 (*Hamilton and Muffler*, 1972). The sensors recorded analogue data which were transmitted by radio signal to a central base station. A three-component sensor operated at the central base station. The WWVB time-code broadcast, and output from a time-code generator were recorded simultaneously. During a 26-day period in 1982 nine three-component sensors (4.5 Hz), were deployed in a 6 km diameter array and the data recorded digitally at 200 samples per second (sps) (*O'Connell*, 1986).

CALNET has monitored seismic activity in northern California continuously since 1969 (Figure 2.4a). The system operates >100, mostly vertical-component sensors (1 Hz) between San Francisco and the MTJ. Analogue signals from stations in The Geysers region are transmitted by microwave, radio or telephone to the western region headquarters of the USGS at Menlo Park, California. An Inter-Range Instrument Group format "E" (IRIGE) signal generator at Menlo Park creates an analogue time-code signal that is digitised at 100 sps simultaneously with analogue seismic signals. The CalTech-USGS Seismic Processing (CUSP) system decodes the digitised time code in near-real-time to time-stamp the seismic data. *P*-phase arrivals are automatically picked and hypocentres and coda-duration magnitudes calculated. Earthquakes recorded by CALNET are catalogued at the Northern California Earthquakes Data Centre (NCEDC), at the University of California, Berkeley. The database is updated daily with earthquake information recorded in the previous 24 hours. Only eight seismic stations are located within a 25-km radius of The Geysers, though more than 40 instruments regularly detect earthquakes within the geothermal area (*Eberhart-Phillips and Oppenheimer*, 1984). The CALNET detection threshold for events at The Geysers has been reduced from M_D=1.2 in 1975 to M_D=0.5 from 1981 onwards (*Eberhart-Phillips and Oppenheimer*, 1984).

The UNT partnership commenced microearthquake monitoring within the steam field in 1985. The network was expanded to cover most of the steam field by 1989 and

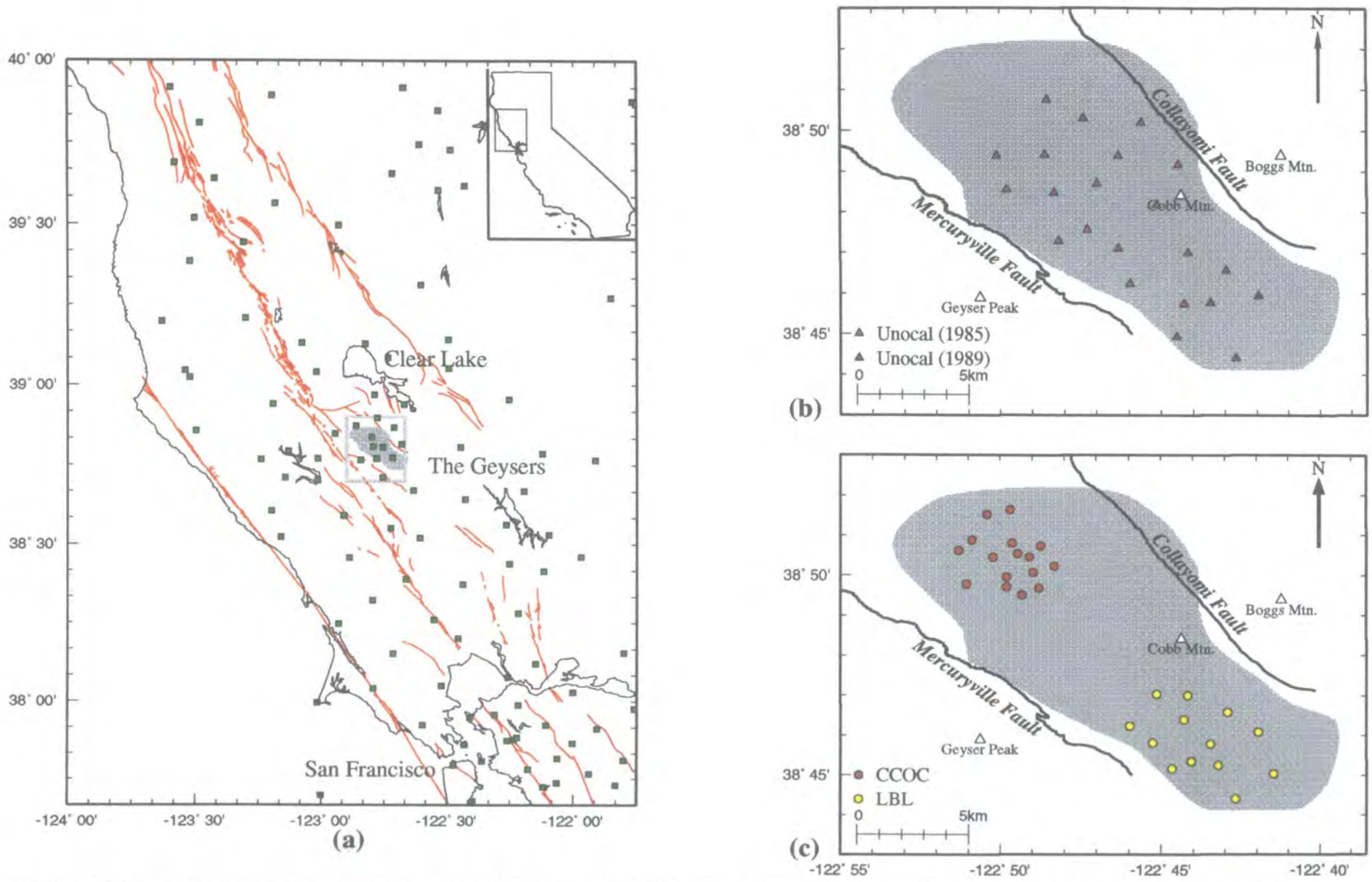

Figure 2.4. (a) Map of CALNET seismometers (green squares) in northern California. The Geysers area is enclosed by the box. Shaded area: production area; Red lines: faults. (b) Map of The Geysers production area showing the location of UNT seismomenters. Magenta triangles: stations deployed in 1985; green triangles: stations deployed in 1989; white triangles: mountains (c) Map of The Geysers showing the CCOC network (red circles) in the northwest and LBL network (yellow circles) in the southeast.

currently includes 22 sensors, 7 of which are three-component, and forms a dense, 15-km diameter array with an average station spacing of about 1500 m (Figure 2.4b; Appendix 1). High-frequency sensors (4.5 Hz) record data using analogue techniques. Construction of the seismic stations varies, with one instrument installed 85 m deep in a borehole, about 50% of the remainder at 30 m depth in boreholes, and the rest installed at the surface (*Stark and Davis*, 1996). Signals are transmitted from each station to a central processing facility via telecommunication lines and digitised at 100 sps. Earthquakes are automatically detected, recorded and processed. Hypocentres are automatically calculated and coda magnitudes determined. The detection threshold is M_D=0.2.

Two small-aperture, dense, permanent networks have recently been installed in the northwest and southeast Geysers. They are more modern than the UNT network and record digital data from three-component sensors (Figure 2.4c; Appendix 1). These presently provide the highest-quality microearthquake data available for The Geysers but their localised geographic distributions and intermittent operation (which is funding dependant) limits effective monitoring of the entire steam field. Lawerence Berkeley Laboratory (LBL) archives and interprets the seismic data recorded by both networks.

The network in the northwest Geysers was installed in 1988 by GEO and is operated by the CCOC, now the CCPA (*Romero et al.*, 1995). The 4-km diameter array contains 16 high-frequency borehole sensors and data are digitised at 400 sps. The network ceased operation in 1989 for legal and technical reasons but recommenced acquisition in October 1993 and continued for part of 1994 (*Romero et al.*, 1994). In the southeast Geysers LBL operates 13 high frequency (4.5 Hz), digital (480 sps), surface-deployed seismometers in an array 7 km in diameter (*Kirkpatrick et al.*, 1995, *Romero et al.*, 1994). The network commenced operation in 1992 and consisted of eight LBL and five Lawrence Livermore National Laboratory (LLNL) stations. This split-array arrangement was inconvenient for data acquisition and processing. In December 1993, LBL replaced the five LLNL stations to allow data from all stations to be telemetered to, and recorded at a central base station. For processing purposes UNT provides LBL with lists of events they have located in the southeast Geysers. LBL then processes only these earthquakes. This arrangement results in many of the small events recorded by the more sensitive LBL network in the southeast Geysers remaining unprocessed. The network ceased operation in December 1995.

2.3 Seismicity at The Geysers

A project investigating the theory that microearthquake activity was intimately related to geothermal systems first established that earthquakes occurred at The Geysers (*Lange and Westaphal*, 1969). The present seismic activity within The Geysers steam

field is characterised by very high levels of continuous, low-magnitude earthquake activity distributed throughout the steam production area. Approximately 140 earthquakes with $M_D \geq 1.2$ are recorded per month. The largest event recorded occurred 3 km bsl in the northwest Geysers in 1992 and had a magnitude of M_D=4.3 (NCEDC). Little information is available about earthquake activity prior to 1975, though several lines of evidence suggest the level of seismicity and its distribution within the steam field have increased dramatically since the early 1960's. *Marks et al.* (1978) compared the level of seismicity ($M_D \geq 2$) within a 60 km radius of the University of California (UC) Calistoga seismic station, northern California for two periods, 1962-63 and 1975-77, and concluded that seismic activity had more than doubled in the later study period. Although locations could not be accurately determined the discrepancy in the level of activity was attributed to increased earthquake activity at The Geysers steam field. Dramatic increases in the level and distribution of seismic activity within the reservoir for the period 1975 to present support this conclusion. Felt reports from the local population indicate that larger earthquakes have occurred more frequently within The Geysers in recent years. Minor damage has been caused to homes and other structures in the area by these earthquakes.

Maps and cross-sections showing the distribution of earthquakes $M_D \geq 1.2$ recorded for periods of one year at The Geysers are presented in Figure 2.5. The data were recorded by CALNET and extracted from catalogues at the NCEDC. The CALNET detection threshold for earthquakes at The Geysers has lowered since 1975, so the data plotted in Figure 2.5 are for events with $M_D \geq 1.2$, in which magnitude range the catalogue is complete for 1975-1995. The USGS commenced continuous monitoring of earthquakes in California in 1969. Prior to 1975 sensor coverage in The Geysers area was insufficient to detect many of the earthquakes there (Figure 2.5a). This is reflected in the small number of earthquakes in the NCEDC catalogue for The Geysers but is not an accurate reflection of the true number of earthquakes which occurred during this period.

A dramatic increase in both the intensity and spatial distribution of activity is observed in the 20 year period 1975-95 (Figures 2.5 b and l). The seismogenic volume was restricted to the central Geysers in 1975 and extends to a depth of about 5 km bsl. In time the seismic volume extended to the northwest Geysers, initially at shallow depths but increasing in depth with time. The seismogenic base in 1995 undulates across the reservoir from NW-SE, is deepest in the central Geysers at just over 5 km bsl and is less clearly defined at shallower depths to the northwest and southeast owing to the diffuse nature of seismicity in these areas.

The earliest complete record of seismicity at The Geysers indicates that activity was restricted to a well-defined area of the central Geysers with events clustering in two depth ranges (sea level-to-2.5 km bsl, and 3-to-5 km bsl) (Figure 2.5 b). This feature is conspicuous in all subsequent yearly depth sections (Figures 2.5 b-l). The seismic rate

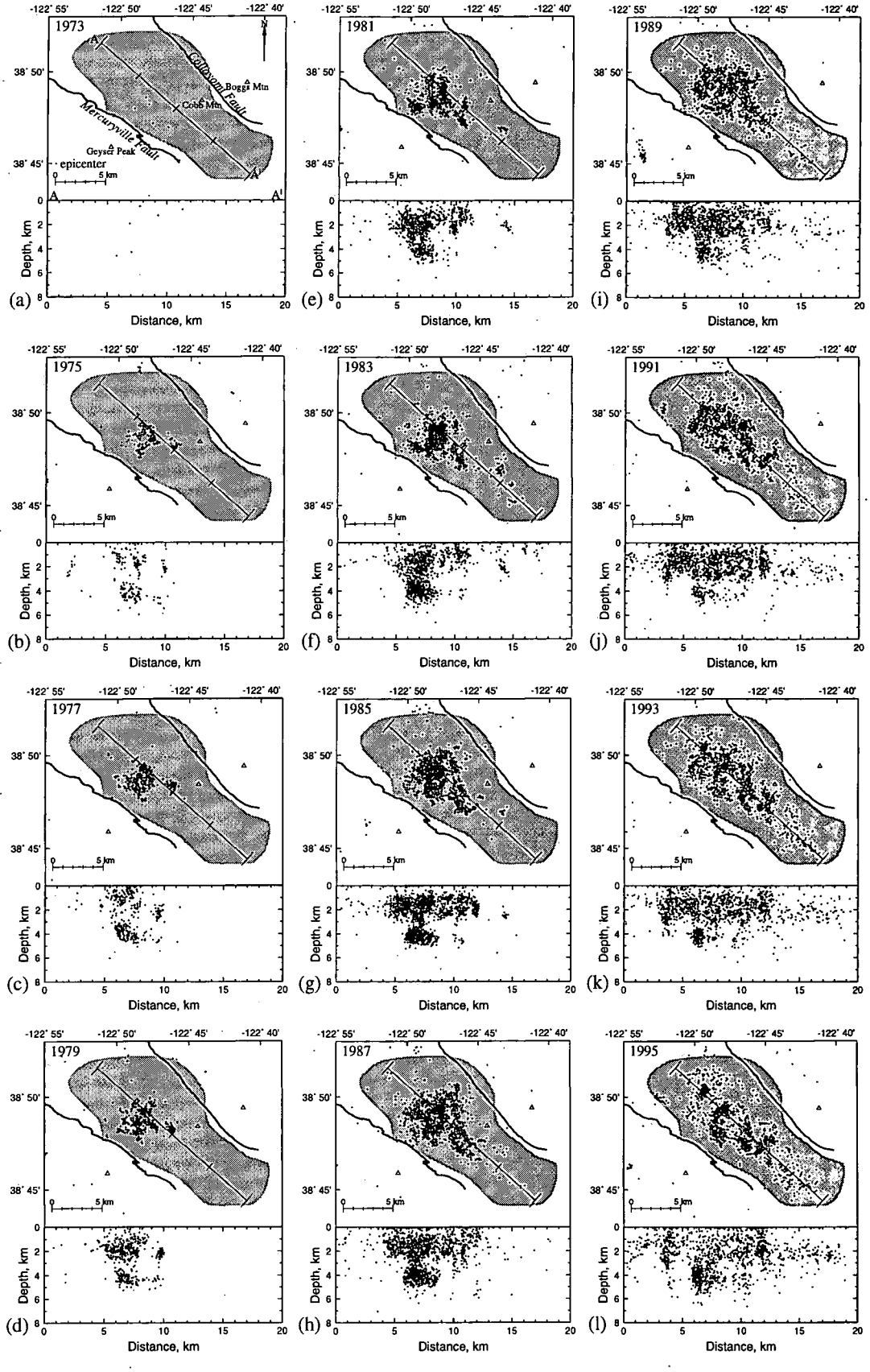

Figure 2.5. CALNET epicentre and hypocentre $M_D \geq 1.2$ maps of yearly seismicity at The Geysers geothermal area, presented at biannual intervals from 1973-95. Hypocentres located within the boundaries of the steam field are presented on the cross-section A-A'. The area enclosed by the production area is as of 1992.

increased steadily through the late 1970's, accompanied by lateral expansion of the seismically-active volume. A particularly rapid increase in both the seismic rate and the expansion rate is evident between 1981-1989 (Figures 2.5 c-d). This represents the most intense period of earthquake activity at The Geysers. The deeper seismically-active volume maintains a consistent shape during this period despite large increases in the number of events associated with it. The onset of earthquake activity in previously-aseismic areas occurred mostly at shallow levels (Figures 2.5 f-l). Spatial clustering of earthquakes first became obvious in about 1981 with a transition to more diffuse seismic activity by 1989. Clustering became more conspicuous in the 1990's and is particularly clear in 1995, along with a clear decrease in the intensity of activity in the central Geysers (Figures 2.5 j-l).

Until 1989 the northwest and southeast Geysers were largely aseismic with only a few randomly-distributed earthquakes. (Figure 2.5e-h). From 1989-95 activity increased both spatially and in intensity in both areas such that by 1993 the production area was a single well defined seismically-active volume. Earthquakes in the northwest and southeast, unlike the central Geysers, deepen with time, and the vertical biomodalism appears to be absent (See Section 7.2.1).

Some volumes within the central Geysers remained aseismic throughout this period. The horizontal aseismic horizon separating the shallow and deep seismogenic volumes (~2.5-3.0 km bsl) in the central Geysers can be traced in each of the yearly hypocentral maps for the area, *e.g.*, Figure 2.5d, g and j. This feature has been observed in previous, independent studies (*Oppenheimer*, 1986; *D. R. H. O'Connell, pers. comm.*). Maps of seismicity also indicate an aseismic zone referred to as the "dead zone" (*M. A. Stark, pers. comm.*) in the centre of the active area. The dead zone has a north-south orientation and is located between the main area of seismicity and a small sub-cluster to the east in Figure 2.5c.

2.4 Seismicity and commercial steam extraction within the steam field

Microearthquake activity at The Geysers is thought to be directly related to both commercial steam extraction and water injection, mirroring changes in production rates and strategies. Seismic activity was probably low prior to exploitation (*Oppenheimer*, 1986). This causal relationship was first proposed as early as 1972 (*Hamilton and Muffler*, 1972) and supported by later workers (*Marks et al.*, 1978; *Majer and McEvilly*, 1979; *Ludwin and Bufe*, 1980; *Allis*, 1982; *Ludwin et al.*, 1982). In the early 1980s various mechanisms were proposed to explain this association (Section 2.5). Strong evidence suggests injecting cool condensate into the reservoir may generate up to 50% of

the earthquakes recorded at The Geysers, with steam production and natural tectonic activity making smaller contributions (*Stark,* 1992). This conclusion is supported by recent independent studies which use accurate three-dimensional velocity models to calculate earthquake hypocentres (*Romero et al*, 1994; *Kirkpatrick et al*, 1995).

The relationship between microearthquakes and production-related activities, both on a field-wide and a local scale produce some striking correlations. Earthquake studies at The Geysers for the period 1975-82 found microearthquakes occurred soon after the onset of production activities in previously undeveloped aseismic areas (*Eberhart-Phillips* and *Oppenheimer,* 1984). I extended this by superimposing operating electrical power plants on each of the yearly epicentral maps (Figure 2.6). The position of the generating units does not exactly correspond to where steam is being extracted or condensate reinjected, but these activities occur in close proximity for engineering reasons. Figure 2.6b shows clearly that the seismic activity in the central Geysers correlates exclusively with the generating units operating at that time. The deepest events correlate with the area of the steam field which had experienced the longest period of production. The small sub-cluster of events to the southeast of the main cluster occur close to a generating unit there. Earthquakes in this cluster have been relocated using a refined velocity model (*Eberhart-Phillips* and *Oppenheimer,* 1984). The events migrated even closer to the power unit.

Throughout the 1980's, as each new power generating unit was installed, steam extraction accompanied the onset of seismic activity. Dramatic increases in the level of seismicity and expansion of the seismogenic volume during this period mirrors rapid increases in electrical power generation suggesting a causal relationship (Figures 2.6e-h). Seismicity in the southeast Geysers appears to have lagged commercial development there and seismic activity in this area has remained relatively low. Power production peaked in 1987, decreasing in following years in response to the field-wide steam pressure decline. Seismicity from 1989-1995 has decreased somewhat, mirroring the steam-production decline (Figures 2.6i-l). Activity in 1995 is restricted to fairly isolated clusters which can be uniquely correlated to power generating units where injection and production activities were ongoing. Areas where generating units were decommissioned underwent significant reductions in seismicity, *e.g.*, *c.f.* Figures 2.6h and 2.6l. On the western edge of the central Geysers PG&E units 1, 2, 3, 4, and 15 were decommissioned between 1989 and 1992 (see Figure 2.7 for power plant locations). A clear reduction in the level of earthquake activity is evident in that vicinity.

Another very clear correlation exists when the average rate of steam extraction is compared to the number of earthquakes (1975-95) recorded on a yearly basis (Figure 2.8). Up until 1988 the actual rate of steam extraction is published (*Barker et al.*, 1992). From 1988-95 I estimated the rate from a steam decline forecast curve (*Williamson*, 1992). From 1975-92 it is clear that the rate of steam extraction almost exactly mirrors the rate of

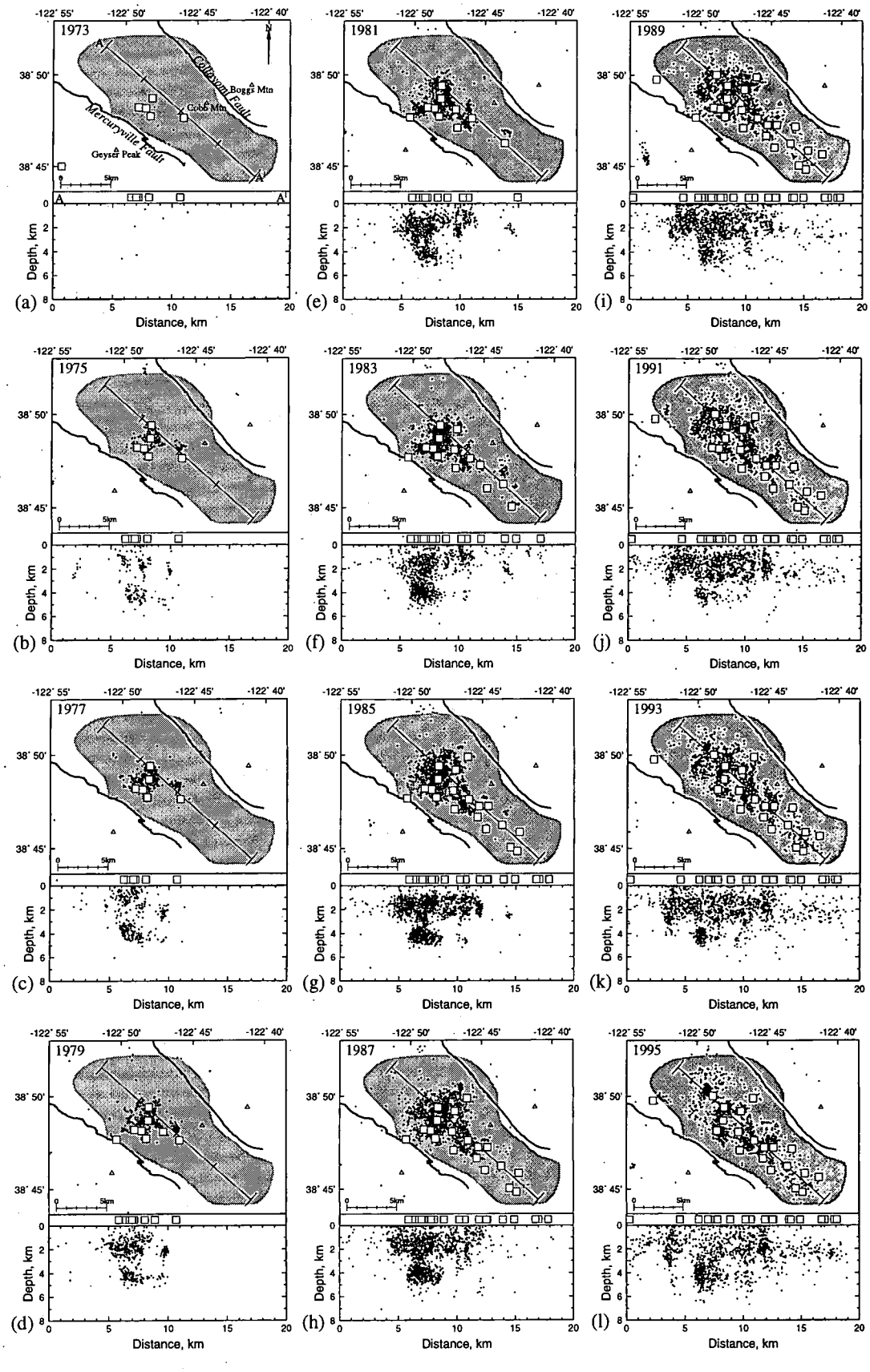

Figure 2.6. As Figure 2.5, with power generating units operating during the year presented superimposed on the yearly seismicity.

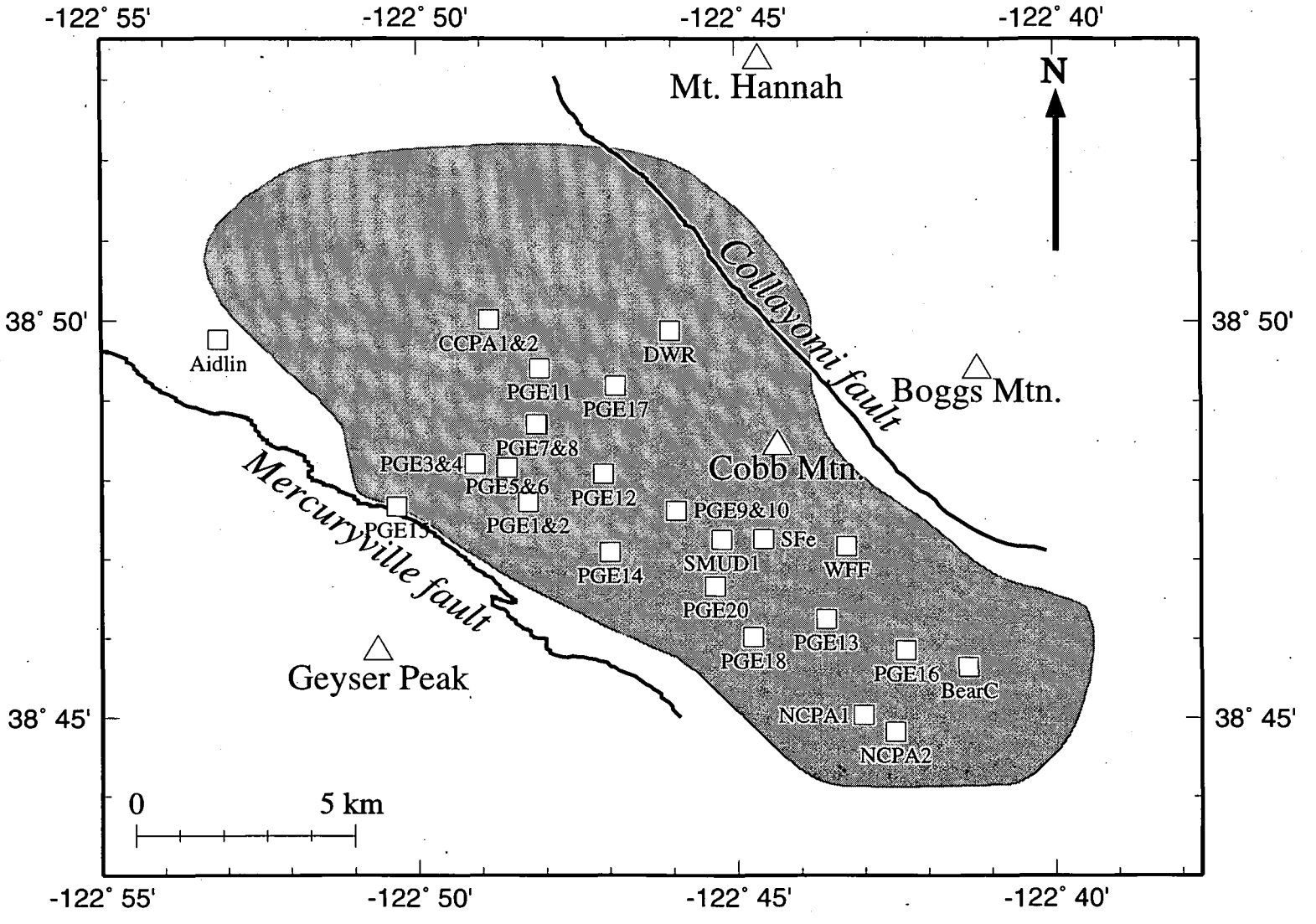

Figure 2.7. Map showing the location of power generating units at The Geysers geothermal area. Sites where two units are indicated means they are housed in the same building. Expla nation of abbreviations: BearC: Bear Canyon; WFF: SFe: Santa Fe; West Ford Flat; see also Table 1.3.

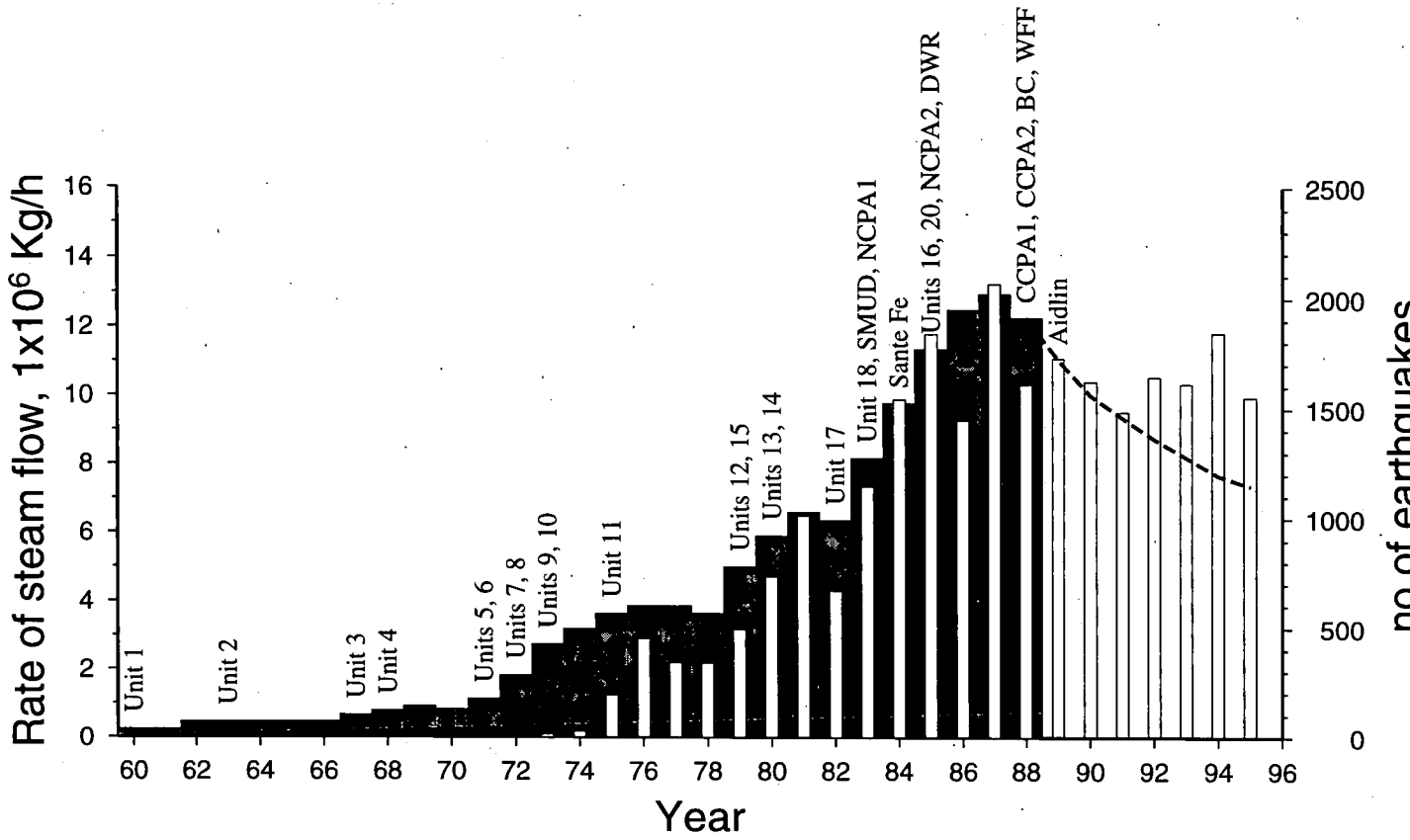

Figure 2.8. Histogram showing the average steam flow rate per hour between 1960-88 (filled columns) (modified from Barker et al., 1992). The dashed line indicates the projected steam flow rate from 1989-95 (modified from Williamson, 1992). The white columns indicate the number of $M_D \geq 1.2$ earthquakes recorded in The Geysers by CALNET between 1973-95 (from the NCEDC). Installation histories of electrical power generating units at The Geysers is indicated.

earthquake occurrence at The Geysers suggesting a strong causal relationship. The correlation appears to be poor for 1992 onwards but this may be due to changes in injection strategies which were not incorporated into the decline-curve calculations.

Microearthquake studies in the vicinity of injection wells before, during and after they were used to return condensate to the reservoir found earthquakes correlating closely with injection at depths of >1 km bsl (Figure 2.9a) (*Stark*, 1990). The correlation is even closer when three-dimensional velocity models are used to locate the earthquake hypocentres (Figure 2.9b) (*Kirkpatrick et al.*, 1995, *Romero et al.*, 1994). Microearthquake clusters extending from the base of injection wells provide three-dimensional images of the path of injected water and can be used to track its migration within the reservoir. Deeper microearthquake clusters tend to stand out from background seismicity, this can be seen particularly well in the northwest Geysers (Figures 2.5j-l).

2.5 Earthquake mechanisms at The Geysers

A variety of mechanisms related to temperature, pressure, volume and reservoir strength changes have been proposed to explain the continuous, low-magnitude seismic activity at The Geysers. It is clear that earthquake occurrence is intimately related to activities associated with commercial steam extraction but the precise mechanism(s) are poorly understood. Tectonics does contribute to the activity but the contribution of "natural" activity to the overall seismicity rate is difficult to estimate in the absence of seismic information prior to commercial exploitation and a diagnostic characteristic (*Stark*, 1990).

Changes to the shear stress field in response to volume changes associated with the removal of large amounts of fluid from the steam field may induce seismic failure within the steam field (*Majer and McEvilly*, 1979). Geodetic studies in the production area tend to support this idea with horizontal and vertical contraction correlating with the most intensely exploited part of the steam field (*Lofgren*, 1981).

Cooling in response to both steam withdrawal on a field-wide scale, and localised reinjection of relatively cool condensate, could cause a reduction in the normal stresses across fracture surfaces (*Denlinger*, 1980). Rocks at The Geysers are close to failure and small, localised changes in the stress field may be sufficient to initiate failure. Long-term injection is thought to cool the rocks surrounding injection wells sufficiently to transfer deformation from near ductile (the normal state of deformation at depths of >3 km bsl) to brittle beneath injection wells.

The *Hubbert and Rubey* (1959) mechanism, cited in many cases of induced seismicity associated with fluid injection in other geothermal systems, or the filling of reservoirs behind dams, provides another candidate mechanism for earthquake generation

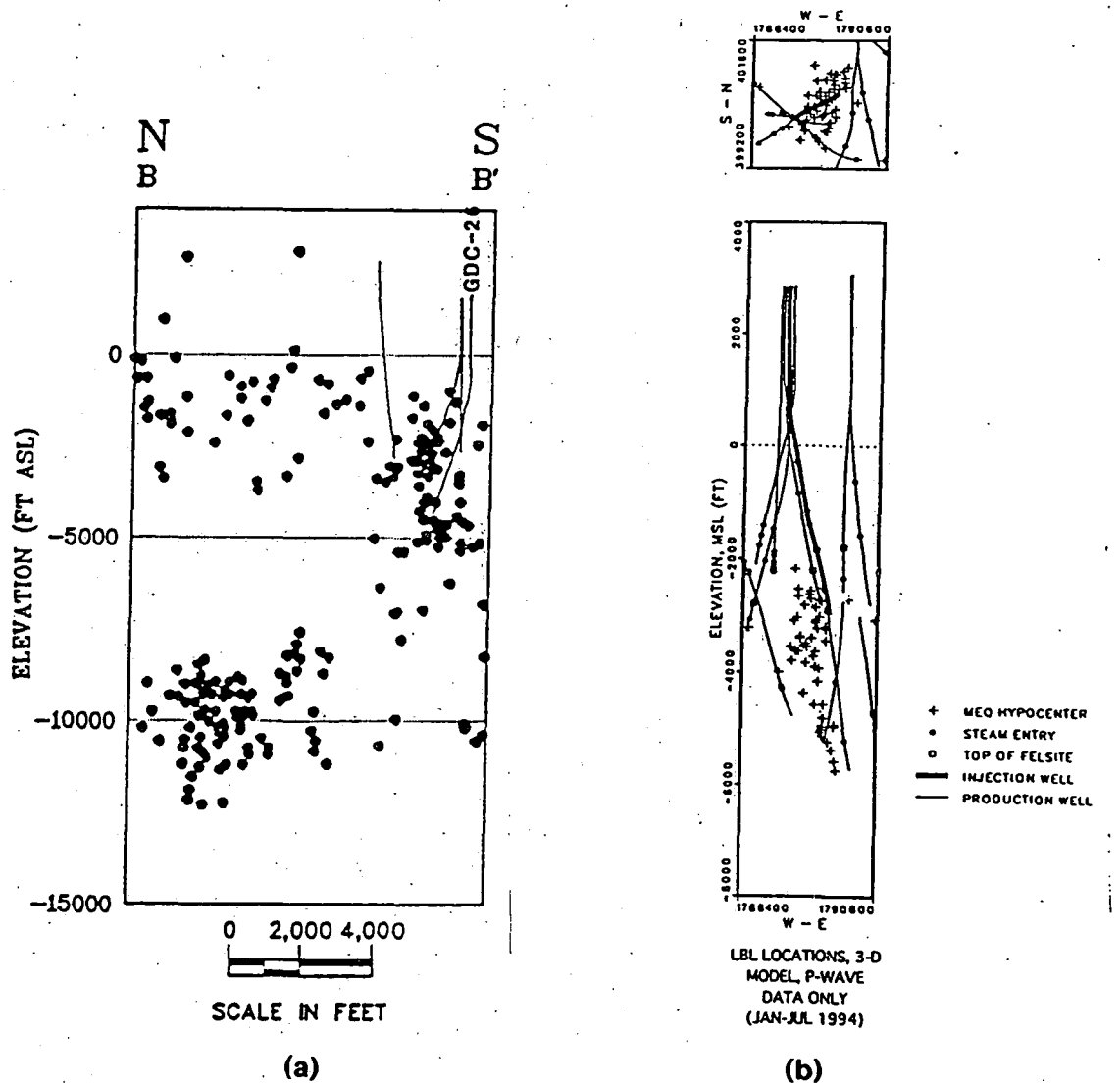

Figure 2.9. (a) Cross-section showing the relation of earthquakes to injection wells within The Geysers reservoir. Earthquakes are located using a one-dimensional velocity model (from *Stark*, 1990). (b) Cross-section showing the distribution of hypocentres in the vicinity of injection wells. Earthquakes are located using a three-dimensional velocity model (from *Kirkpatrick et al.*, 1995).

at The Geysers. Small increases in pore fluid pressure can reduce the effective normal stress (i.e., the difference between normal stress and pore pressure) sufficiently to trigger failure, particularly if the rock is already close to failure. Two opposing view points have emerged regarding the feasibility of such a failure mechanism at The Geysers. One group doubt that the physical conditions exist in the reservoir to induce failure by this mechanism given the sub-hydrostatic pressures and re-injection of condensate at zero well-head pressure (*Majer and McEvilly*, 1979; *Allis*, 1982; *Denlinger and Bufe*, 1982; *Eberhart-Phillips and Oppenheimer*, 1984). The other suggests that water levels within injection

wells stabilise at 10s to 100s of metres above the well base. A vertical column of water 300 m high can generate a pressure of ~3 MPa at its base. Pressures within the reservoir vary between 1.38-3.45 MPa so injection-well fluid columns could transmit sufficient hydraulic pressures into the reservoir to cause failure (*Stark*,. 1990). Earthquakes associated with injection wells may thus be produced by a combination of pore pressure increase and cooling (*Stark*, 1990).

Other possible failure mechanisms include increases in reservoir strength where tectonic deformation which occurred as aseismic creep prior to production transfers to stick-slip deformation after steam extraction commences (*Majer and McEvilly,* 1979; *Allis,* 1982; *Denlinger and Bufe*, 1982). This transition could have been caused by the large fluid pressure decrease which may have accompanied the reservoir change from water-to steam-domination (*Allis,* 1982). An alternative theory suggests that a conversion of aseismic creep to stick-slip failure may have occurred as a result of increasing the coefficient of friction in the rock volume by the deposition of silica on existing fracture surfaces as it precipitated from boiling reservoir fluids (*Allis*, 1982). This conversion could have resulted from reservoir temperature and pressure declines (*Denlinger and Bufe,* 1982). They suggest an additional failure mechanism based on the principle that fracture deflation can induce significant increases in shear stresses in the vicinity of the fracture tip (33-66% of the crack pressure decrease).

Computer derived fault plane solutions for earthquakes recorded by CALNET at The Geysers use *P*-wave first motion data (Appendix 2) (*Oppenheimer*, 1986). The mechanisms are constrained to be double-couple (DC). Solutions exhibit an apparent depth dependency with dip-slip mechanisms dominating at depths >3 km bsl, strike-slip and dip-slip mechanisms between 0-3 km bsl with reverse-slip mechanisms restricted to depths shallower than 1 km bsl. The solutions are spatially inconsistent even over small epicentral distances and lack consistent fault plane orientations. This is thought to result from slip occurring on small, randomly oriented pre-existing fractures. Fault plane solutions have also been determined using wave-form inversion techniques (*O'Connell and Johnson*, 1988). These results support the earlier depth dependency theory with strike-slip mechanisms at shallow depths and dip-slip mechanisms at depth.

2.6 Summary

Earthquakes in northern California generally align to delineate faults east of the San Andreas fault within the San Andreas shear zone. The Geysers geothermal area has anomalously high rates of shallow (<5 km bsl) earthquake activity at least 45 times the regional rate. Continuous monitoring by the USGS of seismic activity at The Geysers commenced in 1975. At present four independent networks operate within and in the

vicinity of The Geysers geothermal area. The USGS has about 40 mostly vertical component sensors within a 20 km radius of The Geysers. These are part of CALNET. The UNT network of 15 vertical and 7 three-component stations operates within the production area. Small, dense digital networks operative in the northwest and southeast Geysers consisting of 16 and 13 three-component stations respectively. These are operated by LBL. The networks use a variety of instruments, array design covers a wide range of apertures and consequently detection thresholds vary. The small permanent networks are able to detect 50-90% more earthquakes than the UNT and CALNET networks respectively. Over the last 28 years, short-period experiments using temporary networks have also been conducted.

The USGS catalogues all earthquakes recorded by CALNET. These are available via a public-domain database held at the NCEDC, University of California, Berkeley. A history of earthquake activity at The Geysers is complete for events with $M_D \geq 1.2$ from 1975 to present day. About 140 earthquakes $M_D \geq 1.2$ are recorded per month. The largest event was a M_D=4.3 recorded in 1992, 3 km bsl in the northeast Geysers. Yearly seismicity maps indicate dramatic increases in both the seismicity and its spatial distribution with time. This can be uniquely correlated with commercial activities such as injection and production. Earthquakes correlate closely with electrical generating plants. The area of most intense activity with the deepest events correlates with the area undergoing the longest period of production. Seismic activity initiates soon after the onset of production in previously aseismic areas and reduces dramatically when production ceases. The rate of seismic activity mirrors almost exactly the rate of steam extraction. Source mechanism studies suggest that most earthquake fault-plane solutions exhibit strike-slip to dip-slip focal mechanism solutions with events in the top 1 km exhibiting reverse-slip mechanisms.

A variety of mechanisms have been proposed to explain this intense activity. Injection of condensate is thought to be capable of producing 50% of the events in the steam field with the remainder a result of both steam production and tectonics.

Chapter 3

Data acquisition and primary data processing

3.1 The field experiment: April, 1991

3.1.1 Introduction

The field experiment was designed to record high-quality local earthquake data within The Geysers geothermal area to model seismic wave-speeds in the steam reservoir and to study earthquake source mechanisms. The existing permanent networks could not provide the high quality three-component information required, and now attainable using the latest portable seismometer stations. The temporary network consisted of fifteen three-component sensors distributed in a 15-km diameter array which was operated from April 1st-May 1st, 1991 through the collaborative efforts of the University of Durham, UK and the USGS (*Julian and Foulger*, 1992a).

3.1.2 Network design

The network geometry was optimised to provide a homogenous distribution of ray-paths and dense coverage of the upper focal hemisphere (Figure 3.1). These are important requirements for both wave-speed modelling and earthquake source mechanism studies. Network configuration was determined by ray-tracing through the best available one-dimensional velocity model (*Eberhart-Phillips and Oppenheimer,* 1984) for a point 3 km bsl within the seismically-active central Geysers (38:48° N, −122:48° W). Logistic

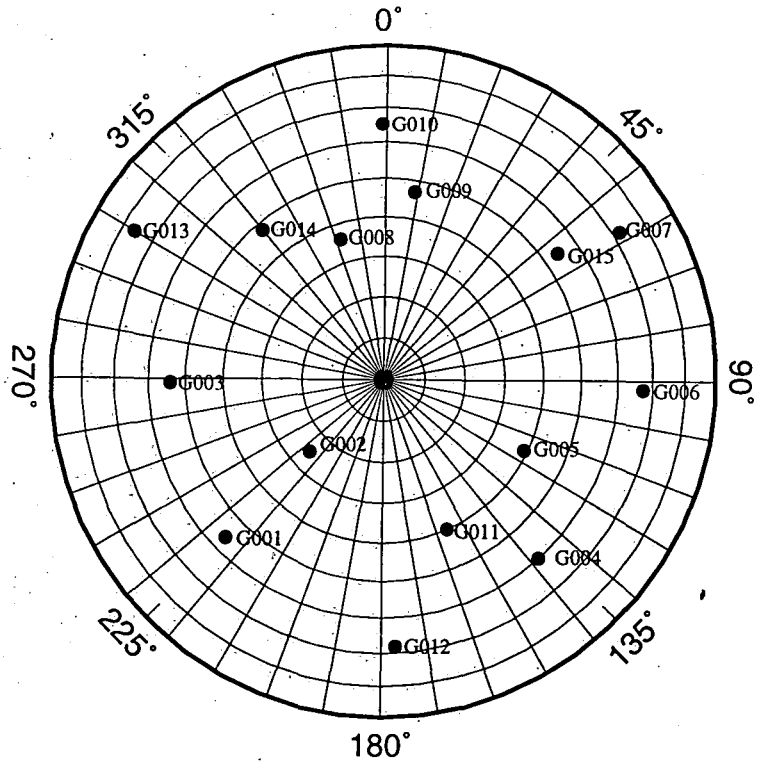

Figure 3.1. Upper hemisphere, equal area projection showing the network geometry. Solid circles indicate station locations determined by ray-tracing through the one-dimensional regional v_P model.

problems such as the rugged terrain and poor accessibility resulted in sensors being deployed somewhat away from their ideal positions, but good focal sphere coverage was nevertheless retained (Figure 3.2).

3.1.3 Equipment

Equipment from the IRIS-PASSCAL equipment pool was used for the field experiment. Fourteen of the stations used three-component Mark Products model L22D 2-Hz sensors. Station G014 used a Geospace Corporation HS-10 sensor (4.5 Hz natural frequency). Data were recorded digitally in the field at 100 sps by 15 REFTEK model 72A-02 Data Acquisition Subsystems (DASes). The storage capacity of the REFTEK Disc Recorder Subsystems was 190 Mbytes. The DAS at each station recorded two data streams, (1) three channels of continuous data from one vertical and two horizontal sensor components, and (2) ten seconds of vertical component data, triggered to record when the instrument recognised a seismic disturbance. The trigger times provided an event list to assist in the extraction of events for subsequent processing (Section 3.2.1). Each DAS unit had an internal crystal oscillator to provide timing information, a Kinematics OMEGA

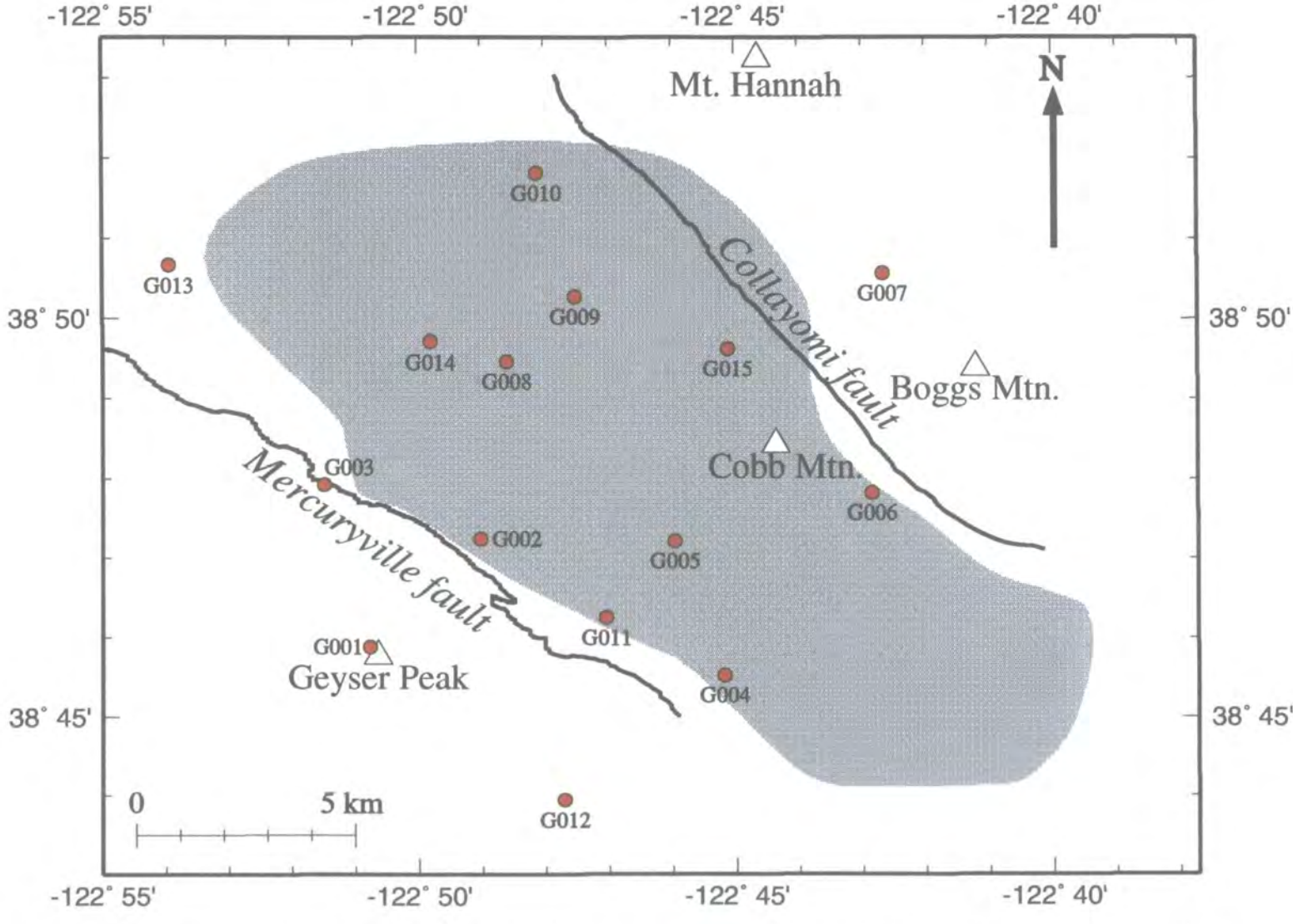

Figure 3.2. Location map of The Geysers geothermal area showing stations in the temporary network (red circles). Shaded area: production area (1992); white triangles: mountains; black lines: faults.

radio receiver and most had a WWVB radio receiver. Electrical power at each station was provided by 85 amp-hr marine lead-acid batteries, each weighing 25 kg.

3.1.4 Seismometer station installation procedure

Instrument deployment commenced in March, 1991. Sensors were cemented to bedrock at depths of 0.5 m, covered with a plastic bowl and buried. Sensor orientations were determined using a handheld Brunton compass, measuring 6-8 feet from the sensor to ensure the compass was unaffected by the sensor magnets. The north component of the sensor was aligned to true north, except for station G012, where it was aligned at 352° N because of difficulties caused by the shape of the outcrop. Station G014 was installed in a 30 m borehole by GEO and is part of the small aperture network in the northwest Geysers (Figure 3.2; Section 2.2). The DAS, disc and battery unit at each station were sited a short distance from the sensor and protected from grazing deer by tarpaulin covers. All electrical cables were buried for similar reasons (Figure 3.3).

3.1.5 Determining station location co-ordinates

Stations of the temporary array were located using Global Positioning System (GPS) which accurately locates points on the Earth's surface by receiving timed signals from orbiting satellites. The method requires two GPS receivers, one continuously recording at a central base station and the other deployed for 15-minute periods at each seismic station location (Figure 3.4). These stations were located relative to the base station with an accuracy of a few centimetres by interferometrically processing the data recorded simultaneously at the base and seismic station (Table 3.1). The base station was located with an absolute accuracy of about 10 m. This technique was also used to locate stations within the UNT network.

3.1.6 Station maintenance and data acquisition procedures

The network was operated for 31 days and was serviced by a field crew of two using one vehicle. All stations were accessible by vehicle except station G001 which required backpacking batteries and discs in a 3-km round trip. The field crew made maintenance visits at three day intervals, since this was the maximum storage space of the field discs operating in continuous recording mode, which meant that five stations per day had to be visited. At each visit discs were exchanged and checks were made to ensure the whole station, including timing and the three sensor components, were operational. A record was taken of the DAS unit number, the installed disc number, and whether the DAS

Figure 3.3. Photograph of a typical station set-up. (Photograph taken in the similar Iceland experiment August-September, 1991).

Figure 3.4. Photograph showing the typical field set-up for a GPS receiver to determine accurate locations of each station in the temporary array.

was locked onto the OMEGA and WWVB radio signals. Batteries were replaced every nine days or if the voltage was projected to fall below 12 V before the next visit.

Table 3.1. Location of stations in the temporary network. Co-ordinates are given in the WGS84 ellipsoid. The orientation of the north sensor component is given along with the duration the mobile GPS receiver recorded signals at each station.

Station code	Station name	Latitude (°N)	Longitude (°W)	Height (m)	Azimuth of north component	Duration of GPS deployment
G001	Geysir Peak	38:45:53.40336	−122:50:44.37724	1015.53	360°N	30 mins
G002	Mercuryville	38:47:15.05548	−122:48:59.53313	892.96	360°N	28 mins
G003	Truitt Creek	38:47:55.96188	−122:51:29.70299	718.51	360°N	24 mins
G004	Socrates Mine	38:45:31.64140	−122:45:09.96710	931.59	360°N	19 mins
G005	Burned Mtn.	38:47:13.69062	−122:45:57.86943	830.11	360°N	24 mins
G006	Ford Flat	38:47:49.55532	−122:42:50.31403	758.56	360°N	11 mins
G007	Boggs Mtn.	38:50:34.25420	−122:42:40.84369	986.59	360°N	30 mins
G008	Squaw Creek	38:49:27.90007	−122:48:37.51063	670.15	360°N	18 mins
G009	Bear Canyon	38:50:16.31845	−122:47:31.71459	950.34	360°N	20 mins
G010	Higgins Ranch	38:51:48.98260	−122:48:07.58314	734.90	360°N	28 mins
G011	Cadd Fire Trail	38:46:15.59994	−122:47:00.83818	1008.76	360°N	26 mins
G012	Gauer Ranch	38:43:56.88720	−122:47:41.33932	527.92	352°N	34 mins
G013	Alder Creek	38:50:40.33265	−122:53:58.03892	741.50	360°N	24 mins
G014	Black Oaks	38:49:42.98632	−122:49:48.84715	586.40	360°N	31 mins
G015	Pine Grove	38:49:37.48337	−122:45:06.47180	911.08	360°N	<10 mins

Approximately 450 Mbytes of data were recorded per day. At the field headquarters, located at the UNOCAL field office in The Geysers two SUN workstations were used to download the field data from disc to exabyte tape. Two versions were archived, the raw, disc-dump data and a version converted to SEGY format. Seismic data recorded at each station were inspected on a daily basis to ensure the instruments were functioning correctly.

3.1.7 Data recorded

The field experiment recorded 3906 earthquakes amongst the 18 Gbytes (348 station-days) of continuous data collected. From April 4th-28th a 84% data return rate

was achieved. The continuous-recording mode of operation greatly increased the success of the experiment as many high-quality seismograms did not cause event triggers because of a variety of factors such as low-frequency microseismic noise, emergent signals, and swarm-like clustering of earthquakes. If event triggering had been employed many important data would have been lost. A selection of some of the seismograms recorded is displayed in Appendix 3.

Some data were lost primarily because of hardware failures. On four occasions the DASes spontaneously shut down. Such abnormal behaviour was not recognised until similar symptoms were experienced in a similar experiment in the Hengill volcanic area, Iceland, conducted in August and September, 1991 (*Julian and Foulger*, 1992b; *Miller*, 1996). Other hardware failures included the failures of one DAS unit, one disk unit and one component in two of the sensors.

3.2 Data processing

3.2.1 Earthquake identification and data extraction

Earthquakes were extracted using information recorded on data stream 2 at each station. An event was considered potentially interesting if three or more stations triggered within a 5 s period. Thirty second event segments with 2 s of pre-trigger data were extracted from the continuous data at all stations for all potentially interesting events. Event segments were extended if additional triggering occurred during the 30 s window. The scheme adopted to uniquely identify each earthquake has the format *ddd.hhmmss.n* where *ddd* is the day of year, *hhmmss* is the time in hours, minutes and seconds when the event segment starts and *n* is the earthquake number within that particular segment. This scheme will be used through the remainder of this thesis.

3.2.2 The final data set

The UNT and CALNET permanent networks were also in operation at the time the temporary network operated. Data from these networks were added to the final set, greatly improving the station coverage (Figure 3.5). The final data set contains 3906 earthquakes recorded on up to 90 vertical and 22 horizontal-component sensors.

3.2.3 Detection thresholds

The detection thresholds of the different networks vary considerably because of differences in the instrumentation, number of stations and network geometry. Analysis of

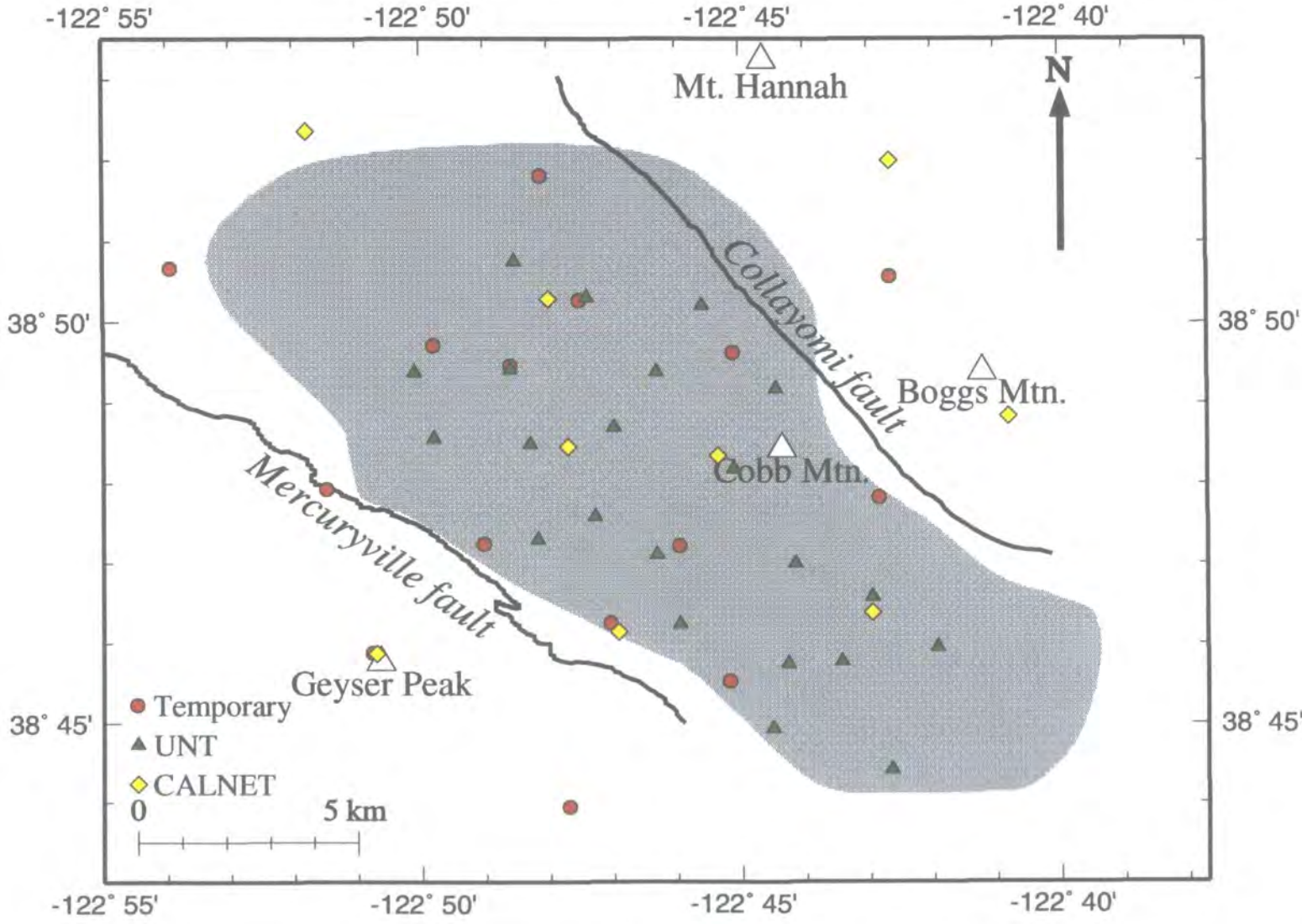

Figure 3.5. Location map of The Geysers geothermal area showing stations of the CALNET (yellow diamonds) and UNT (green triangles) permanent networks and the temporary network (red circles). Other map features are the same as for Figure 3.3

b-value diagrams for April, 1991 shows that the temporary network detected all earthquakes of $M_D \geq -0.6$ (*D. J. Barton, pers. comm.*). CALNET reported only 8% and UNT 45% of the events recorded by the temporary network over the same period. Two additional permanent networks operate intermittently in the northwest and southeast Geysers (Section 2.2). The LBL network in the southeast Geysers detects about 50% more events than the UNT network which means that it has a similar detection threshold to our temporary network. The CCOC network in the northwest is thought to have a similar detection threshold. Data from these small aperture arrays were not used in the present study.

3.2.4 Clock corrections

Each DAS unit uses an internal, temperature-compensated crystal oscillator to record time information. The crystal oscillator drifts by a few tens of milliseconds over a 24 hour period and must be periodically calibrated using an external time signal. Very low frequency (~10 kHz) OMEGA radio navigation signals broadcast second marks at 10 s intervals on a continuous basis from a global network of eight transmitters. The DASes receive and decode the OMEGA signal transmitted from one of these sites and correct drift in the internal clock (Figure 3.6). This ensured that stations across the network are synchronised. Transmission time between the OMEGA source and receiver is automatically determined by the DAS. When a continuous, clear OMEGA signal is received the crystal oscillator is said to be phase-locked to the time signal and tracks Universal Time Code (UTC) to an accuracy better than 1 ms. For periods when the signal is weak or of low signal-to-noise ratio then the internal oscillator is unlocked and will run freely until signal quality improves and the phase lock is re-established. If at this point the internal oscillator has drifted by more than +10 ms or less than –5 ms from UTC a "time jerk" is applied and a record made in the DAS log files. For smaller amounts of drift the internal oscillator is slewed until it is again synchronised with the OMEGA signal. The drift is assumed to be linear during periods when the internal oscillator is unlocked. Clock corrections were applied to each arrival-time measurement via clock files.

Five stations in the temporary network failed to lock reliably to the OMEGA time signal (Table 3.2). The clock error in four of these stations could be determined and corrected for part or all of the unlocked period. Forward planning had anticipated such eventualities and another source of timing information was provided by the WWVB time base. WWVB is a low frequency (60 kHz) radio signal transmitted from Boulder, Colorado which broadcasts accurate time information at one minute intervals. It has a slightly lower time resolution than the OMEGA signal, but was adequate for this study. WWVB radio receivers were deployed at most of the temporary stations. Stations G007

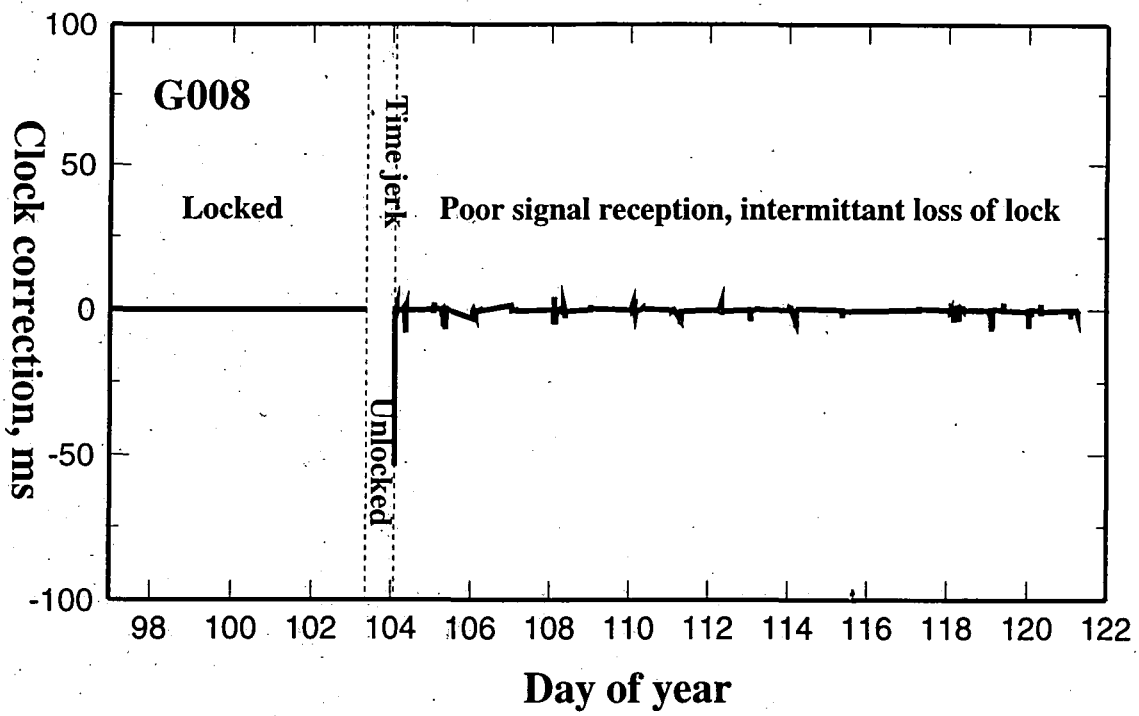

Figure 3.6. Example of clock-corrections made to the internal clock of station G008 during the field experiment. The station was unlocked for 14 hours on day 103 and a time jerk was applied when phase-lock was re-established. During periods of poor signal reception, between days 104-121, numerous short-period losses of phase lock caused minor amounts of clock drift.

and G014 did not lock onto the OMEGA signal but they did record WWVB information. By comparing the UTC time provided by WWVB with the DAS internal clocks, drift curves were constructed (Figure 3.7). Appropriate corrections were applied to arrival-time measurements on traces recorded at these stations via clock files, using the convention

$$\text{UTC (WWVB)} - \text{internal clock time} = \text{clock correction.} \qquad 3.1$$

The correction is positive for an internal clock running behind UTC and negative if running ahead of UTC.

Stations G003 and G015 did not lock onto the OMEGA signal nor record WWVB information. Internal clock drift at these stations could be determined for portions of the field experiment using a third timing method which had been implemented during the field experiment. At each station visit a master clock was connected to the DAS unit and a time mark registered in the log file of the DAS. The master clock was synchronised with UTC at the start of the field experiment but in time the clock itself drifted. A drift curve was determined for the master clock by comparing the time marks registered at stations phase-

locked to UTC. Having calibrated the drift curve for the master clock, a drift curve could be determined for the internal clocks of stations G003 and G015. A drift curve for station G013 could not be determined for the unlocked period. Earthquakes recorded at this station for the duration of the unlocked period were discarded in subsequent analysis.

Table 3.2. Seismic stations which were not phase-locked to UTC for some or all of the field experiment. All other stations in the temporary network remained synchronised throughout the recording period.

Station code	Periods when stations were unlocked
G003	Day 091-114
G007	Never locked
G013	Day 090-104
G014	Never locked
G015	Never locked

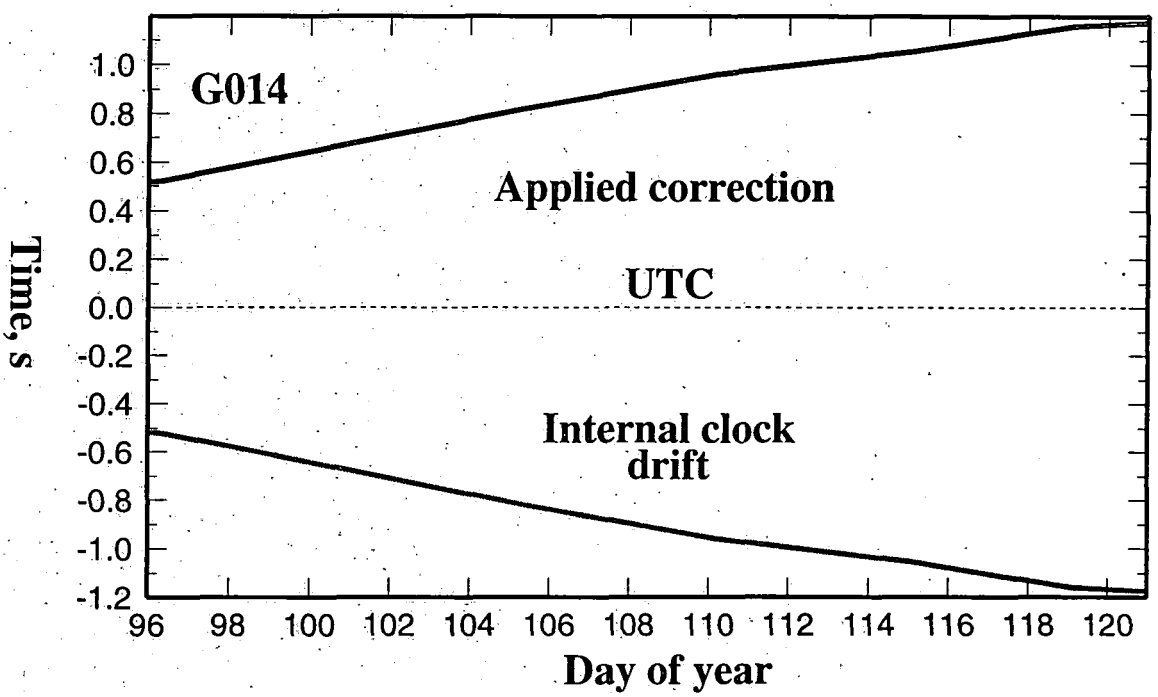

Figure 3.7. Internal clock drift for station G014 was corrected by comparing UTC time provided by WWVB with the internal clock. In this case the internal clock ran more slowly than UTC (grey line) and a positive correction was applied (black line).

3.2.5 Automated measurement of *P*-phase arrival times

Processing the earthquakes was considerably simplified by the use of an automated method for measuring *P*-phase first arrival-times. The approach is based on the fact that the signal preceding the first *P*-wave arrival is uncontaminated by coda from earlier waves and therefore the signal-to-noise ratio is good. The program *autopick* was used. The original version written by R. Crossen, University of Washington was modified by M. O'Neil, B. R. Julian and A. D. Miller. The program processes one earthquake at a time and makes two passes along each vertical component seismogram comparing the ratio of two sliding, triangularly-weighted sums of the seismogram amplitude and calculating an "fbcurve". If the signal-to-noise ratio is large then the seismogram amplitude after the *P*-arrival will be larger than before the arrival and the fbcurve will have a maximum at the phase arrival. The first pass identifies the approximate arrival time and the second refines it. The program assigns a phase code, an estimate of the pick quality which is either weight zero (good) or weight 4 (poor) and the polarity. Generally *P*-phase arrival picks with quality zero were correct to within one sample (10 ms) when compared with hand-picked data.

3.2.6 Earthquake selection procedures

Initial processing involved amalgamating data from all three networks for each earthquake. The labelling scheme of the two permanent networks uses the event origin time as the timebase label, in contrast with the temporary network (Section 3.2.1). The UNIX Bourne-shell script "*match*" compared origin times of events in the permanent network with the segment start times of traces recorded by the temporary network for each day of the field experiment (Appendix 4). A match was reported if the temporary network start time was within 30 s of the estimated origin time of the earthquake. A second program "*combinelist*" appends a list of seismograms recorded by the permanent networks to an ASCII list file for the temporary network. Each line of the list file specifies the name of a digital seismogram file followed by an integer to specify the position of the seismogram within this file. Over 90% of earthquakes recorded on the UNT permanent network were successfully matched with those recorded by the temporary array.

Processing the 3906 earthquakes recorded was considerably simplified by analysing the size of autopick files, since earthquakes with good, clear impulsive arrivals could be easily detected by the autopick program and therefore had relatively large pick files. The information contained in an arrival-time measurement uses 48 bytes of disk space. In the initial stages of event processing earthquakes recorded by the temporary network and either one or both of the permanent networks proceeded to the next processing stage if 20

or more *P*-wave arrivals were detected by the autopick program. This condition was later relaxed to 8 *P*-wave arrivals for earthquakes recorded by only the temporary network.

3.2.7 Interactive measurement of *P*- and *S*-phase arrival times

Earthquakes were visually examined and processed using the interactive pick program *epick* (*B. R. Julian, pers. comm.*) which is an extensively-modified version of an earlier program *sunpick* (*R. Ryan, pers. comm.*). *epick* operates in the X-windows environment and enables the user to display seismograms for one earthquake at a time, measure or make changes to phase arrival times and estimate hypocentre co-ordinates and origin times (Appendix 5). Each earthquake is defined by an ASCII file containing a list of seismograms (Section 3.2.5). Seismograms can have different start times, segment duration and sampling rates. If a file exists with the same name as the list file and the suffix "ep" then this is assumed to contain measurements made earlier, which are automatically displayed. Files containing automatic *P*-phase measurements have the suffix "ap", and to view these an additional command line option must be specified. A 'pick' consists of a time measurement (accurate to 10 ms) and a phase identification label. The arrival type (emergent or impulsive), a quality factor, polarity, amplitude and frequency measurements are optional additions.

All automatic *P*-phase picks made on vertical component seismograms were examined and modified where necessary. Typically, quality zero picks required a change of less than one sample (<0.01 s) and automatic picks of quality four were discarded. Only *P*-phase arrivals with good signal-to-noise ratios and impulsive arrivals were included. *S*-phase arrivals were picked on horizontal component seismograms where they were most clearly recorded and are accurate to about 0.02 s. If both horizontals recorded clear *S*-phase arrivals then the earliest arrival was measured.

Over 500 earthquakes were hand picked. Of these 296 were of sufficient quality to be included in the final data set and represented 5658 *P*-wave arrivals and 1426 *S*-wave arrivals. No shot (a source of known location and origin time) or blast data (a source of known location but unknown time) were available.

3.3 Earthquake locations

3.3.1 Location procedure and the initial, one-dimensional wave-speed model

The procedure for locating earthquakes involves iteratively refining estimates of hypocentre co-ordinates and origin times from a trial solution by minimising some function

of the travel-time residuals. The program *qloc* (*B. R. Julian, pers. comm.*) performs an iterative, damped inversion on *P*- and *S*-wave arrival time data to minimise the sum of the travel-time residuals. As an initial estimate the hypocentre is located vertically beneath the station with the earliest arrival time at a depth of 3 km bsl. Both *P*- and *S*-wave arrival-time picks are weighted according to the uncertainty in the pick time. *S*-waves are consistently down-weighted since they arrive within the *P*-wave coda. The program reads in arrival-time measurements in *epick* format and outputs an ASCII list containing hypocentre information, origin time and details of each arrival-time measurement. A UNIX Bourne-shell script *eloc* controls the operation of *qloc*.

For *qloc* to estimate hypocentre and travel-time residual estimates an appropriate, user-defined, one-dimensional, layered velocity model for compressional wave-speed (v_P) and shear wave-speed (v_S) must be supplied. In this case the one-dimensional v_P velocity model generated by inverting *P*-wave travel-times from the northern Coast Ranges was the best available model for The Geysers (Table 3.3; Figure 3.8) (*Eberhart-Phillips and Oppenheimer*, 1984). The v_S model was determined from the v_P model assuming an average v_P/v_S ratio value of 1.8.

Table 3.3. The one-dimensional layered model used to locate earthquakes (*Eberhart-Phillips and Oppenheimer*, 1984).

Depth bsl to top of velocity layer, km	Thickness of velocity layer, km	v_P, km/s	v_S, km/s
0.00	1.50	4.43	2.46
1.50	1.50	5.12	2.84
2.75	1.25	5.47	3.04
4.50	1.75	5.58	3.10
6.50	2.00	5.62	3.12
13.50	7.00	5.86	3.26
23.50	10.00	6.80	3.78

3.3.2 Hypocentral distribution

Earthquakes are distributed almost exclusively within the steam production area between the Collayomi and Mercuryville fault zones, from sea level to 4 km bsl (Figures 3.9 and 3.10). The seismogenic area in map view mirrors the contours of the steam production area expanding from 3 km broad in the southeast to 6 km in the northwest (Figure 3.9). The pattern of seismicity varies across the field with little diffuse activity in

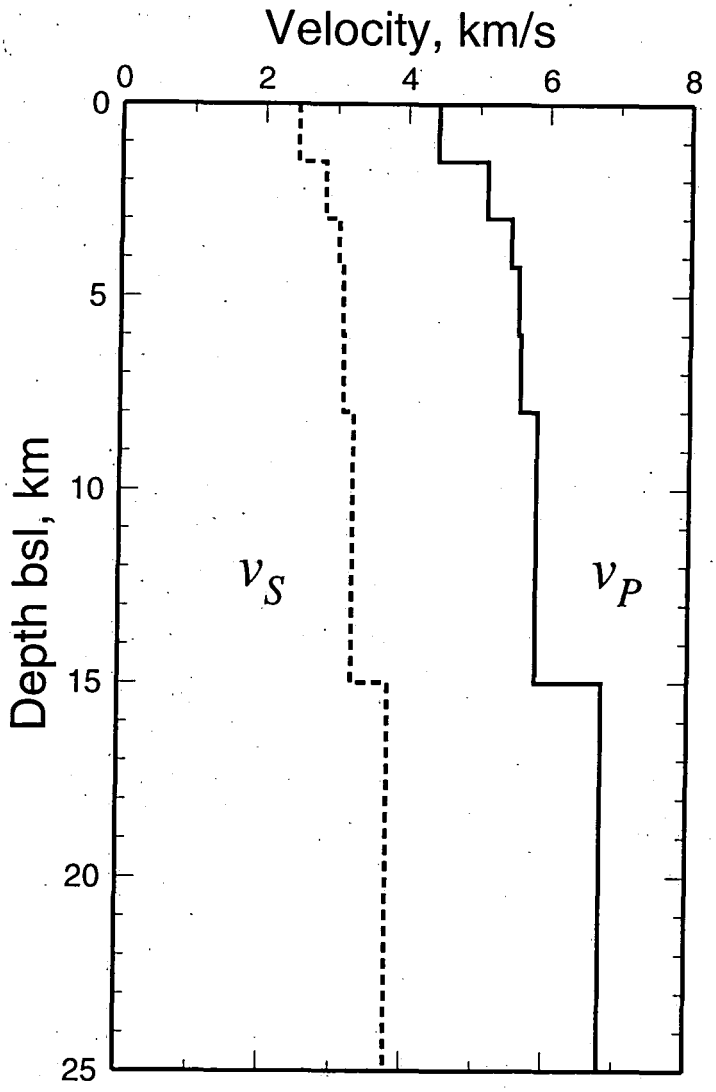

Figure 3.8. Velocity-depth profile of the one-dimensional velocity models for v_P and v_S. The v_P model is the regional, one-dimensional model for the northern Coast Ranges (*Eberhart-Phillips and Oppenheimer*, 1984). The v_S model is derived from the v_P assuming a constant v_P/v_S ratio of 1.8.

the southeast restricted to depths exceeding 1 km bsl. The seismogenic base in this area is poorly defined. The most intense activity occurs in the central Geysers with activity predominantly restricted to dense clusters of earthquakes separated by relatively aseismic areas. There, the seismogenic area is wider laterally and vertically than in the southeast with a well-defined seismogenic base at about 4 km bsl. Activity in the northwest Geysers is again diffuse, with less clustering and the seismogenic base shallows to about 3 km bsl. In contrast to the southeast the northwestern limit of the main seismogenic area in The Geysers is well defined by an apparent alignment of earthquakes to form a linear feature trending northeast-southwest. This dips steeply to the northwest and

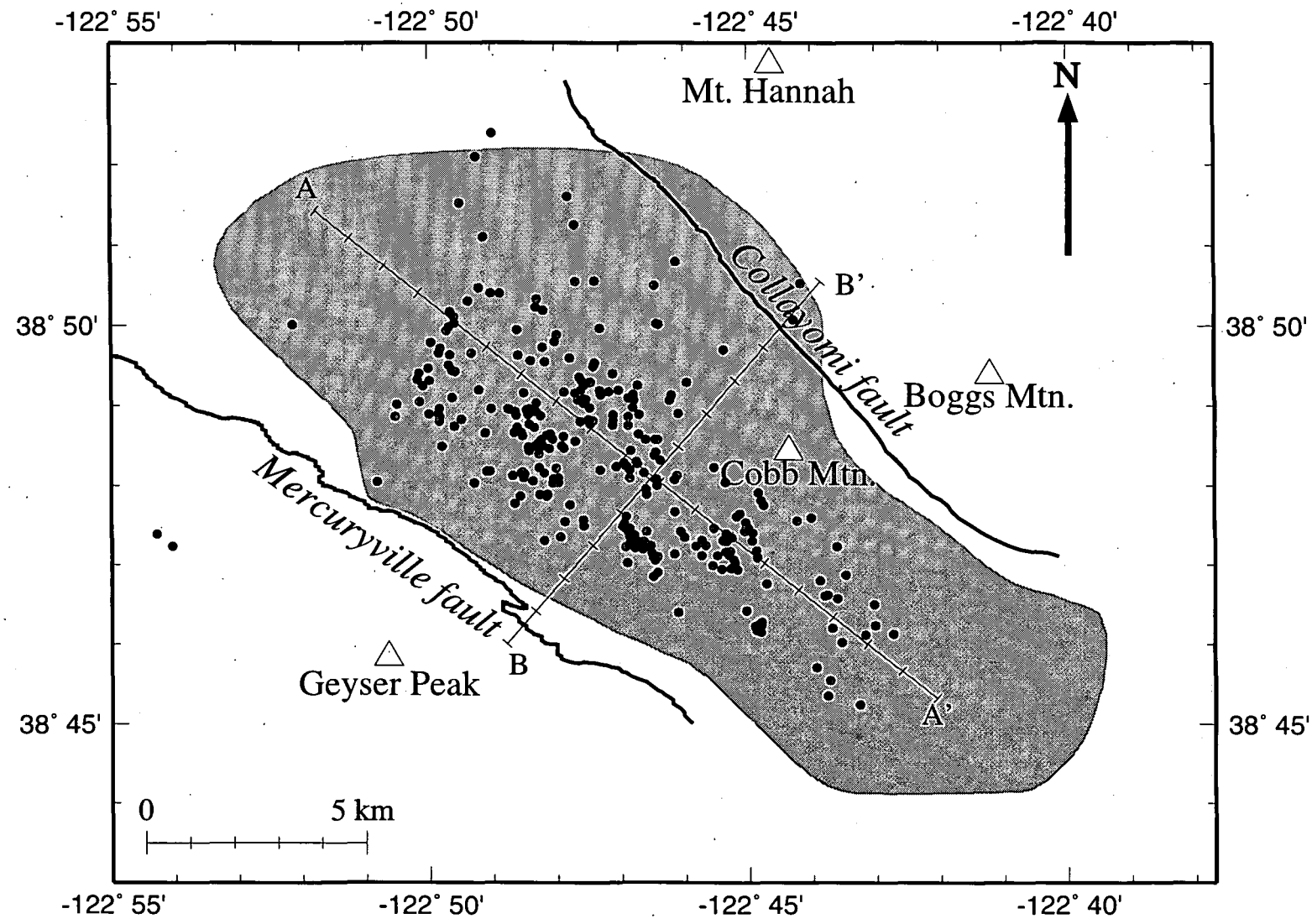

Figure 3.9. Map of The Geysers geothermal area showing the epicentral distribution of earthquakes in the final data set. Perpendicular lines of cross-section are labelled A-A' and B-B'. Other map features are the same as for Figure 3.3.

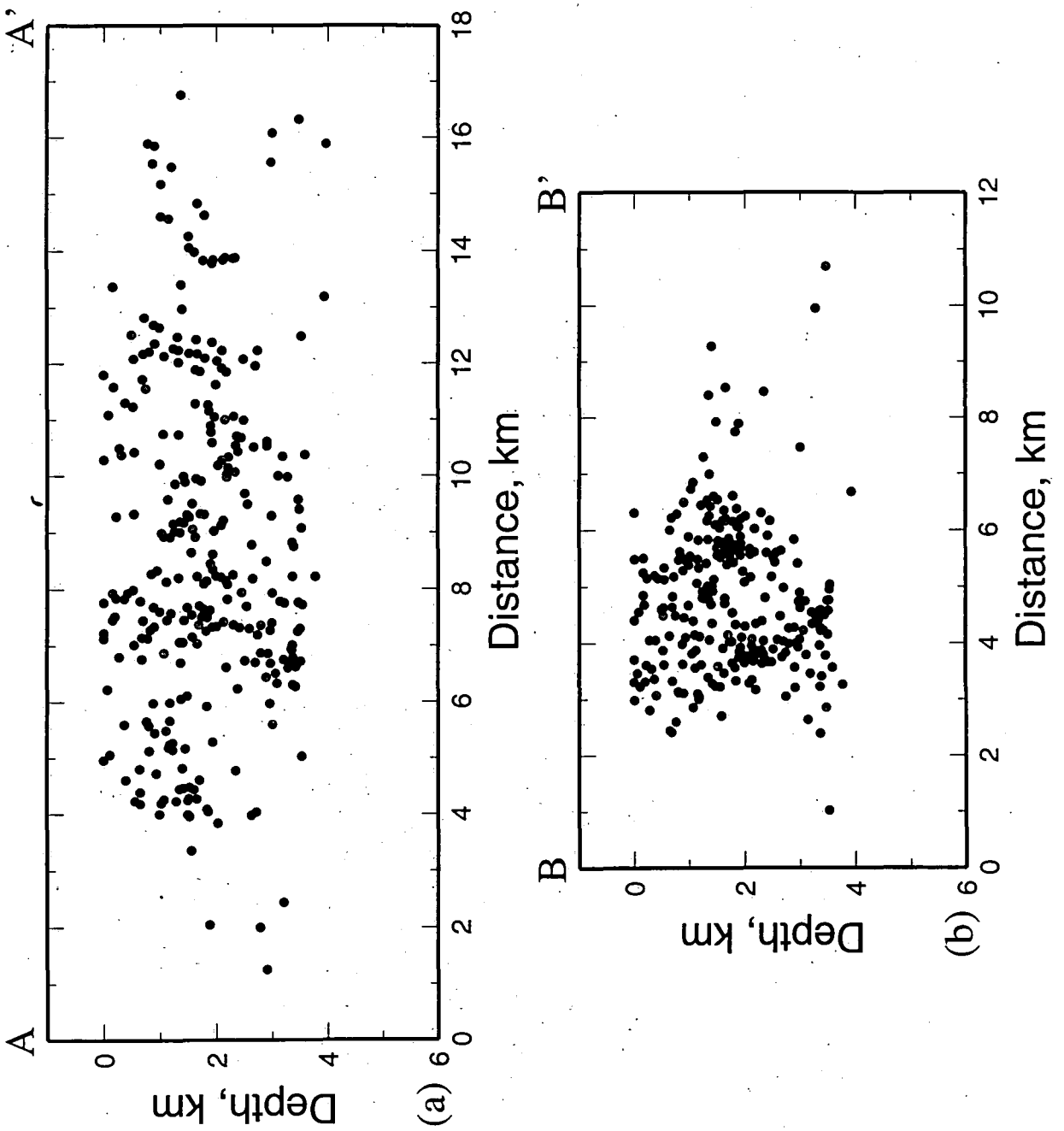

Figure 3.10. (a) Northwest-southeast cross-section showing the distribution of hypocentres (solid black circles) within the geothermal area. (b) Southwest-northeast cross-section showing the distribution of hypocentres (solid black circles) within the geothermal area.

extends to about 2.5 km bsl (Figure 3.10). Only a very few events occur northwest of this feature. Earlier studies at The Geysers suggested the horizontal and vertical standard errors on earthquakes located using this one-dimensional might be ± 0.4 km and ± 0.7 km (*Eberhart-Phillips and Oppenheimer*, 1984). See Section 7.5.5 for further discussion of location errors.

The distribution of handpicked earthquakes mirrors that for M_D>1.2 events recorded by CALNET during 1991 with intense activity in the central Geysers and shallower, reduced seismicity to the northwest and southeast (Figures 3.9 and 3.10; Figure 2.5j). The seismogenic base is ≤4 km for the handpicked data and 5 km for the CALNET data. Handpicked events in the 1991 experiment correlate closely with the power generating units in the central Geysers (Figure 3.11). The correlation is less clear in the southeast and for generating units at the periphery of the production area. This may be a function of the limited number of hand-picked events.

3.3.3 Temporal distribution of earthquakes

The temporal distribution of earthquakes during the field experiment indicates that The Geysers geothermal area is extremely and continuously seismically active (Figure 3.12). On average 163 earthquakes of M_D>–0.6 occurred per day with a maximum of 287 events recorded on April 6th. The rate of daily activity can, however, vary enormously and there does not appear to be a pattern. The apparent low seismic rate at the start of the experiment is probably due to a reduction in detection efficiency resulting from initial network operational difficulties. The distribution of events hand-picked and used in this study compared to the total number recorded shows a bias towards the second half of the field experiment. This is because the network operated most efficiently later on in the experiment and events recorded during that period were thus concentrated on. Events recorded in the first half of the experiment were studied as an after-thought in an attempt to improve ray-coverage for the tomographic study by including events located in relatively aseismic areas and higher-quality events in previously sampled areas.

3.4 Summary

The field experiment was designed to record high-quality earthquake data for use in tomographic wave-speed modelling and earthquake source mechanism studies. Station coverage was optimised by ray-tracing through the best one-dimensional velocity model available for The Geysers geothermal area. Fifteen state-of-the-art three-component digital seismometers and DAS units from the IRIS-PASSCAL equipment pool were used. Stations were accurately located using differential GPS. The network operated in

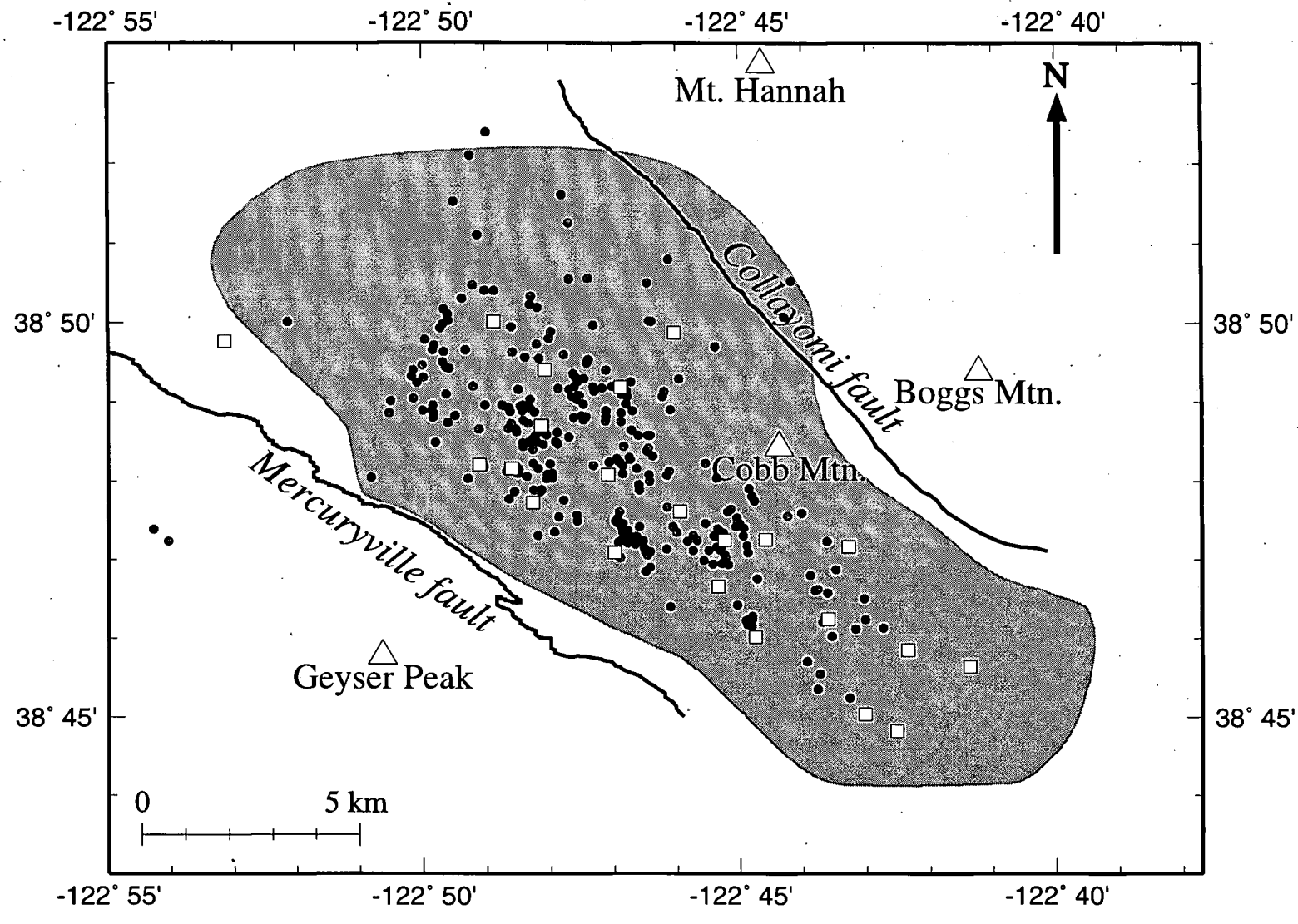

Figure 3.11. Same as Figure 3.9 but now with power plants (white boxes) operating during April, 1991.

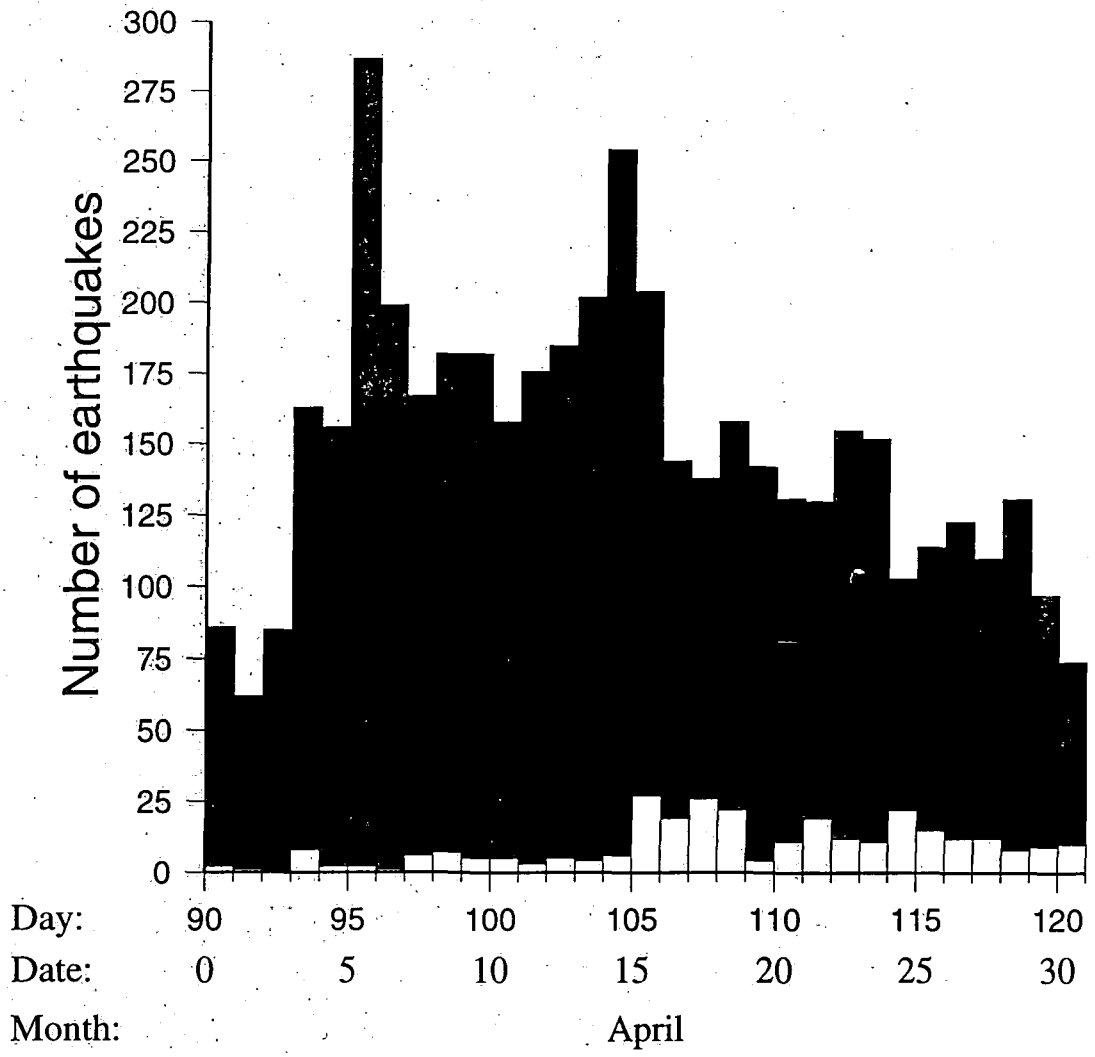

Figure 3.12. Histogram showing the number of earthquakes (black fill) with M_D>–0.6 recorded on each day of the field experiment. Superimposed is a histogram showing the distribution of hand-picked events (white fill) included in the final data set.

continuous mode for a 31 day period and recorded 3906 earthquakes. Station coverage was improved by including data from the two permanent networks operating during the recording period. The final data set has events recorded by up to 90 vertical and 22 horizontal component sensors.

P-phase arrivals were automatically measured for each earthquake and refined by hand. The final processed data set consisted of 296 earthquakes with a total of 5658 *P*-wave arrivals and 1426 *S*-wave arrivals. Earthquakes were located using the computer program *qloc* and the best available 1-d velocity model. Events are restricted almost exclusively to, and mirror the shape of, the geothermal production area. Hypocentres extend from sea level to 4 km bsl in the central Geysers and a shallower levels in the

northwest and southeast. Events occur in clusters in the central area but have a more diffuse distribution in the southeast and northwest Geysers. Events cluster in a similar spatial pattern as M_D>1.2 events recorded by CALNET in 1991. A good spatial correlation between event clusters and generating units was observed in the central Geysers. During the field experiment an average of 163 earthquakes per day were recorded with a maximum of 287 events recorded in 24 hours.

Chapter 4

Local Earthquake Tomography: Theory and examples of applications

4.1 Introduction

4.1.1 Three-dimensional seismic tomographic methods

Seismic tomography is a technique for imaging three-dimensional Earth structure using a large set of observations (*Evans et al.*, 1994). Most seismic tomography images infer the spatial distribution of seismic-wave speeds using seismic travel-time data. There have been many successful applications on local, regional and global scales, equipping the geoscientist with a powerful tool. A range of techniques are available which use teleseismic phases, local earthquake *P*- and *S*-waves, surface waves, normal modes and controlled sources.

Global surface wave tomographic inversions have provided insight into active tectonic regions, hotspots, ridges and back-arcs, while body-wave inversions have illuminated coarse mantle structure (*Li and Tanimoto*, 1993). Teleseismic tomography has successfully modelled undulations on the core-mantle boundary mantle structure on global and regional scales and the upper mantle and lithosphere (*Morelli,* 1993; *Dueker et al.*, 1993). Oceanic crust subducting under continental crust has been imaged *e.g.*, in north America and Japan (*Rasmussion and Humphreys*, 1988; *Benz et al.*, 1992; *Harris et al.*, 1991; *Hirahara, 1981*). The technique has illuminated significant lateral velocity heterogeneities in the continental crust such as the Baltic shield in Norway and provided an insight into continental rift-zones (*Aki et al., 1977; Dahlheim et al.*, 1989; *Davis et al.*,

1984). The teleseismic method has had most success in defining low velocity zones in the upper mantle or crust beneath volcanic centres, which have been interpreted as magma chambers or zones of partial melt (*e.g.*, The Geysers-Clear Lake, Long Valley-Mono Lake and Coso areas, California, Newberry Volcano, Oregon and Larderello, Italy), hotspots and active volcanoes (*e.g.*, Iceland, Yellowstone, Wyoming and Hawaii) (see *Iyer and Dawson*, 1993 for a review).

Small scale and extreme lateral heterogeneities characterise geothermal and volcanic areas. Teleseismic tomography uses low-frequency seismic waves and can therefore only resolve large-scale features. Techniques such as LET and NeHT which increase resolution by using higher frequency data from local earthquakes and explosions are more suited to studying these areas. Active source NeHT tomography uses one or more rings of controlled sources to undershoot a central target volume beneath a receiver array. The method has been successfully applied to Medicine Lake volcano, California, and Newberry Volcano, Oregon (*Evans and Zucca*, 1993). LET uses earthquakes within a model crustal volume to generate three-dimensional images of the velocity structure (*Thurber*, 1993; *Eberhart-Phillips*, 1993).

4.1.2 Comparison of the LET and NeHT methods

LET and NeHT tomographic techniques have inherent advantages and disadvantages compared with one another. LET methods can only be applied to seismogenic areas, although these are usually sites of primary scientific interest *e.g.*, geothermal areas, volcanoes and active fault zones. Advances in instrument design now make it possible to routinely record high quality digital data on portable three-component seismic stations which can either supplement existing permanent networks or provide information in areas of new seismic activity. This is considerably more cost-effective and easier to implement than NeHT experiments which use multiple explosive sources. Earthquakes are excellent generators of compressional- and shear-wave energy whereas explosions are poor generators of shear energy. The precise origin time and near-surface location of controlled sources may be accurately measured, but in the case of LET methods hypocentre and origin-time estimates must be treated as free parameters. The distribution of natural seismic activity restricts and determines the depth and lateral extent of well-resolved areas of the model volume. In the case of NeHT tomography these can be chosen by appropriate experimental design. Both methods resolve structure on the scale of ~1 km. The cost and environmental issues associated with NeHT tomography mean that it is seldom applied compared to LET methods.

4.2 Local Earthquake Tomography (LET)

4.2.1 Introduction

Earthquakes are usually located using a simplified one-dimensional Earth model to calculate the time for seismic rays to propagate from source to receiver. The differences between the observed and calculated travel times are minimised iteratively in the least squares sense to estimate the hypocentre and origin time (Section 3.3.1).

In reality the crust is laterally heterogeneous. Faults, discontinuities, elevated temperatures, partial melt, variations in pore fluids and intrusions are just some of the factors contributing to this complexity. One-dimensional velocity models are adequate for quick initial estimates of earthquake locations but accurate hypocentres and seismic-ray take-off angles (for focal mechanism studies) require a better description of the seismic velocity field *i*.e., a three-dimensional model. LET can model three-dimensional *P*- and/or *S*-wave velocity structure and is thus an appropriate tool for high-accuracy natural earthquake studies.

4.2.2 LET methods

"The goal of LET is to improve the estimates of the model parameters (structure and hypocentres) by perturbing them in order to minimise some measure of the misfit to the data" (*Thurber,* 1993). All LET computational approaches are founded on the principle that a body-wave travel-time T for a ray propagating from source i to a receiver j can be expressed as:

$$T_{ij} = \int_{\text{source}}^{\text{receiver}} u \, ds \qquad 4.1$$

where u is the slowness (reciprocal of velocity) and ds is an element of the path length (Figure 4.1). For actual observations, only the arrival time t_{ij} and the receiver location are known. The origin time τ_i, hypocentre co-ordinates (x_1, x_2, x_3), ray-path (Section 4.2.3.5) and velocity model are the unknown model parameters. The arrival time t_{ij} can be expressed as a combination of the origin time and the travel time, where:

$$t_{ij} = \tau_i + T_{ij} \, . \qquad 4.2$$

From a set of *P*- or *S*-wave arrival-time observations t_{ij}^{obs} recorded on a network of stations we can predict the arrival times t_{ij}^{cal} (assuming an *a priori* velocity model), trial

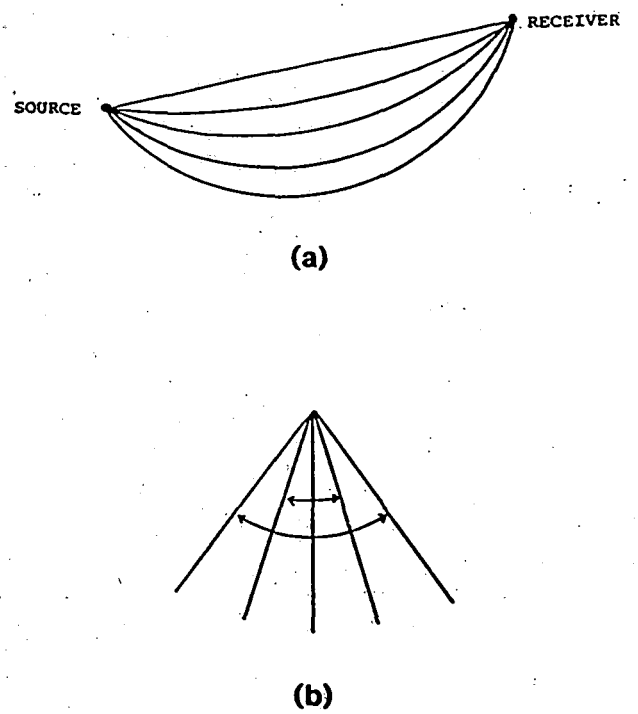

Figure 4.1. Schematic representation of the approximate ray tracing technique, after *Thurber* (1983). (a) A series of circular paths of varying radii of curvature are constructed connecting source and receiver. (b) The plane containing the paths is rotated about the source-receiver axis with the shortest travel-time adopted as the best estimate of the true ray path.

hypocentre co-ordinates and an origin time. A measure of the misfit between observed and predicted arrival times is the travel time residual r_{ij}:

$$r_{ij} = t_{ij}^{obs} - t_{ij}^{cal} \quad . \qquad 4.3$$

The data variance can be reduced by perturbing the velocity structure in three-dimensions, the hypocentral co-ordinates and the origin time. Travel-time residuals are related to these perturbations by a linear approximation assuming a finite parameterization of the velocity structure:

$$r_{ij} = \sum_{k=1}^{3} \frac{\partial T_{ij}}{\partial x_k} \Delta x_k + \Delta \tau_i + \sum_{l=1}^{L} \frac{\partial T_{ij}}{\partial m_l} \Delta m_l \qquad 4.4$$

where x_k represents the three hypocentre co-ordinates, $\partial T_{ij} / \partial x_{ij}$ hypocentre partial derivatives, $\Delta \tau_i$ is the change in earthquake origin time, m_l is the L velocity model parameters and $\partial T_{ij} / \partial m_l$ the velocity model partial derivatives.

Virtually all LET approaches apply Equation 4.4 with modification dependent on the treatment of six aspects of the inversion problem:

- parameterization of the velocity structure
- scheme for ray-path and travel-time calculations
- treatment of velocity structure-hypocentre coupling
- method of inversion
- inclusion of *S*-waves or not
- assessment of solution quality

The most critical of these is the scheme adopted to represent the Earth's velocity structure and the treatment of velocity structure-hypocentre coupling. Some applications represent velocity structure as constant velocity layers (*Crosson*, 1976), blocks of constant velocity (*Aki and Lee*, 1976), many small blocks of constant velocity (*Lees and Crosson*, 1989) and laterally-varying velocity layers (*Hawley et al.*, 1981). Others define velocity structure by means of a three dimensional grid of discreet nodes (*Thurber*, 1981; 1983; 1993). This method was extended to interpolate using cubic *b*-splines which produces a smoother result (*Michelini and McEvilly,* 1991). A variation of the grid approach uses four neighbouring nodes to define the vertices of a tetrahedron (*Lin and Roecker*, 1990).

Early LET methods perturbed the velocity structure but kept the hypocentres fixed at their initial values. Hypocentre determination, however, is part of the inverse problem and this approach can introduce model bias due to systematic hypocentre mislocation. Simultaneous inversion treats the problem by coupling perturbations of the velocity structure with updates to the hypocentre co-ordinates at the termination of each iteration (*Thurber*, 1993).

A good tomographic method should feature a generalised parameterization of the model volume which minimises the need for *a priori* information, an accurate ray-tracing algorithm, a model that may vary in three-dimensions without sharp block boundaries, and it should include an option to model *S*-waves *e.g.*, using the ratio of compressional to shear wave speeds (v_P/v_S). The modified simultaneous inversion technique of *Thurber* (1981; 1983; 1993) fulfils these requirements and is used in this thesis.

4.2.3 Three-dimensional simultaneous tomographic inversion: Theory

4.2.3.1 The Thurber inversion for v_P

The method of *Thurber* (1981; 1983) inverts *P*-phase arrival times to determine a three-dimensional v_P model. It is suitable for use with local earthquakes measured

by a dense homogenous network of seismometers distributed evenly over the surface of the model volume (*Evans et al.*, 1994). Shots (with known location and origin time) and blasts (explosions with known location but unknown origin time) can also be included.

The *Thurber* (1993) inversion like most other LET techniques is based on Equation 4.4. For the *i*th event, the coupled inverse problem can be expressed by a set of simultaneous equations:

$$r_i = H_i \Delta h_i + M_i \Delta m \qquad 4.5$$

where r_i is the residual vector of L travel time residuals, H_i and M_i are the matrices of hypocentre and velocity partial derivatives respectively, and Δh_i and Δm are vectors containing the four hypocentre unknowns and the N velocity perturbations respectively. All the terms are partial vectors or matrices of the complete system of equations, with the exception of Δm.

A set of equations involving only velocity model parameters can be sequentially accumulated without loss of formal wave speed-hypocentre coupling by making use of the sparse nature of the matrix represented in Equation 4.4 (*Pavlis and Brooker*, 1980). A matrix Q_o is constructed which has the property:

$$Q_o^T H_i = 0 \qquad 4.6$$

(*Lawson and Hanson*, 1974) which, when applied to Equation 4.5, results in:

$$Q_o r_i = r'_i = Q_o H_i \Delta h_i + Q_o M_i \Delta m = M'_i \Delta m, \qquad 4.7$$

which simplifies to:

$$r' = M' \Delta m \ . \qquad 4.8$$

The corresponding set of normal equations is given by:

$$(M'^T r') = (M'^T M') \Delta m \ . \qquad 4.9$$

As each earthquake is processed the matrix $M'^T M'$ and the vector $M'^T r'$ are accumulated sequentially to produce a symmetric matrix and vector of fixed size. A damping parameter is included to suppress large model fluctuations. A solution to the set of normal equations is determined using damped least squares. The best estimate of the perturbation $\Delta\tilde{m}$ of the velocity parameter adjustments Δm is given by:

$$\Delta\tilde{m} = (M'^{T}M' + \varepsilon^2 I)^{-1} M'^{T} r' \qquad 4.10$$

(*Arnott*, 1990). Velocity model changes are applied to the starting model and hypocentre estimates recalculated using the updated model.

4.2.3.2 Modelling the v_P/v_S ratio

The *Thurber* (1981; 1983) inversion was extended to include *S*-waves by modelling of the v_P/v_S ratio (*Eberhart-Phillips*, 1989). If v_P/v_S is assumed to be initially constant then the ray-paths are identical for both *P*- and *S*-waves and the observed *S-P* time differences dt_{ij} can be expressed as:

$$dt_{ij} = \int_{path} \left[(v_P/v_S) - 1 \right] / v_P \, ds \quad . \qquad 4.11$$

Using a three-dimensional *P*-wave velocity model and constant v_P/v_S ratio the predicted *S-P* travel times, dt_{ij}^{cal} are compared to the observed times dt_{ij}^{obs} to produce *S-P* time residuals which are inverted to calculate perturbations to the v_P/v_S nodes. During the one-step inversion both the v_P model and the hypocentres remain fixed. Revised hypocentre estimates are calculated by first updating perturbations to the v_P/v_S ratio model to calculate a three-dimensional grid of v_S and then re-determining the *S*-wave travel times.

4.2.3.3 Ray tracing

One of the most important aspects of the LET problem is determining the travel-time between source and receiver. This involves determining the propagation path of seismic rays between these two end-points. The method of *Thurber* (1983) calculates the velocity at a given point (x_1, x_2, x_3) by linearly interpolating the eight surrounding nodal values in a three-dimensional grid. An initial ray-path is determined using an approximate ray-tracing (ART) algorithm which constructs circular paths of varying curvature between source and receiver and systematically rotates the plane containing these paths about the source-receiver axis (Figure 4.1). The path with the shortest travel-time is adopted as the best initial estimate of the true ray path. The program finds a better approximation to the true ray-path by taking this initial ray-path and applying an iterative pseudo-bending algorithm which no longer constrains the ray to be planar or arcuate (*Um and Thurber*, 1987).

4.2.3.4 The derivative-weight sum

The derivative weight sum (DWS) provides a measure of the ray-density near a given velocity node. It is weighted according to how close each ray passes and is used to design the three-dimensional grid of discrete velocity nodes used in the tomographic modelling process. The DWS is defined as:

$$\mathrm{DWS}(n) = N \sum_i \sum_j \left(\int_{P_{ij}} w_n(\mathrm{x}) ds \right) \qquad 4.12$$

for the nth velocity model parameter x_n where, i and j are station and event indices, P_{ij} is the ray-path between i and j, N is the normalisation factor that accounts for the volume influenced by the nth model parameter and w_n is the weighting of the nth model parameter used to interpolate the wave-speed at position x. A cut-off value of 50 has been suggested to distinguish well-resolved from poorly-resolved nodes (*Arnott and Foulger*, 1994a).

4.2.3.5 Model resolution

The non-uniform distribution of seismometer stations and earthquakes controls the distribution and density of ray-path coverage within the modelled volume. Usually some parts of the model are poorly constrained. A statistical measure of model resolution and the reliability of each velocity node is required. This is provided by the *spread* function:

$$spread = \left[\left\| R_j \right\|^{-2} \sum_k D_{jk}^2 R_{jk}^2 \right]^{1/2} \qquad 4.13$$

(*Foulger et al.*, 1996), where $\left\| R_j \right\|$ is the Euclidean (L2) norm of the jth row of the resolution matrix, D_{jk} is the distance between the jth and kth nodes, and R_{jk} is the (j, k) element of the resolution matrix.

The velocity determined for a particular grid point is a weighted average of the velocity throughout a localised volume. Each row of the resolution matrix contains information on the relative influence of other velocity parameters on the wave-speed calculated at a particular node. The spread function yields a value for each grid point which expresses the degree of local averaging involved in determining that particular wave-speed value. Small spreads indicate well-resolved wave-speeds. Extensive testing of this parameter in a companion study of the Hengill-Grensdalur volcanic system suggests

a cut-off *spread* value ≤ 4 can distinguish "well resolved" areas of the model that are sufficiently reliably constrained to warrant interpretation (*Foulger et al.*, 1996; *Miller*, 1996).

4.2.4 The *SIMULPS12* program

The *SIMULPS12* program performs a damped least squares inversion on *P*-wave travel-times and optionally *S-P* travel-times from local earthquakes and surface explosions to model three-dimensional v_P and v_P/v_S velocity structure. The program is controlled by a set of user defined input parameters specified in a *control* file (Appendix 6). Most parameters are set to standard values recommended by the authors of the source code (*Evans et al.*, 1995). Several parameters are data dependent and choice of optimum values must be determined by experiment.

The program requires a minimum of four input files and inversion details are recorded in a series of output files. The most important of these are:

Input files

fort.1 Control file
fort.2 Seismometer station location information
fort.3 Starting wave-speed models and nodal locations
fort.4 Earthquake travel-time data and initial hypocentral locations

Example input files are given in Appendix 6

Output files

fort.16 Changes to model and earthquake locations at each iteration plus the final model and hypocentres
fort.17 Resolution matrix
fort.20 Travel-time residuals for each iteration
fort.23 Final velocity model
fort.24 Earthquake travel-time data for final hypocentres
fort.36 Iteration summary

Miller (1996) wrote a suite of Bourne shell scripts to facilitate using SIMULPS12, presenting the results from a tomographic study of the Hengill-Grensdalur volcanic area, Iceland. I tested and adapted these scripts for the present project. A selection of the many

additional programs I developed for both processing and presentation are presented in Appendix 7. Colour and grey-scale images of the velocity models were generated using the Generic Mapping Tool (GMT) software (*Wessel and Smith*, 1991).

4.2.5 Inversion approach used in this thesis

4.2.5.1 Event selection

The most accurate *P*- and *S*-wave arrival-time measurements are made on seismograms with a good signal-to-noise ratio. Many events recorded at The Geysers met this requirement but their hypocentres cluster in space. Seismic rays from a cluster of earthquakes sample the same portion of the study volume and no additional velocity-structure information is provided by including all these events in the modelling process. Only the best of these earthquakes or, for large clusters, several of the best events were included. An even spatial distribution of ray-paths within the modelled volume is desirable, since the wave-speed in some finite volume will be more accurately constrained by a large number of seismic rays criss-crossing and sampling the volume in three-dimensions.

Earthquakes were chosen based on a set of general phase selection criteria defined in previous tomographic studies:

- good signal-to-noise ratio
- impulsive *P*- and *S*-wave arrivals
- good azimuthal ray coverage and maximum azimuthal gap between adjacent stations $<180^{o}$
- a uniform distribution of events

I defined three additional phase selection criteria:

- at least seven *P*-wave arrivals per earthquake
- RMS travel-time residual less than 0.4 s
- where possible, only fast *S*-waves were included to simplify interpretation in the presence of anisotropy

To increase ray-path coverage in relatively aseismic areas of the study volume at The Geysers the selection criteria in some cases were relaxed. A few earthquakes of slightly reduced quality were included in the tomography data set.

4.2.5.2 The initial one-dimensional wave-speed model

The starting model used in LET modelling can have considerable effect on the final three-dimensional model. Including *a priori* information such as that taken from previous geological and geophysical interpretations can give apparently reasonable results but can also anchor the final result to the starting model or bias it with preconceived ideas (*Eberhart-Phillips*, 1993). The most reasonable result is produced using the best average one-dimensional wave-speed model and allowing model complexity to be included in the inversion only where supported by the data.

Using the inversion program *VELEST Kissling et al.* (1994) proposed a scheme to determine the best one-dimensional layered v_P model termed the "minimum" one-dimensional v_P model for a given set of earthquake travel-time measurements (*Ellsworth,* 1977; *Kissling*, 1988). The program iteratively improves estimates of an initial one-dimensional velocity model, simultaneously updating hypocentres and travel-times until a final minimum velocity model is derived. The starting one-dimensional model for this procedure is usually one derived in past controlled-source studies such as refraction experiments. The earthquake travel-times, seismometer stations and Earth model dimensions should be those selected for the later three-dimensional modelling.

A minimum one-dimensional layered v_P model for The Geysers geothermal area was determined using this procedure. The initial one-dimensional v_P model was that generated by inversion of *P*-wave travel times in the northern Coast Ranges (Section 3.3.1). The input layered model was designed such that the centres of the layers were at the depths of the intended node layers in *SIMULPS12*. This simplified the conversion of the layered model into the *SIMULPS12* input model format. Good initial estimates of the average v_P/v_S ratio for The Geysers were determined by taking the median value of a series v_P/v_S ratio estimates calculated from Wadati diagrams.

4.2.5.3 Parameterizing the model volume

The method of *Thurber* (1983) defines wave-speed structure in the modelled volume at a series of discrete nodes formed by the intersection of three sets of orthogonal planes forming a grid of velocity nodes (Figure 4.2). A linear wave-speed gradient is assumed between adjacent nodes. Closely-spaced vertical-planes of nodes are restricted to areas of the model volume where ray-path coverage is dense with more widely-spaced planes elsewhere. The model space is bounded at large distances in all directions by planes of "exterior" nodes such that no ray will travel more than half the distance between the "interior" and exterior nodes. Exterior nodes remain fixed throughout the modelling process.

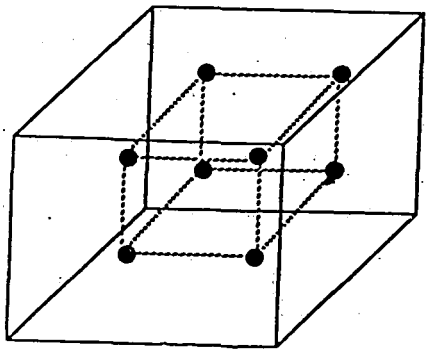

Figure 4.2. Schematic representation depicting the grid-of-nodes method of parameterizing the wave speed model, after *Thurber* (1993). Seismic velocity is defined at a series of discrete nodes defined by the intersections of one horizontal and two vertical nodal planes. A linear velocity gradient is assumed between adjacent nodes.

Vertical nodal planes in the present study were oriented parallel and perpendicular to geological features and the tectonic fabric of the San Andreas shear zone since the expected high wave-speed gradients across features such as the Mercuryville or Collayomi fault zones can be much better constrained by placing nodes close to and either side of a discontinuity. The model volume was chosen to maximise ray-coverage by enclosing as many seismic stations as possible from the three networks available. Parameterization of the model volume was controlled by the density of ray-paths, a measure of which was made empirically using the DWS (Section 4.2.3.3). Nodes with a DWS less than pre-defined value in the control file (Appendix 6) were held fixed throughout the inversion. A layer of unmodelled nodes were assigned reasonable upper crustal velocities and placed above the shallowest modelled layer and below the deepest modelled layer since this has been shown to stabilise inversions in previous LET studies (*Dawson et al.*, 1990).

4.2.5.4 Damping trade-off curves

Damped least squares inversions are sensitive to the choice of damping parameter ε^2. The most appropriate damping value must be evaluated at each nodal configuration even if the wave-speed model and travel-time data remain unchanged (*Eberhart-Phillips*, 1993). Appropriate damping values allow a large reduction in data variance without making the model overly complicated. Using too low a damping value produces large changes to the velocity model for relatively little decrease in data variance and the inversion can behave non-linearly. Inappropriately large damping values suppress changes to the model that are supported by the data.

Damping parameters for inversions of The Geysers data were determined empirically by performing a series of one-iteration inversions for a range of damping values *e.g.*, 0.1-999 (*Eberhart-Phillips*, 1986; 1993). The input nodal configuration, velocity model and travel times were identical to those used in the subsequent inversion for wave-speeds. The reduction in data variance was plotted against model variance to produce a damping trade-off curve from which an appropriate damping value could be determined (Figure 4.3).

4.2.5.5 Terminating the inversion

SIMULPS12 will terminate an inversion in one of four situations:

- the *F*-test fails: variance reduction becomes insignificant.
- the number of iterations reaches the maximum allowed in the input *control* file (Appendix 6)
- the weighted RMS falls below a pre-defined value in the *control* file
- the solution norm falls below a pre-defined value in the *control* file

4.2.5.6 LET inversion procedures and strategies

The LET technique is inherently non-linear and can converge to a local minimum. The most desirable result is the global minimum and attaining it requires careful consideration of data quality, parameterization of the model volume, starting one-dimensional model, choice of values guiding the inversion and conservative use of the inversion programs. There are two approaches to the inversion procedure, termed the "graded" and "direct" inversion. In a graded inversion the initial coarse grid configuration is made progressively finer during successive inversions. Each refined model is initialised from velocities computed in the proceeding coarser inversion. Input hypocentres and travel-time residuals are also those output in the preceding inversion. This procedure allows structural detail and model complexity to be gradually introduced reducing the likelihood of the model converging to a local minimum. Generally v_P and v_P/v_S can be inverted at each stage of the inversion or alternatively reserve solving for v_P/v_S until the final iteration when a detailed v_P model has been derived. Proceeding directly to a coarse model of v_P/v_S is considered reasonable because the v_P/v_S field is typically much smoother than either v_P or v_S. The direct inversion proceeds directly to the finest nodal configuration and inverts for both v_P and v_P/v_S. This is attractive since it is fast, does not require interpolation of velocity models to finer nodal spacing and is computationally inexpensive. However, the procedure increases the possibility of converging to a local

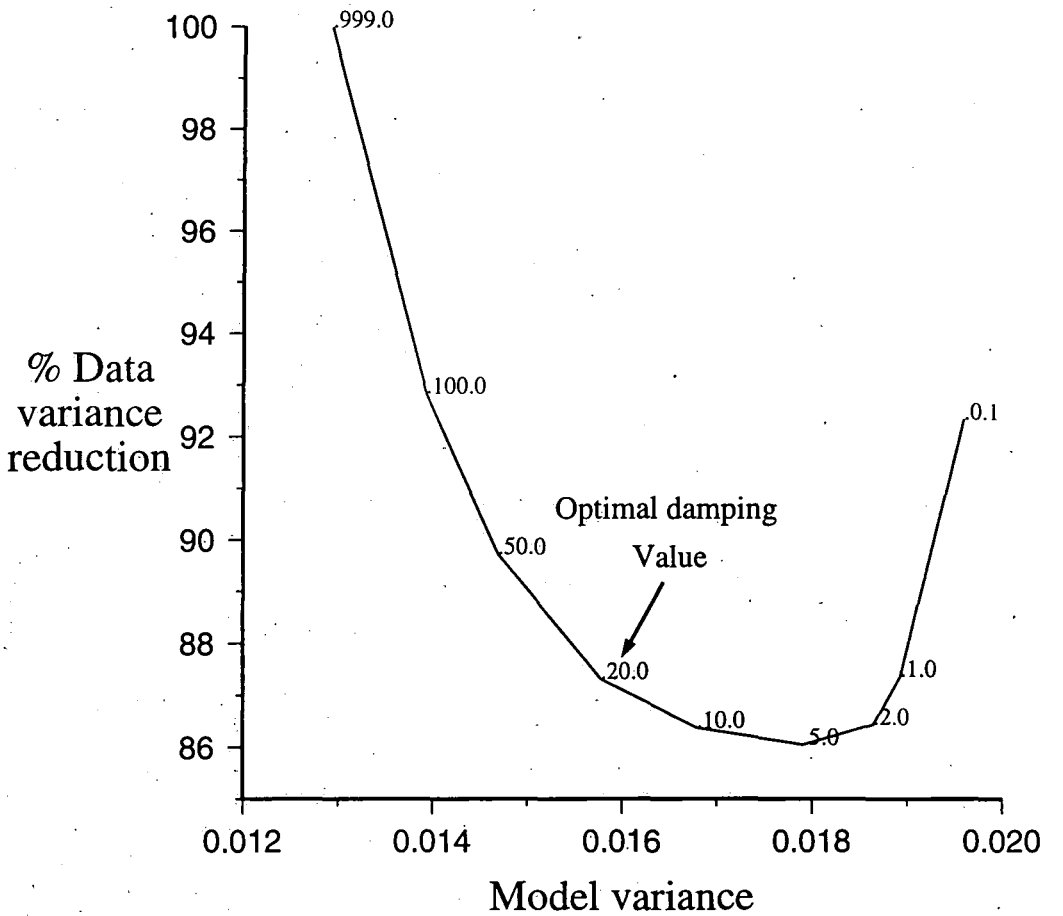

Figure 4.3. Example of a damping trade-off curve for selecting optimal damping value. The optimal damping value is that which produces a substantial data variance reduction without a disproportionately large increase in model variance.

minimum and is most useful for testing nodal configurations and identifying data outliers.

Both graded and direct inversions were performed. The direct inversion used the same three-dimensional grid of nodes as the final stage of the graded inversion. Including *S-P* times improves the location accuracy of earthquakes so v_P/v_S nodes were included but remained fixed when inverting for v_P. In the three graded inversions v_P/v_S was inverted at each of the two finest nodal configurations.

A comprehensive program of graded inversions tested the data, the modelling process, the *SIMULPS12* program and the stability of the final wave-speed models. In some early inversions travel-time residuals were analysed at the end of each inversion run. Unstable travel-time residuals were removed from the data set. The weighting of the travel-time residuals was also varied. Inversions were performed with the vertical nodal planes at various orientations relative to the tectonic fabric. The minimum one-dimensional v_P model and the initial v_P/v_S ratio estimate were replaced with the regional one-dimensional v_P model and v_P/v_S=1.8 (Section 4.2.5.2). Any bias in the final model

produced by the input hypocentres and travel-time residuals generated by *qloc* was sought by forcing hypocentres to be 1 km deeper than calculated. Separate inversions of data recorded by the temporary and UNT networks tested the concordance of the data sets.

4.3 Some examples of LET studies

Iceland: Iceland is an extremely good laboratory for local tomography studies as it has many seismogenic volcanic and geothermal areas such as the Hengill-Grensdalur area in the southwest and the Krafla area in northeast Iceland (*Foulger and Toomey,* 1989; *Toomey and Foulger*, 1989; *Arnott*, 1990; *Foulger and Arnott*, 1993; *Arnott and Foulger*, 1994; *Foulger et al.*, 1995). Two independent tomographic studies of the Hengill-Grensdalur area have been performed, for v_P using data collected in 1981, and for both v_P and v_P/v_S using data collected in 1991. This provides a rare opportunity to assess the repeatability of LET (*Foulger et al.*, 1995). Well resolved high-v_P anomalies were detected in both studies that correlated well geographically though anomaly amplitude varied between the two studies. The most coherent v_P/v_S anomaly correlates well with the high-temperature geothermal area there, and is thought to be caused by a combination of altered clay minerals and local changes in pore-fluid temperature or saturation. The lack of high v_P/v_S anomalies suggested that partial melt is absent in the upper 6 km of the crust. LET studies of the v_P structure in the Krafla area image high-velocity bodies under the caldera ring fault, interpreted as solidified high-density gabbroic intrusives. A high velocity body south of the caldera underlies an ash cone and was interpreted to be a solidified intrusive body which fed the surface eruption. Low velocity anomalies correlate with the geothermal field within the caldera and a subsidiary geothermal area 15 km further south (*Einarsson*, 1978; *Arnott and Foulger*, 1994).

Kilauea Volcano, Hawaii: A LET investigation of the crustal v_P structure beneath Kilauea Volcano, Hawaii found high velocity material underlying the summit caldera, which was interpreted as solidified magma forming the roof of the magma chamber (*Thurber*, 1984). High velocity bodies were also imaged under the rift zones which radiate from the volcano, and were interpreted as high density intrusives. An aseismic, low-velocity body under the caldera was interpreted as a volume of partial melt.

Loma Prieta, California: Three-dimensional images of v_P in the Loma Prieta M=7.1 after-shock zone imaged a deep, high-velocity body along the southeast portion of the main rupture zone and moderately high velocities in the northwest (*Thurber et al.*, 1995). Steep velocity gradients mark the limit of the rupture zone to the southeast. A sharp increase in v_P/v_S in the upper portions of the rupture zone is interpreted as a change in the elastic

properties of the crust with depth. These were thought to be responsible for the upward termination of the Loma Prieta rupture (*Wallace and Wallace*, 1993). Based on differences in v_P/v_S from northeast and southwest the deep high velocity body is interpreted to consist of two segments, differing in composition, and faulted together, rather than a single unbroken body.

4.4 Local earthquake tomography at The Geysers geothermal area

Eberhart-Phillips (1986): Three regional tomographic models for v_P which incorporated The Geysers geothermal area have been previously calculated using the method of *Thurber* (1983) (*Eberhart-Phillips*, 1986). Ray-path coverage varied enormously over the study area. The Geysers had the highest density ray path coverage and therefore yielded the most detailed wave-speed model. The model adopted a grid spacing of 2 to 3 km and used 170 earthquakes (Table 4.1). The highest velocities were imaged at shallow depths ($\leq$2 km) east of the Mercuryville fault zone in the central and southeast Geysers (Figure 4.4). These are interpreted to result from Franciscan metasandstones and slabs of Coast Range ophiolite. Low velocities to the northwest correlate with the Clear Lake volcanics. Lower wave-speeds in the steam production zone compared to the surrounding region were interpreted to result from the steam-saturated reservoir or a variation in rock type. The sparse nature of the velocity grid prohibited resolution of small-scale structural detail within the reservoir.

Table 4.1. Statistics for the LET studies of The Geysers geothermal area

Reference	Modelled Parameter		Number of seismic stations 3-comp. vertical		Number of earthquakes	Number of seismic phase arrivals		Dimensions of modelled volume, km
	v_P	v_P/v_S				*P*-wave	*S*-wave	
Eberhart-Phillips (1986)	yes	no	14	64	170	NA	NA	18x15x5
O'Connell (1986)	yes	yes	9	8	38	469	294	NA
Zucca et al. (1994)	yes	no	NA	NA	NA	NA	NA	8.5x5.5x5
Romero et al. (1994)	yes	yes	16	0	480	9700	2700	5x5x4
Foulger et al. (1996)[1]	yes	yes	7	15	146	2522	656	20x20x7

[1] Study described in Chapter 7

NA: Information not available

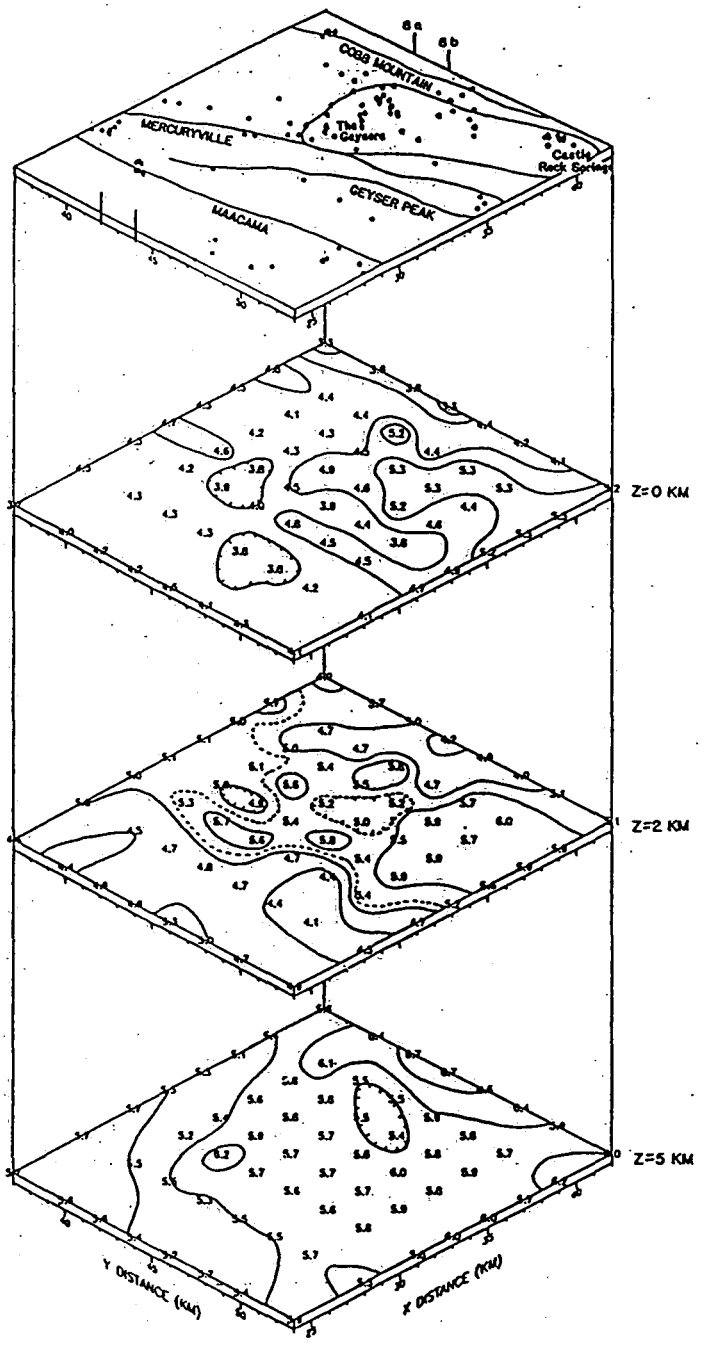

Figure 4.4 Perspective plot of the v_P model computed for The Geysers geothermal area, by *Eberhart-Phillips* (1986). The top level maps the principal faults, commercial production area, earthquakes and seismic stations (indistinguishable in this reproduction). The lower three levels depict the v_P model at sea level, 2 km bsl and 5 km bsl. Final nodal velocities in km/s are indicated and solid lines are 0.5 km/s contours.

O'Connell (1986): v_P was computed using the graded inversion method of *Pavlis* (1982), extended to incorporate *S*-waves (Table 4.1) (*O'Connell*, 1986). High-v_P velocities in the southeast Geysers and lower velocities to the northeast are consistent with results of *Eberhart-Phillips* (1986) (Figure 4.5a). High v_P/v_S values correlate with the fluid-saturated condensation zone above the primary production zone the latter being depleted of pore fluids and characterised by lower v_P/v_S (Figure 4.5b). Increases in v_P/v_S below the shallow primary production zone suggest increased liquid saturation or changes in rock composition.

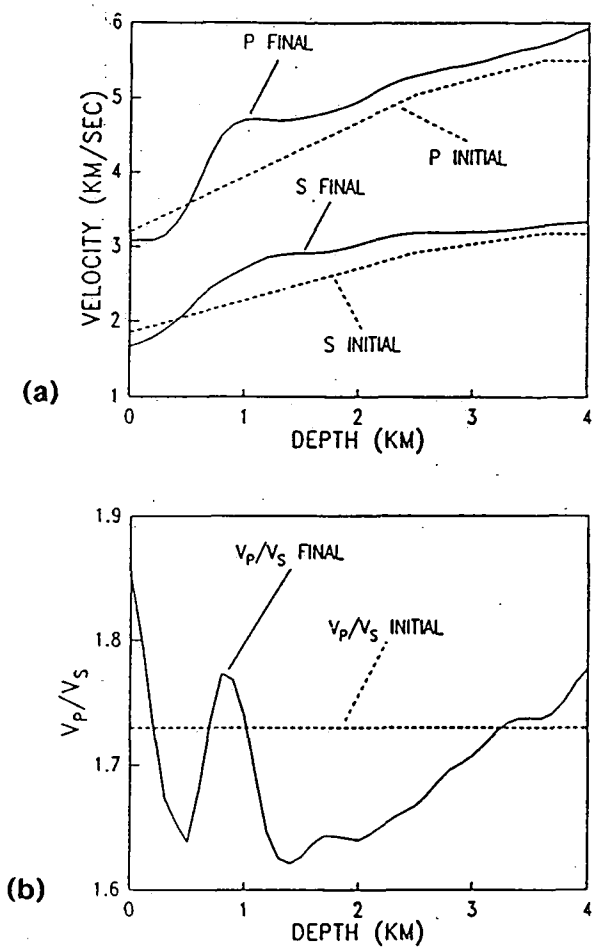

Figure 4.5. One-dimensional seismic wave speed models for the central Geysers, from *O'Connell* (1986). (a) Solid lines show the variation of final *P*- and *S*-wave velocity models with depth, dashed lines are the starting one-dimensional velocity models. (b) Initial (dashed line) and final (solid line) v_P/v_S ratio model.

Zucca et al. (1994): A high-resolution (0.6 km) v_P model computed for The Geysers production area (Figure 4.6) used the modified Thurber approach (Table 4.1)

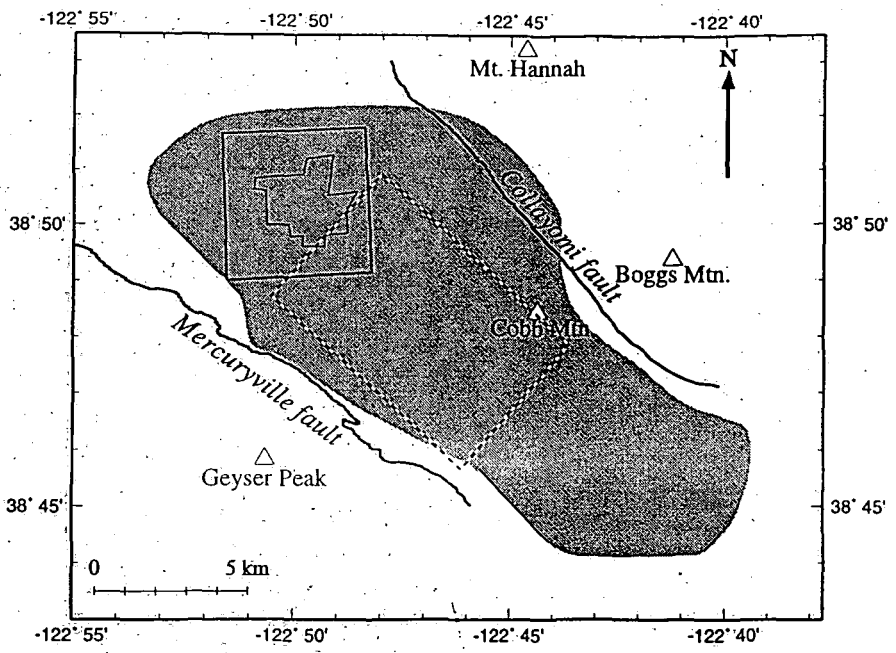

Figure 4.6. Map showing the surface area of Earth volumes modelled by *Zucca et al.* (1993) (white and black dashed rectangle) and *Romero et al.* (1994) (black square).

(*Eberhart-Phillips*, 1993). High velocities in the central area of the shallowest layer (0.3 asl) are interpreted as a lens of ultramafic material (Figure 4.7). Low velocities correlate with the reservoir particularly at 0.9 km bsl where the modelled layer intersects with the reservoir. This relation is inferred but less clear at 0.3 km bsl. The lowest modelled layer (1.5 km bsl) is completely within the reservoir which is now also hosted in upper portions of a felsite batholith. This intrusion correlates with a series of high velocity anomalies but the contrast between this body and the reservoir greywacke is weaker than expected.

Romero et al. (1994): A high-resolution study (1 km) in the northwest Geysers modelled v_P and v_P/v_S using the modified *Thurber* (1983) algorithm of *Michelini and McEvilly* (1991) (Table 4.1). Earthquakes were recorded on a well-distributed, small-aperture, digital network which provided a high-quality data set with a uniformly dense ray coverage (Figure 4.6) (Section 2.2). Resolution is lost on both models at depths exceeding 3 km bsl and the felsite batholith (which is deeper than 3.5 km bsl) could not be imaged. The v_P velocity structure consists of two isolated, high wave-speed anomalies to the north at sea level and a prominent high-wave speed anomaly in the upper 1 km to the southeast (Figure 4.8). These were interpreted to represent greenstone and metagreywacke units. Low wave-speeds in the central area at shallow depths migrate to the north with depth and are interpreted to represent Franciscan melange and brecciated basalt flows. Low wave-speed anomalies underlying the southern area at 1-3 km bsl may result from the high gas content of the underlying HTR (Section 1.3.2).

High v_P/v_S values (up to 1.8) were imaged in the central and western areas at sea

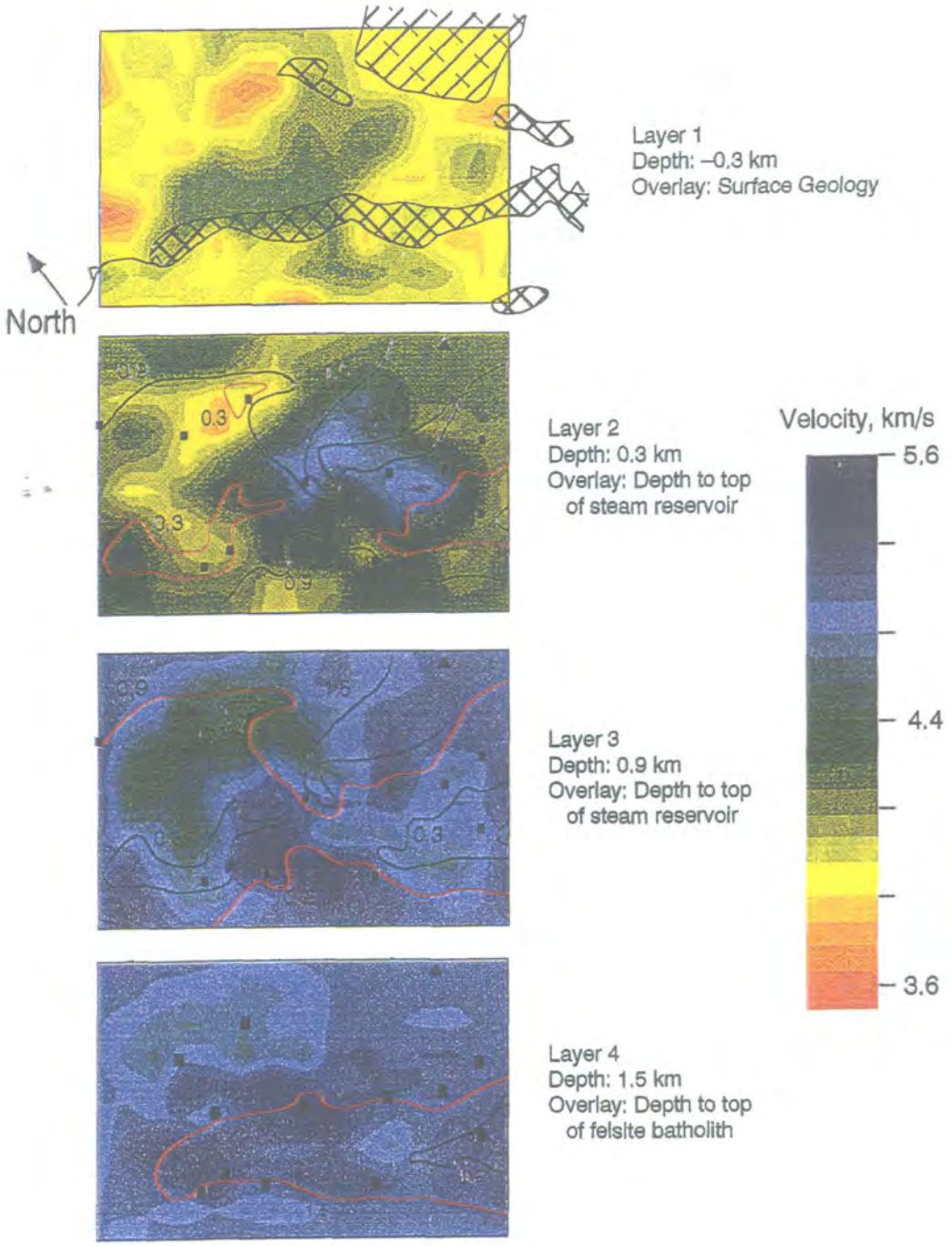

Figure 4.7 Three-dimensional v_P model for The Geysers geothermal area, after *Zucca et al.* (1994). The velocity structure is presented in four horizontal depth slices with anomalies in red indicating lower wave speeds grading to anomalies in blue indicating higher wave speeds. The hashed areas in layer 1 (0.3 km asl) indicate the surface exposure of igneous rocks. The Big Sulphur Creek fault zone is marked with a solid line (saw-toothed). The black and red contours in layers 2 and 3 show the depth to the top of the steam reservoir. The black and red contours in layer 4 show depth to the top of the felsite batholith. The red contour is the closest depth contour to the modelled layer in each case. Black contours are shallower or deeper. The number beside each contour gives the precise contour depth. The locations of electrical power generating units are indicated by black squares.

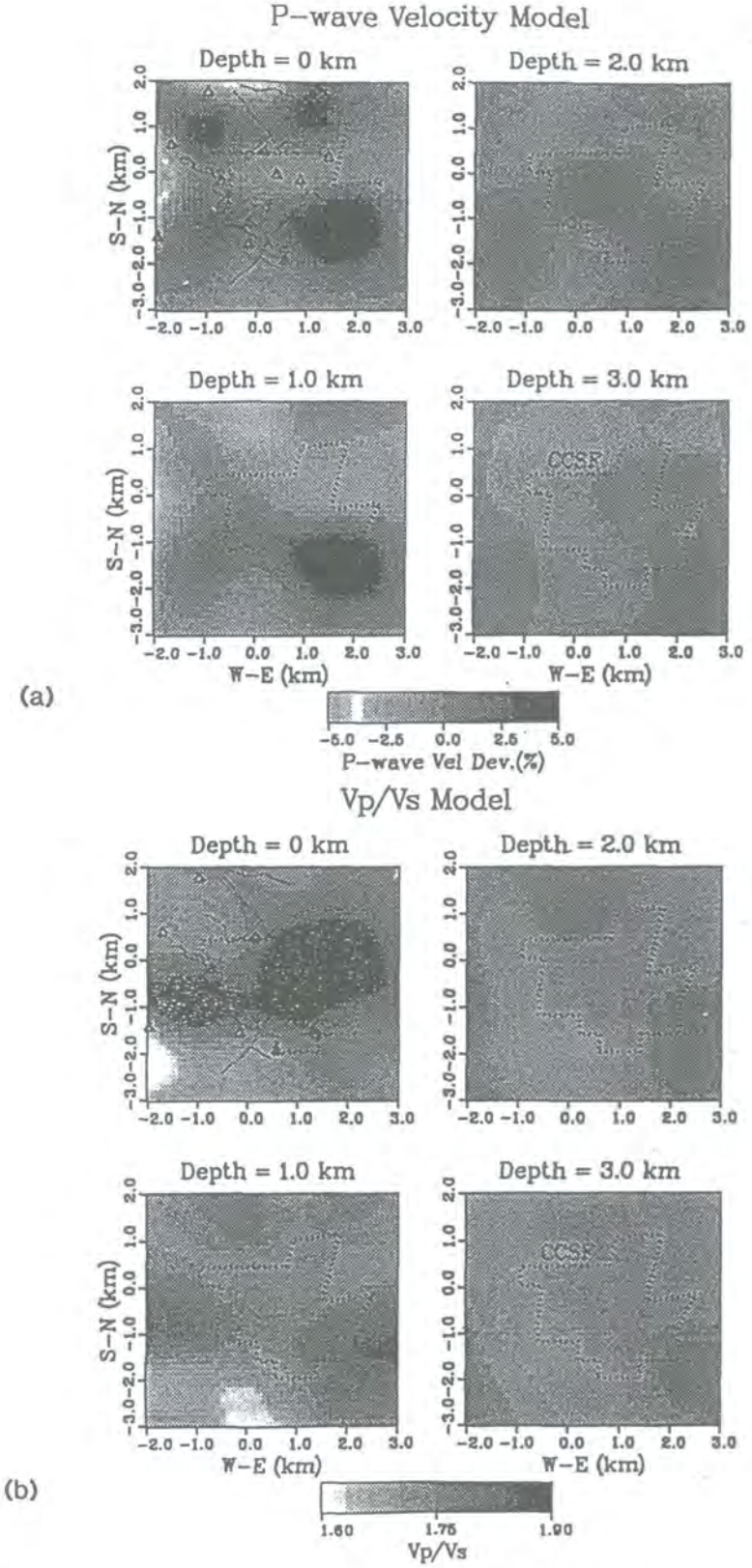

Figure 4.8 Three-dimensional velocity models for the northwest Geysers, after *Romero et al.* (1994). The models are presented in horizontal depth slices. The dashed line encloses the Coldwater Creek steam field (CCSF) and the triangles in the shallowest layers of each model are seismometer stations. (a) The v_P model shows percentage deviation from mean layer velocity. Light shading indicates speeds lower than average and dark shading higher than average. (b) v_P/v_S model: absolute values are shown.

level (Figure 4.8b). The western anomaly is continuous, though less well resolved, down to 1 km bsl with another high imaged to the southeast of the area at the same depth. The anomalies are interpreted as liquid-saturated zones in the near surface or zones affected by surface recharge. The deeper anomalies may also indicate a liquid-saturated zone of condensation. Low v_P/v_S anomalies (down to 1.6) dominate the central and southern areas at depths of $\geq$1 km bsl. Most steam entries are found in this zone, inferring that the low v_P/v_S anomaly correlates with the liquid-deficient production zone. *Romero et. al.*, (1994) suggest this may be one means of monitoring temporal changes in the steam zone.

4.5 Summary

Seismic tomography has been successfully used to model Earth structure on local, regional and global scales. Teleseismic and global surface-wave inversions resolve relatively large scale features. The cost and environmental issues associated with NeHT studies mean that LET methods are more commonly applied.

LET methods use *P*- and *S*-phase earthquake travel-time data recorded by a dense array of seismometers distributed evenly over the model volume. Three-dimensional variations in velocity structure are determined by perturbing the velocity structure within a model volume to minimise the misfit between observed and calculated travel-time residuals. The earthquake data set consisted of events with accurate *P*- and *S*-phase travel-time measurements distributed evenly over the model volume. The one-dimensional starting model was derived using the program *VELEST*. An initial v_P/v_S ratio estimate was determined from Wadati diagrams. Velocity structure was defined at a series of discrete nodes formed by the intersection of two vertical and one horizontal nodal plane. A linear velocity gradient is assumed between adjacent nodes.

Both graded and direct inversions were conducted. The v_P/v_S ratio was modelled at each nodal configuration, the two finest grid configurations and the final nodal grid. For each velocity grid a damping trade-off curve provided appropriate damping values. A comprehensive program of graded inversions tested various aspects of the data set, modelling procedure, *SIMULPS12* program and robustness of the wave-speed models.

LET has been successfully applied to several seismically active geothermal and volcanic areas imaging solidified gabbroic bodies under calderas in Iceland and Kilauea Volcano, Hawaii, and identifying rupture zones in active fault zones such as Loma Prieta. Various LET techniques have been applied to tomographic studies of The Geysers. Wave-speeds are generally lower than regional values due to variation in rock type or the steam-saturated reservoir. The higher velocities in the reservoir are thought to be produced by lenses of ultramafic material. Areas of high v_P/v_S values are interpreted as liquid-saturated zones and low v_P/v_S anomalies correlate with the liquid-deficient steam reservoir.

Chapter 5

The tomographic inversion results

5.1 Introduction

The v_P and v_P/v_S models presented in this chapter were generated by a graded inversion using the minimum one-dimensional v_P model determined by *VELEST* and improved v_P/v_S ratio estimate. The v_P/v_S model was held fixed at inversions with horizontal node spacing of 10 km, 4 km and the initial inversion for v_P at 2 km, proceeding then to full inversions of both v_P and v_P/v_S at 2 km and 1 km node spacings. The RMS travel-time residual was reduced by 63% to 0.027 s (0.022 s for *P*-waves; 0.044 s for *S*-waves) with model variance reduced by 81%.

5.2 Inversion configuration

5.2.1 The modelled data set

One hundred and eighty-five events were selected for tomographic modelling from a data set of 296 earthquakes, giving a total of 4032 *P*- and 1000 *S*-wave arrival times (Section 3.2.7). Of these, 46 arrivals were found to be unstable during preliminary modelling and discarded from the data set. The numbers of arrivals recorded by the 44 seismic stations used in this study are shown in Figure 5.1. Seismometer stations located within the seismically-active zone yielded the largest numbers of arrivals. The epicentral distribution of the events is shown in Figure 5.2. No shot or blast data were available .

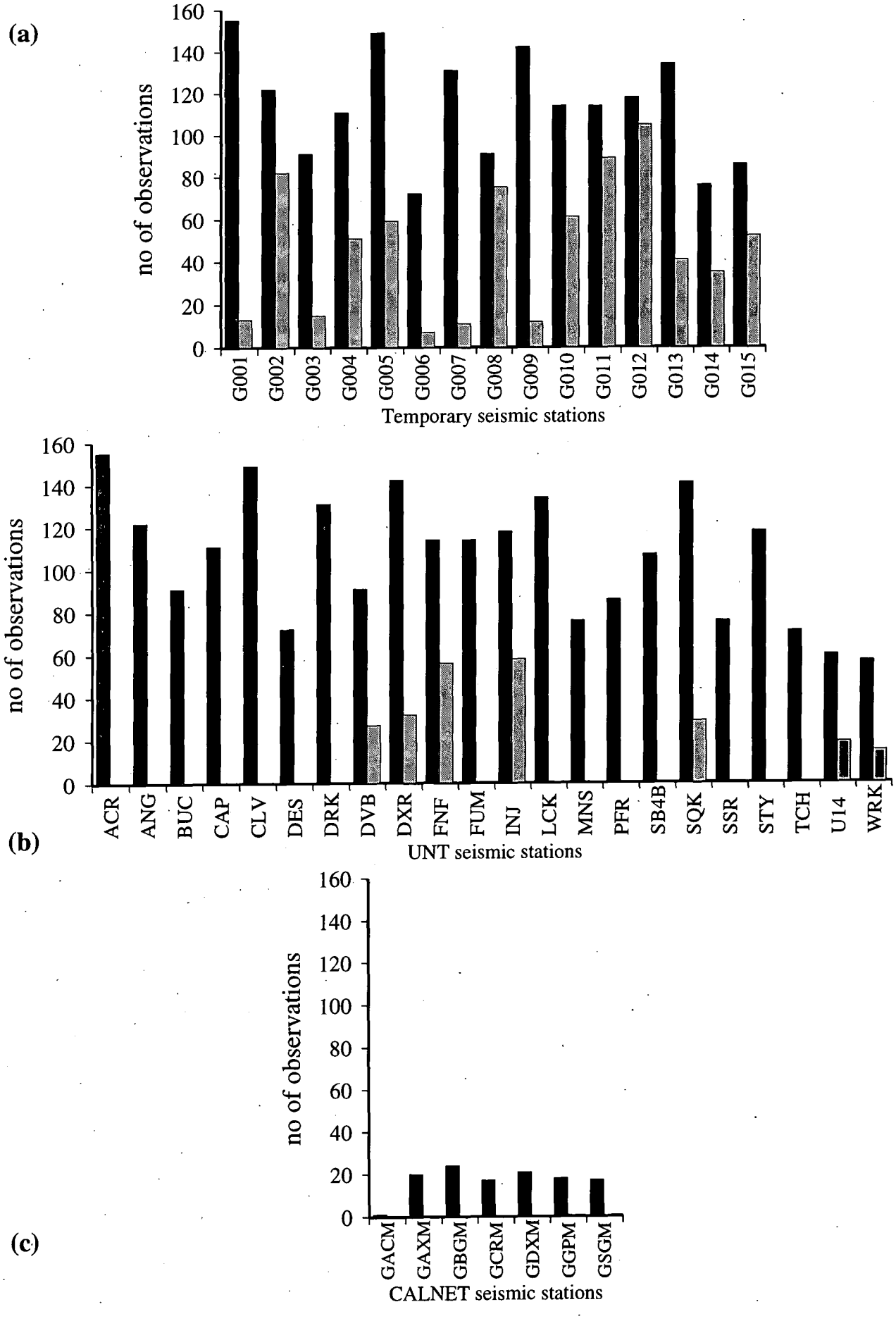

Figure 5.1. Numbers of P- and S-wave arrivals recorded at each station within the (a) temporary, (b) UNT, and (c) Calnet networks. Black columns: P-wave arrivals; shaded columns: S-wave arrivals.

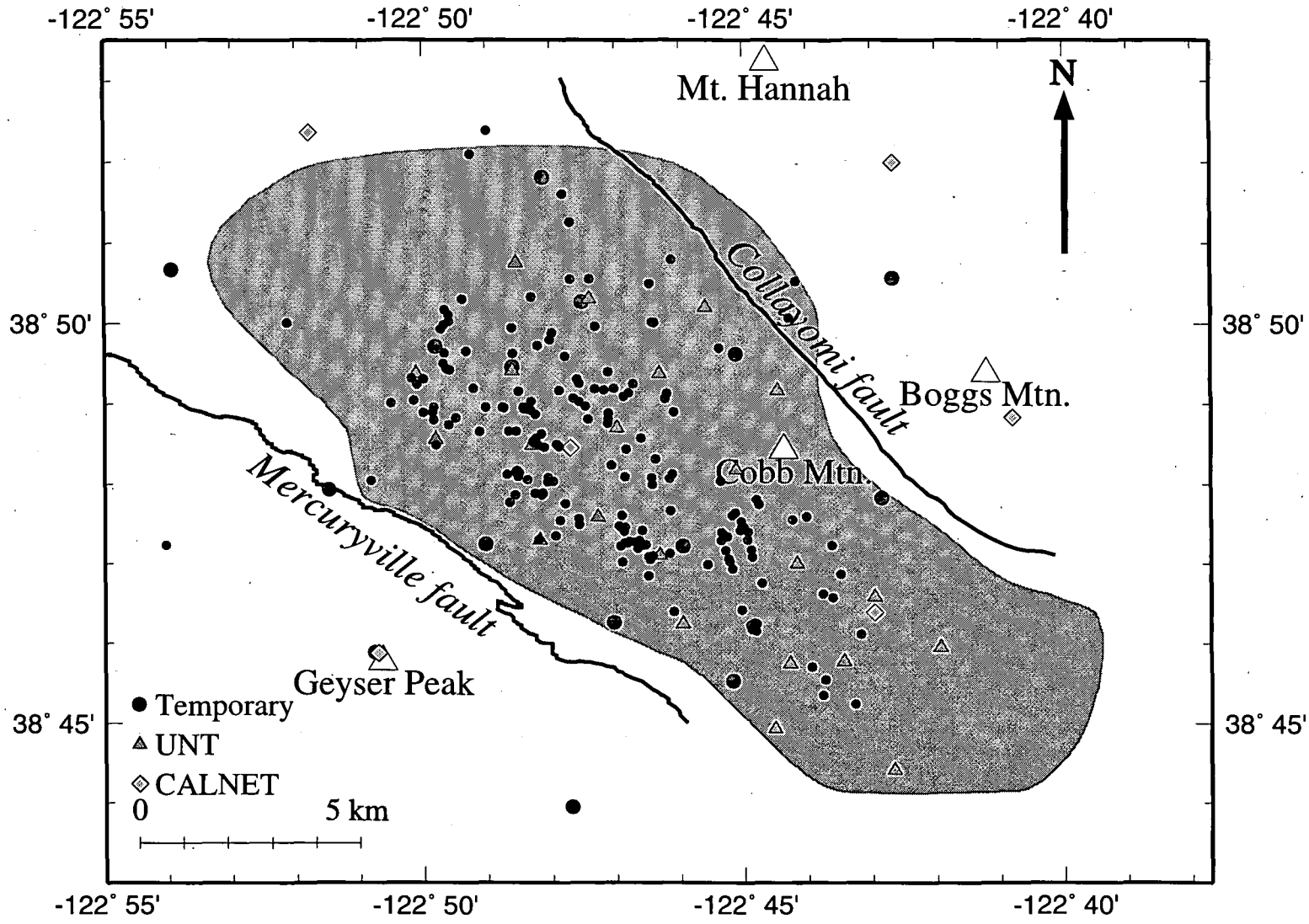

Figure 5.2. The epicentral distribution of the 185 earthquakes used in the tomographic modelling. Most events locate within the steam production area (shaded) and were chosen to maximise ray-path coverage. Shaded circles: temporary stations; shaded triangles: UNT stations; shaded diamonds: CALNET stations.

5.2.2 The starting one-dimensional v_P model and v_P/v_S ratio estimate

The one-dimensional v_P model generated by *VELEST* differed only slightly from the starting v_P model but produced a 24% decrease in the RMS travel-time residual from 0.058 s to 0.044 s (Figure 5.3) (Section 4.2.5.2). The final v_P model was converted to SIMULPS12 input format with wave-speeds defined at horizontal layers of nodes.

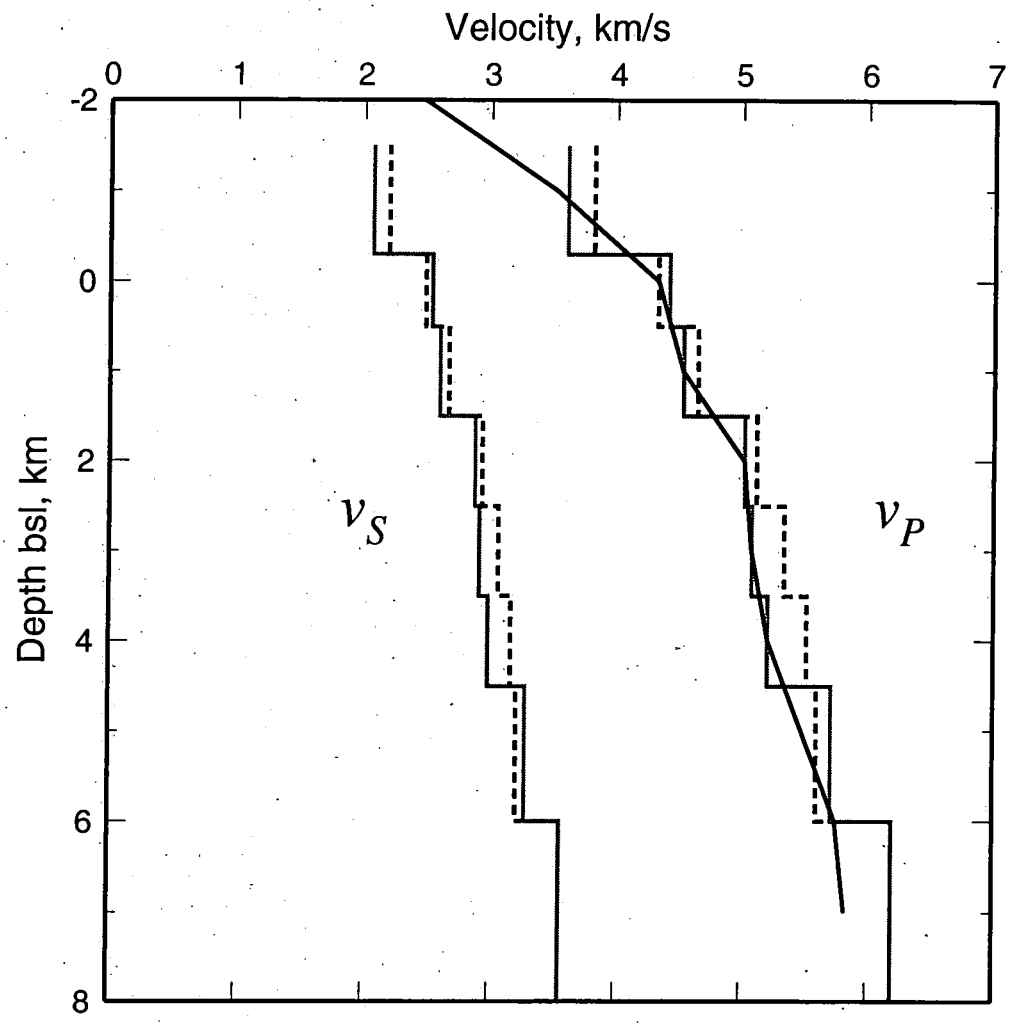

Figure 5.3. Final one-dimensional layered v_P model derived from *VELEST* (shaded line). The one-dimensional regional v_P layered model is represented by the dashed line (Section 3.3.1). The continuous, one-dimensional v_P model used initially by *SIMULPS12* is indicated by the solid black line. The one-dimensional v_S model used by *qloc* to determine input hypocentre and travel-time estimates was calculated from v_P assuming a constant v_P/v_S ratio of 1.74. The regional v_S model was calculated from the regional one-dimensional v_P model assuming a v_P/v_S ratio of 1.80.

The starting v_S model used along with the v_P model to generate input hypocentres and travel-time residual estimates for SIMULPS12 was calculated from the v_P model assuming a constant v_P/v_S ratio (Figure 5.3). An improved estimate of this ratio, 1.74, was determined from the median of 126 v_P/v_S values determined from Wadati diagrams for earthquakes with five or more *S-P* travel-time measurements (Figure 5.4).

The minimum one-dimensional model and improved estimate of v_P/v_S is only slightly different from the regional model and v_P/v_S value but it does produce a decrease in the RMS travel-time residuals. Horizontal and vertical location uncertainties are less than those suggested for the one-dimensional regional v_P model and v_P/v_S estimate. See Section 7.5.5 for discussion of location errors.

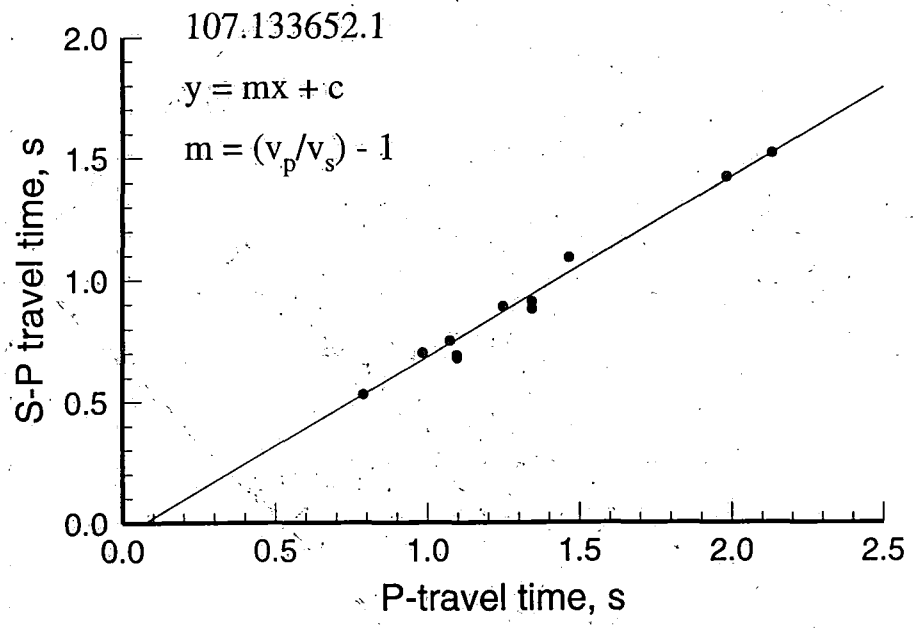

Figure 5.4. Wadati diagram of *P* vs. *S-P* travel-times recorded at eleven stations for event 107.133652.1. The v_P/v_S ratio is determined from the slope (m) on a line of best fit (linear regression) to the data points. In this case v_P/v_S=1.74.

5.2.3 Parameterization of the model volume

The model volume is 20 × 20 km in area and 6 km deep, rotated 45° from north and centred on the point 38:48.60° N –122:47.05° W in the seismically-active area (Figure 5.5). The area encloses 44 seismic stations and all the earthquakes used in the tomographic modelling.

The two vertical orthogonal nodal planes were oriented parallel (y-axis) and perpendicular (x-axis) to the northwest striking tectonic faults which bound the steam field to the northeast and southwest (Figure 5.5 and 5.6). The nodal configurations used in each stage of the graded inversion are shown in Figure 5.6. They consist of an initial, coarsely-spaced grid (63 nodes, 10 km horizontal spacing) which was made progressively finer during successive inversions (4 km, 2 km and 1 km). The final grid has 1232 velocity nodes and 1 km (horizontal) spacing where ray density is greatest. This corresponds to the area within the production zone. Nodal separation was increased to 2-4 km at the periphery of the modelled volume where ray-path coverage is poor (Figure 5.6). The vertical separation of horizontal planes of nodes remained unchanged throughout the graded inversion at 1 km between 1 km asl and 4 km bsl, increasing to 2 km at depths exceeding 4 km bsl. Fixed planes of nodes were placed at depths of –149.0 km, –2.0 km, 7 km and 149.0 km, and at ±149.0 km horizontally (Section 4.2.5.3).

5.2.4 Damping trade-off curves

A suite of damping trade-off curves were used to select damping values for each nodal configuration (Table 5.1; Figure 5.7). Damping values were large in the early inversions to suppress large fluctuations to the v_P model. Smaller values are appropriate as the model approaches the final model. Damping for the v_P/v_S model remained at 2 s (Figure 5.7b).

Table 5.1 Velocity damping values chosen for each nodal configuration.

Minimum horizontal node spacing, km	Damping value chosen from damping trade-off curve	
	v_P model, s^2	v_P/v_S ratio model, s
10.0	20.0	not modelled
4.0	20.0	not modelled
2.0	5.0	2.0
1.0	2.0	2.0

5.2.4 Resolution

Well-resolved areas of the wave-speed models were assessed using the spread function value (*Foulger et al.*, 1996). Velocity nodes with spread ≤4 km are considered to be well-resolved. These are mostly restricted to the production area which has the most dense coverage of ray-paths. Resolution is lost at depths exceeding 3 km bsl where only a

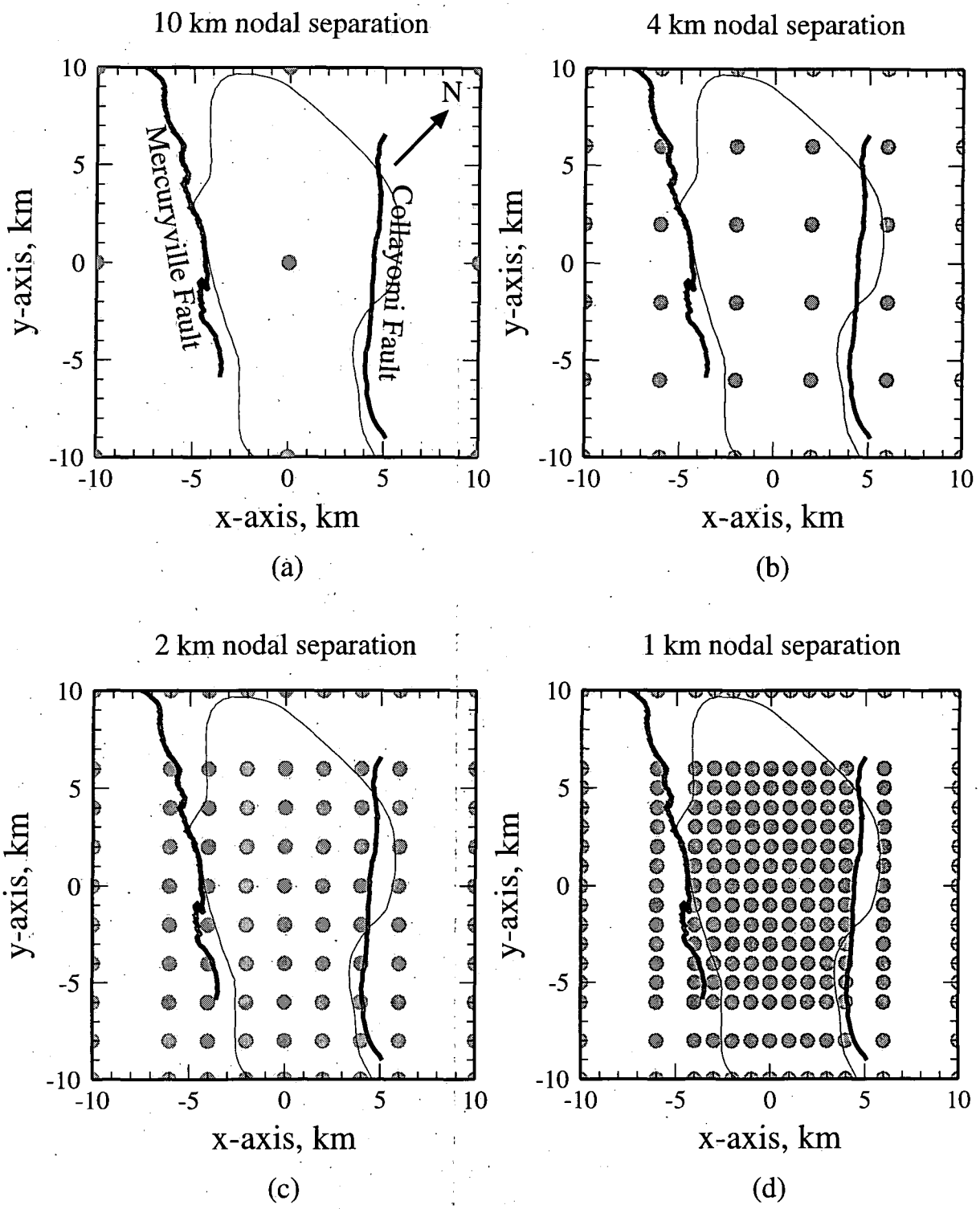

Figure 5.6. Horizontal layers of velocity nodes used at each stage of the graded inversion. Nodal separation varies from (a) 10 km, (b) 4 km, (c) 2 km, and (d) 1 km. Area enclosed by the thin black line is the 1992 production area. Thick black lines: faults; shaded circles: velocity nodes.

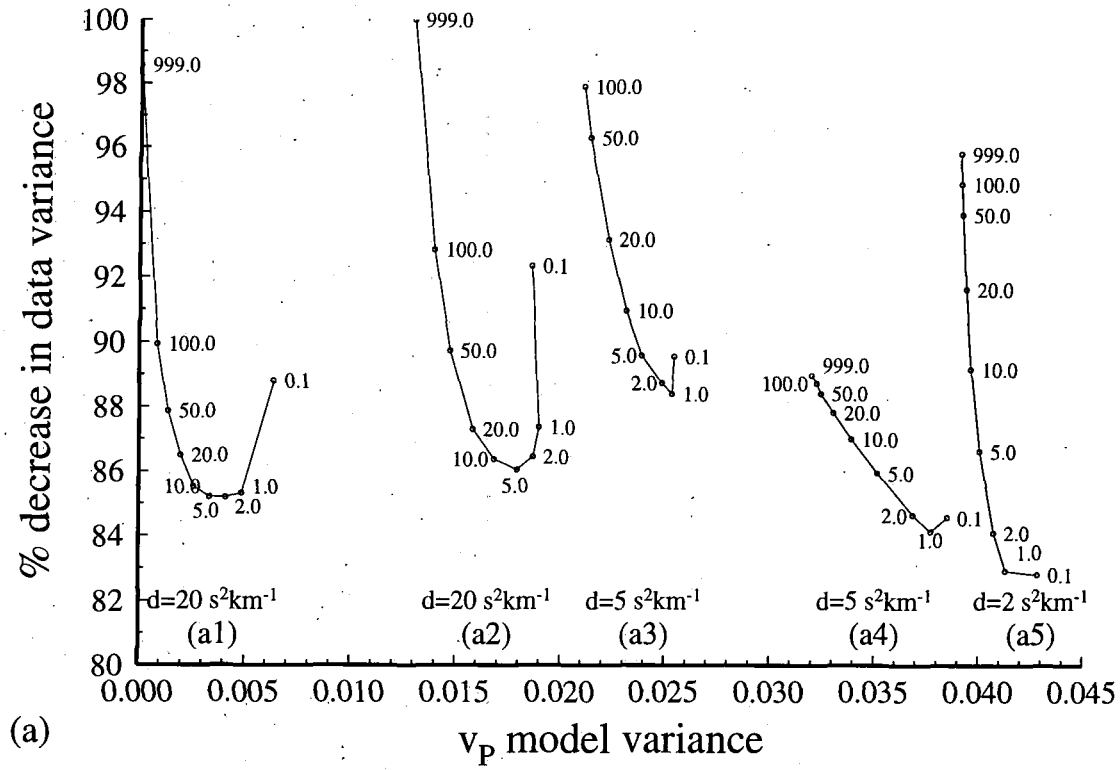

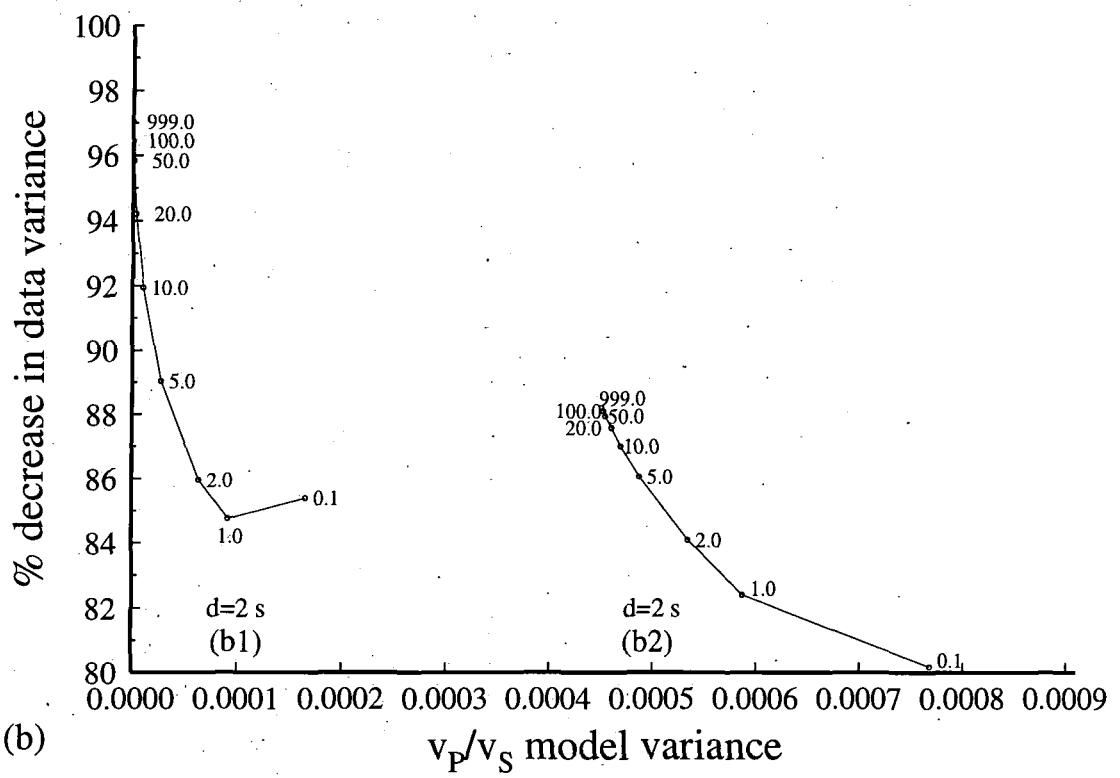

Figure 5.7. Damping trade-off curves showing model variance against percentage decrease in data variance for graded inversion modelling (a) v_P and (b) v_P/v_S. "d" denotes the selected damping value for the respective curve. (a) Damping curves a1, a2 and a3 were determined for v_P using velocity grids with a horizontal nodal separation of 10 km, 4 km and 2 km, respectively. Curves a4 and a5 are damping trade-off curves at 2 km and 1 km 1 km grid spacing where both v_P and v_P/v_S are modelled. (b) Damping curves for v_P/v_S at 2 km (b1) and 1 km (b2) where both v_P and v_P/v_S are modelled.

small number of events occur. Within well-resolved areas anomalies are considered to be significant if defined by more than one node *i.e.*, anomalies with areas >1 km^2.

5.2.5 The three-dimensional v_P model

The v_P model is presented in Figures 5.8 and 5.9. Variations of up to +28.63% (0, −2, 0) and −27.5% (10, 0, −1) from the average layer velocity are resolved. The v_P model has several broad trends within the production area. Low velocities at shallow depths within the northwest Geysers revert to more normal velocities at 2 km bsl (Figures 5.8a-d). This contrasts with the central and southeast Geysers where high-velocity anomalies occur at all depths (Figure 5.8a-e). Sharp velocity contrasts are detected across the Collayomi fault zone.

Two spatially-distinct low-velocity anomalies in the surface layer (−2, 4, −1 and 1, 4, −1) merge into a single, complex feature at sea level (Figures 5.8a and b). The anomaly continues to 1 km bsl but is restricted to a small area on the north margin of the reservoir (Figures 5.8c and 5.9b) The anomalies in the surface layer are up to −21% slower than the average reducing to <−8% by 1 km bsl.

High-velocity anomalies in the central and southeastern parts of the steam field are generally narrow and elongate at shallow depths (Figures 5.8 a-b) increasing spatially and becoming more circular in shape at depth (Figures 5.8 c-d). Maximum velocity contrasts of up to +24% (−2, −6, −1), +29% (0, −2, 0) and +18% (−2, −2, 1) greater than the average layer velocity are observed in the shallowest three layers.

Other features include the thin (<0.5 km) circular low-velocity anomaly centred on Cobb Mtn. (2, −2, −1) which is up to 26% slower than average (Figure 5.8 and 5.9a and g-h). The feature deepens to 1 km bsl in the northwest (at y=0 km Figure 5.9a). Steep velocity gradients (Figures 5.9e-h) coincide with the surface trace of the Collayomi fault zone (at x=5 km, Figure 5.9 e-f). v_P is reduced by up to 29% northeast of this fault zone while wave-speeds remain close to the starting model to the southeast. No such velocity contrast is observed across the Mercuryville fault zone (at x=−4 km, Figure 5.9e-h).

There is no consistent correlation between v_P anomalies and either the felsite batholith or the steam reservoir. A suite of complementary diagrams to Figure 5.8 showing final wave speeds at each modelled node is presented in Appendix 8.

5.2.6 The three-dimensional v_P/v_S model

Anomalies in the v_P/v_S model are smaller in magnitude (±9.77%) and simpler in shape. A striking low v_P/v_S ratio anomaly dominates the model, and is enclosed by a high v_P/v_S ratio envelope on all well resolved margins (Figure 5.10). Horizontal slices and

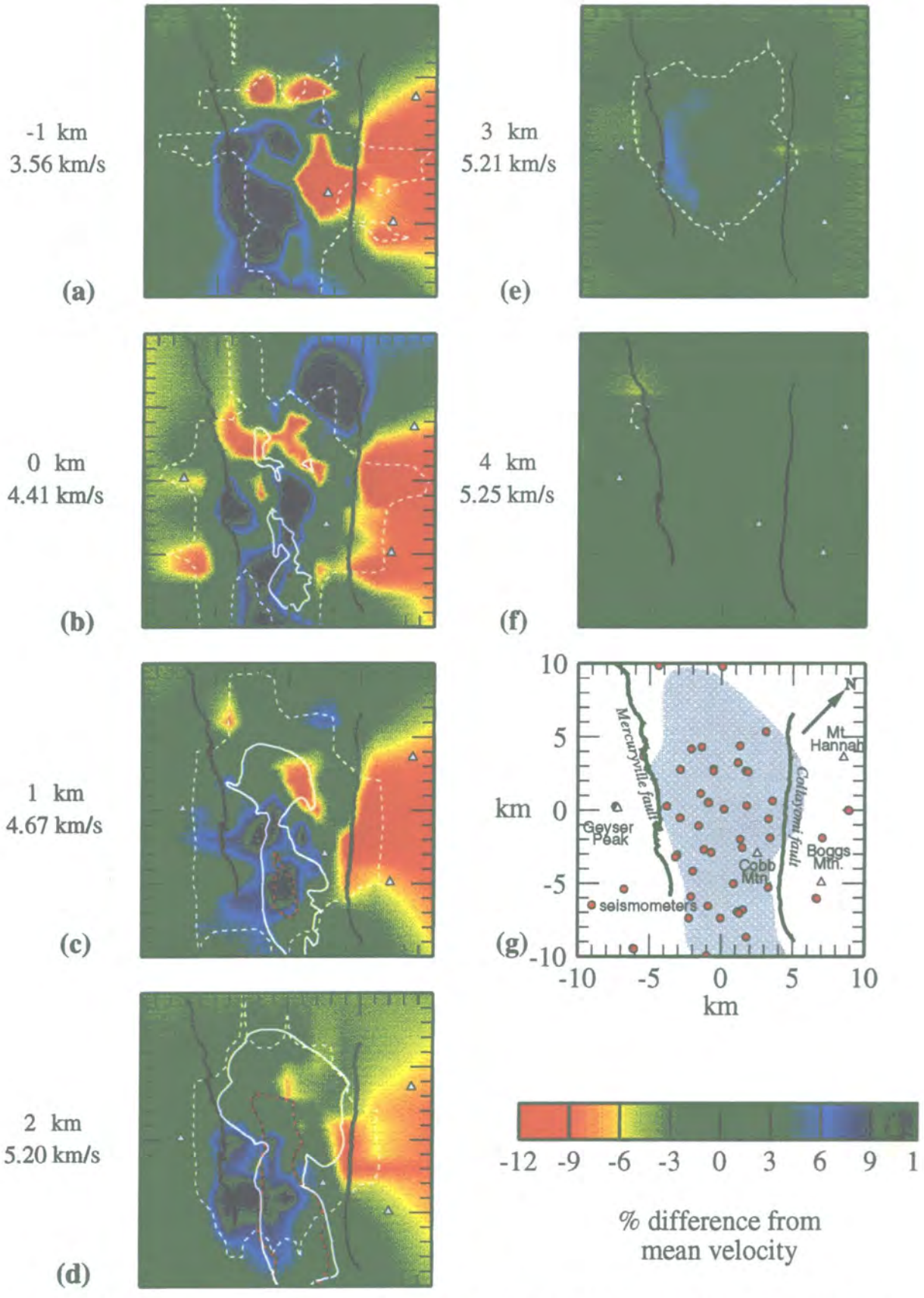

Figure 5.8. Maps showing percentage variation in v_p from mean values for horizontal depth slices through the model (values to the left of map). The location map (g) details surface features within the modelled volume including the 1992 production area (shaded) and seismometers (red circles). Areas enclosed by white dashed lines (a-f) are well resolved (spread <4 km). Solid white lines: boundary of steam reservoir; black and red lines: boundary of the felsite batholith; white triangles: mountains; black lines: faults

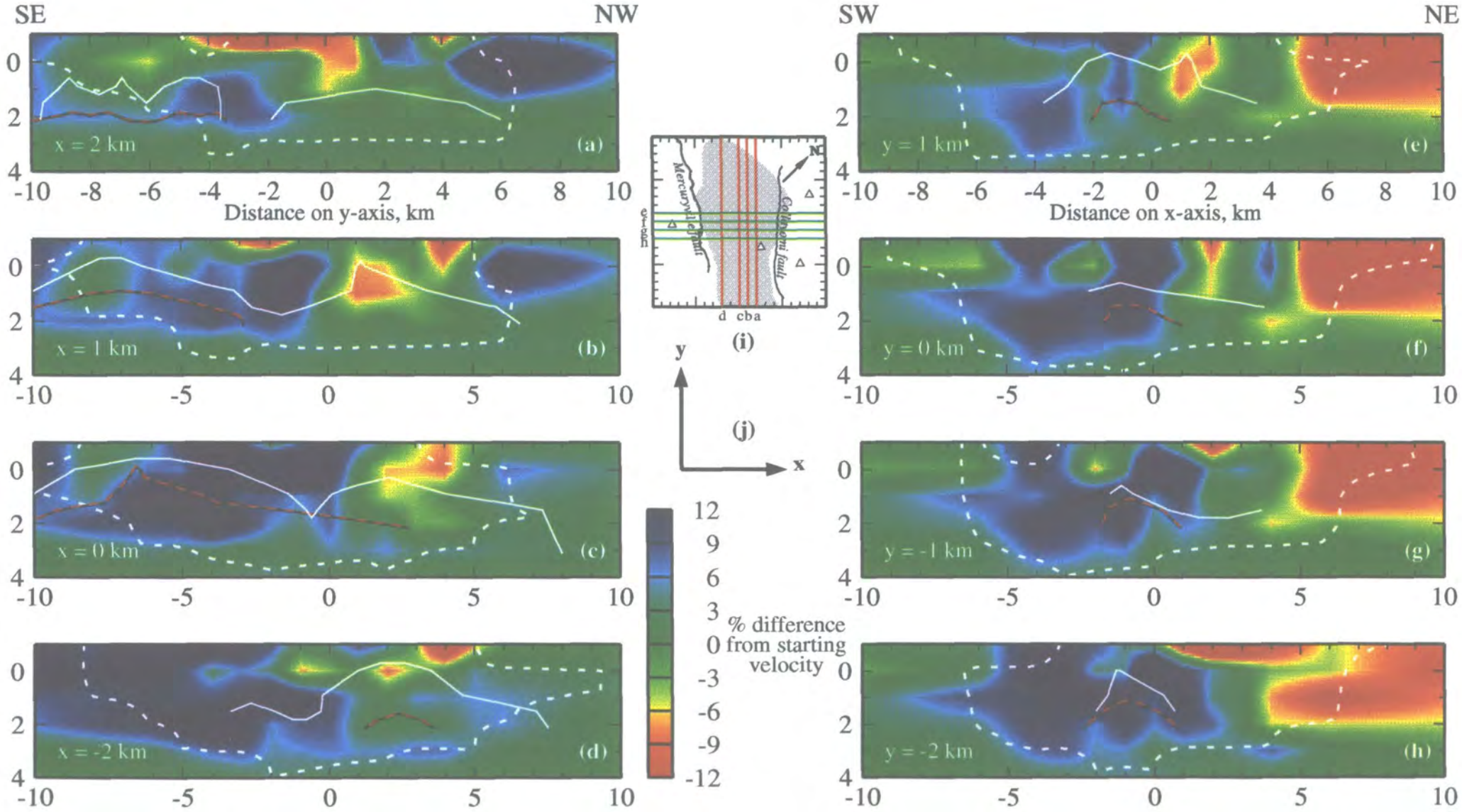

Figure 5.9. Cross-sections through the v_p model showing percentage difference from mean layer velocity. (a-d) Southeast-northwest cross-sections. (e-h) Southwest-northeast cross-sections. The same convention is adopted as in Figure 5.8. (i) Map of the model volume showing principal surface features. Red lines: cross-sections (a-d); green lines; cross-sections (e-h)

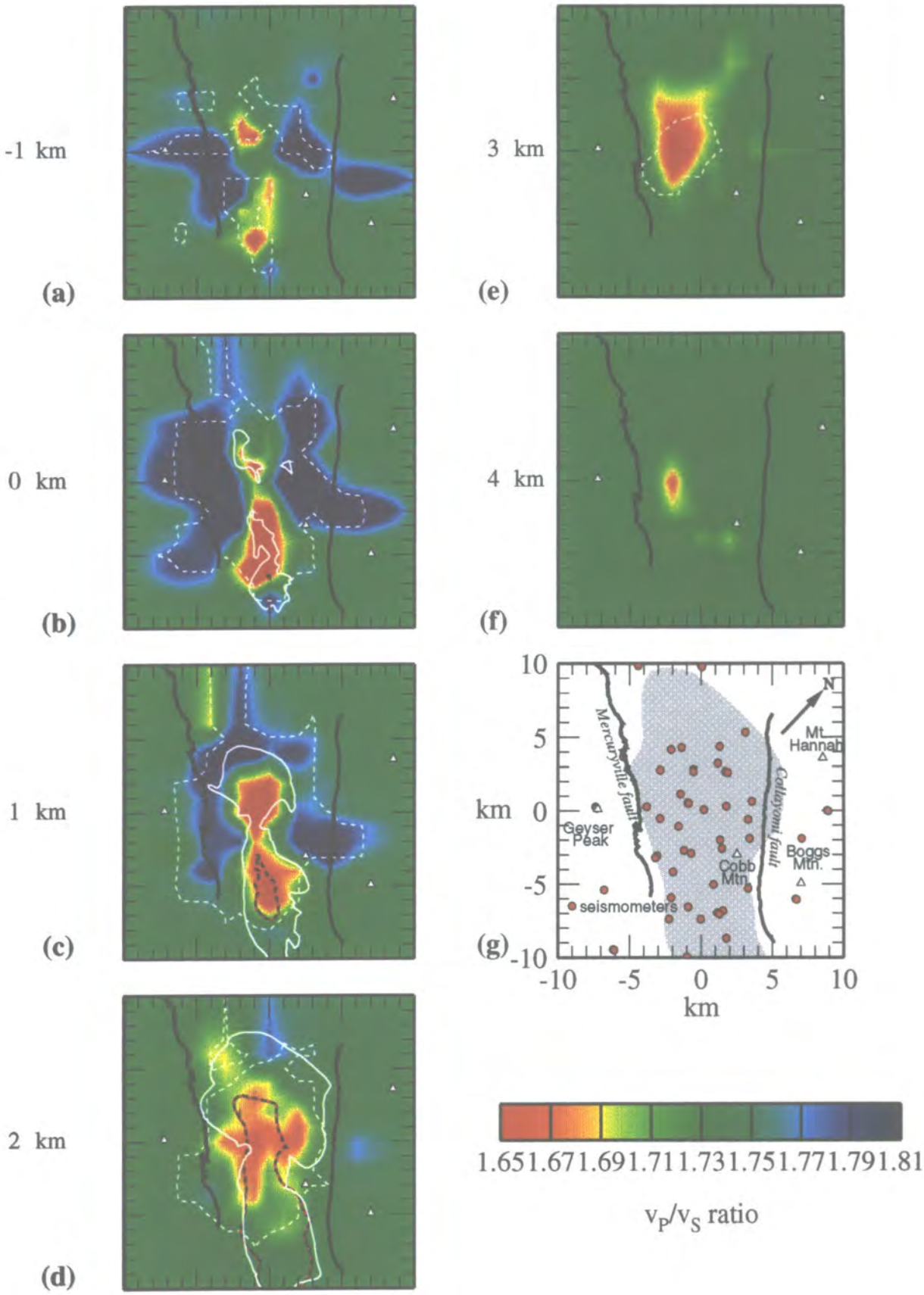

Figure 5.10. Maps showing variation in v_P/v_S for horizontal depth slices through the model. v_P/v_S varies from 1.64 to 1.84 with and average of 1.74. The same convention as Figure 5.8 is used for map features.

vertical cross-sections parallel and perpendicular to the reservoir axis are presented in Figures 5.10 and 5.11.

Two distinct areas (–1, –5, –1 and –1, 1, –1) of low-v_P/v_S anomalies in the surface layer continue down to sea level (Figure 5.10a). The southeastern anomaly forms a northwest-southeast trending body 6 km in length (Figure 5.10b). The two anomalies merge into a single, coherent body at 1 km bsl consisting of a circular body 2.5 km in diameter to the northwest (–1, 1, 1), connected by a thin neck (–1, –2, 1) to an oblong-shaped body to the southeast (Figure 5.10c). The anomaly expands laterally to the northeast and southeast at 2 km but is absent in the southeast (Figure 5.10d). Southeast-northwest cross-sections through the centre of this body show the anomaly is about 2 km thick in the southeast and is restricted to shallow levels in the crust (Figure 5.11c). The anomaly deepens to the northwest, increasing in thickness to a maximum of about 4 km (–1, 1, 3) before thinning and tapering to terminate in the northwest (Figure 5.11c). This transition is also found in southwest-northeast cross-sections perpendicular to the axis of this anomaly (Figures 5.11e-h).

High-v_P/v_S ratio anomalies at the periphery of the low-v_P/v_S anomaly are restricted to depths shallower than 2 km bsl (Figures 5.10a-c). Anomalously high-v_P/v_S ratios are found east and west of the low-v_P/v_S anomaly at sea-level. These high-v_P/v_S extend to the northwest at 1 km bsl to form an envelope to the low-v_P/v_S anomaly. It is unclear if the anomaly continues to the southeast due to a loss of model resolution in this area.

In contrast to the v_P model the low-v_P/v_S anomalies correlate very closely with the steam reservoir at all depths and appear to be restricted to its limits (Figures 5.11b, c and e-h). The correlation is most striking at 1 km bsl with the anomaly following the reservoir contours almost exactly, even narrowing as the reservoir does at (0, –1, 1) (Figure 5.10c). The anomaly does not extend as far to either the northwest or southeast as the reservoir. In the southeast the discrepancy may be an artefact of limited resolution but in the northwest the difference is real. In contrast, the high v_P/v_S anomalies are restricted almost exclusively to areas outside the reservoir (Figure 5.11a and e-h). There appears to be no correlation between the felsite batholith and v_P/v_S anomalies. A suite of complementary diagrams to Figure 5.10 showing final v_P/v_S ratios at each of the modelled nodes is presented in Appendix 8.

5.3 The results for different inversion strategies

Direct tomographic inversion produced structurally similar v_P and v_P/v_S models to those generated in the graded inversions but the anomalies were of lower amplitude and structural detail and resolution was reduced. The graded inversion produced a better data variance reduction and a 33% decrease in RMS travel time residual compared to the

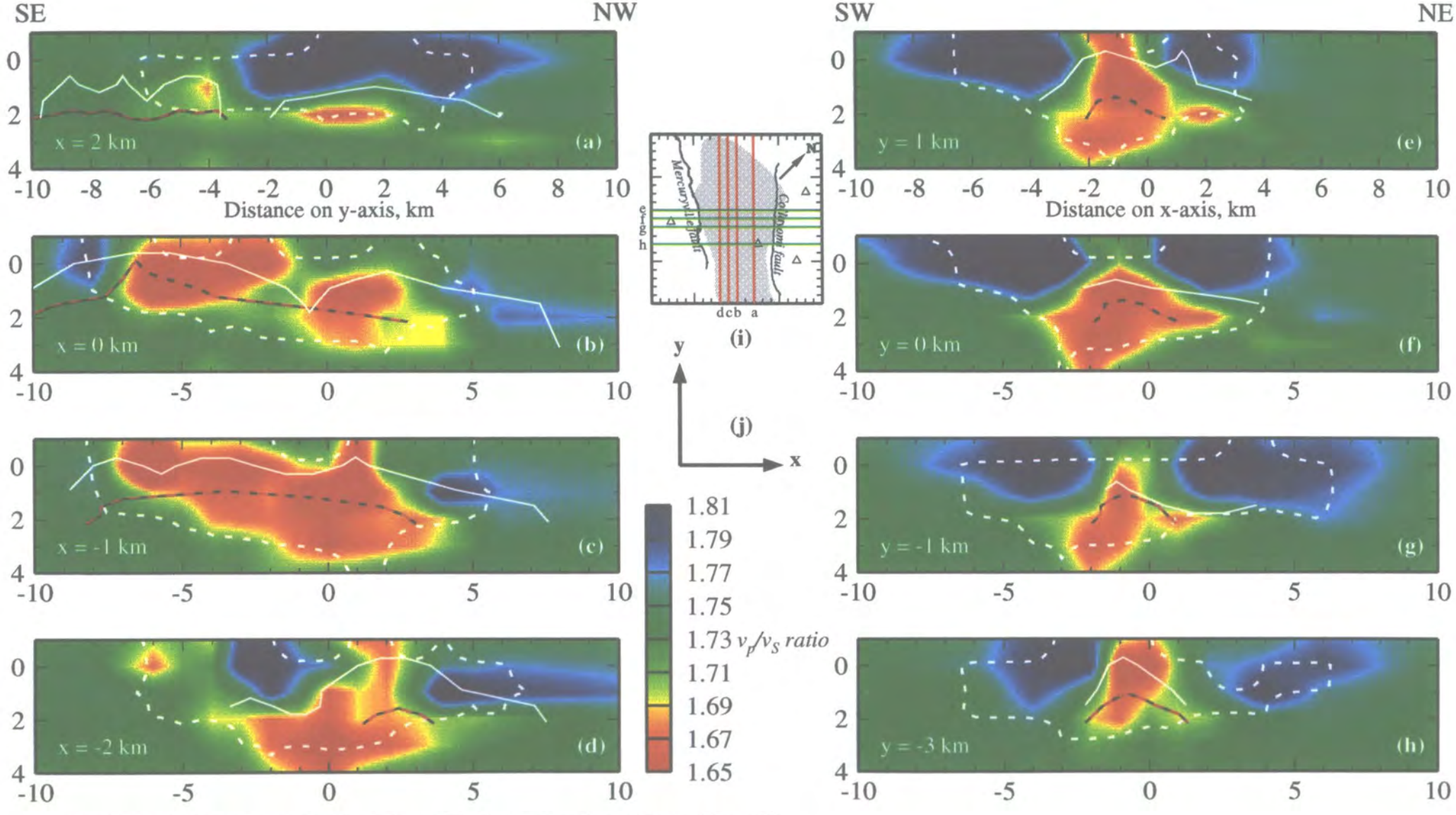

Figure 5.11. Cross-sections through the v_P/v_S model. Same convention adopted as Figure 5.9.

direct inversion.

All three graded inversion strategies tried produced virtually identical v_P models. They differed principally in the v_P/v_S model. Graded inversions modelling v_P/v_S at each stage, and the final two nodal configurations only, produced structurally similar models though anomalies in the final inversion have larger amplitudes. The final RMS travel-time residuals for both inversions differed by <0.11% in favour of the v_P/v_S model generated by inverting v_P/v_S at the two final stages. Inverting for v_P/v_S at only the final grid spacing produced similar but lower amplitude anomalies. Resolution of structural detail was also reduced.

Graded inversions using (a) the minimum one-dimensional v_P model and an improved estimate of the v_P/v_S ratio, and (b) the regional one-dimensional model and v_P/v_S ratio estimates, produced structurally similar v_P and v_P/v_S models. Anomalies in both v_P/v_S models are of similar amplitude. Using the minimum one-dimensional model a 5% improvement in the RMS travel-time residual was achieved over using the regional model.

Forcing input hypocentres to a graded inversion to be 1 km deeper than the best *qloc* locations produced similar wave-speed models, resolving the same anomalies and structural detail as the optimum locations. Final RMS travel time residuals differed by <0.18%. Over 80% of the enforced depth discrepancy was recovered in the initial relocation stage *SIMULPS12* performs prior to modelling wave-speeds. The average final depth discrepancy between the inversions differed by only 0.009 km.

Graded inversions were performed using data recorded on both the temporary and the UNT networks together and separately. Separate inversions of temporary and UNT network data model broadly similar v_P anomalies but these tend to be less continuous than anomalies modelled in inversions of the full data set. In contrast both inversions resolved very similar v_P/v_S structure which is consistent with the v_P/v_S model generated in inversion of the full data set. The temporary network data included 168 earthquakes consisting of 1557 *P*-wave arrivals and 699 *S*-wave arrivals. The final RMS travel-time residual was 0.033 s. The 163 earthquakes used in the inversion of UNT data used 2268 *P*-wave arrivals and 226 *S*-wave arrivals. The final RMS travel-time residual was 0.022 s. The structural detail of wave-speed anomalies within the reservoir in inversions excluding CALNET data were unaffected. Some model resolution was lost in the periphery of the model volume but these areas are poorly resolved anyway.

Varying the weighting of the travel-time residuals had little effect. Residual weighting mainly affected v_P/v_S reflecting the higher number of *S*-phase arrivals with relatively high travel-times residuals.

An inversion was conducted for v_P using the same model volume but with the grid oriented due north, *i.e.* such that the vertical nodal planes were no longer aligned with the tectonic fabric. The v_P model was virtually identical to that produced when the grid was

parallel to the tectonic fabric.

The v_P model was susceptible to rapid fluctuations between adjacent nodes during the later stages of a graded inversion. Such changes were suppressed by choosing somewhat more conservative damping values than were suggested by damping trade-off curves.

5.4 Earthquake locations

5.4.1 Earthquake relocations

The final data set of 296 earthquakes was relocated with the three-dimensional wave-speed models using the program *qloc3d* (*B. R. Julian, pers. comm.*). The program determines hypocentres using a similar approach to *qloc* (Section 3.3.1) but employs a bending algorithm in the ray-tracer (*Julian and Gubbins*, 1977).

The average horizontal and vertical change to earthquake locations between the one-dimensional regional model (Section 3.3.1) and the final three-dimensional model are 0.34 km and 0.29 km respectively. The maximum relocation was 2.97 km horizontally and 2.54 km vertically. Spatially close earthquakes tend to relocate towards the centre of their respective clusters (Figure 5.12). Epicentres south of Cobb Mtn. generally relocate to the east while events west of Cobb Mtn generally migrate north. Hypocentres relocate deeper at depths exceeding 3 km bsl (Figure 5.13). No trend is evident at shallower levels.

5.4.2 Final earthquake locations

Earthquakes located with the three-dimensional wave-speed model had final *P*- and *S*-wave travel time residuals of 0.041 s and 0.074 s respectively. This represents an improvement in RMS travel-time residual over the regional one-dimensional model of 24% for *P*-waves and 45% for *S*-waves. The general pattern of seismicity remains unchanged though definition of seismic and aseismic areas (*e.g.*, the dead-zone; Section 2.3) is improved (Figure 5.14). A thin (<0.4 km) aseismic horizon at about 3.0 km bsl divides seismicity at The Geysers into two vertically distinct zones (Figure 5.15). The shape of the seismogenic base remains unchanged but deepens by 0.5 km to 4 km in the central Geysers. The three-dimensional wave-speed models probably locate earthquakes with an accuracy of $\pm$0.2 km horizontally and vertically. Location errors are discussed in Section 7.5.5.

Earthquakes located with the three-dimensional wave-speed models and one-dimensional regional models are compared with power plants operating during the field experiment (Figure 5.16). There is no correlation between earthquakes and production

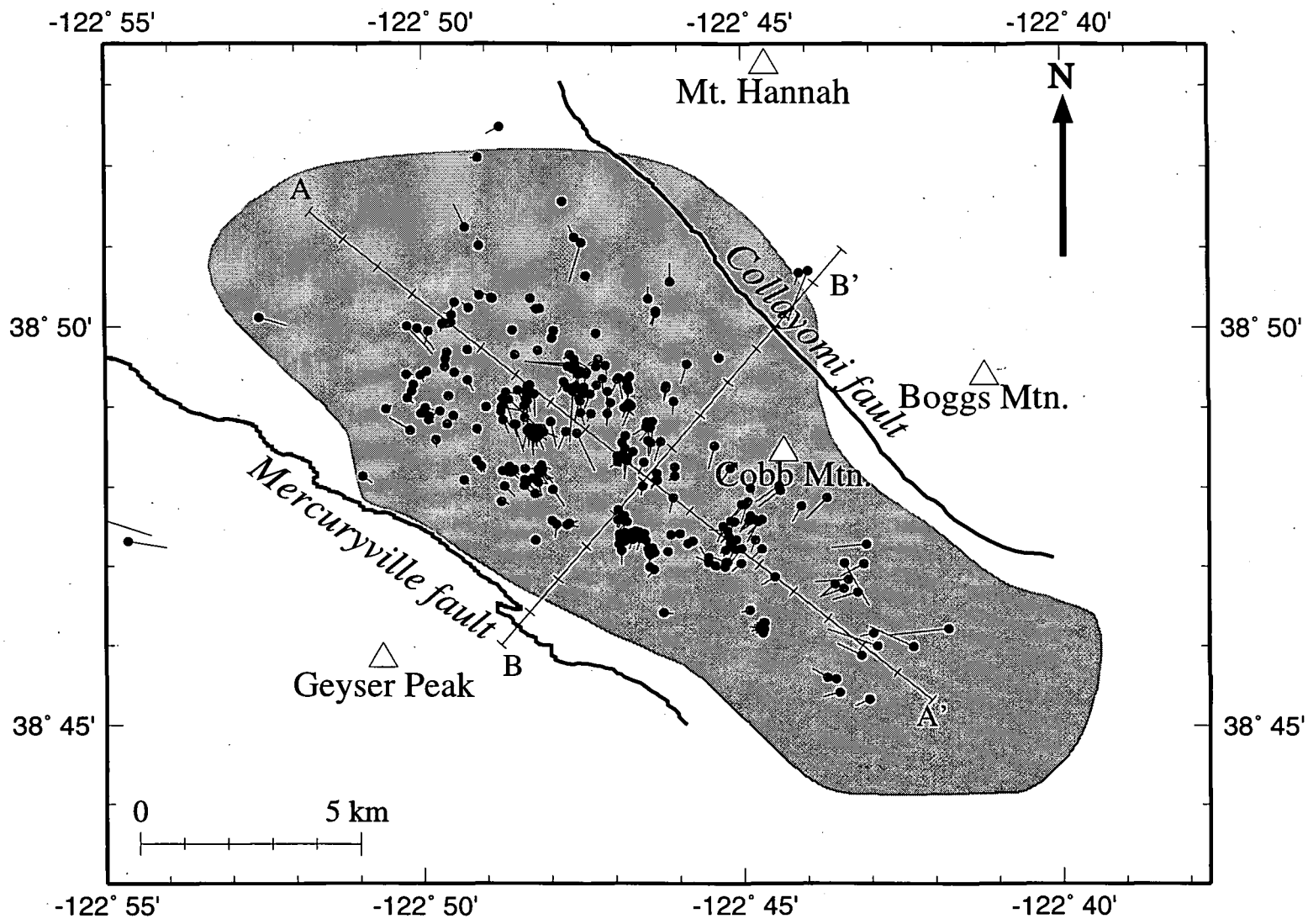

Figure 5.12. Map showing relative change to epicentres located with the regional one-dimensional v_P model and the final three-dimensional v_P and v_S models. Black circles are the three-dimensional location, a vector connects them to the location determined with the one-dimensional model. A-A' and B-B' are the lines of cross-section used in Figure 5.13.

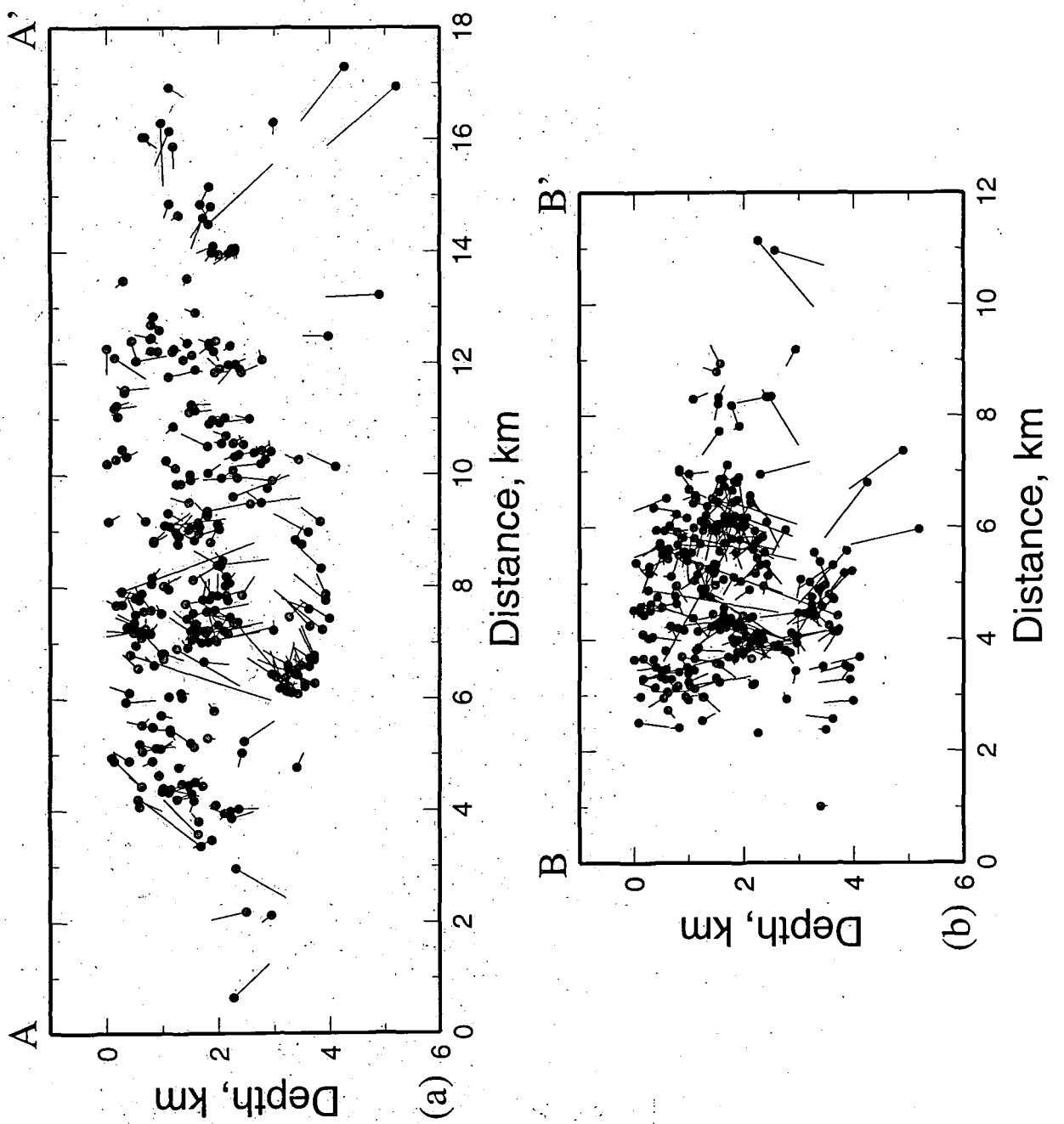

Figure 5.13. (a) Northwest-southeast and (b) southwest-northeast cross-sections showing changes between hypocentres located with the regional one-dimensional and the final three-dimensional wave-speed models. Symbol convention is the same as Figure 5.12.

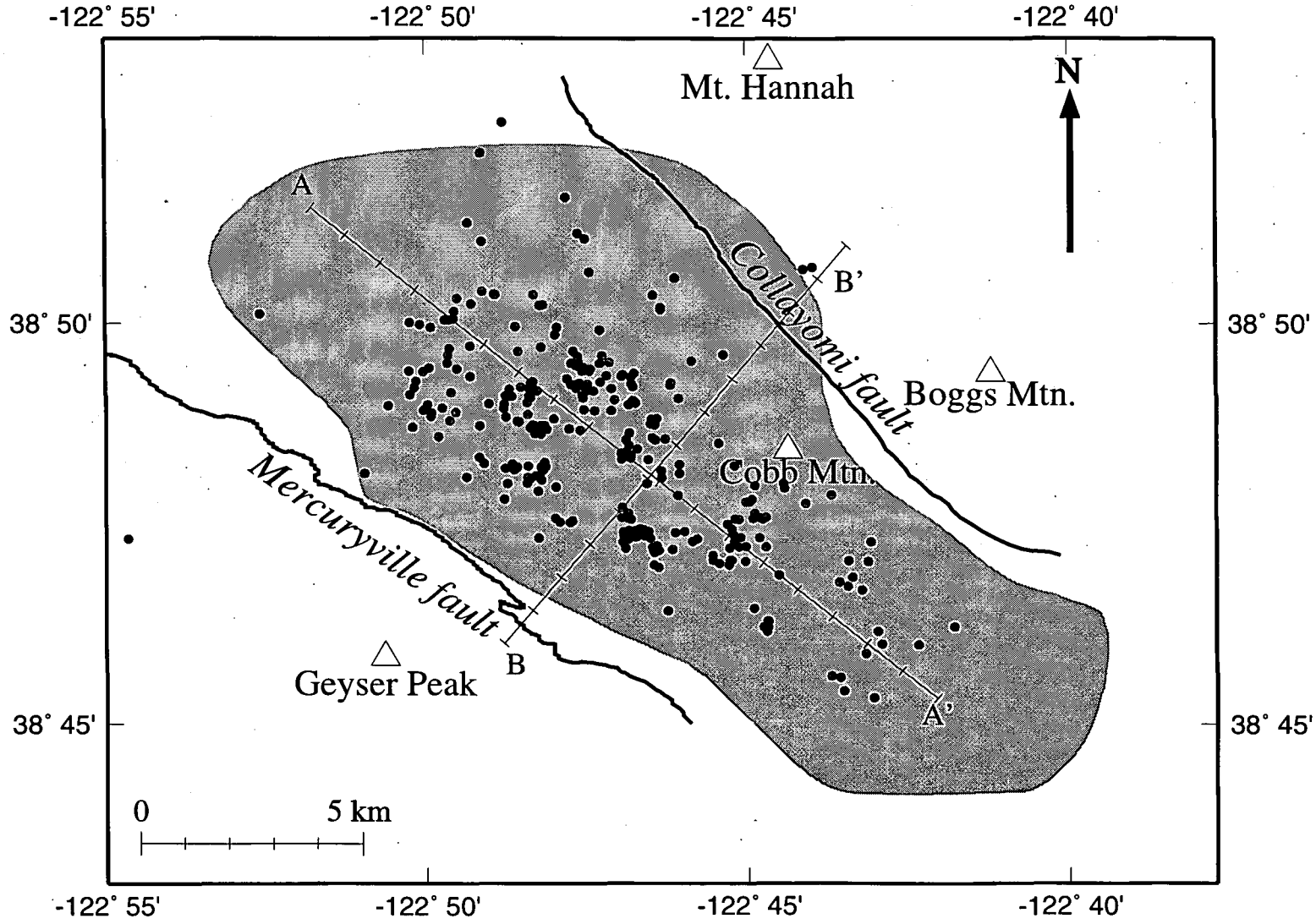

Figure 5.14. Map showing earthquake locations (black circles) determined using the three-dimensional v_P and v_S models. A-A' and B-B' are the lines of cross section used in Figure 5.15.

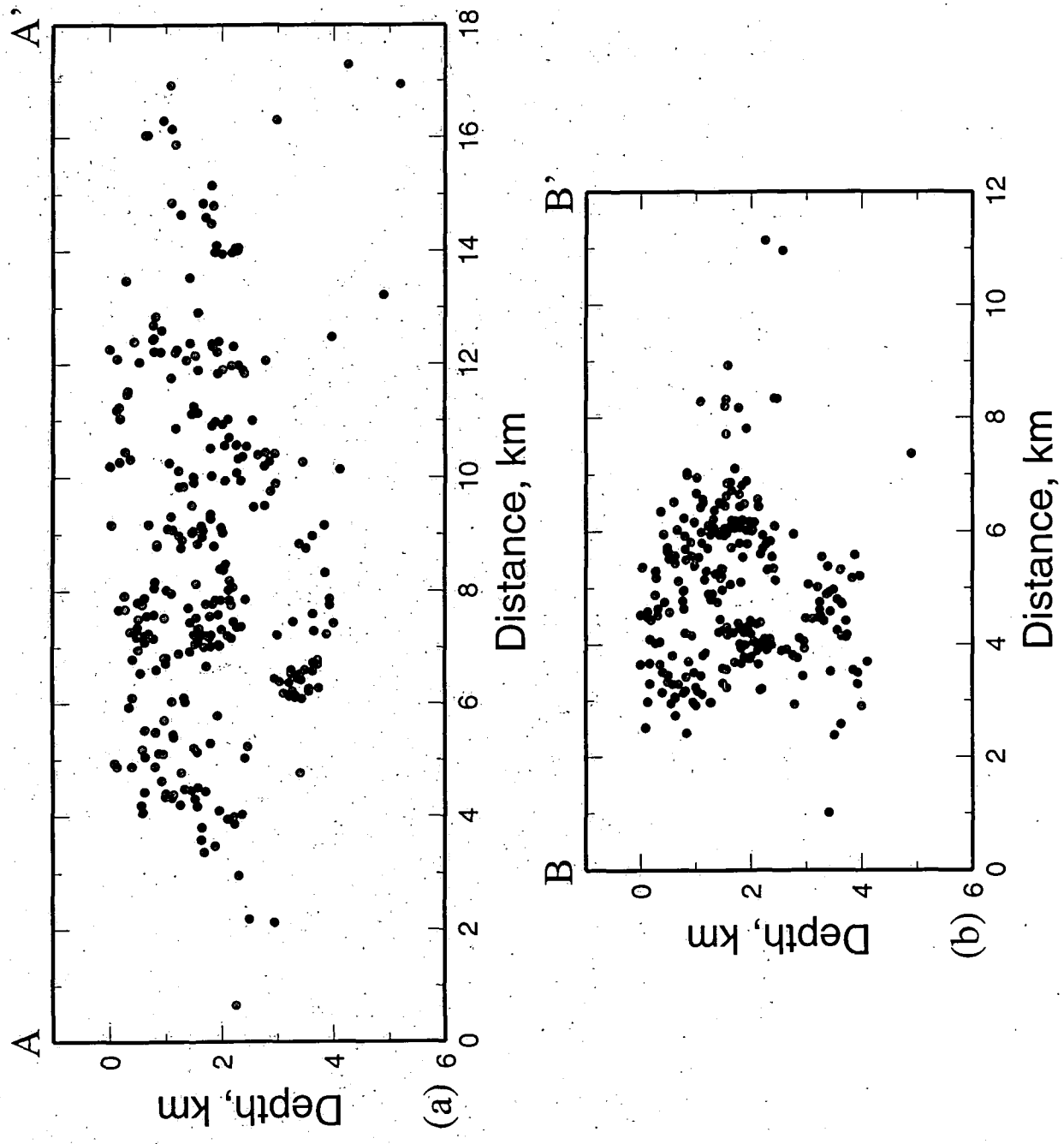

Figure 5.15. Same as Figure 5.13 without relocation vectors.

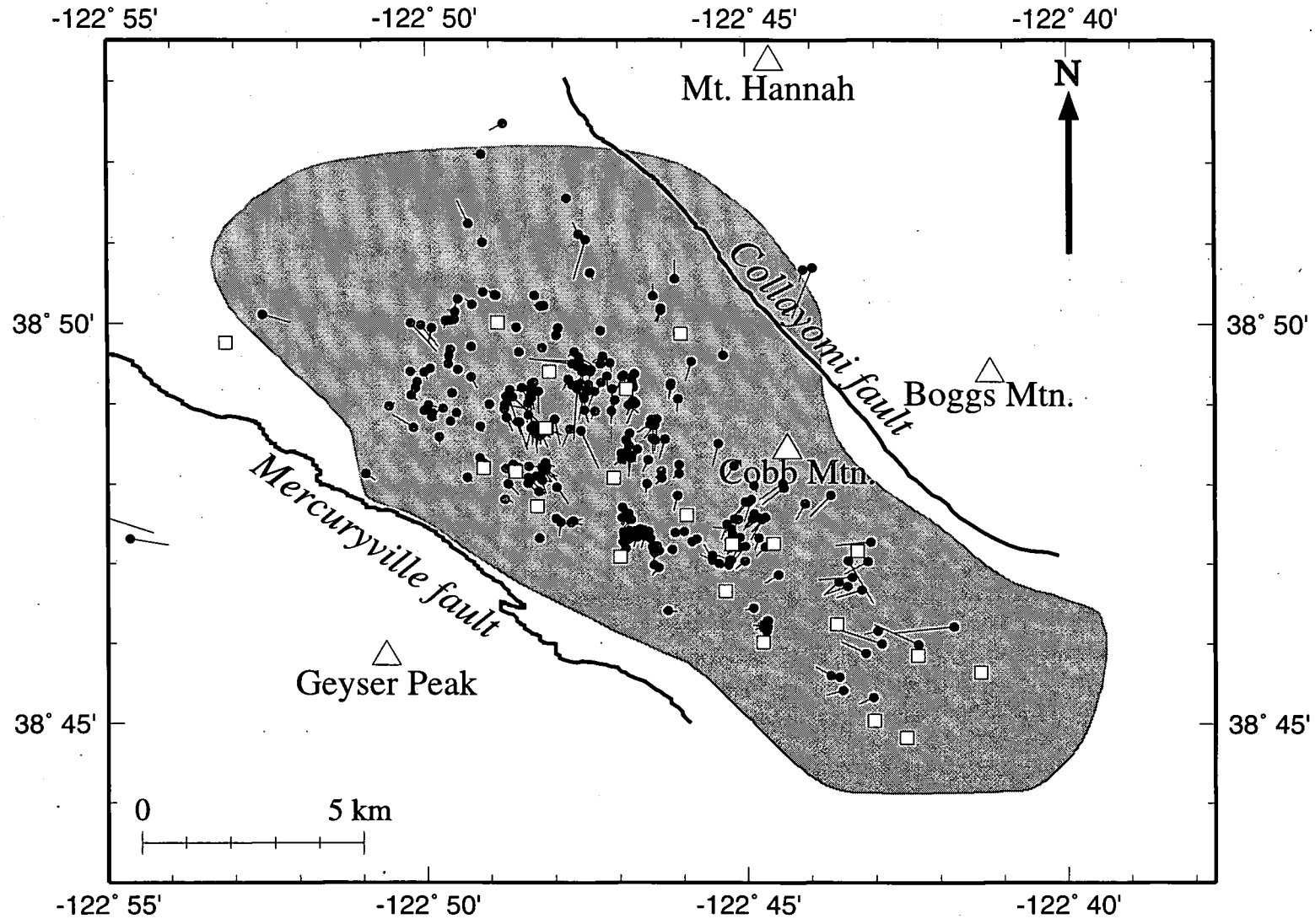

Figure 5.16. Same as Figure 5.12 with power plants (white squares) operating during the field experiment included

activities in the extreme northwest and southeast Geysers. In contrast, earthquake clusters in the seismically active central Geysers show a distinct spatial correlation with power plants (around which steam production and water injection is assumed to occur). The three-dimensional wave-speed models generally relocate earthquakes into tighter clusters which have migrated closer to the power plants.

5.5 Summary

The graded inversion produced more structurally detailed wave-speed models and consequently the RMS travel-time residual was reduced by 33% compared to the direct inversion approach. The three graded inversion strategies produced similar v_P models with slight variations in the structural detail of the v_P/v_S models, a reflection of the stage at which modelling for v_P/v_S commenced during the graded inversion.

Structurally similar wave-speed models were generated using different one-dimensional starting models though a 5% improvement in the final RMS travel-time residual was achieved using the model generated by *VELEST*. The same was found for models produced by inputing hypocentres forced 1 km deeper than the normal graded inversion. The final RMS travel-time residuals differed by <0.18% in favour of the inversion using unrestricted input hypocentres.

Graded inversions using data recorded on the temporary and UNT networks differed little from inversions with the full data set which is not unexpected given the small number of *P*-arrivals recorded by CALNET. Graded inversions of data recorded by the UNT network and temporary network produced v_P models with grossly similar features to the inversion of the full data set but differed considerably in detail. The v_P/v_S model generated in both inversions compared closely with one another and the inversion of the full data set. Rotating the model volume by 45° made no change to the v_P model.

The optimum tomographic model calculated was generated using a graded inversion and the best one-dimensional v_P model and v_P/v_S ratio estimate. One-hundred and eighty-five events were used. The model volume is 20 x 20 km in area and 7 km deep, centred on the steam reservoir and rotated 45° west of north. The modelled area enclosed 44 seismic stations. The final models produced a 63% reduction in RMS travel time residual with final *P*-phase travel times having an RMS of 0.022 s and *S*-travel times having an RMS of 0.044. Model variance was reduced by 81%.

v_P varies between –27.5% and +28.6% from the starting one dimensional v_P model. Shallow, low-velocity anomalies in the northwest area of the reservoir revert to more normal velocities at 2 km bsl. In contrast, the central and southeast areas have anomalously high velocities at all depths. Large velocity contrasts at all resolved depths are coincident with the surface trace of the Collayomi fault zone. There is no correlation

between anomalies in the v_P model and either the felsite batholith or steam reservoir.

The v_P/v_S model is much simpler and is dominated by a central low v_P/v_S anomaly in the reservoir surrounded by high v_P/v_S anomalies. The coherent low v_P/v_S body is spatially coincident with the steam reservoir, appearing to be contained within it.

The relocated hypocentres of the earthquakes migrated into more compact clusters compared with the one-dimensional locations. Hypocentres >3 km bsl relocated to deeper levels. Hypocentres separate into two vertically-distinct seismic volumes separated by a thin (<0.4 km), well-defined aseismic horizon (<0.4 km) 2.5 km bsl. The three-dimensional model improved location accuracy to between 20-70 m horizontally and vertically.

Chapter 6

Moment tensors

6.1 Introduction

Until recently most earthquake source mechanism studies have assumed shear motion. The radiation pattern is equivalent to a double-couple (DC) for an isotropic medium. The type of shear mechanism was determined using fault-plane solutions where orthogonal nodal planes were fitted by hand to compressional first motion observations on an upper or a lower focal sphere. The geometry of this pattern determined the "focal mechanism", and one of the nodal planes represented the slip surface. With more sophisticated analysis techniques and higher quality digital data many earthquakes have been observed to have mechanisms which are inconsistent with shear faulting *i.e.*, non-DC (*Miller et al.*, 1996).

Numerous theories have been proposed to explain non-DC earthquakes (see for a review *Julian et al.*, 1996; *Miller et al.*, 1996). Many are thought to result from processes producing a component of motion normal to a fault surface. Earthquakes with large isotropic components are particularly well observed in volcanic and geothermal areas such as the Hengill-Grensdalur volcanic complex, Iceland (*e.g.*, *Foulger and Long*, 1984; *Miller*, 1996). High-temperature, high-pressure fluids in geothermal systems may facilitate crack opening at depth in young volcanic areas.

It is extremely difficult to determine non-DC mechanisms from first-motion polarity data alone unless the mechanisms have large isotropic components. Amplitude data can constrain mechanisms much better than polarity data alone. Their use, however, is hampered because Earth heterogeneity distorts the amplitudes of waves as they

propagate from source to receiver. Such effects can be significantly reduced by using the ratios of amplitudes such as *P* and *SH*, *P* and *SV* or *SH* and *SV*. Earthquake focal mechanisms presented in this chapter are determined by the linear programming technique of *Julian* (1986) and *Julian and Foulger* (1996).

6.2 Moment tensors

6.2.1 Moment tensor representation of a seismic source

When an earthquake occurs material in the source region moves suddenly enough to radiate seismic waves. The amplitude variation of seismic energy leaving the source region is described by a second-order moment tensor **m** (*Julian et al.*, 1996). The moment tensor describes the source in terms of 9 elementary force systems, each element of which describes the strength of one force component:

$$\mathbf{m} = \begin{pmatrix} M_{xx} & M_{xy} & M_{xz} \\ M_{yx} & M_{yy} & M_{yz} \\ M_{zx} & M_{zy} & M_{zz} \end{pmatrix} \qquad 6.1$$

where the moment tensor components are arranged according to the right-hand co-ordinate system such that x, y and z represent north, east and vertically down respectively. Diagonal elements M_{xx}, M_{yy}, M_{zz} of the moment tensor are linear dipoles while off-diagonal elements are force couples. The source is assumed to exert no net torque so off-diagonal elements actually correspond to pairs of force couples. The moment tensor is therefore symmetric with 6 independent components.

To simplify comprehension moment tensors can be completely described by rotating the co-ordinate system and expressing the moment tensor in terms of three orthogonal principal moments m_1, m_2, m_3 and three values specifying the orientation of this principal axis co-ordinate system. This completely describes the force system and source information is then independent of orientation information.

6.2.2 Decomposing a moment tensor

In order to understand a moment tensor better, we may decompose it into an isotropic and a deviatoric part:

$$\begin{bmatrix} m_1 \\ m_2 \\ m_3 \end{bmatrix} = m^{(I)} \begin{bmatrix} 1 \\ 1 \\ 1 \end{bmatrix} + \begin{bmatrix} m_1' \\ m_2' \\ m_3' \end{bmatrix} \qquad 6.2$$

where $m^{(I)}=(m_1+m_2+m_3)/3$ is the isotropic moment. The deviatoric part can be further decomposed into a DC (principal moments in the ratios of 1:−1:0) and a "Compensated Linear Vector Dipole" (CLVD) (principal moments in the ratios $1:-{}^1/_2:{}^1/_2$):

$$\begin{bmatrix} m_1' \\ m_2' \\ m_3' \end{bmatrix} = m^{(DC)} \begin{bmatrix} 0 \\ -1 \\ 1 \end{bmatrix} + m^{(CLVD)} \begin{bmatrix} -\frac{1}{2} \\ -\frac{1}{2} \\ 1 \end{bmatrix} , \qquad 6.3$$

where $m^{(DC)}=m_1' - m_2'$, $m^{(CLVD)} = -2m_1'$ and the principal moments are arranged so that $|m_1'|\leq|m_2'|\leq|m_3'|$ (Figure 6.1) (*Knopoff and Randall*, 1970). A CLVD describes uniform outward (or inward) motion in a plane accompanied by inward (or outward) motion normal to this plane such that volume is conserved.

Other parameters useful for understanding moment tensors include:

$$\varepsilon = \frac{m_1'}{|m_3'|} , \qquad 6.4$$

which describes the departure of the deviatoric part from a DC. For a pure DC ε is zero and ± 0.5 for a pure CLVD. A measure of the relative volumetric change in the source is given by:

$$k \overset{def}{=} \frac{m^{(I)}}{|m^{(I)}| + |m_3'|} \qquad 6.5$$

with $-1\leq k\leq 1$. For a purely deviatoric source mechanism $k=0$.

6.3 Moment tensor determination: Theory

Linear programming methods are extensions of linear algebra to include inequalities. They maximise a given linear objective function:

$$z = a_{01}x_1 + a_{02}x_2 + \cdots + a_{0N}x_N \qquad 6.6$$

of the N independent variables $x_1,\cdots, x_N$ involving N constants $a_{01},\cdots, a_{0N}$. The variables are required to be non-negative:

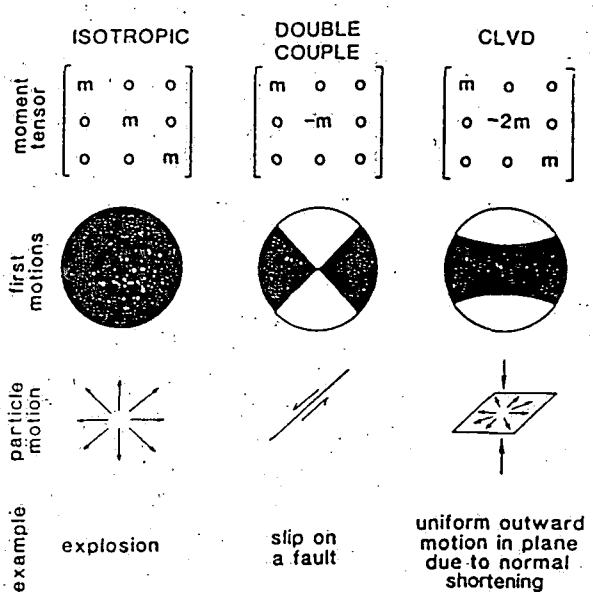

Figure 6.1. Schematic representation of a moment tensor decomposed into the isotropic, DC, and CLVD components (from, *Apperson*, 1991). *P*-wave polarity fields are plotted on focal hemispheres.

$$x_1 \geq 0; \quad x_2 \geq 0; \quad \ldots \quad x_N \geq 0 \qquad 6.7$$

and to satisfy a set of additional constraints U=$u_1 + u_2 + u_3$, u_1 of them of the form:

$$a_{i1}x_1 + a_{i2}x_2 + \cdots + a_{iN}x_N \leq b_i \quad , \qquad 6.8$$

u_2 of them of the form:

$$a_{j1}x_1 + a_{j2}x_2 + \cdots + a_{jN}x_N \geq b_j \quad , \qquad 6.9$$

and u_3 of them of the form:

$$a_{k1}x_1 + a_{k2}x_2 + \cdots + a_{kN}x_N = b_k \quad . \qquad 6.10$$

The set of non-negative values $x_1, \cdots, x_N$ satisfying these constraints is called a "feasible vector". The situation is most easily described geometrically with each constraint from Equations 6.2 and 6.3 defining a hyperplane that bounds the "feasible region" in *N*-dimensional space. This is visualised easily here in two-dimensions (Figure 6.2). Vectors satisfying all constraints lie within the feasible region. There generally is either no feasible vector or an infinite set of them. The "simplex" method solves linear programming methods by first finding an initial feasible vector and then increasing the objective function

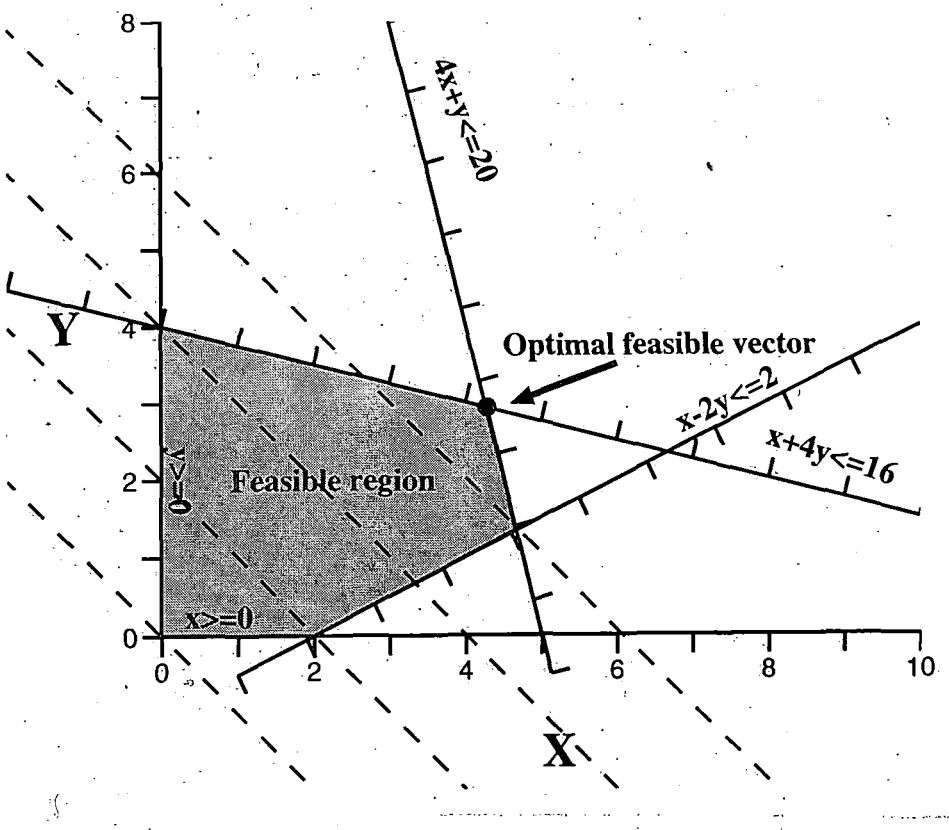

Figure 6.2. Geometrical representation of a linear programming problem in two-dimensions. The shaded area bounded by the inequality constraints is the feasible region. Feasible vectors lie on the vertices of the feasible region. The optimal feasible vector (black circle) maximises the linear objective function Z=X+Y. Dashed lines indicate contours of Z.

in a series of steps until the optimal feasible vector is found.

Any seismic-wave amplitude is a linear function of the moment-tensor components, so amplitudes can be fitted using standard linear algebra. However, polarity observations provide inequalities, which introduce nonlinearity. Linear programming techniques and the simplex method can deal with just this kind of nonlinear problem (inequalities involving linear forms) and can therefore be applied to earthquake focal mechanism studies. Polarities, amplitudes and amplitude ratios of seismic waves from local earthquakes can be expressed as linear inequalities and inverted for moment tensor solutions (*Julian*, 1986; *Julian and Foulger*, 1996). Let 6 independent components of a moment tensor for a point source can be arranged as a column vector:

$$\mathbf{m} \overset{def}{=} [M_{xx}\, M_{xy}\, M_{yy}\, M_{xz}\, M_{yz}\, M_{zz}]^{\mathrm{T}} \quad . \qquad 6.11$$

The right-handed co-ordinate system defined in Section 6.2.1 is used. The amplitude of a

seismic wave u is linearly related to the moment tensor components by:

$$u = \mathbf{g}^{\mathrm{T}}\mathbf{m}, \tag{6.12}$$

where

$$\mathbf{g} = [g_{xx}\ g_{xy}\ g_{yy}\ g_{xz}\ g_{yz}\ g_{zz}]^{\mathrm{T}} \tag{6.13}$$

is a column vector of a Green's function for a particular seismic phase, *P*, *SH*, *SV*, Love or Rayleigh and source and station locations. Components of $\mathbf{g}$ for a seismic wave radiating in an homogeneous medium are given by *Julian* (1986).

A polarity observation is expressed as:

$$\mathbf{g}^{\mathrm{T}}\mathbf{m} \leq 0$$

or (6.14)

$$\mathbf{g}^{\mathrm{T}}\mathbf{m} \geq 0$$

depending on polarity.

Amplitude observations are expressed as a pair of inequalities defined by maximum and minimum amplitude values:

$$\mathbf{g}^{\mathrm{T}}\mathbf{m} \geq u_{min}$$

and (6.15)

$$\mathbf{g}^{\mathrm{T}}\mathbf{m} \leq u_{max}.$$

Similarly, the amplitude ratio r of two seismic waves $\mathrm{A}^{(1)}$ and $\mathrm{A}^{(2)}$ is expressed as an inequality involving the bounding values r_{max} and r_{min}:

$$u^{(1)} \leq r_{max}u^{(2)}$$

and (6.16)

$$u^{(1)} \geq r_{min}u^{(2)}$$

Amplitude ratios are related to a moment tensor by inequalities of the form:

$$\mathbf{g}^{(1)\mathrm{T}}\mathbf{m} \leq r_{max}\mathbf{g}^{(2)\mathrm{T}}\mathbf{m}$$

and (6.17)

$$\mathbf{g}^{(1)\mathrm{T}}\mathbf{m} \geq r_{min}\mathbf{g}^{(2)\mathrm{T}}\mathbf{m}$$

where $\mathbf{g}^{(1)}$ and $\mathbf{g}^{(2)}$ are the Green's functions for the two seismic phases involved. These

inequalities can be written as:

$$(\mathbf{g}^{(1)\mathrm{T}} - r_{max}\mathbf{g}^{(2)\mathrm{T}})\mathbf{m} \leq 0$$

and 6.18

$$(\mathbf{g}^{(1)\mathrm{T}} - r_{min}\mathbf{g}^{(2)\mathrm{T}})\mathbf{m} \geq 0$$

Reversing signs in the appropriate Green's function for Equations 6.14, 6.15 and 6.18 allows all these inequalities to be expressed in the form:

$$\mathbf{g}^{\mathrm{T}}\mathbf{m} \leq a \qquad 6.19$$

Amplitudes and amplitude ratios are now expressed in the same form as inequalities for a pair of polarity observations but with different Green's functions and can then be inverted in the same way. The simplex algorithm seeks a feasible solution consistent with the data for this system of inequalities by minimising the "objective function" E:

$$E \equiv \sum_{i \in S} |\mathbf{g}_i^{\mathrm{T}}\mathbf{m} - a_i| \qquad 6.20$$

where S is the set of unsatisfied inequalities. Alternatively the objective function is expressed in terms of amplitudes by:

$$E = \sum_{i \in P} w_i |u_i| + \sum_{i \in Q} w_i |u_i - a_i| + \sum_{i \in R} w_i |u_i^{(1)} - r_i a_i^{(2)}| \qquad 6.21$$

where P, Q, and R are the set of polarity, amplitude and amplitude-ratio constraints which are unsatisfied. A weighting factor w_i is applied to each inequality because in most cases the data are not of equal quality. If all the constraints are satisfied then E will be zero and there is a non-empty set of feasible solutions. The simplex algorithm can be applied again with a different set of objective functions which maximise or minimise extreme physical characteristics of the moment tensor *e.g.*, the maximum explosive and implosive components (*Julian*, 1986). Alternatively if a feasible solution does not exist the simplex algorithm may minimise a weighted L1 norm of the residuals unsatisfied in the E.

6.4 Moment tensor determination: Application

6.4.1 Seismic wave-speed models

Wave-speed models can strongly affect how observations are mapped onto focal

spheres. Using an overly simple model such as a one-dimensional wave-speed model can severely distort the true radiation pattern if the area studied is heterogeneous. For example, a one-dimensional model of the Hengill-Grensdalur area, Iceland, miscalculated the positions of stations on the focal sphere by up to 40° compared to a three-dimensional model (*Foulger and Julian*, 1993). In the present study observations were mapped onto the focal sphere using information derived from earthquakes located with the program *qloc3d* and using the three-dimensional wave-speed models presented in Sections 5.2.5 and 5.2.6.

6.4.2 Earthquake selection

Good focal mechanism solutions require an even spatial distribution of observations over the focal sphere. Of the 185 earthquakes used in tomographic modelling, thirty events (16%) were selected for further focal mechanism analysis. All locate within or close to the central Geysers and the recordings have a wide azimuthal variation and most have good focal sphere coverage.

6.4.3 Polarity and amplitude measurements

Polarity and amplitude measurements were made on seismograms recorded by the temporary network supplemented with polarity data from CALNET stations (Section 2.2). Data from the UNT network contributed only to estimating earthquake locations, and not focal mechanisms, because the instrument polarities are unknown.

Processing errors were minimised by implementing a standard operating procedure. Clipped traces, probably caused by the digitiser, were discarded. *P*-wave arrivals are much easier to identify and measure than S-wave arrivals because they are uncontaminated by preceding seismic signals. Numerically rotating horizontal seismograms from their field orientations enhances identification of *S*-wave arrivals. Transverse- and radial-component seismograms are oriented perpendicular and parallel to the source-receiver azimuth using the program *ahrotate* (*B. R. Julian, pers. comm.*). The sign convention has positive radial component away from the source and positive transverse component to the left as viewed from source-to-receiver. Source-to-receiver azimuths were determined by the bending method (*Julian and Gubbins*, 1977). Measured *S*-wave arrival times made on unrotated horizontal traces were displayed on the rotated seismograms. These arrival times were examined and re-measured where appropriate. Changes were generally small ($\leq$0.01 s).

Wave-propagation effects such as scattering and attenuation most strongly influence the high-frequency components of a seismic signal. Using low-frequency components of the signal minimised these effects. Polarities and amplitudes were

measured on seismograms that had been low-pass filtered with a three-pole Butterworth filter with a corner frequency of 5 Hz. Events were discarded if their rotated and filtered seismograms had low signal-to-noise ratios. Measurements of *P*-wave arrival times and amplitudes were made on vertical-component seismograms. *S*-waves are more complex since an *S*-wave can be divided into two orthogonal components, *SH* and *SV*, which propagate independently but at the same speed. The particle motion for *SH*-waves lies in a horizontal plane perpendicular to the propagation ray-direction so *SH*-phases were measured on transverse component seismograms (Figure 6.3). The particle motion of *SV*-waves lies in the vertical plane containing the ray direction so *SV*-phases were measured on radial component seismograms. Amplitudes were measured from the first onset to first peak, and only signals with similar rise times were used in ratios (Figure 6.4).

6.4.4 Correcting amplitudes and amplitude ratios for wave-propagation effects

Seismic waves incident on and reflected at the free-surface are amplified. The ground motion at a seismic station is the sum of the motions related to the incident and reflected phases. *SH* waves incident at the free surface are reflected as *SH*-waves but either *P*- or *SV*-waves undergo mode conversion and produce two reflected phases (*P* and *SV*). The amplification factor is a function of the angle of incidence at the surface and the wave speeds. A "free-surface" correction was computed using the method of *Frazier* (1970) and applied to measured amplitudes. Plane waves incident on the surface of a homogenous half space with a v_P/v_S ratio of 1.74 are assumed. For incidence beyond the critical angle, correction is practically impossible so for SV-waves only those emerging within 25° of the vertical were included.

The Earth is not perfectly elastic. As a seismic wave propagates through it energy is lost and converted to dissipated heat. This phenomenon attenuates the wave amplitudes, particularly at high frequencies. Attenuation is quantified by the "figure of merit" $Q(f)$, which is inversely proportional to attenuation.

Observed amplitudes were corrected for attenuation using the relation:

$$A(f) = A_0(f) R^{-1} \exp\left[-\frac{wt}{2Q(f)}\right] \qquad 6.22$$

where A_0 and A are the seismic-wave amplitudes at the source and observation point respectively, R is the geometrical spreading coefficient, w the angular frequency and t is the travel-time (*Menke et al.*, 1995).

The ratio of *P*- to *S*-wave amplitudes at the source is:

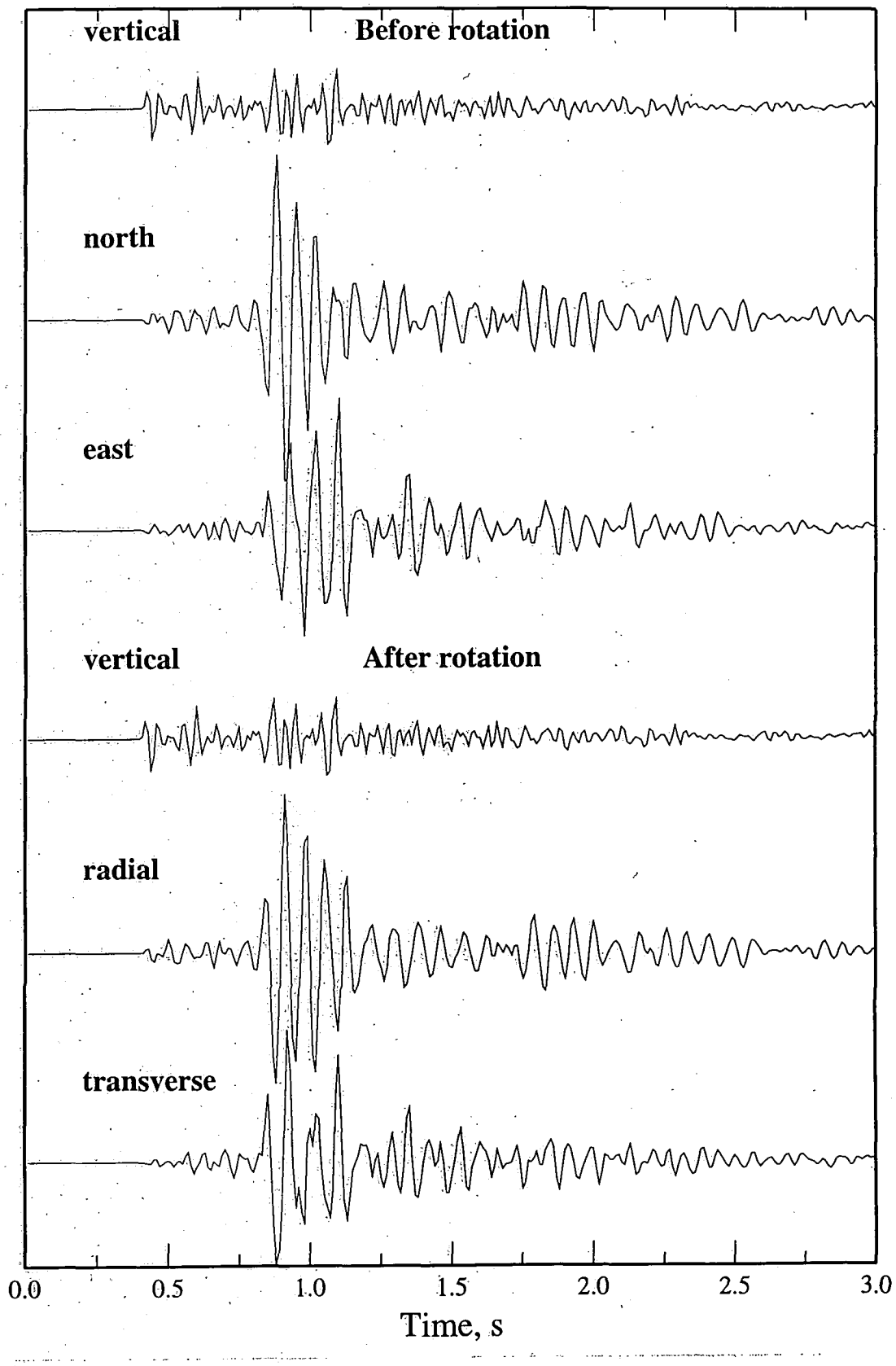

Figure 6.3. Example of unrotated and rotated seismograms recorded at station G004 for event 119.012140.1 with corner frequency f=42 Hz. The north component is aligned to true north. The bottom two traces show the rotated radial and transverse horizontal components. The *SH* and *SV* arrivals are more easily inspected on the rotated traces.

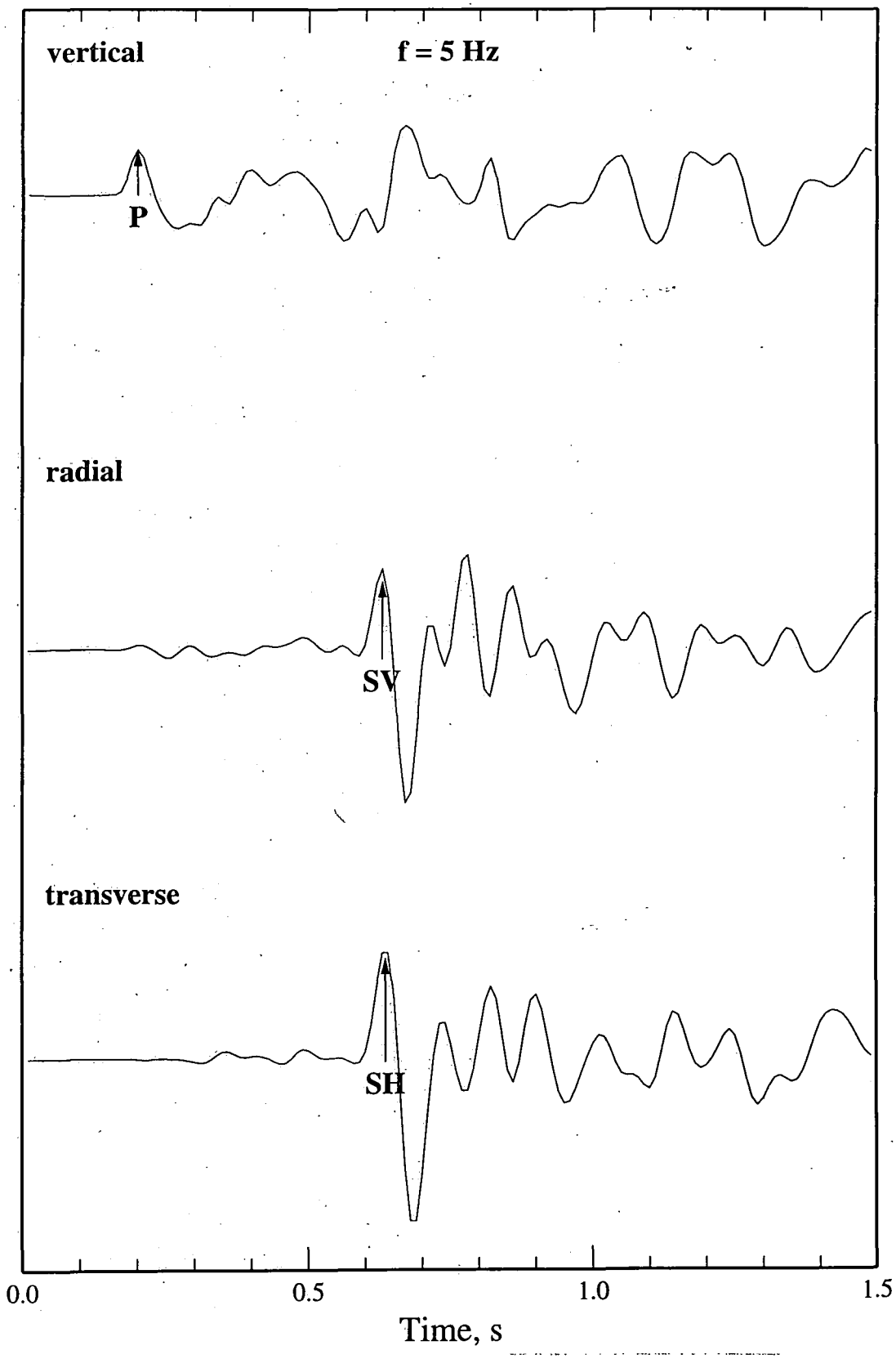

Figure 6.4. The rotated traces shown in Figure 6.3 after low-pass filtering using a three-pole Butterworth filter (corner frequency of 5 Hz). The vertical trace is enlarged vertically three times relative to the radial and transverse components.

$$\frac{A_{P_o}}{A_{S_o}} = \frac{A_P}{A_S}\frac{R_P}{R_S}\exp\left[\frac{w}{2}\left(\frac{t_P}{Q_P} - \frac{t_S}{Q_S}\right)\right] \qquad 6.23$$

where A_P and A_S are the observed amplitudes, Q_P and Q_S are the quality factors and t_P and t_S are travel-times for the respective *P*- and *S*-phases. If the variations in v_P/v_S are assumed to be small then $R_P \cong R_S$ and geometrical spreading can be neglected for amplitude ratios. Attenuation studies at The Geysers suggest Q_P=60 is a reasonable value for the reservoir (*Zucca et al.*, 1993). Q_S has not been measured, so moment tensors were determined using a range of Q_S values and the fit to the data assessed.

Amplitude measurements used to determine scalar moments were corrected for the effects of geometrical spreading. Consider a tube of rays propagating from source O to a receiver X at the surface of an elastic half-space (*Julian and Gubbins*, 1977). The pencil of rays subtending a solid angle $d\Omega$ at O diverge to cover an surface area dA at X. The total power within the pencil is the same at O and X, neglecting attenuation effects. The ratios of power per unit area at O and X are:

$$\frac{E}{I} = \frac{d\Omega}{dA\cos i_P} \qquad 6.24$$

where i_P is the angle between the incident ray at X and nadir (*Julian and Gubbins*, 1977). The element of solid angle subtended at the source:

$$d\Omega = di_o dj_o \sin i_o \qquad 6.25$$

is related to the element of area dA at the surface:

$$\mathrm{dA} = \mathrm{r}^2 \sin\vartheta_X d\vartheta_X d\phi_X \quad , \qquad 6.26$$

where (r, ϑ_X, ϕ_X) are spherical co-ordinates of X, by:

$$\frac{E}{I} = \frac{\sin i_o}{r^2 \sin\vartheta_X \cos i_X}\begin{vmatrix} \frac{\partial i_o}{\partial\vartheta_X} & \frac{\partial j_o}{\partial\vartheta_X} \\ \frac{\partial i_o}{\partial\phi_X} & \frac{\partial j_o}{\partial\phi_X} \end{vmatrix} \qquad 6.27$$

The geometrical spreading coefficient R is defined as:

$$R^2 = \frac{I}{E} \qquad 6.28$$

(*Aki and Richards*, 1980, p 99).

6.4.5 Estimating amplitude ratio and amplitude error bounds

The linear-programming technique requires that amplitudes and amplitude ratios be expressed in terms of bounding values. Measured amplitudes are subject to uncertainties arising from seismic noise and unmodelled wave-propagation affects. Provided the two phases of an amplitude ratio are affected similarly then wave-propagation effects are decreased for this parameter. The uncertainties are used to determine appropriate error bounds for amplitudes and amplitude ratios.

The estimated total uncertainty σ_{total} for amplitude ratios is :

$$\sigma_{total} = \sigma_a + \sigma_b + \sigma_p \qquad 6.29$$

and for an amplitude:

$$\sigma_{total} = \sigma_a + \sigma_p \qquad 6.30$$

where σ_a and σ_b are the fractional uncertainties in the measured amplitudes of two seismic-phases (*e.g.*, *P* and *SH*) attributed to seismic noise and σ_p measures modelling errors. Seismic noise was quantified using the program *noisepick* (*A. D. Miller, pers. comm.*). The program calculates the RMS amplitude for a 1 s segment preceding the *P*-phase arrival and for a time period equal to 50% of the *S-P* time prior to an *S*-phase arrival. The fractional uncertainty is the RMS amplitude due to noise divided by the measured amplitude.

The three-dimensional wave-speed models are imperfect, as are the corrections for attenuation and geometrical spreading. σ_p is however difficult to quantify. In the absence of a rigorous statistical analysis polarity and amplitude ratio data from several events were inverted for a range of values for σ_p and a value selected which resulted in about half of the events yielding feasible solutions (see Section 6.6.1).

6.4.6 Determining moment tensors

The program *focmec* (*B. R. Julian, pers. comm.*) determines moment tensor solutions for any combination of *P*, *SH*, *SV* polarity, amplitude or amplitude ratio observations using the simplex algorithm. Such a source mechanisms are given in moment-tensor form and can be constrained to be purely deviatoric (zero volume change). *focmec* seeks a moment tensor solution which is consistent with the data (the initial

feasible solution). This solution is not unique but one of a set of moment tensors which are consistent with the polarity and amplitude data. A set of user-defined objective functions can be applied to search for physically motivated, extreme linear combinations of the moment-tensor components. If no feasible solution exists then the moment tensor that minimises the L1 norm of the residuals is determined.

The programs *el2fm.abs* and *el2fm.rat* (*A. D. Miller, pers. comm.*) prepare polarity and amplitude information output by *qloc3d* to the required input format for *focmec*. *el2fm.abs* is used when the scalar moment, M_0, is determined by inverting polarities and amplitude measurements while *el2fm.rat* is used when moment tensors are determined by inverting polarities and amplitude ratios. The programs normalise the measured amplitudes to unit distance from the source and correct for wave-propagation effects. To compensate for systematic differences between radiated compressional- and shear-waves, amplitudes are multiplied by $4\pi\rho v^3$ and amplitude ratios by v^3 where ρ is the density and v is the appropriate wave-speed (v_P or v_S) at the source.

6.4.7 Graphical presentation of results

We display observations on equal-area projections of the upper focal sphere. A focal sphere is an imaginary sphere surrounding the earthquake hypocentre to which observations are often referred (Figure 6.5a). A theoretical amplitude ratio A:B is represented as an arrow of unit length whose slope is A/B (Figure 6.5b). The arrow orientation depends on the polarities of A and B but is independent of its position on the focal sphere and does not cause visible distortion when one amplitude is small. Pairs of lines indicate ranges compatible with the observations (Figure 6.5c). An observation is consistent with the theoretical ratio if the arrow lies between the pair of lines (1) and inconsistent otherwise (2).

The "source-type plot" enables a depiction of the focal mechanism that is independent of its orientation (Figure 6.6) (*Hudson et al.*, 1989). The lozenge shape achieves a uniform probability density of sources over the plot. The parameter k (vertical co-ordinate) is plotted against T=–2ε (horizontal co-ordinate). T quantifies the departure of the deviatoric part of the moment tensor from a DC. k varies from +1 at the top of the plot to –1 at the bottom with constant values along sub-horizontal contours. T varies from 1 at the right to –1 on the left, with constant values along sub-vertical contours.

6.5 Determining earthquake moment-magnitudes (M_W)

Earthquake moment magnitudes are determined using the scalar moment M_0 which is related to the principal moments m_i by:

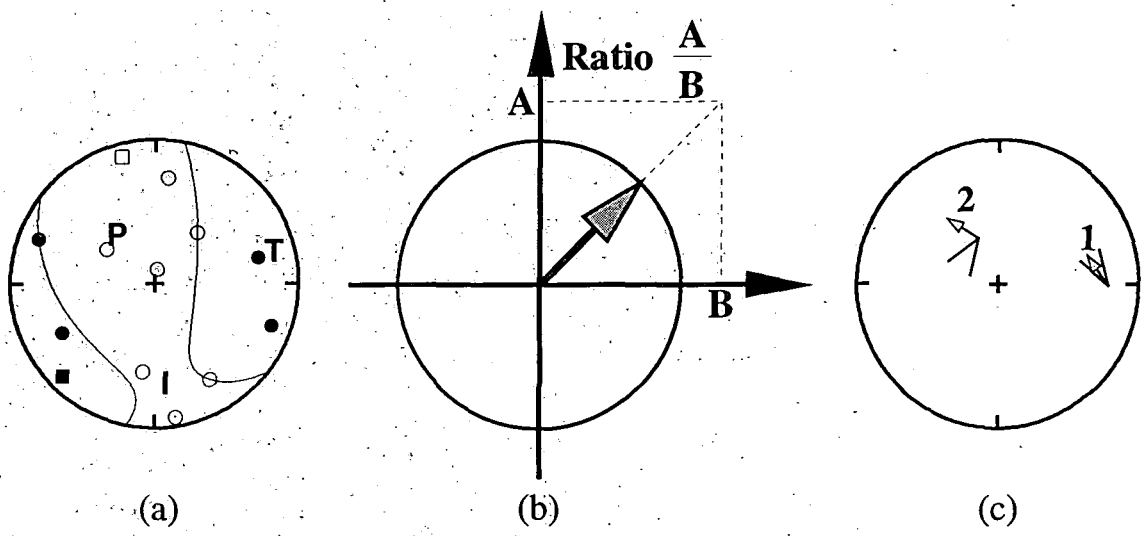

Figure 6.5. Graphical presentation schemes used for observations. (a) Upper-hemisphere wave-polarities in equal-area projection. Open symbols: dilations; filled symbols: compressions; square symbols: lower-hemisphere observations plotted at their antipodal points; lines: theoretical nodal surfaces. (b) Amplitude ratios A:B represented by the direction of a unit vector: (c) Upper hemisphere plot showing theoretical amplitude ratios (arrows) with pairs of lines indicating ranges compatible with the observations. Theoretical amplitude ratio 1 is compatible with the observations and observation 2 is not.

$$M_o = \sqrt{\tfrac{1}{2}\sum_i |m_i|^2} \quad , \qquad 6.32$$

(*Silver and Jordan*, 1982). Magnitudes are expressed using the moment-magnitude scale:

$$M_W = \tfrac{2}{3}\log M_o - 6.0 \quad . \qquad 6.33$$

If it is assumed that moment release at the source is a step-like function of time then the far-field motion is expected to be a delta function. The seismogram represents the response of the station to that ground motion. The amplitude of the first motion of the seismogram is then linearly related to actual amplitude of ground motion by a proportionality constant.

For this study an expedient approach was taken to calibrating moments calculated by *focmec* using seismogram amplitude measurements. This was to regress the magnitudes with coda-magnitudes reported by CALNET, UNT and D. B. Barton, a fellow Durham student who has calculated coda-magnitudes for earthquakes from The Geysers using UNT seismograms (*D. B. Barton, pers. comm.*), (Figure 6.7). The correlations with CALNET and Barton magnitudes are similar because the coda-duration magnitude scales

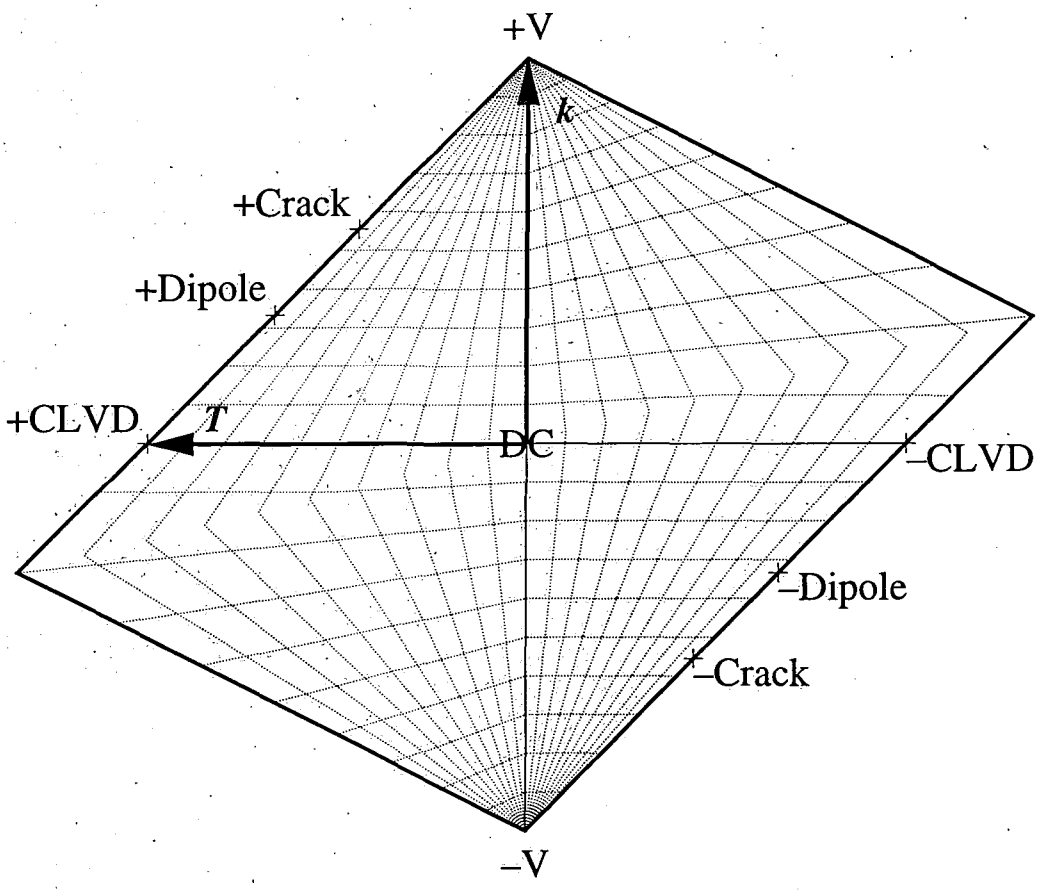

Figure 6.6. Equal area "source type plot" used to display orientation-independent descriptions of focal mechanisms (*Hudson et al.*, 1989). k (the relative volumetric change) is plotted against T (the departure of the deviatoric component from a DC). k varies from +1 at the top of the diagram to –1 at the bottom. For purely deviatoric sources k=0. k is constant on sub-horizontal contours. T varies from +1 on the left to –1 on the left, with constant values along sub-vertical contours.

were calibrated using CALNET magnitudes (*D. B. Barton, pers. comm.*). There is a systematic difference between CALNET magnitudes and UNT magnitudes (Figure 6.7c and d). I chose to calibrate the moment magnitudes output by *focmec* with CALNET magnitudes because the latter are more commonly used.

The conversion equation used is:

$$M_w = \frac{M_w(\text{amp}) - 1.135}{0.823} \qquad 6.34$$

where M_w is the corrected moment-magnitude and M_w(amp) is the moment-magnitude determined by polarity and amplitude data.

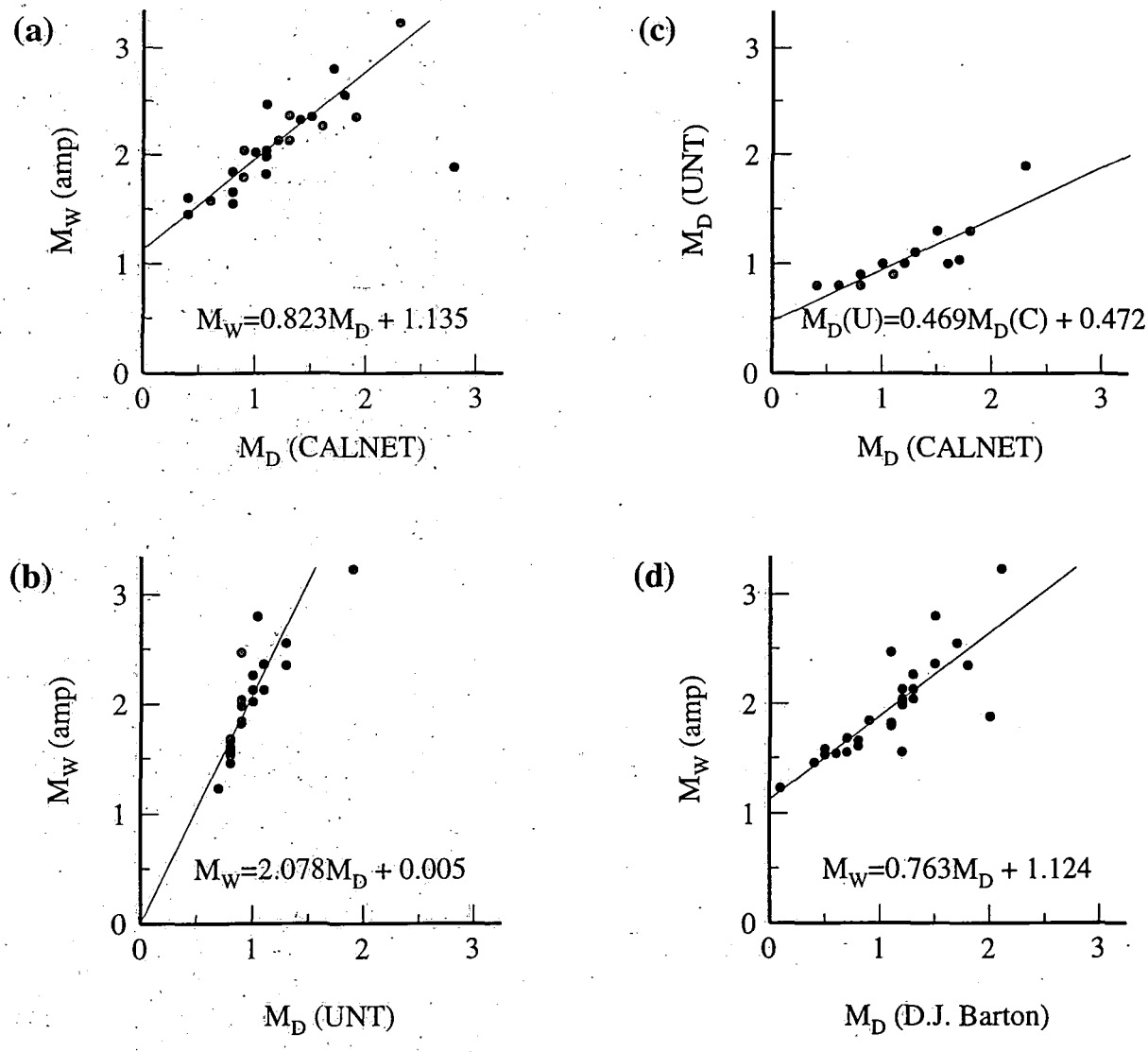

Figure 6.7. Calibration graphs comparing moment magnitudes determined from seismic amplitudes with coda-duration magnitudes in the CALNET and UNT catalogues and an independent catalogue (D. B. Barton, *pers. comm.*). (a) M_D(CALNET) vs. M_W(amp). (b) M_D(UNT) vs. M_W(amp). (c) M_D(CALNET) vs. M_D(UNT). (d) M_D(D. J. Barton) vs. M_W(amp). M_W(amp): moment magnitude determined using amplitudes.

6.6 Results

6.6.1 Amplitude and amplitude ratio uncertainties

An appropriate additional fractional error bound σ_p was added to the estimated noise to account for unmodelled wave-propagation effects. This was estimated by inverting polarity and amplitude-ratio data for several events. Focal mechanism solutions

for an example, event (120.021319.1) which has 23 polarity, 21 amplitude and 8 amplitude ratio observations are presented in Figure 6.8. A value of 40% for σ_p just made the data yield a feasible solution. This value was applied to the whole data set and resulted in 47% of the events yielding feasible solutions.

6.6.2 *S*-wave attenuation

Classical attenuation occurring only by shear anelasticity results in the ratio Q_P/Q_S=2.25 (*Aki and Richards*, 1980, p 192). Attenuation caused by scattering from cracks and voids produces a ratio Q_P/Q_S=1.4 (*Menke et al.*, 1995). *P*-wave amplitudes were corrected for attenuation using Q_P=60. The appropriate value for Q_S was determined by inverting *P*-, *SH*- and *SV*-waves with *S*-phase amplitudes corrected for attenuation using a range of values (5-500). The calculated goodness-of-fit of the resulting moment tensors was relatively insensitive to Q_S. A value Q_S=84 was chosen for The Geysers, corresponding to Q_P/Q_S=1.4.

6.6.3 Amplitude ratio data needed for good moment tensor results

To test at which point moment tensors become poorly constrained as a result of insufficient data a series of inversions were performed on event 116.052923.1 which has 11 *P*-, 10 *SH*-wave polarity observations and 10 amplitude ratios (Figure 6.9). Moment tensors were determined initially with all available polarity and amplitude observations. In each subsequent inversion observations from one station were discarded. The same set of inversions were performed for polarity data (Figure 6.10). Stations were selectively removed in such a way as to maintain an even distribution of stations over the focal sphere.

The focal mechanism solutions remain remarkably consistent even when determined with as few as 3 amplitude ratios, 4 *P*-wave and 3 *S*-wave polarity observations (Figure 6.9). The orientations of the principal axes are successfully recovered in each inversion. In comparison the moment tensors calculated from polarity observations alone require at least 7 *P*- and 6 *SH*-wave polarity observations. Reducing the data set further severely degrades the result. Theoretical and observed amplitude ratios in Figure 6.10 are included for information only. They were not included in the inversion.

6.6.4 Solutions for the whole data set

Moment tensor solutions are presented for 30 of the best earthquakes. Most events locate within the two vertically-distinct seismic zones in the central region of The

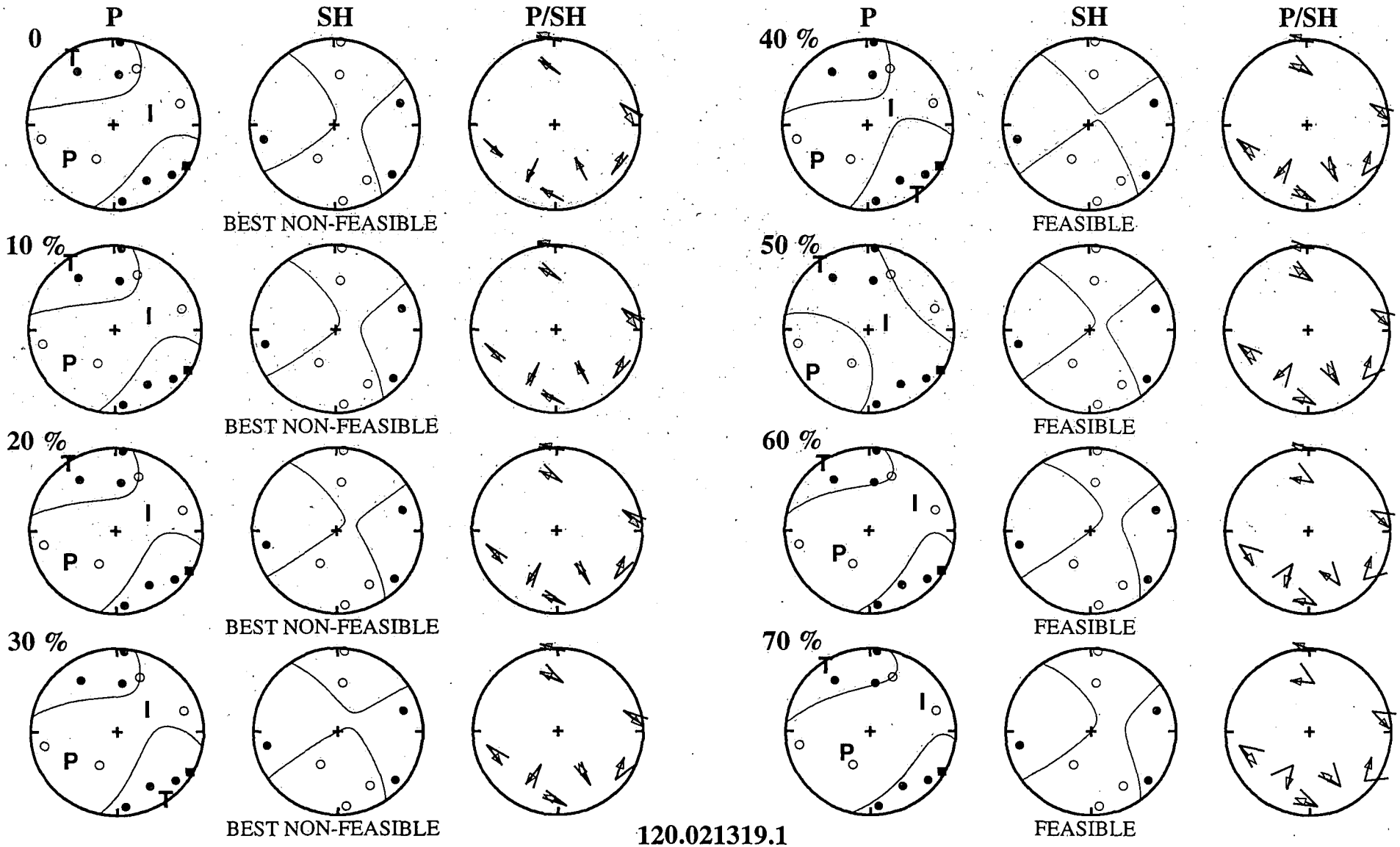

Figure 6.8. Focal mechanism solutions for event 120.021319.1 determined using a suite of additional fractional errors σ_p (0-70%). The focal mechanism solutions are presented in three upper hemisphere plots. Left: P-wave polarities; centre: SH-wave polarities; right; P:SH amplitude ratios. Symbols are the same as for Figure 6.4. The σ_p value value used is indicated to the left of each triplet plot.

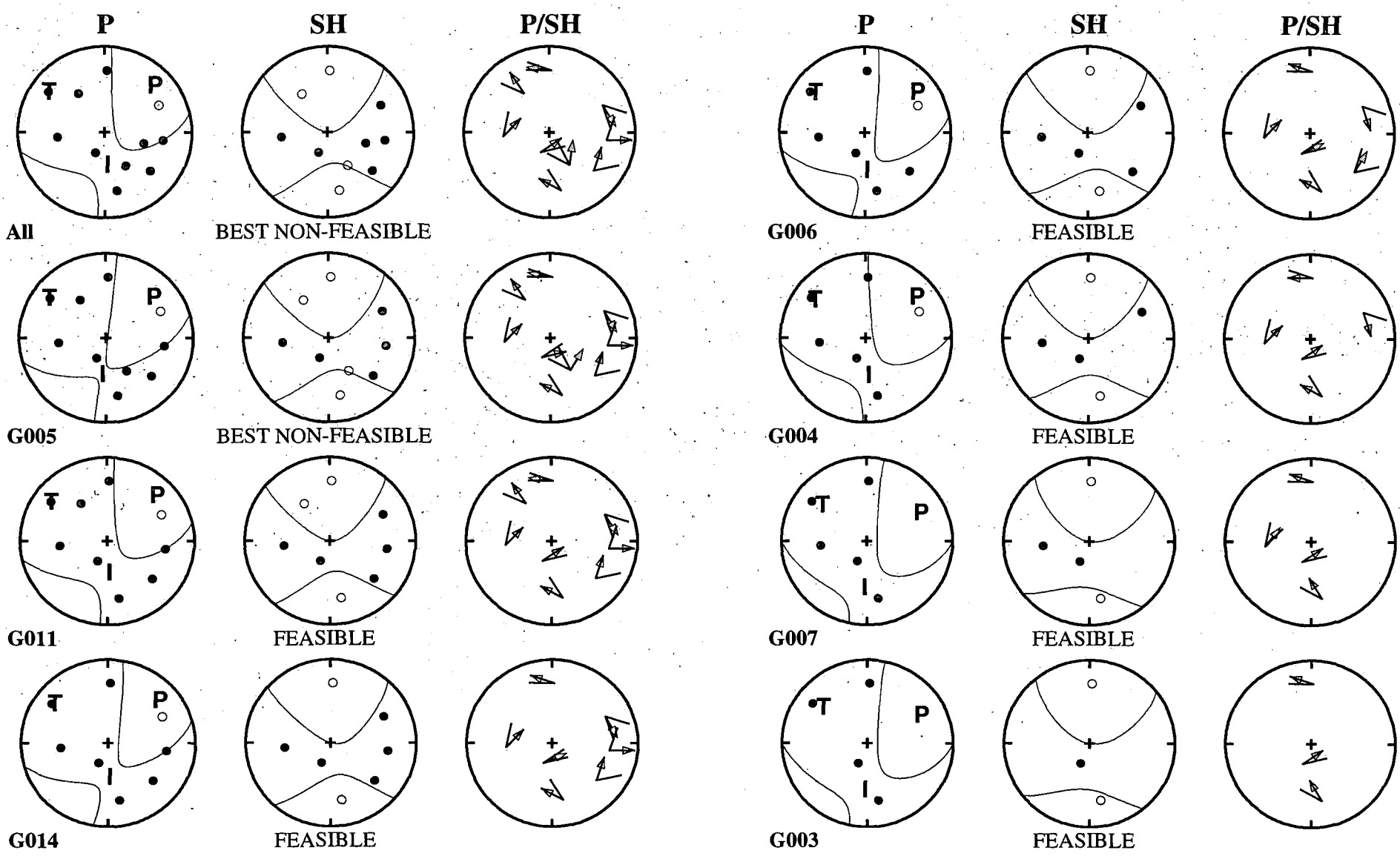

Figure 6.9. Focal mechanism solutions for event 116.052923.1 determined initially with all available polarity and amplitude data and then in each of the subsequent plots with observations from one station discarded.

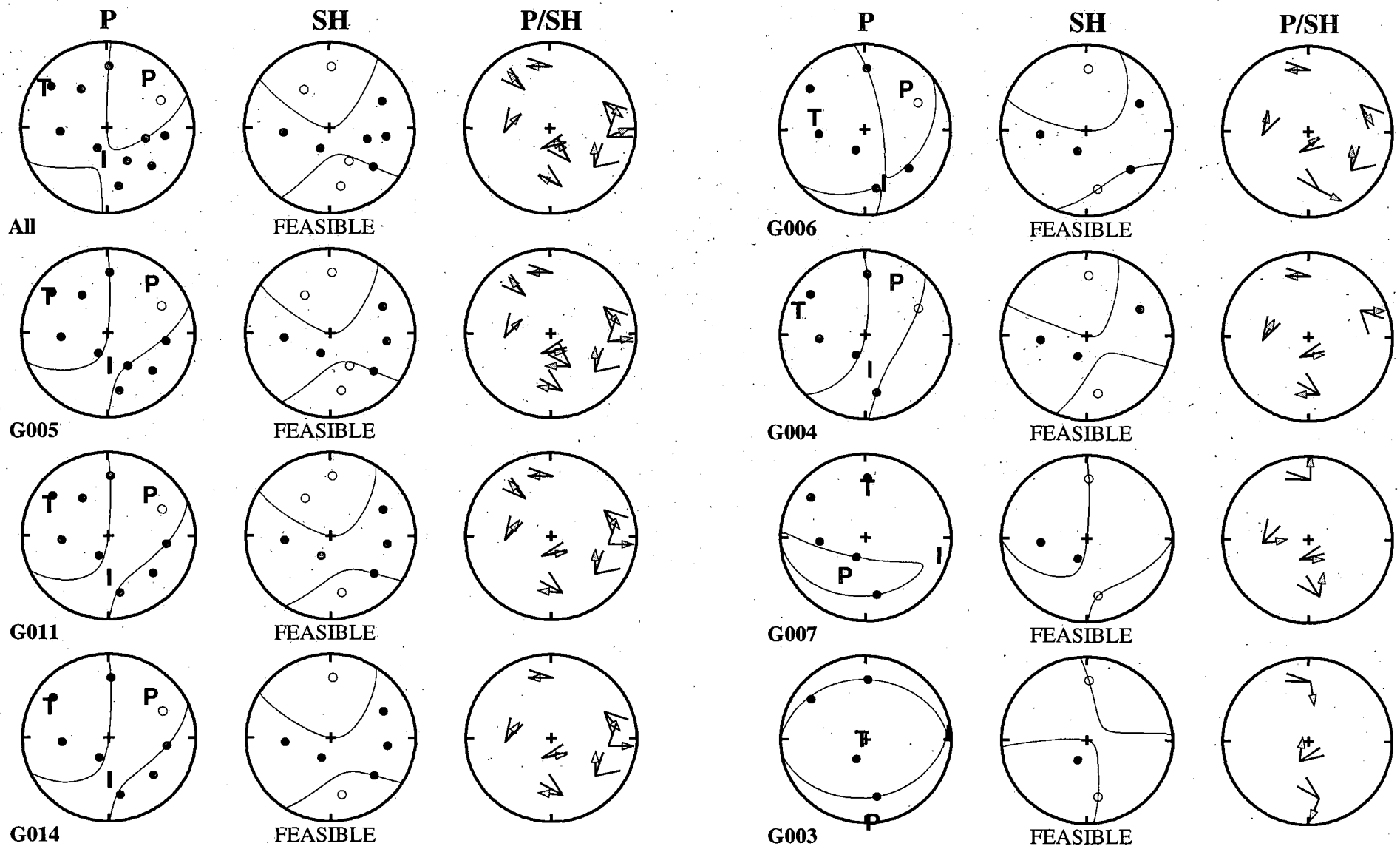

Figure 6.10. Same as Figure 6.9 using polarity data only.

Geysers production zone (Figure 6.11; Table 6.1). Their hypocentral depth varies between 0.78 and 3.98 km bsl. Moment tensor solutions are calculated with up to 27 polarity observations and 10 amplitude ratios with an average of 20 polarity observations and 5 amplitude ratios (Table 6.1). Moment magnitudes range from M_W=0.12 to M_W=2.55 with an average of M_W=1.0 (Table 6.1).

Moment tensor solutions are presented on a source-type plot in Figure 6.12. These are either a randomly selected moment tensor taken from the non-empty of solutions that fit the data within the (too lenient) bounds requested, or the solution which fits the data best by minimising the residuals of unsatisfied constraints. The results show a considerable range of solutions, with some deviatoric while others have mechanisms with significant positive or negative volumetric components (Table 6.2). Events define a broad band stretching from the DC locus to the ±Dipole loci. None of the events are close to the ±Crack loci. The distribution is systematic with as many implosive as there are explosive events. About 50% of the mechanisms have significant volumetric components of ≥20% with the volumetric components of 5 events (event numbers 1, 2, 7, 9 and 10) exceeding 30% (Table 6.2). About 27% of the events are deviatoric. Event 1 lies directly on the +Dipole locus while events 9 and 10 lie very close to the –Dipole locus. The band of solutions broadens in the central region about the DC locus. These events are well constrained e.g., event 30 which is furthest from the ±Dipole/DC line, is constrained by 25 polarity observations and 7 amplitude ratios.

Moment tensor solutions are presented in upper hemisphere focal mechanism plots with maps and cross-sections indicating their locations relative to one another in the reservoir (Figures 6.13 to 6.24). Where possible the events have been grouped such that similar populations on the source-type plot (such as events 1-8) are presented together. The moment tensor solutions generally show a good fit to the data with few and minor polarity and amplitude misfits. Events located at depths ≥2 km bsl within the central Geysers give the best focal sphere distribution. Of particular interest is event 1 which shows only compressional first motions over the focal sphere. The nodal planes define an insignificant area of dilational arrivals. The *S*-wave observations associated with this event were very poor (Figure 6.13).

Implosive events (<–10%) are restricted to depths shallower than 2 km bsl (Figure 6.25a), however, there is no correlation with depth for the explosive (Figure 6.25a) and CLVD components of the moment tensor (Figure 6.25.b). Moment magnitudes are also independent of the size of the volumetric and CLVD components (Figure 6.25c and d). There appears to be no temporal dependence on the type of mechanism. For example, events 17 and 24 occur 30 s apart, at almost the same location (Table 6.1; Figures 6.19, 6.20 and 6.21). These events are both well constrained with good polarity and amplitude information. They exhibit substantially different focal mechanism solutions, whereas the

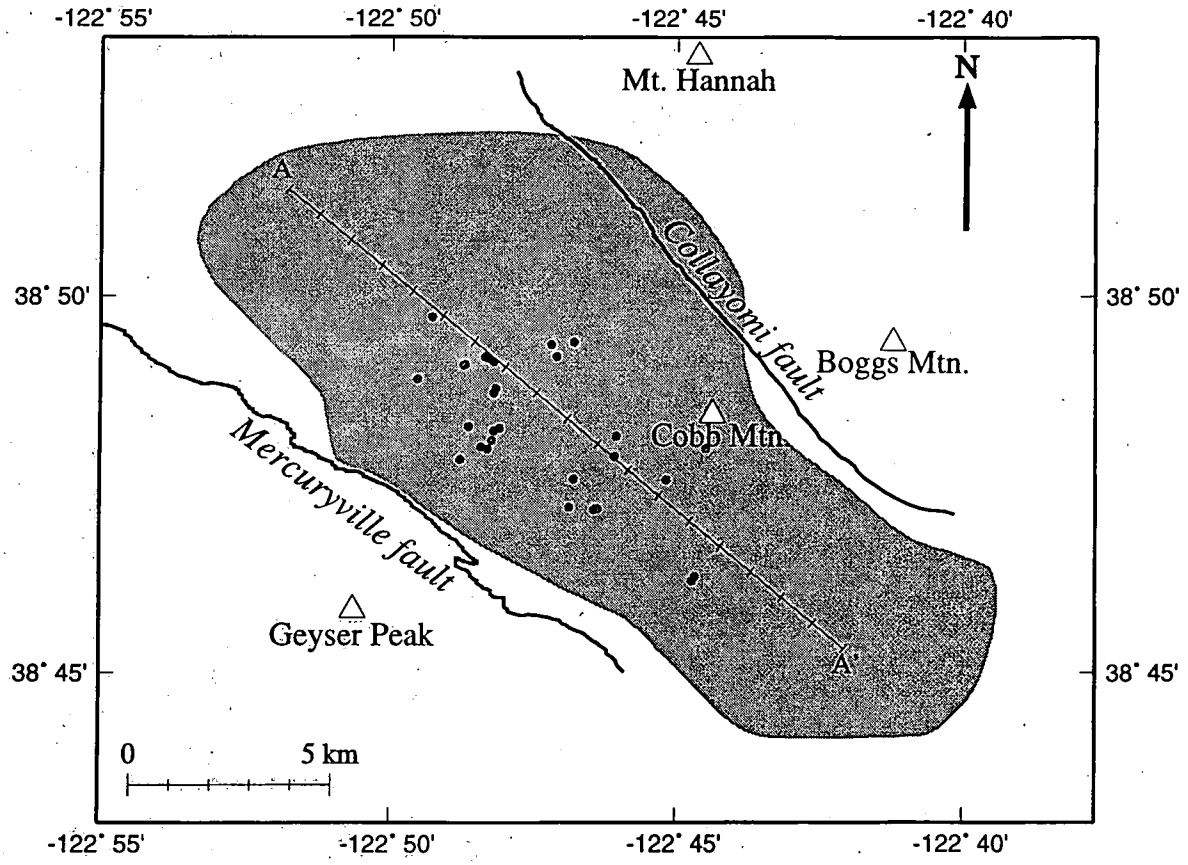

(a)

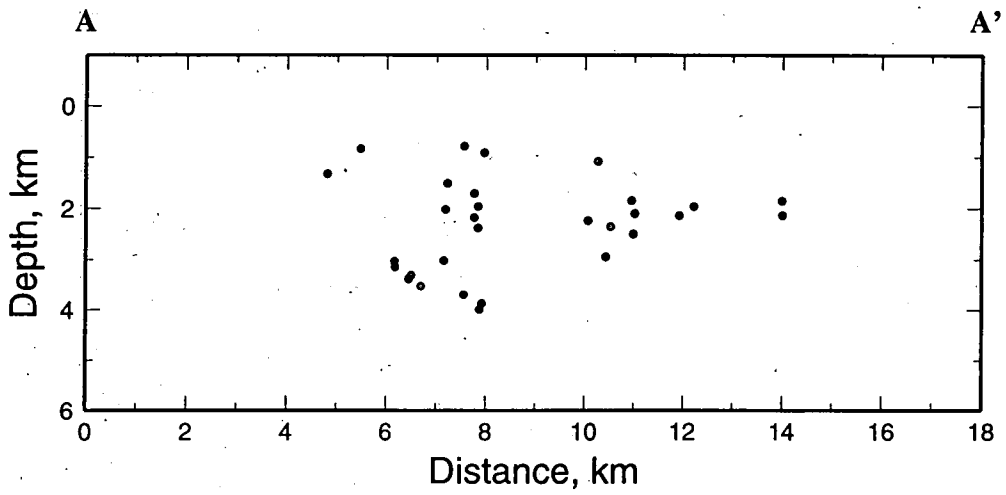

(b)

Figure 6.11. (a) Map, and (b) cross-section A-A' of The Geysers geothermal showing the locations of the 30 events for which focal mechanisms were calculated.

Table 6.1. Number of polarity and amplitude-ratio observations used to calculate moment tensors for the best 30 events.

Event number	Event name	Latitude	Longitude	Depth, km (bsl)	No. of polarity observations	No. of amplitude ratio observations	M_W
1	104.002347.1	38:47.203	−122:46.876	2.94	17	2	1.62
2	117.062926.1	38:49.127	−122:48.205	3.52	17	5	0.66
3	117.153329.1	38:48.264	−122:48.631	1.51	26	5	1.21
4	115.155752.1	38:47.182	−122:46.375	2.10	17	6	0.54
5	101.021650.2	38:48.137	−122:46.049	1.07	26	10	1.48
6	111.093646.1	38:47.975	−122:44.476	1.96	26	7	0.86
7	107.164134.1	38:49.195	−122:47.105	2.38	19	6	0.80
8	116.052923.1	38:47.969	−122:48.315	3.88	22	1	0.64
9	106.220554.1	38:49.354	−122:47.194	0.78	18	5	1.37
10	116.201219.1	38:49.386	−122:46.802	0.91	24	6	1.72
11	114.212724.1	38:49.716	−122:49.279	1.32	22	4	1.49
12	114.015820.1	38:47.564	−122:45.166	2.14	16	6	0.39
13	118.033015.2	38:47.185	−122:46.398	2.49	15	4	0.91
14	119.021240.1	38:46.281	−122:44.661	1.85	20	5	1.21
15	108.021016.2	38:47.830	−122:48.783	3.70	11	3	0.55
16	107.051947.1	38:47.575	−122:46.807	2.23	11	3	0.12
17	120.013734.1	38:49.091	−122:48.699	3.14	19	8	0.49
18	120.021319.1	38:47.998	−122:48.421	2.18	19	8	0.83
19	107.163420.2	38:46.220	−122:44.717	2.14	25	5	1.48
20	114.214421.1	38:47.876	−122:46.083	2.35	15	4	1.03
21	115.160329.1	38:49.174	−122:48.323	3.30	19	7	0.50
22	107.225324.1	38:48.767	−122:48.167	3.02	16	6	0.48
23	115.142606.1	38:48.212	−122:48.199	1.70	27	9	1.10
24	120.013734.2	38:49.078	−122:48.726	3.03	18	7	0.50
25	099.193503.1	38:48.897	−122:49.533	0.83	21	4	2.02
26	107.133652.1	38:48.706	−122:48.204	2.02	22	9	0.58
27	115.143339.1	38:48.240	−122:48.103	1.96	19	6	1.10
28	104.073739.1	38:47.174	−122:46.441	1.85	26	2	2.55
29	115.085212.2	38:49.193	−122:48.352	3.38	18	6	1.44
30	116.040529.1	38:48.084	−122:48.237	3.98	25	7	1.08

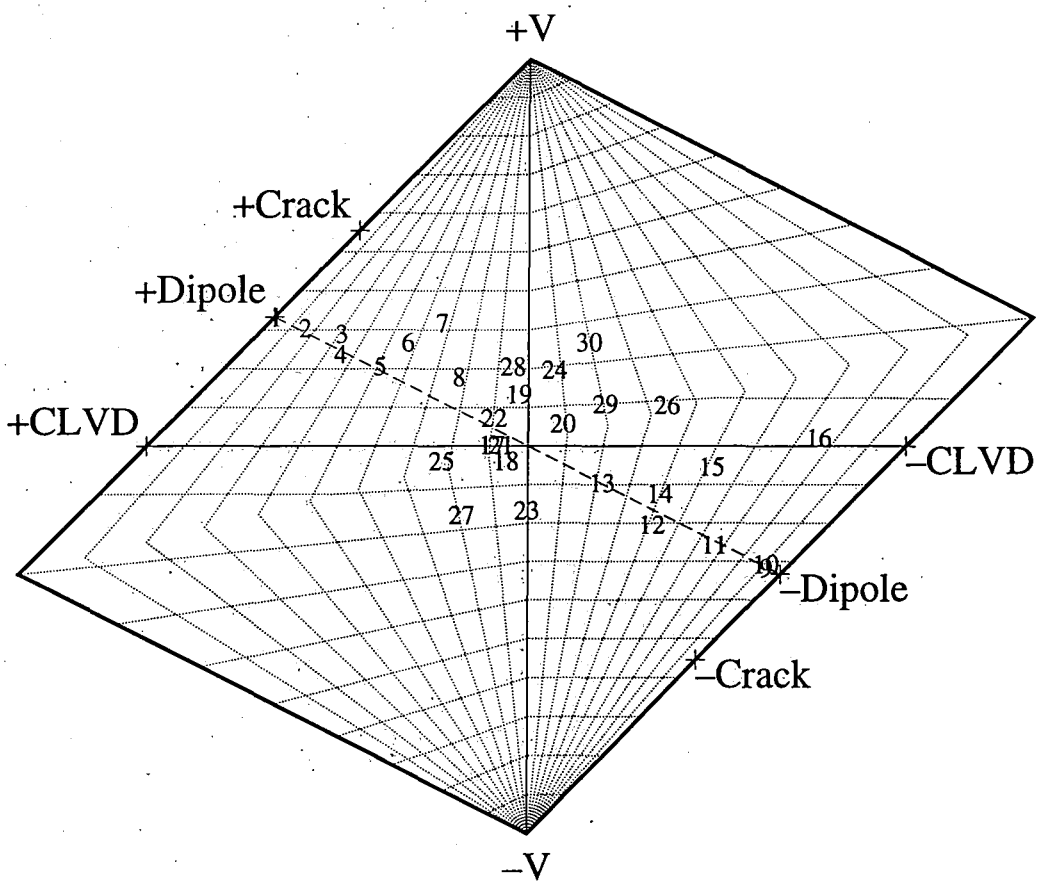

Figure 6.12. Source-type plot for events 1-30. DC: double couple mechanism; +/–Crack: opening/closing tensile crack; +/–Dipole: force dipole with force directed inward/outward; +/–CLVD: Compensated Linear Vector Dipole with dominant pole directed inward/outward.

Table 6.2. Moment tensors decomposed into percentage volumetric, DC and CLVD components.

Event number	Event name	% volumetric component	% DC component	% CLVD component
1	104.002347.1	33.34	0.28	66.38
2	117.062926.1	30.48	10.87	58.65
3	117.153329.1	29.01	22.02	48.98
4	115.155752.1	23.76	26.87	49.37
5	101.021650.2	20.71	40.27	39.02
6	111.093646.1	26.76	41.49	31.75
7	107.164134.1	31.86	45.54	22.60
8	116.052923.1	18.08	63.59	18.33
9	106.220554.1	−31.59	5.43	−62.90
10	116.201219.1	−30.70	6.48	−62.82
11	114.212724.1	−25.72	24.86	−49.42
12	114.015820.1	−20.29	46.90	−32.70
13	118.033015.2	−9.42	70.98	−19.60
14	119.021240.1	−12.31	52.77	−34.92
15	108.021016.2	−5.27	46.04	−48.69
16	107.051947.1	2.13	24.29	−73.58
17	120.013734.1	0.28	90.21	9.51
18	120.021319.1	−3.68	90.60	5.72
19	107.163420.2	13.42	84.09	2.49
20	114.214421.1	5.59	85.87	−8.54
21	115.160329.1	0.41	92.48	7.10
22	107.225324.1	7.25	83.63	9.13
23	115.142606.1	−16.60	82.99	0.41
24	120.013734.2	19.17	74.29	−6.54
25	099.193503.1	−3.62	75.38	21.00
26	107.133652.1	9.05	59.91	−31.04
27	115.143339.1	−16.40	67.50	16.04
28	104.073739.1	20.62	75.27	4.11
29	115.085212.2	10.04	71.48	−18.48
30	116.040529.1	25.01	60.22	−14.78

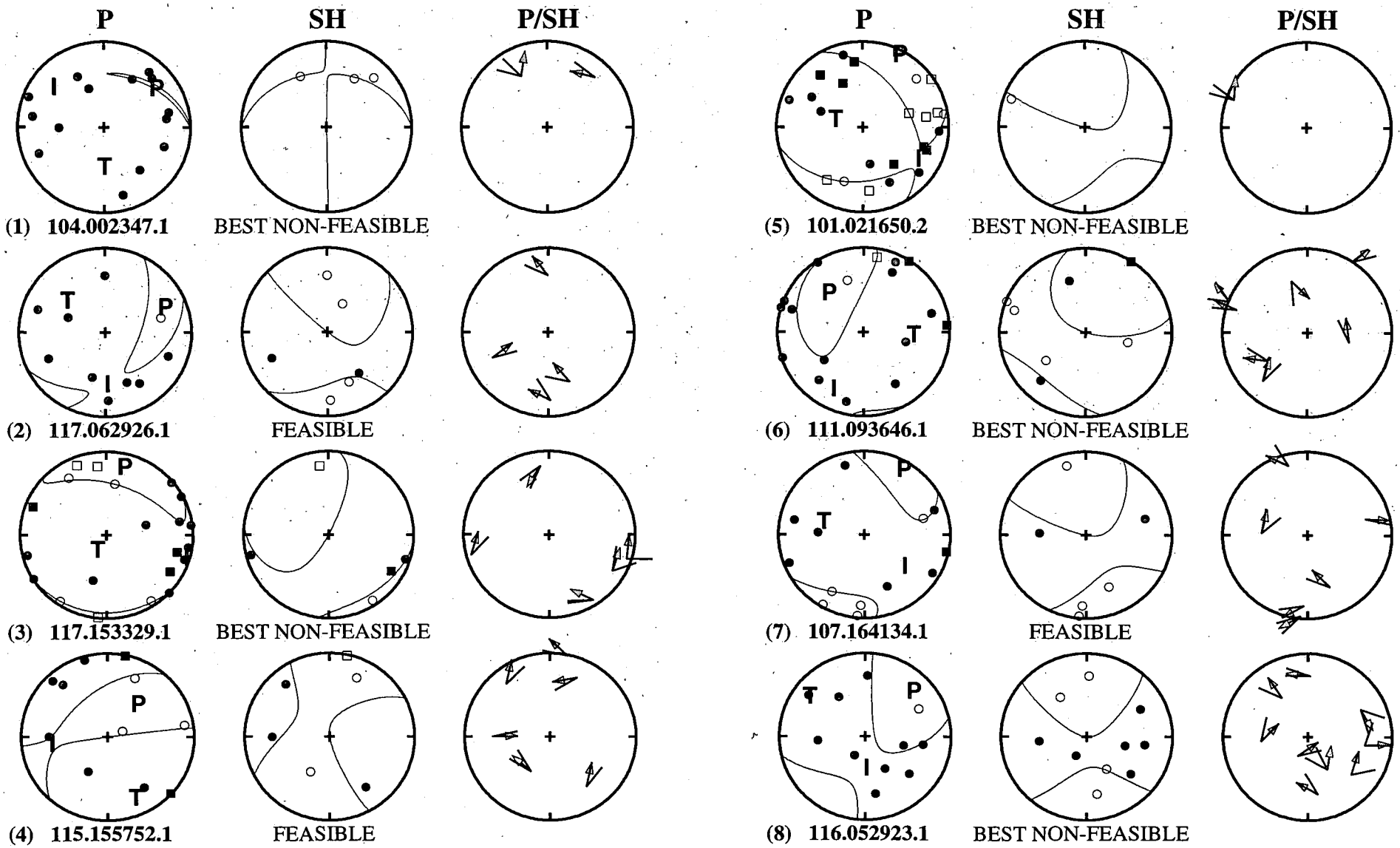

Figure 6.13. Focal mechanism solutions for events 1-8. The solutions are presented in upper hemisphere plots. Left: P-wave polarities; centre: SH-wave polarities; right: observed and calculated P:SH amplitude ratios.

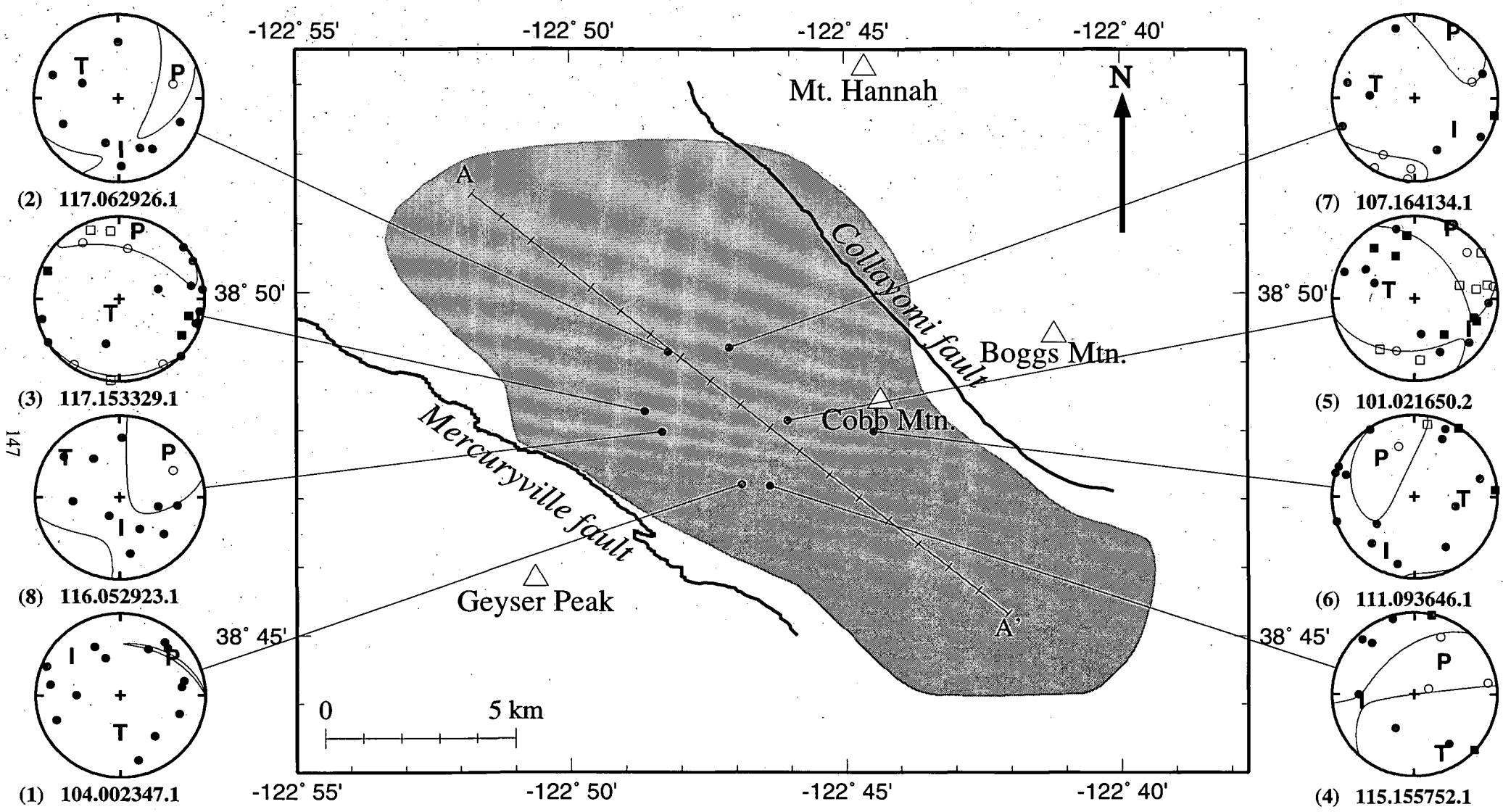

Figure 6.14. Map showing the location of events presented in Figure 6.13. For each earthquake a line connects the epicentre with the P-wave polarity plot. A-A' is the line of cross-section presented in Figure 6.15.

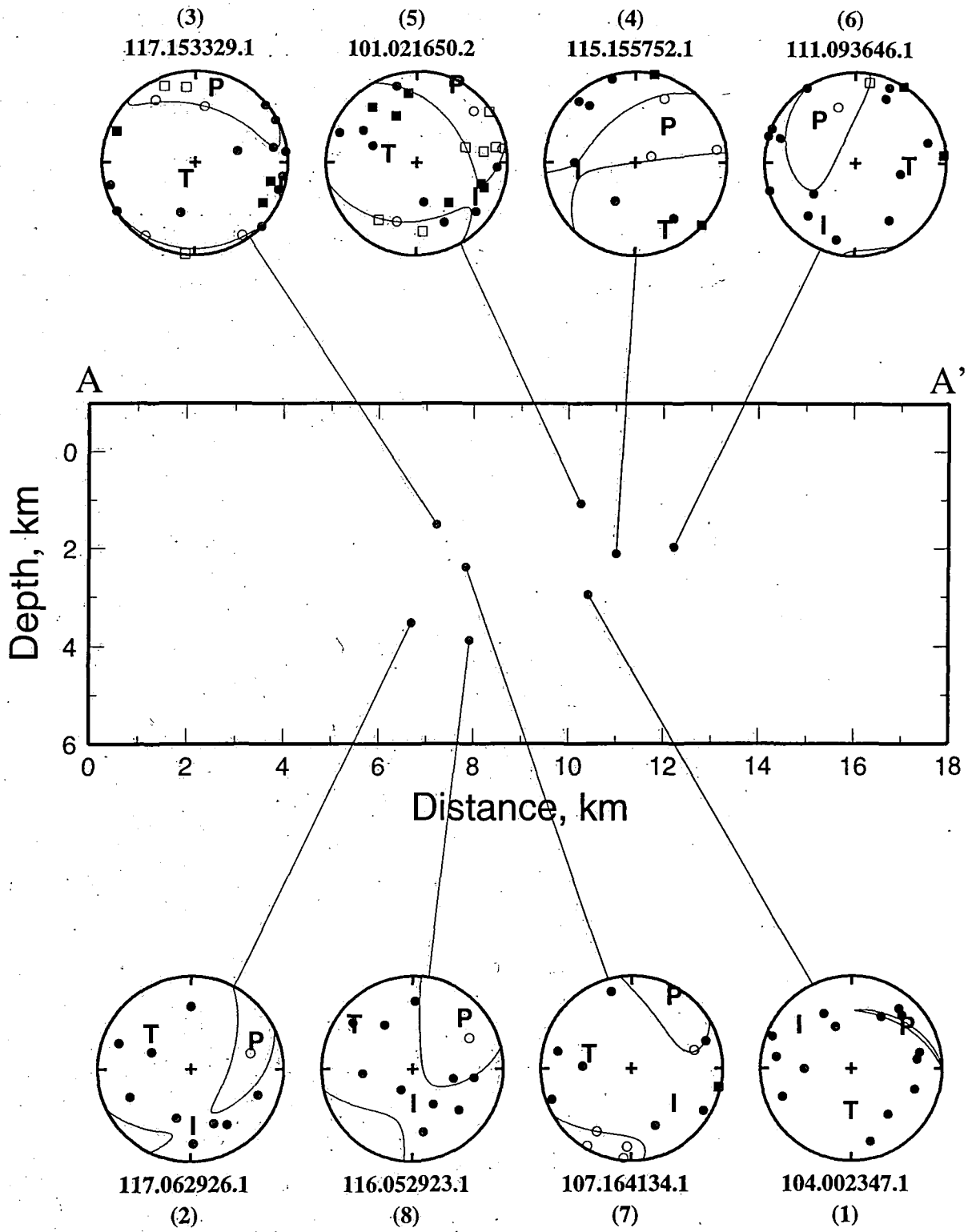

Figure 6.15. Northwest-southeast cross-section (A-A') showing hypocentres of the 8 earthquakes presented in Figures 6.13 and 6.14. A line joins each hypocentre to the *P*-wave polarity plot.

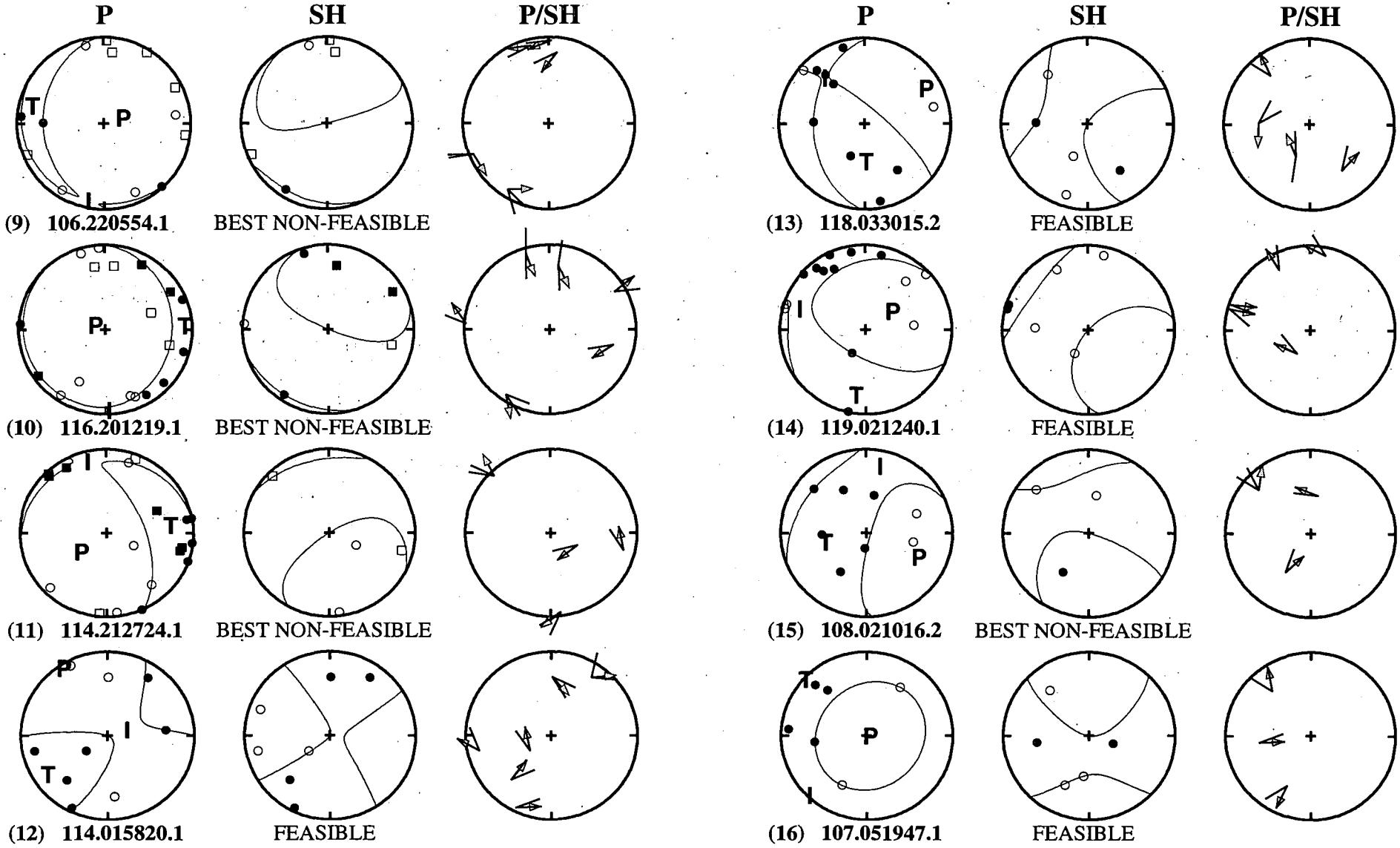

Figure 6.16. Same as Figure 6.13 for events 9-16.

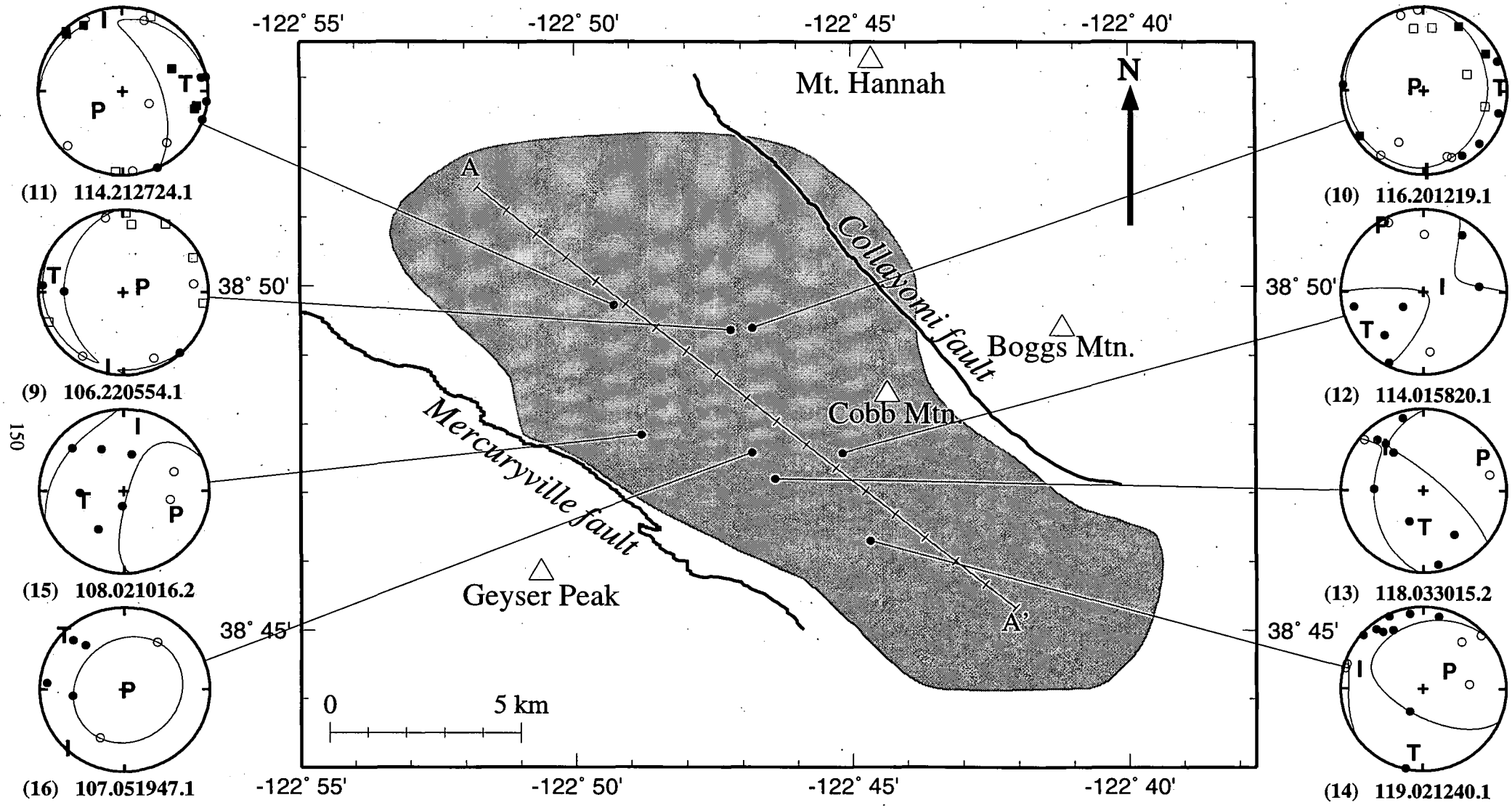

Figure 6.17. Same as Figure 6.14 for events 9-16.

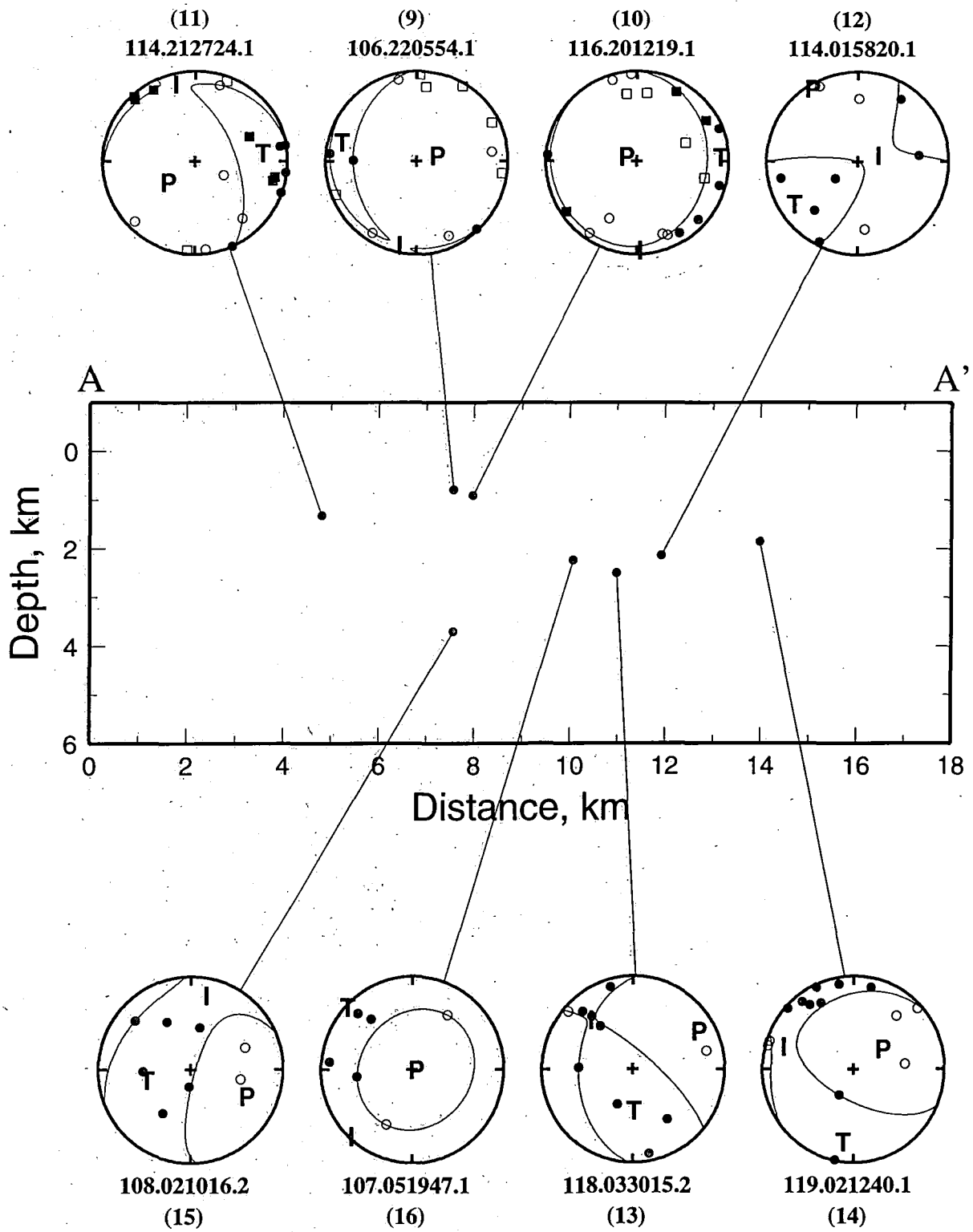

Figure 6.18. Same as Figure 6.15 for events 9-16.

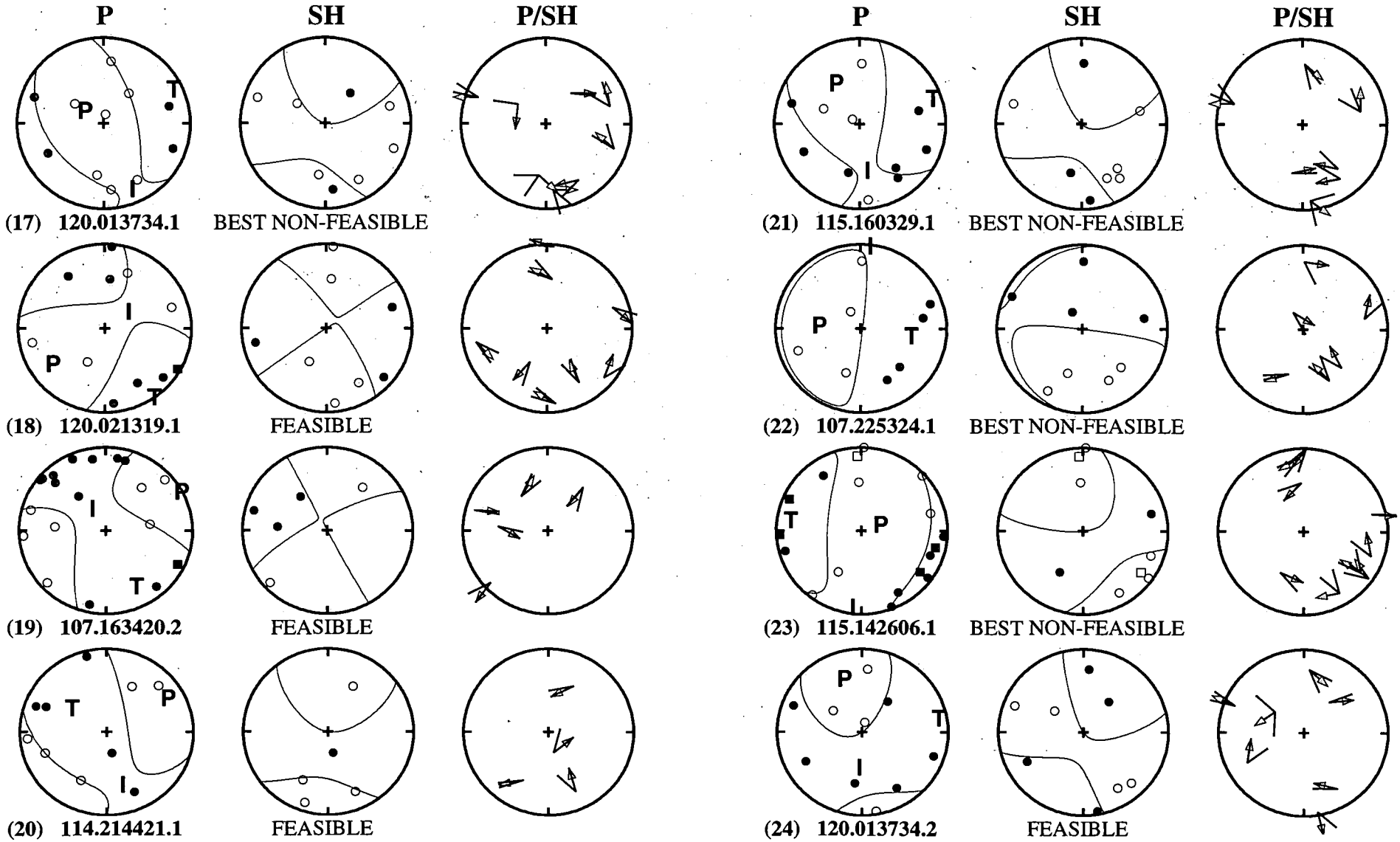

Figure 6.19. Same as Figure 6.13 for events 17-24.

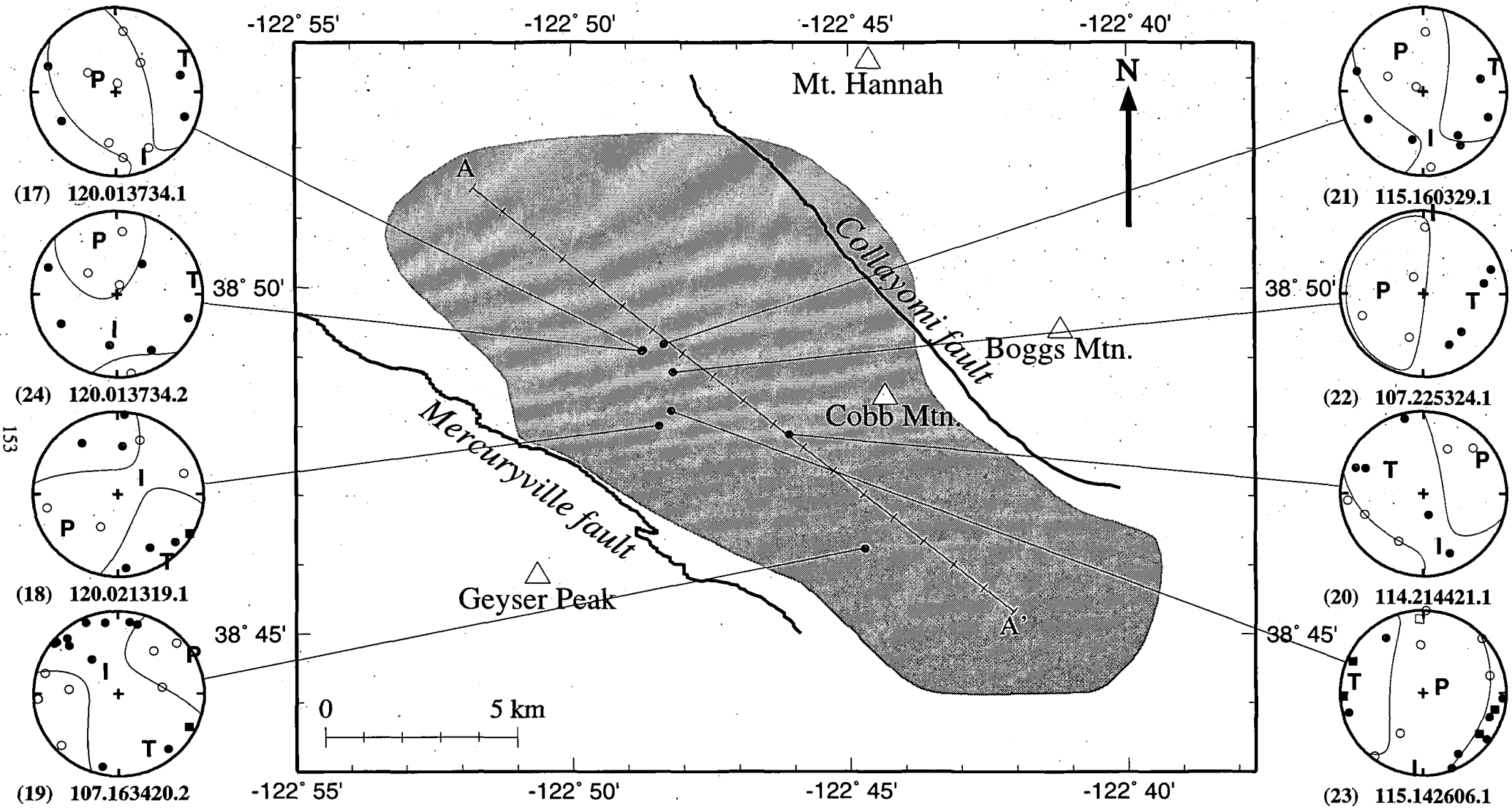

Figure 6.20. Same as Figure 6.14 for events 17-24.

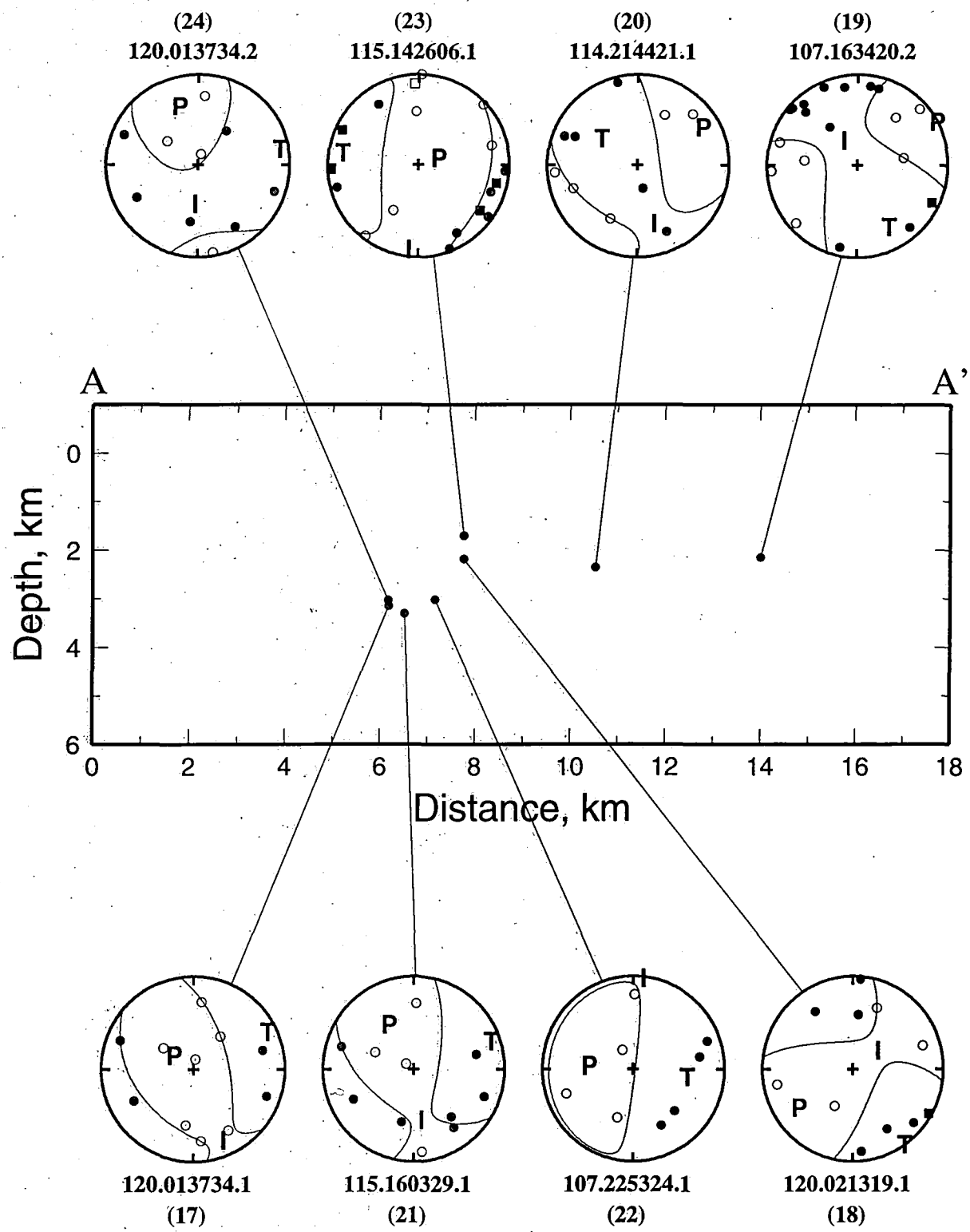

Figure 6.21. Same as Figure 6.15 for events 17-24.

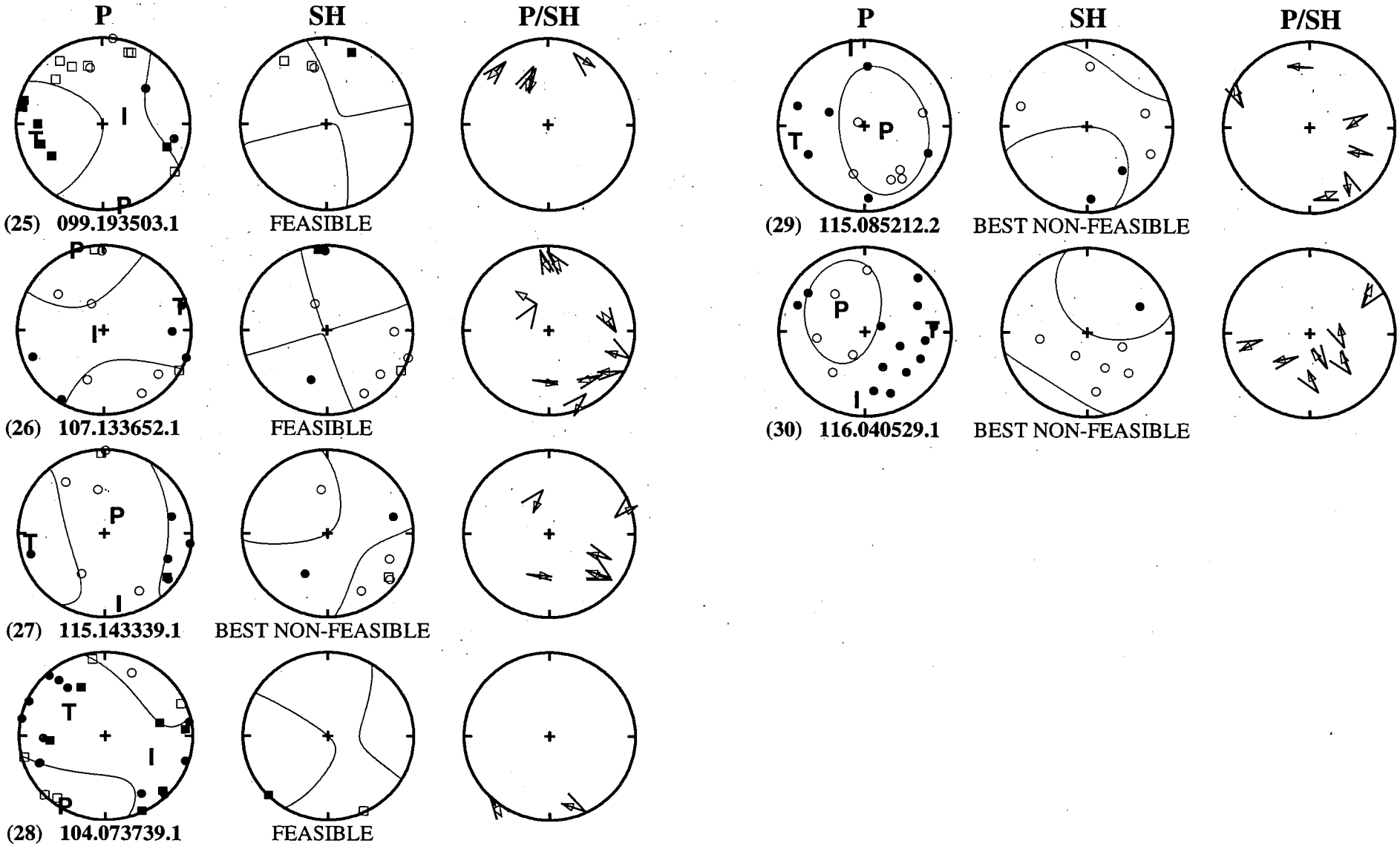

Figure 6.22. Same as Figure 6.13 for events 17-24.

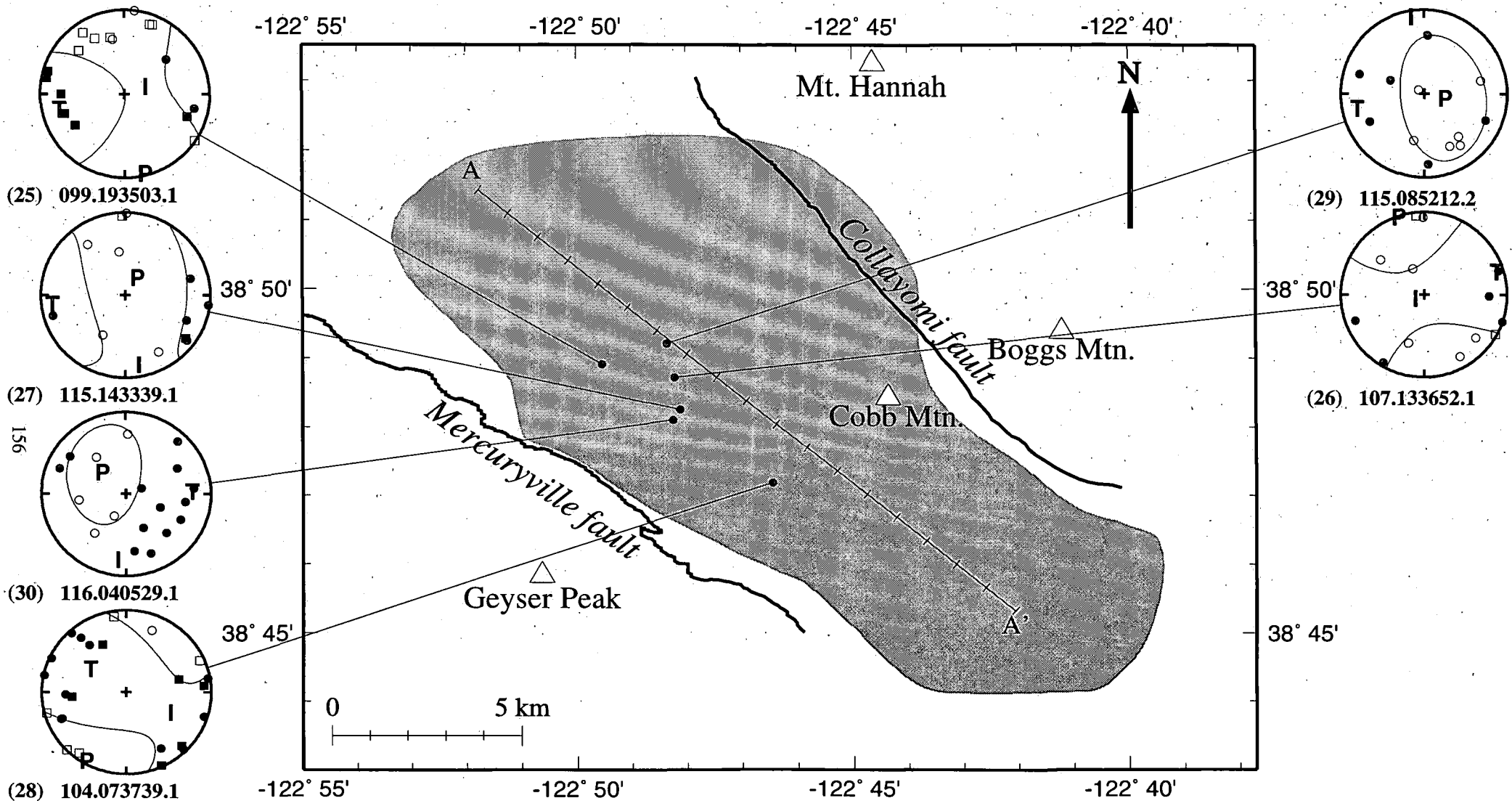

Figure 6.23. Same as Figure 6.14 for events 25-30.

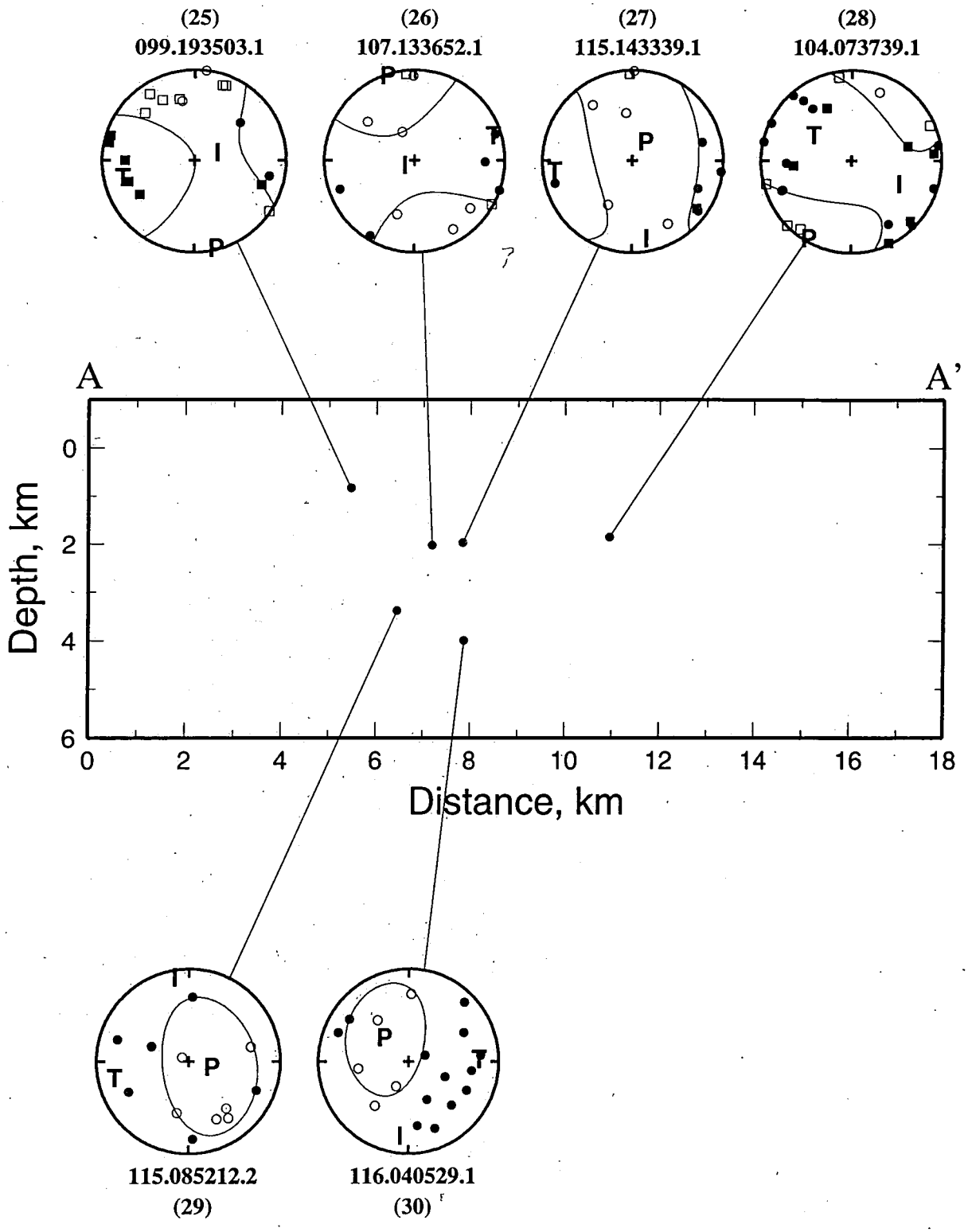

Figure 6.24. Same as Figure 6.15 for events 25-30.

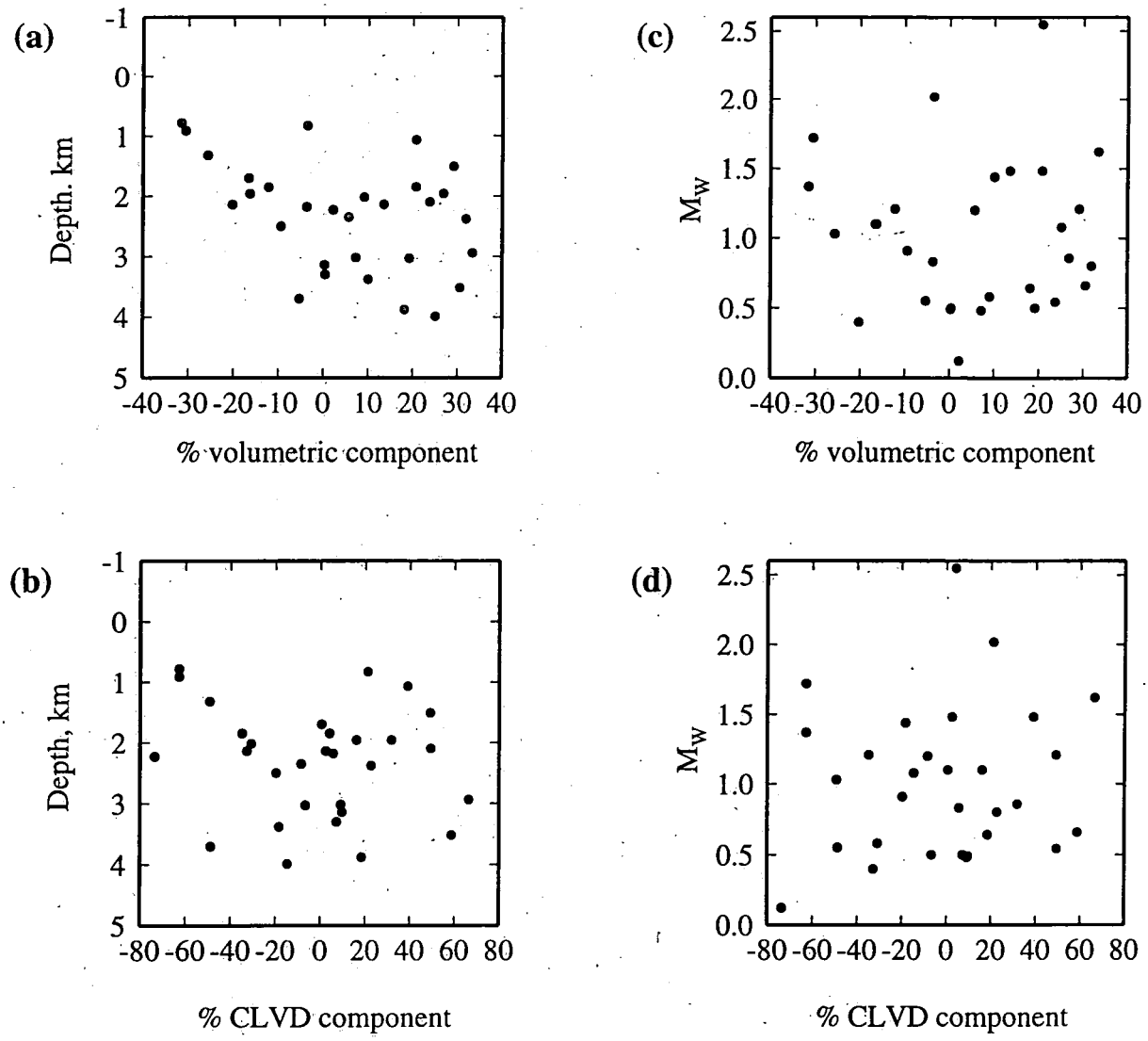

Figure 6.25. Variation of the (a) volumetric and (b) CLVD components of the 30 (solid dots) moment tensor solutions with depth. Variation of the (c) volumetric and (d) CLVD components of the 30 moment tensor solutions with M_W.

P- and *T*-axes have similar orientations.

The orientations of the *P*- and *T*-axes show considerable variation (Figure 6.26). The average plunges of both the *P*- and *T*-axes are shallow at 37° and 29° respectively. The *P*-axes have mostly azimuths ranging from northeast to northwest. The azimuths of the *T*-axes are even more variable. The orientations of *P*- and *T*-axes do not show evidence of depth dependence (Figure 6.27). At 2 km bsl the plunges of the *P*-axes vary from 0° to ~90° and those of the *T*-axes from 0° to ~50°.

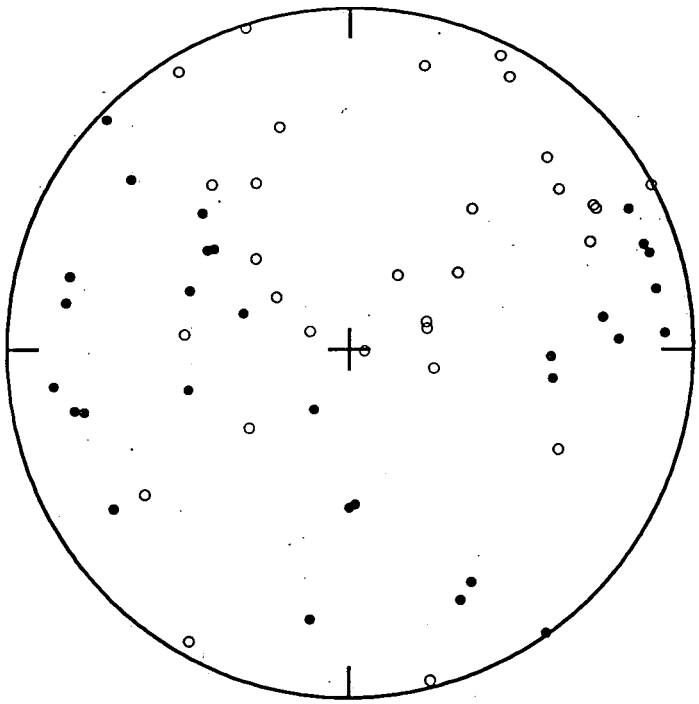

Figure 6.26. Equal-area, upper hemisphere projection showing *P*- (open dots) and *T*-axes (solid dots) orientations for the 30 events.

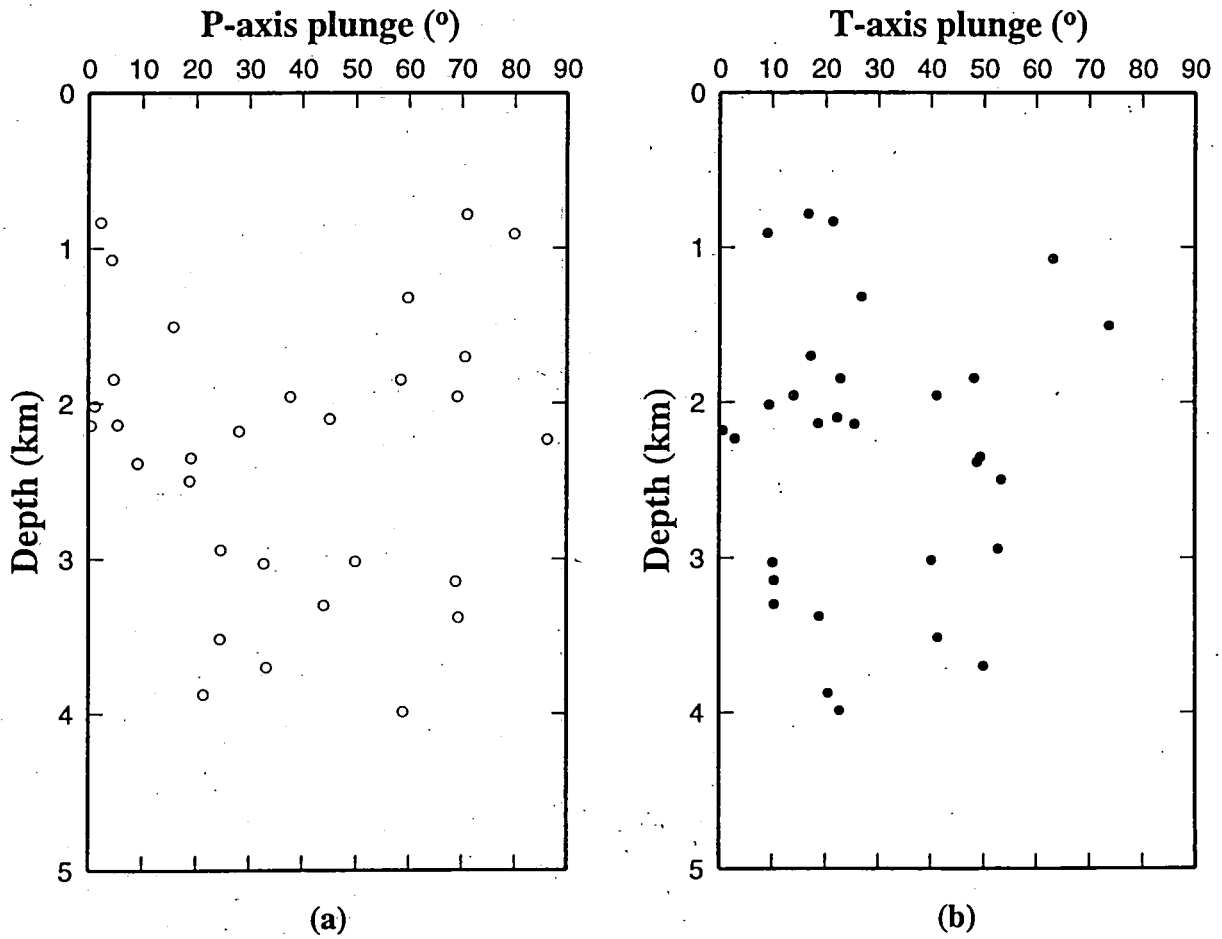

Figure 6.27. Plunge of (a) *P*-axes and (b) *T*-axes with depth for the 30 events.

6.6.5 Exploring physically-motivated extremes of the feasible solution vector

Many events presented in Section 6.5.4 have significant volumetric components. For events where the moment tensor is chosen randomly from the non-empty of solutions it is important to assess how the volumetric component of other solutions in this non-empty set vary. *focmec* can search the solution set for the moment tensor with the maximum or minimum trace. This is equivalent to maximising or minimising the positive volume change *i.e.*, obtaining moment tensors with maximum explosive and implosive components. The moment tensor can also be constrained to deviatoric.

Consider event 2 which has a feasible solution, well constrained with polarity and amplitude observations (Table 6.2). The maximum explosive and implosive solutions are similar to the initial solution and the event has a large positive volumetric component (Figure 6.28a, b and c; Table 6.3). Constraining the solution to be deviatoric produces a solution with considerable polarity and amplitude ratio violations (Figures 6.28d and e). This strongly suggests that event 2 has a significant explosive component. It also demonstrates that the range of feasible solutions is typically not large for these earthquakes.

Table 6.3 Moment tensor decomposition of event 2.

Moment tensor solution type	% volumetric component	% DC component	% CLVD component
Automatic initial feasible	30.48	10.87	58.65
maximum explosive	31.84	10.18	57.98
maximum implosive	29.74	16.00	31.75
deviatoric	0.00	98.21	1.79

6.7 Summary

Moment tensor solutions are calculated for 30 earthquakes in the central Geysers by inverting polarities and amplitude ratios using linear programming techniques. The distorting effect of the Earth's heterogeneity on seismic wave amplitudes is reduced by using amplitude ratios to constrain moment tensors. Moment magnitudes were calculated by inverting polarities and amplitudes to determine scalar moments. Polarities are specified as inequalities and both amplitudes and amplitude ratios as pairs of inequalities. Polarity and amplitude measurements were made on low-pass filtered seismograms to

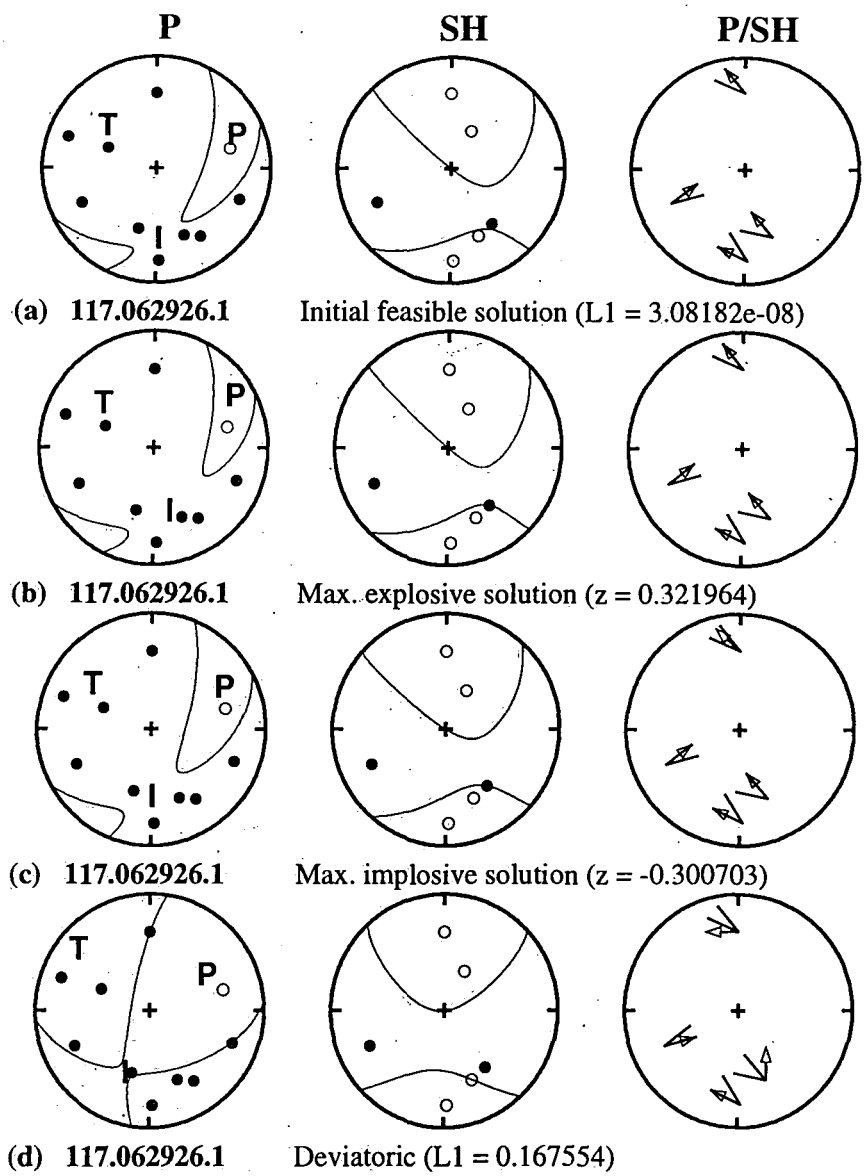

Figure 6.28. Focal mechanism solutions determined by *focmec* for event 2. Focal sphere plots labelled P, SH and P/SH shows the polarity and nodal surfaces for *P*-, *SH*-waves and observed amplitude ratio bounds and calculated amplitude ratios for the respective seismic phases. (a) Initial feasible solution. (b) Maximum explosive solution. (c) Maximum implosive solution. (d) Moment tensor solution constrained to be deviatoric.

remove complicated wave-propagation effects. Amplitude ratios are corrected for attenuation and free-surface effects, and amplitudes were additionally corrected for geometrical spreading. Rays are traced through three-dimensional wave-speed models. Uncertainties in amplitude measurements arising from background noise and unmodelled propagation effects were used to estimate appropriate error bounds.

The linear programming method is a powerful technique which can accurately

constrain moment tensor solutions with only a small number of polarity and amplitude ratio observations. Moment tensors for 30 earthquakes were constrained with an average of 20 polarity observations and 5 amplitude ratios. The largest moment magnitude is M_W=2.55. The resulting moment tensors form a band joining the ±Dipole loci and passing through the DC locus on a source-type plot. About 50% of the events have volumetric components exceeding 20% with equal proportions of explosive and implosive events. One event displays compressional arrivals only. About 27% of the earthquakes are deviatoric. There appears to be no temporal or depth dependence on the type of mechanism. *P*- and *T*-axes are highly variable with their orientations also independent of depth. Azimuths of *P*-axes range from northwest to northeast but the *T*-axes are even more variable.

Chapter 7

Discussion and conclusions

7.1 Commercial development of The Geysers geothermal area

The Geysers geothermal area is one of the largest steam fields in the world. Large scale commercial development commenced in 1960. Operators forecast an almost limitless future for the resource and saw little need to invest in research programs aimed at understanding the reservoir and processes within it. Development grew steadily until 1980, which was a critical turning point in the history of The Geysers. The success of the PGE/UNT partnership, coupled with government incentives encouraging development of alternative energy sources, saw an influx of new investors and developers. Against the advice of independent experts, who saw over-development of the resource a real possibility, growth in new capacity almost doubled annually. By 1989 The Geysers had a potential generating capacity of 2043 MW. Small declines in steam pressure have been known since the 1960s but they increased significantly in 1987. This irreversible decline increased such that today the actual electrical power generated is only two-thirds of the maximum installed capacity (1989). Better resource management, involving a sensible research program, could have predicted the impending decline and allowed steps to be taken to delay its onset. If production had been maintained at the 1980 level of 943 MW the 14 power generating plants might have been operating today at full strength and a lot of money saved (*Kerr*, 1991). Today, after the horse has bolted, developers and operators are seeking methods to mitigate the decline. To this end much of the proprietary information has been released to the scientific community.

Injection of condensate has largely been successful in maintaining well productivity with the steam temperature remaining steady even after prolonged periods of injection (*Enedy et. al.*, 1992). There are plans to substantially increase injection by using two pipelines to transplant partially treated sewage ("grey water") from nearby towns. The first of these will commence injecting at 200 kg/s in the southeast Geysers in spring 1997. This may be compared with 700 kg/s injected into the entire field in the 1980s. Condensate is reinjected at temperatures of 25-30° C. However, the treated sewage will be injected at much lower temperatures (<10° C). It remains to be seen whether this will raise the likelihood of water break-throughs at the base of production wells or whether the reservoir can sustain long term injection such as this.

7.2 Seismicity at The Geysers

7.2.1 Aseismic zones in The Geysers steam reservoir

Conspicuous aseismic volumes within the most seismically-active zone in the central Geysers are continuous in time (Figure 2.5). The most obvious of these is a thin <0.4 km horizon at about 3.0 km bsl separating the seismicity in the central Geysers into two vertically distinct zones (Figures 2.5, 5.14 and 5.15). This feature has been noted in other independent studies (*Oppenheimer*, 1986; *D. R. H. O'Connell, pers. comm.*). Earthquakes recorded by the dense network in the northwest Geysers also show vertical bimodalism suggesting the aseismic horizon extends into this area (Figure 7.1a) (*Romero et al.*, 1994). This feature is absent in the southeast Geysers (Figure 7.1b) (*Romero et al.*, 1994). The aseismic areas probably result from presence of slices of less fractured rock within the reservoir.

7.2.2 Seismicity: A direct relation to commercial production activities

Commercial production activities induce earthquakes at The Geysers. The nature of this relationship with its environmental implications is currently a hot-bed of debate (Section 7.2.3). My work has produced two kinds of evidence which show that seismic activity at The Geysers is not only intimately related to, but perhaps controlled by, commercial activity. Epicentral maps of earthquakes recorded by CALNET between 1975-95 show that seismicity initiates in areas surrounding newly installed generating units (Figure 2.6). These areas return to their pre-exploitation aseismic state once production has ceased (Section 2.4).

I infer a linear relationship between earthquake occurrence and the volume of steam extracted (Section 2.4). However, the volume of water reinjected mirrors the

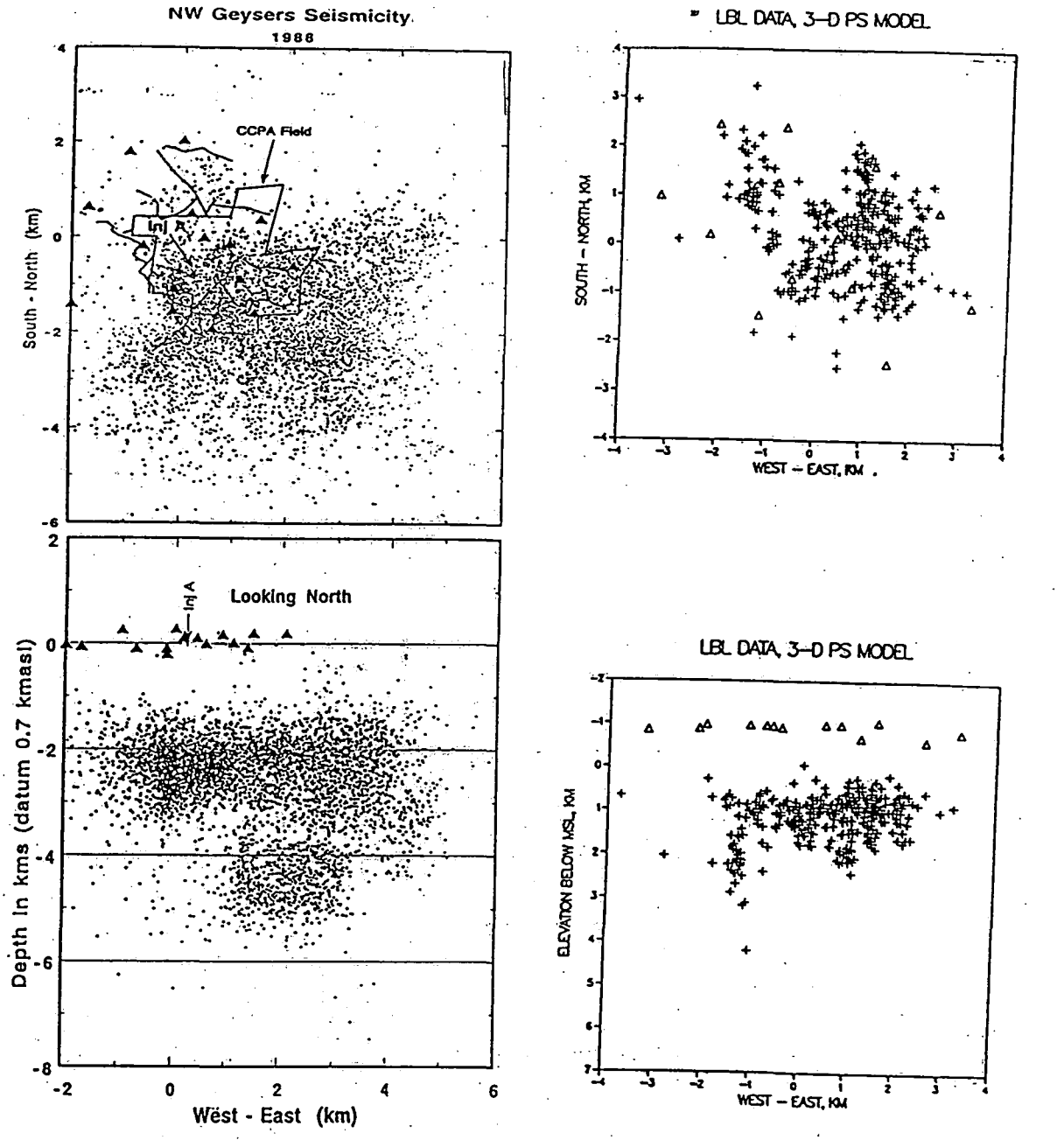

(a) (b)

Figure 7.1. Maps and west-east cross-sections of seismicity in (a) the northwest Geysers for 1988 and , (b) the southeast Geysers for 1994, from *Romero et al.* (1994). For the northwest Geysers; dots: earthquake locations; solid triangles: seismic stations. For the southeast Geysers; crosses: earthquakes locations; open triangles: seismic stations.

volume extracted so one could conclude equally well that the level of earthquake activity is sensitive to the volume of injected water. This is supported by the fact that activity in The Geysers was very much less prior to exploitation and from this it may be concluded that the seismicity rate in the steam field will reduce significantly when production ceases, probably approaching the pre-exploitation level .

7.2.3 The effect of increased injection

In a number of independent studies of seismicity at The Geysers earthquakes have been found to cluster around injection wells. Explanations for this phenomenon have included localised chilling of rocks converting the mode of deformation from ductile to brittle and reduction in the normal stresses across fracture surfaces enabling slip at lower shear stresses. The column of water in the injection well can also communicate considerable pressures to the well base producing an increase in pore-pressure in the reservoir enabling failure by the Hubbert and Rubey mechanism (*Stark*, 1992; *Hubbert and Rubey*, 1959). The Geysers generates on average about 120 M_D>1.2 earthquakes per month. The increased volume of water injected into the reservoir when the new pipelines start has the potential to generate perhaps 30-40 more of these earthquakes. This might be a good opportunity to find out which of the commercial activities is the more dominant process for inducing earthquakes because if injection increases without increasing production but is accompanied with increases in seismicity then the degree to which injection controls seismicity may be deduced.

7.2.4 Commercial development at The Geysers: Political implications

The Geysers geothermal area was considered to be a model alternative energy resource. It was cheap, and thought to be pollution free and limitless. In recent years, however, there has been growing public opposition to further development of this resource. The local population have reported larger earthquakes occurring at more frequent intervals in recent years, resulting in property damage. They have been concerned that the construction of the two new pipelines to increase injection may produce even larger earthquakes which could represent seismic hazard. They are also concerned about the effects of injecting treated sewage into the reservoir may have on the ecology of the surrounding area.

Operators are reluctant to accept that their activities induce earthquakes. With mounting evidence to the contrary they suggest that the induced earthquakes are very small and do not pose a public hazard. Unfortunately, or fortunately depending on your perspective, there is little possibility of independently investigating this matter. The

present permanent networks operating in continuous mode are inadequate. A more efficient network and a research team dedicated to the task is required.

7.3 The 1991 field experiment

The Geysers field experiment of April, 1991 recorded continuous digital seismic data at a high rate. This was the first experiment of this kind and had been deemed an impossible goal in professional circles at the time. Despite obvious operational and logistical difficulties the experiment was a complete success. Event lists compiled from an event triggering stream indicated that many events would have been missed by a triggered mode of field operation.

Over the 31-day recording period 3906 high-quality earthquakes were recorded. The average daily rate of activity varied enormously, ranging from 75-286 earthquakes with an average of 163. There is no apparent pattern to this daily activity on a field-wide scale. However, local changes in seismicity associated with the onset of injection are now well-documented (*Stark*, 1988). Earthquakes are induced on some occasions after a lag of only days.

Continuous recording mode, although labour intensive, is now the preferred field operation strategy used in short-duration experiments. In time, with field equipment designed specifically to operate in continuous mode, and equipped with larger recording disks, the logistics of such experiments will be greatly simplified.

7.4 Data processing and LET modelling procedures and strategies

7.4.1 Software development

In the course of LET modelling a suite of computer programs was developed to assist with data processing, wave-speed modelling and graphical presentation of the results. Many were designed with a broader application and can be used with SIMULPS12 in any LET study.

It took about 15 months to complete data processing and test the various inversion strategies before the final models presented in Chapter 5 were produced. The software developed enabled a Durham MSc student to successfully process and model a second earthquake data set from The Geysers in only three months (Section 7.5.4). This gives an indication of the efficiency afforded by the programs.

7.4.2 Rotating seismograms

Computer programs which numerically rotate horizontal seismograms from their field orientations were in the development stage when the LET work was done. *S*-phase identification and measurement was clearly enhanced by rotating seismograms in the focal mechanism study (Chapter 6). The *S*-phase arrivals used in LET studies were generally clear and impulsive so changes to measured arrivals made on unrotated and rotated traces tended to be small, and less than the picking error. Remeasuring the *S*-waves would therefore have little effect on the final wave-speed models presented in Sections 5.2.5 and 5.2.6. This is however a useful step and should be included as a standard processing procedure for LET studies in future.

7.4.3 Inversion strategies

The literature offers a range of inversion strategies likely to produce reasonable final models (*Evans et al.*, 1994; *Eberhart-Phillips*, 1993). I tested many of these variations. Wave-speed models giving the largest reduction in RMS travel-time residual are not necessarily the best since this can be achieved by simply reducing damping. In the present study careful consideration was given to model stability, if the result was geologically reasonable and to the inversion strategy used. Some inversions are labour and computationally intensive but the resulting models may produce only a small improvement in model fit over simpler inversions. The final models presented in Sections 5.2.5 and 5.2.6 used the minimum one-dimensional v_P model derived by VELEST and improved v_P/v_S ratio estimate as starting models. The three-dimensional v_P/v_S model was inverted for the two finest nodal configurations only.

The direct inversion strategy is fast, taking about a day to complete. A graded inversion initially took two to three weeks to complete. Familiarity with both the procedure and programs reduced this to about 4 days. The most computationally expensive parts of the inversion procedure, particularly for the finest nodal configurations, are the one-iteration inversion runs used to determine damping trade-off curves. These can take up to three times longer than the actual inversion for velocity structure. I improved work efficiency by running these overnight. The graded inversion strategy produced much better structural detail and significantly better final RMS travel-time residuals compared to the direct inversion. In other areas, however, wave-speed models generated by the direct inversion approach were preferred as they gave smoother models and acceptable RMS travel-time residuals (*Miller*, 1996).

A comparison was made of models obtained by a) inverting for v_P/v_S at every stage in the graded inversion, b) finest grid and c) at the two finest nodal configurations only.

Very similar v_P/v_S models were obtained from all these strategies but b) and c) required considerably less computation time. Inverting at more stages produced models with enhanced structural detail compared to the model generated by inverting v_P/v_S at the final grid only.

Wave-speed models generated using different starting models were almost identical. Reasonable initial one-dimensional models adequately model the major features of the velocity structure.

The location and ray-tracing routines of SIMULPS12 adequately recover poorly-located hypocentres. Final wave-speed models appear to be insensitive to the accuracy of initial hypocentre and travel-time residual estimates. In a test inversion initial event locations were forced 1 km deeper than their optimum locations and travel-time residuals recalculated. SIMULPS12 recovered >80% of the discrepancy in the first relocation interaction. The subsequent graded inversion produced almost identical wave-speed models with the final RMS travel-time residual differing by <0.18%.

Differences in the models generated by subsets of the total data set recorded on the three seismometer networks are due primarily to the different station distributions. The v_P model is much more susceptible to differences than the v_P/v_S model. The UNT data set has a smaller number of *S*-wave arrivals, with stations distributed over a smaller geographical area than the temporary network. This explains the lower final RMS travel-time residual for models derived using data recorded by the UNT network.

Vertical nodal planes are normally aligned parallel and perpendicular to the tectonic fabric since this is thought to provide better constraint *e.g.*, on faults. What is less clear is how well SIMULPS12 can resolve these features when vertical nodes do not align. This is important for LET studies in areas where the tectonics are poorly understood. I performed an inversion in which the vertical nodal planes were rotated by 45° from their conventional orientations so that they were no longer aligned parallel and perpendicular to the tectonic fabric. The final models were very similar and the strong velocity contrast across Collayomi fault coincided exactly with that modelled in inversions using the conventional grid. This is an important finding and suggests that if there is a sufficient velocity contrast then major tectonic boundaries and structures will be faithfully imaged by LET irrespective of the orientation of vertical planes of nodes.

In my experience there is no easy method to generate tomographic models and I must therefore echo the sentiments of experienced practitioners. Each study area is unique and one should proceed cautiously, testing both the performance of the SIMULPS12 program and the data used.

7.5 Interpretation of the three-dimensional wave-speed models

7.5.1 Introduction

Interpretation of tomographic images is difficult and it is best to regard them as transforms of the data, not pictures of the Earth (*Evans et al.*, 1994). The Geysers is a very complex area with a diverse mix of rock types which can change dramatically over a short distance and which have very different seismic characteristics. Model resolution is about 1 km and therefore only gross structural details may be recovered.

Some v_P models present absolute velocity variations (*Zucca et al.*, 1993) while others show perturbations in v_P for each model layer (*Miller*, 1996; *Romero et al.*, 1995). I prefer the latter method as it is more useful for interpreting spatially-distinct velocity anomalies that are a significant feature of volcanic and geothermal areas. In contrast the v_P/v_S model is much smoother and varies little with depth. Absolute v_P/v_S values were thus presented.

7.5.2 The v_P model

The accuracy of any derived v_P model is always a concern and can only be quantified by comparison with a more accurate model. The maximum resolution of the v_P model presented in Section 5.2.5 is about 1 km and probably this is much smoother than the truth. Of other tomography studies at The Geysers, that of *Zucca et al.* (1994) (hereafter called "the Zucca model") is probably the best, having a high resolution (0.6 km) v_P, and using a large data set of earthquakes well-recorded by the UNT network (Section 4.4). The Zucca model is completely enclosed within the well-resolved portion of the v_P model derived in the present study (Figure 7.2). For a direct comparison model layers in the Zucca model were interpolated to the same depth slices and perturbations from mean layer velocity are presented rather than absolute values (Figure 7.2). The Zucca model appears to have many more isolated anomalies and this may be a consequence of lower damping values or the finer model grid of 0.6 km. The models are broadly similar.

Between the Mercuryville and Collayomi fault zones v_P is systematically about 10% lower in the northwest Geysers than the central area at all resolvable depths. This anomaly locates within the steam reservoir and probably reflects variations in the lithology, temperature or increased compressibility of the pore fluid. The steam reservoir consists of a thin, normal reservoir overlying a HTR which is restricted to this area. Temperature can effect the elasticity of minerals which in turn can cause changes in the seismic wave-speeds. The HTR is ~100° C hotter than the normal reservoir but this could only account

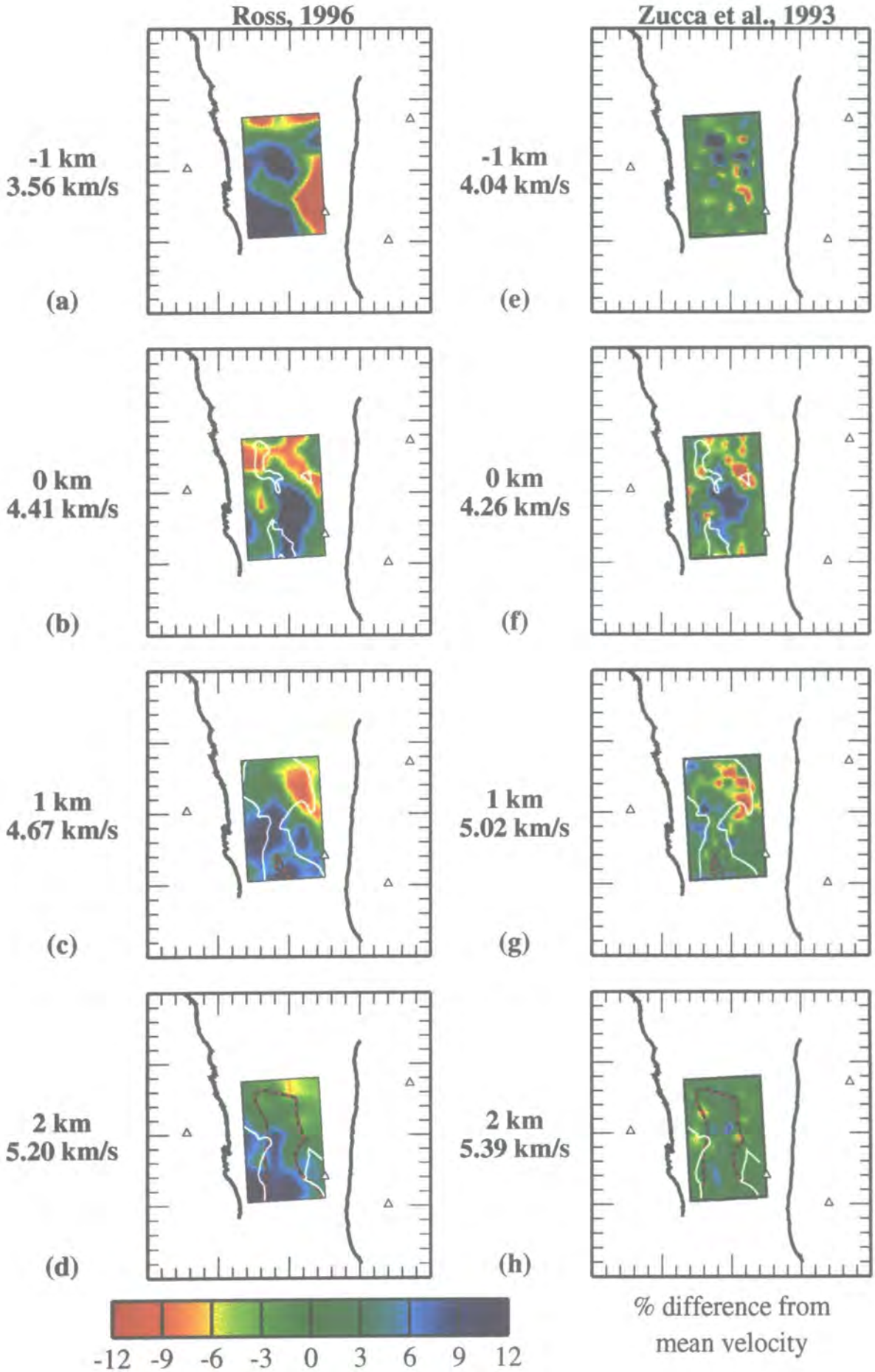

Figure 7.2. Maps showing the variations in v_p from mean for the model generated in the present study (a-d) and from Zucca et al. (1994) (e-h). Only areas of the v_p model from the present study which overlap with the Zucca model area are presented. The Zucca model is interpolated to the same depths. White lines: steam reservoir; dashed black and red lines: felsite batholith; white triangles: mountains; black lines: faults.

for about 3% of the anomaly. Higher gas concentrations in the northeast could also produce velocity decreases (*Romero et al.*, 1995). *Zucca et al.*, (1993) suggests the felsite and indurated reservoir greywacke should have roughly equivalent velocities but because the felsite is likely to be less fractured it may have a slightly higher velocity. Blotchy (*sic*) high velocities are tentatively associated with the felsite body (*Zucca et al.*, 1993). The weak velocity contrast with the greywacke may explain this blotchy nature The felsite body correlates with high velocities in my model but with a larger model volume than Zucca it is clear that this association is non-unique (Figure 5.8c).

The uppermost layer (1 km asl) is completely above the reservoir and should be influenced mostly by surface geology. Of particular interest is the shallow, circular-shaped low-velocity anomaly centred on Cobb Mtn. and low-velocity anomalies to the northeast of the Collayomi fault (Figures 5.8a-d and 5.9e-g). Cobb Mtn. is a volcanic plug and the low-velocity anomaly correlates almost perfectly with mapped units of Clear Lake volcanics (Figure 1.13). The feature is not resolved at depth. Shallow low-velocity anomalies correlating with similar geological features in other volcanic areas have been interpreted as a product of weathering, where surface fractures provided conduits for meteoric water to invade the surface layers (*J. R. Evans, pers. comm.*) Fractures in Cobb Mtn. may provide paths for precipitation to recharge the steam reservoir (*Truesdale et al.*, 1993) and it therefore seems likely that the low velocities are also a product of a similar weathering process.

Low-velocity anomalies are also imaged at all resolvable depths northeast of the Collayomi fault. The shallow anomalies again correlate with the Clear Lake Volcanics. The Collayomi fault zone is a steeply-dipping structure and slices of ophiolite are juxtaposed along it (Figure 1.13). Ophiolite extends under the Clear Lake volcanics northeast of the fault. Steep velocity gradients correlate exactly with the mapped surface trace of the Collayomi fault (Figures 5.8a-d and 5.9e-g). This feature is a major tectonic boundary which has been well constrained in v_P considering its proximity to the periphery of the well-resolved area. Ophiolite is a reasonable choice for the source of the low velocities anomalies at depth. In contrast the Mercuryville fault has no equivalent seismological signature despite evidence for slices of ophiolite within the fault zone. The slices of ophiolite may be too small to be resolved seismologically or the Mercuryville fault zone may have a weaker geometry with respect to the seismic rays that sample it, as it is dipping to the east and not vertical like the Collayomi fault zone (see cross-sections B-B' and C-C', Figure 1.13).

7.5.3 The v_P/v_S model

This is the first three-dimensional model of the v_P/v_S structure derived for

The Geysers geothermal area (Figures 5.10 and 5.11). There is a striking correlation between low v_P/v_S anomalies up to –9% and the geothermal reservoir at all well-resolved depths. A halo of high v_P/v_S ratio surrounds the reservoir. The low v_P/v_S anomaly does not extend as far as the reservoir to either the northwest or the southeast but this discrepancy is real. Although in the southeast it might appear as an artefact of limited resolution, independent LET studies in the southeast Geysers have also imaged the low v_P/v_S anomaly terminating at the same location (*A. Kirkpatrick, pers. comm.*) One can conclude, therefore, that the low-v_P/v_S anomaly corresponds to the most intensely exploited part of the reservoir between sea-level and at least 2 km bsl.

Some of the relevant factors that influence v_P/v_S include fluid saturation, pore-pressure, pore fluid phase, temperature, partial melt and confining pressure (see *Miller*, 1996 and *Romero et al.*, 1993 for a review). Increased saturation raises v_P/v_S while under-saturation (dry or gas-filled fractures) depresses it (*Toksoz et al.*, 1976; *Nur and Simmons*, 1969). Laboratory experiments have determined the behaviour of v_P/v_S with changes in pore pressure (*Ito et al.*, 1979) and changes in temperature (*Spencer and Nur*, 1976). Acoustic velocities were measured for a water-filled Berea sandstone with variable pore-pressure at constant temperature (*Ito et al.*, 1979). The pressure and temperature conditions spanned the liquid-vapour phase transformation boundary, mimicking changes that may occur in a steam reservoir. v_P/v_S decreases as the liquid in the pore-space changes from liquid to vapour because v_P decreased at a higher rate than v_P/v_S (Figure 7.3). Increasing the temperature of a saturated sample of Westerly Granite produced a decrease in v_P/v_S since v_P decreases with temperature while v_S is relatively unaffected (*Spencer and Nur*, 1976). Partial melt increases v_P/v_S (*Mavko*, 1980). v_P/v_S decreases with depth as a result of increased confining pressure (*Nickolson and Simpson*, 1985; *Walck*, 1988; *Thurber and Atre*, 1993). For homogenous rock this has been attributed to the closing of cracks produced by increased confining pressure.

In the northwest Geysers, high v_P/v_S values were attributed to a saturated, shallow condensation zone above the reservoir (*Romero et al.*, 1995). Low v_P/v_S values at 1-3 km bsl correlate with the steam zone. Low v_P/v_S anomalies up to –4% in the Hengill-Grensdalur Volcanic area, Iceland, were explained as a combination of factors including decreased pore fluid pressure, increased steam content and silicic alteration products.

Table 7.1 gives estimates of the v_P/v_S anomalies that would be caused by differences in pore-fluid phase, temperature, and pore pressure, for rocks with porosities of zero and 0.02, the approximate value in the reservoir (*Julian et al.*, 1996). For zero porosity, the v_P/v_S ratio equals that of the rock matrix and the effects of pressure and temperature are much too small to contribute significantly to the observed anomaly. At finite porosities the compressibility of the pore fluid strongly affects v_P/v_S. The largest effect is caused by replacement of liquid by vapour, although the dependence of vapour

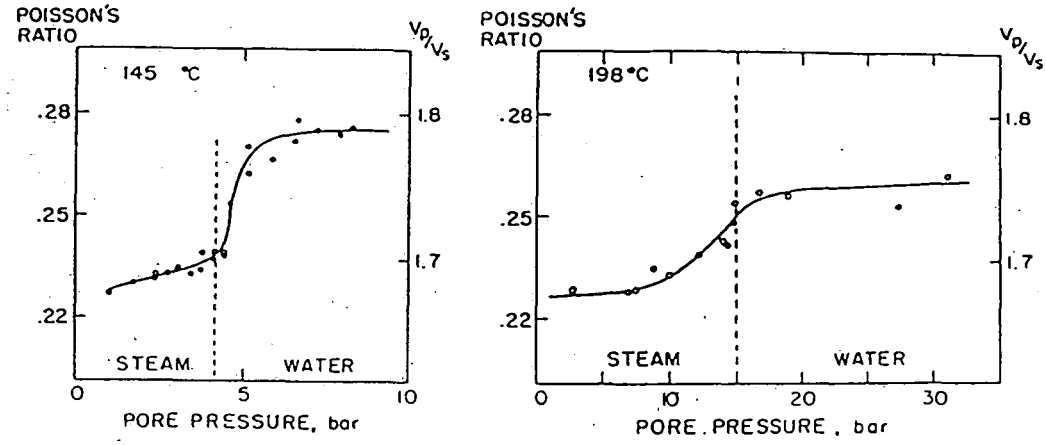

Figure 7.3. Graphs showing the variation of Poisson's ratio and the v_P/v_S ratio as the pore-fluid pressure traverses the liquid-vapour transition for a sample of Berea sandstone at temperature of (a) 145° C, and (b) 198° C (from *Ito et al.*, 1979).

Table 7.1. Theoretical v_P/v_S anomalies (from *Julian et al.*, 1996).

Cause	Porosity ϕ	
	0	0.02
Liquid → Vapour	0.00%	−14.00%
$\Delta T = +10^{\circ}$ C (Liquid)	−0.06%	−1.70%
$\Delta T = +10^{\circ}$ C (Vapour)	−0.06%	+0.10% to +0.68%
$\Delta P = -1$MPa (Liquid)	+0.004%	−0.20%
$\Delta P = -1$MPa (Liquid)	+0.004%	−6.6% to −10.0%

ΔT: Temperature change
ΔP: Pressure change

compressibility on temperature and pressure is also significant.

The low v_P/v_S anomaly at The Geysers is probably caused mostly by vapour in the rock pores. The magnitude of the anomaly in 1991 (–9%) could be explained entirely by relative dryness of the reservoir compared with the surrounding rocks. Drilling has confirmed the absence of partial melt in the upper 4 km of the Geysers reservoir. The reservoir was vapour-rich in its natural state, whereas the surrounding rocks are not, so the reservoir may have had a large v_P/v_S anomaly before exploitation began.

Production will have worked to increase the magnitude of the anomaly and increase its extent, by boiling away interstitial liquid and decreasing steam pressure. Between 1968 and 1988, borehole pressures decreased by as much as 2.0 MPa in places,

and they vary spatially by more than 1.0 MPa, which could cause v_P/v_S variations of 6.6% or more (*Barker et al.*, 1992). The two largest pressure minima coincide with the two v_P/v_S minima found at depths of 0 and 1 km from tomography (Figure 7.4). High temperatures in the northwest Geysers cannot explain the low v_P/v_S there, because the temperature effect is very small.

Although pore fluid properties affect the v_P/v_S ratio primarily by changing v_P the anomaly is not clear in the v_P field alone (Figure 5.8). This is doubtless because variations of v_P due to lithology dominate and conceal the second-order anomalies due to variations in pore fluid state.

I infer that decreases in both liquid saturation and pressure produced by industrial exploitation of The Geysers steam field can be measured seismologically. This represents an intriguing finding that could allow seismologists to remotely monitor the expansion of the steam zone at The Geysers in time by measuring temporal variations in v_P/v_S. This amounts to performing pseudo four-dimensional seismics with LET, and has considerable potential for industrial application.

This hypothesis was tested in 1995 by a Durham MSc. student (C. C. Grant) who performed a LET inversion of earthquake data recorded in December 1994, 3.7 years after the initial Geysers experiment. I worked closely with Grant on the project and the work was done using my software and experience (Section 7.5.4).

7.5.4 Monitoring depletion of a steam reservoir using pseudo four-dimensional LET

Earthquake data recorded by the UNT network in December 1994 was used to generate three-dimensional models of v_P and v_P/v_S. These results are compared with wave-speed models derived in the 1991 inversion to reveal interim changes in the reservoir (*Foulger et al.*, 1996).

The 1994 data set consists of 163 earthquakes, 2522 *P*- and 656 *S*-wave arrival times. This inversion used the same processing procedures, initial velocity model, inversion strategies, and nodal configuration. The v_P and v_P/v_S models generated in a 1991 inversion using earthquakes recorded on the UNT network only are compared with the 1994 results (Figure 7.5). That data set consisted of 163 events, 2268, P-waves and 226 S-waves.

The 1994 v_P/v_S model images a strong low v_P/v_S anomaly correlating with the most intensely exploited part of the reservoir (Figure 7.5). The anomaly became stronger by about 0.07 (4%) and increased spatially in the intervening 3.7 years (Figure 7.6). When compared with the full inversion of all the 1991 data (Figure 5.10) an even higher-amplitude and spatially more extensive increase in the v_P/v_S anomaly is obtained.

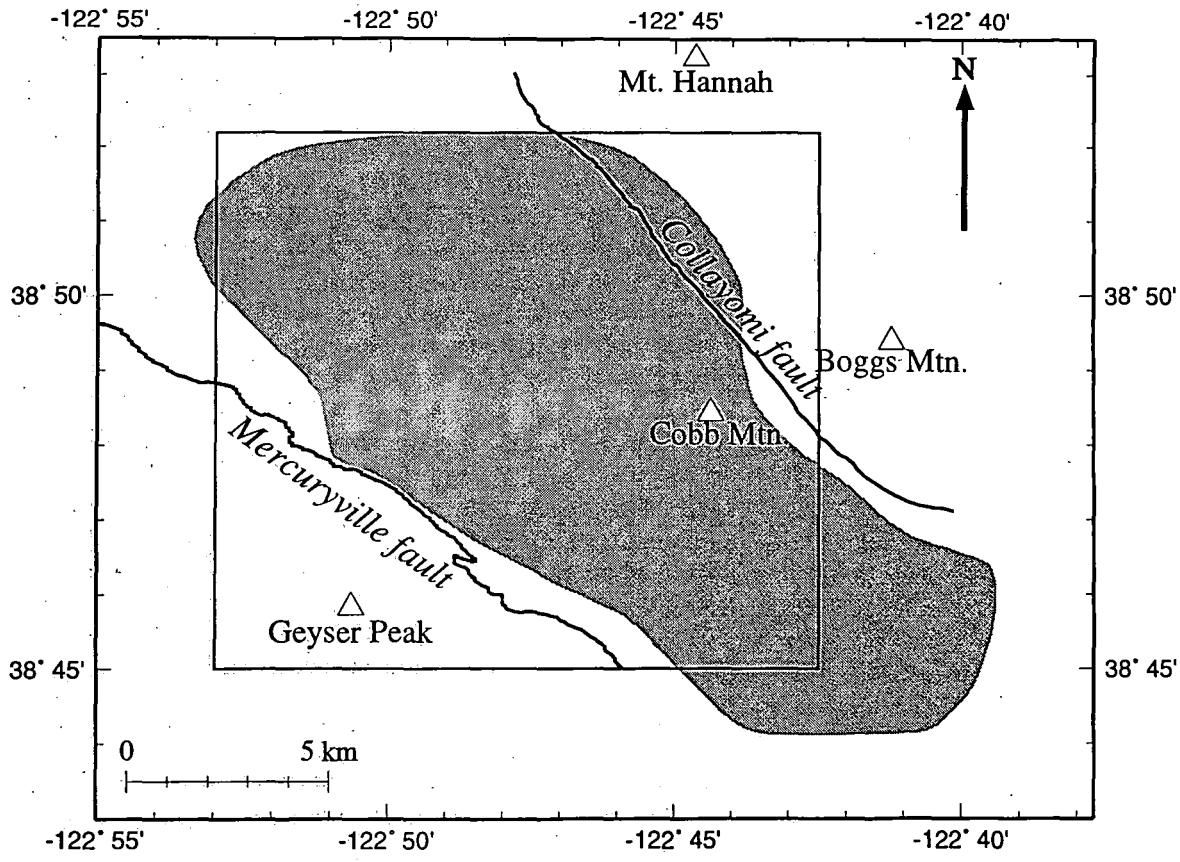

(a)

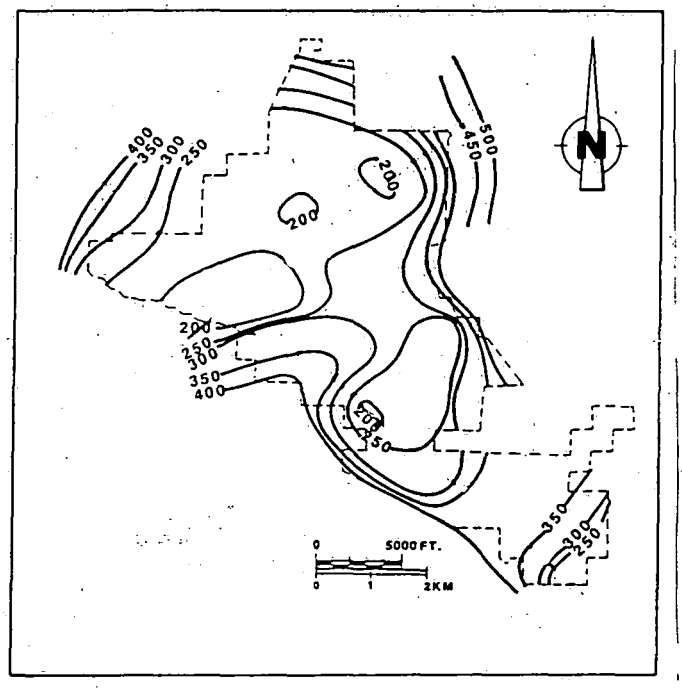

(b)

Figure 7.4. (a) Location map of The Geysers geothermal area. The box defines the area shown in (b), an isobaric map of steam pressures at sea-level with in the reservoir for 1988, contours are in pounds per square inch, *Barker et al.* (1992).

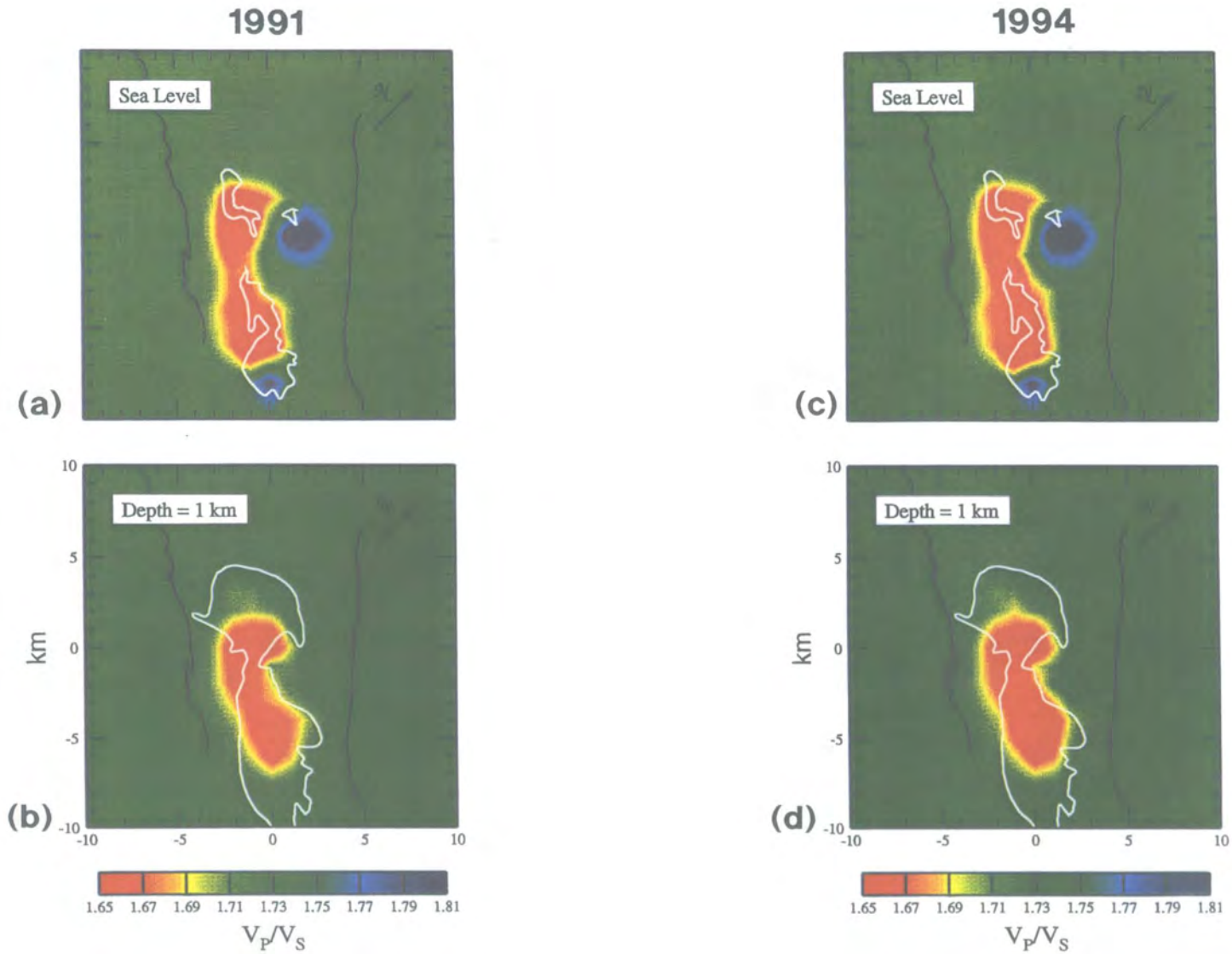

Figure 7.5. Maps of the v_P/v_S ratio at two well-resolved depths for April, 1991 (a and b) and December, 1994 (c and d) (from Foulger et al., 1996). Only data from UNT stations were used. White lines: boundary of steam reservoir; black lines: faults.

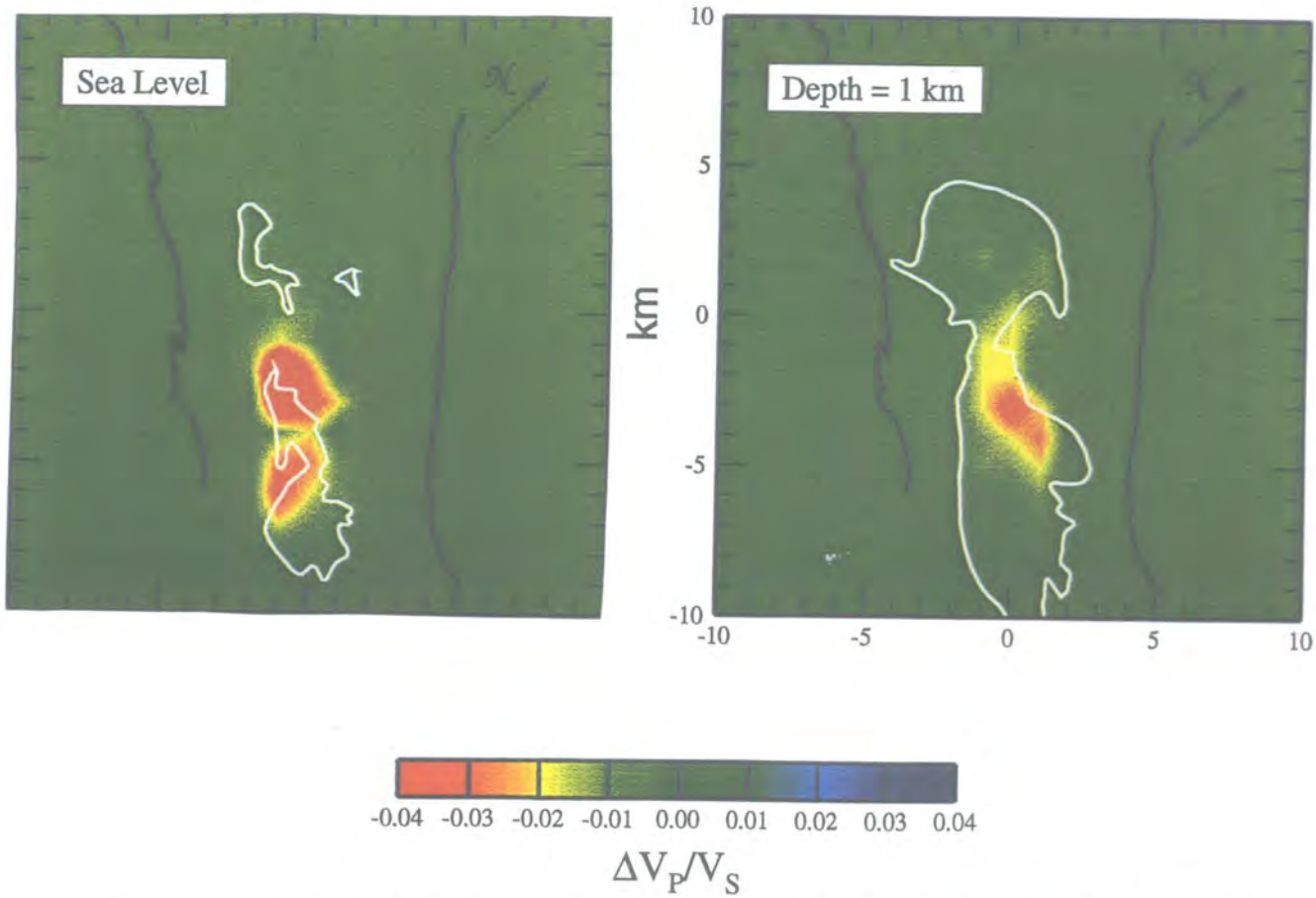

Figure 7.6. Maps showing the difference in (a) Figures 7.4a and c, and (b) Figures 7.4b and d. This shows the change in the v_P/v_S ratio between 1991 and 1994 (from *Foulger et al.* (1996)).

The change in the v_P/v_S anomaly is most likely a result of continued decreasing pressure and further depletion of the remaining pore water between 1991 and 1994. This is consistent with the sparse published information based on well data. An increase of 25° C in the water-saturated reservoir could theoretically produce the observed change in v_P/v_S but the reservoir temperature remained constant between 1991-95 (*M. A. Stark, pers comm.*). These results demonstrate that seismic tomography can be used to monitor temporal depletion of geothermal reservoirs and perhaps other systems where gas and liquid exchange takes place.

7.5.5 Earthquake location errors

Location errors are both random and systematic. Random errors may be assessed using the RMS travel-time residuals. These uncertainties are the most commonly quoted in the literature but they are lower bounds on the true uncertainties because they reflect only random observational errors. Systematic errors arise, for example, when one-

dimensional crustal models are used but the true structure is significantly three-dimensional. Three-dimensional wave-speed models substantially reduce this problem.

Suggested standard horizontal and vertical location errors for the regional one-dimensional v_P model I used are $\pm$0.4 km and $\pm$0.7 km respectively (Section 3.3.2) (*Eberhart-Phillips and Oppenheimer*, 1984). This model located a shot point in the southeast Geysers to a horizontal accuracy of 0.3 km. No information about the model performance in the vertical was given. In the present study most earthquakes were recorded by at least 35 stations, about half of which had three-component sensors. With a much larger number of stations in the geothermal area and the inclusion of *S*-wave data, event locations must be much more accurate than those of *Eberhart-Phillips and Oppenheimer* (1984) who used CALNET data only.

Relocation vectors and improvements in RMS travel-time residuals, obtained using the three wave-speed models are given in Tables 7.2 and 7.3. The horizontal median relocation vector for events located with the regional one-dimensional and three-dimensional models is five times that for the regional and minimum one-dimensional models due to larger systematic errors associate with one-dimensional models (Table 7.2). In contrast the median vertical relocation vector for the regional and minimum one-dimensional models is of similar magnitude for events located with regional one-dimensional and three-dimensional models.

A conservative estimate is that the three-dimensional wave-speed models presented here reduce location errors from the one-dimensional model by 50% with a further 50% remaining due to systematic error. Final horizontal and vertical location errors may then be about $\pm$0.2 km.

7.6 Moment tensors

7.6.1 Introduction

High-quality seismic data inverted using more sophisticated data analysis techniques can reveal radiation patterns incompatible with DC force systems. Such mechanisms have been routinely determined in earthquake studies of some volcanic and geothermal systems (*e.g.*, *Arnott and Foulger*, 1994a, b; *Miller et al.*, 1996; *Miller*, 1996).

The Geysers geothermal field is a likely source of non-DC earthquakes because large volumes of steam are extracted and condensate reinjected in the course of commercial exploitation. These processes might cause the opening or closing of cracks and cavities.

Table 7.2.. Median horizontal and vertical relocation vectors for the 296 hand-picked earthquakes using three wave-speed models.

Models used	Median relocation vector, km	
	horizontal	vertical
Regional and minimum one dimensional	0.057	0.170
One dimensional regional and three-dimensional	0.290	0.210

Table 7.3. Final RMS travel-time residuals for earthquakes located with three wave-speed models.

Model	RMS travel-time residual, s			% difference from regional one-dimensional model
	P-wave	*S*-wave	Total	
Regional one-dimensional model	0.054	0.113	0.077	0.0 0.0 0.0
Minimum one-dimensional model	0.053	0.113	0.069	3.0 16.0 10.0
Three-dimensional models	0.041	0.075	0.058	24.0 44.0 25.0

Earthquake focal mechanisms from The Geysers which did not fit a DC interpretation have in the past been disregarded even though upwards of 10-15% of solutions have polarities of one type covering the focal sphere with polarity fields devoid of data assumed to derive a DC result (*Julian et al.*, 1993; *Oppenheimer*, 1986; Appendix 2).

7.6.2 Moment tensor results

Non-DC earthquakes are convincingly determined in The Geysers by this study. On a source-type plot events define a zone extending from the +Dipole through the DC to the -Dipole locus with a symmetrical spread (Figure 6.12). Events with a positive volumetric component generally have a positive CLVD component while events with negative volumetric components have negative CLVD components. A similar study in the Hengill-Grensdalur volcanic area, Iceland produced a very different distribution on the source-type plot (Figure 7.7) (*Miller*, 1996). Earthquakes tended to have moment tensors with dominantly explosive volumetric component which occupy both the +CLVD and -

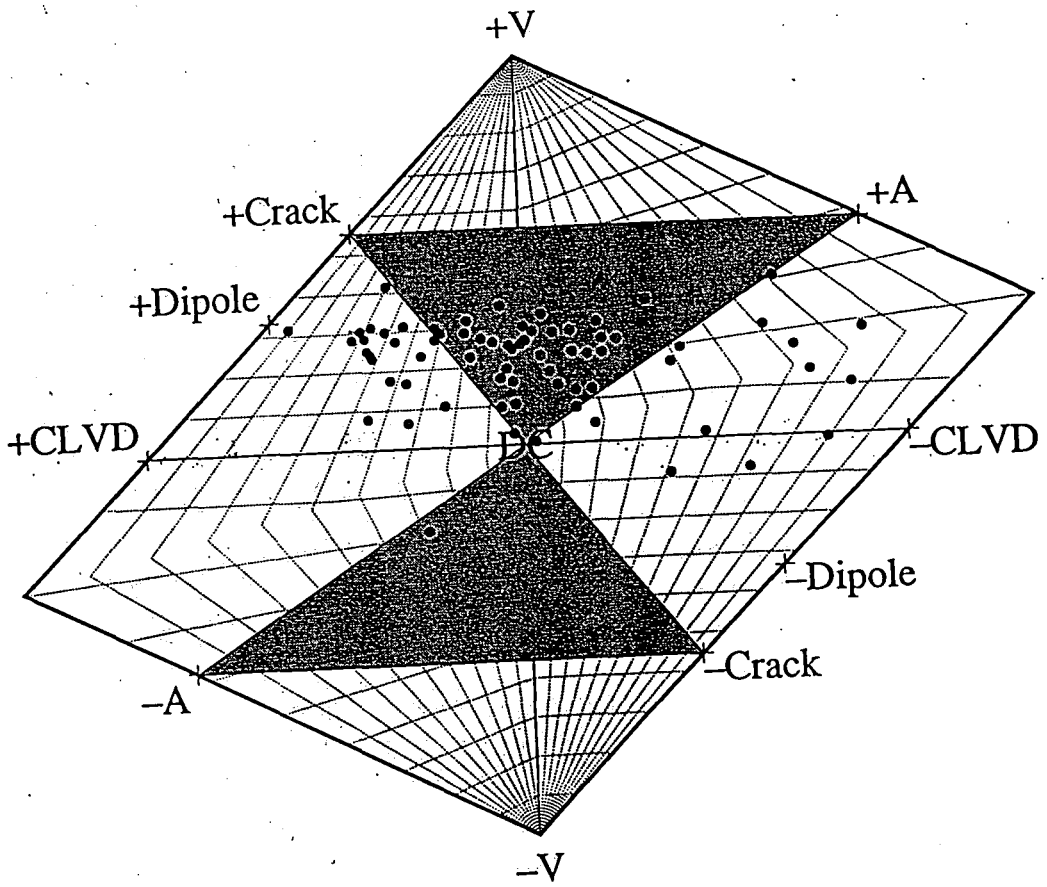

Figure 7.7. Source type plot showing the distribution of moment tensors (solid dots) for 70 earthquakes from the Hengill-Grensdalur volcanic area, Iceland (from *Miller et al.*, 1996). Shaded area: area of plot where moment tensors may be explained as a combination of a DC and a tensile fault.

CLVD quadrants. *Miller* (1996) explained these results as the combination of a DC and +Crack, and implied the observed deviation from the DC+Crack locus was largely data error. That study used the same processing technique as The Geysers study and therefore if this was true a similar distribution would be expected for The Geysers events. Clearly this is not so (*c.f.* Figure 6.12 and 7.7). This suggests that the CLVD components in the Hengill-Grensdalur results are not all error.

Source processes in the Hengill-Grensdalur volcanic area, Iceland must be different from those at The Geysers geothermal area. This may be because of different reservoir processes associated with that two-phase reservoir and natural heat loss compared to The Geysers which is steam dominated and under intense commercial exploitation. Different ambient stress fields in the two fields may also be a contributing factor.

The Hengill-Grensdalur area lies in a spreading segment and thus has a strong

extensional stress field. The Geysers lies within the shear stress regime associated with the San Andreas Fracture Zone.

Crack or cavity opening or closing is required to produce volumetric earthquakes. Such processes could be caused by increases in pore-pressure due to injected fluid and thermal contraction. Sudden local increases in pore-pressure caused by superheated water flashing to steam may generate explosive events and simultaneously produce implosive events by compressing adjacent fractures (*Kirkpatrick et al.*, 1996). Fracture deflation due to mass steam withdrawal is another possible generator of implosive events. Many of the volumetric events at The Geysers must also involve the compensating flow of fluids, because their moment tensors form a distribution around the ±Dipole locus, not the ±Crack locus. In the case of The Geysers mobile fluids must be responsible.

Explosive mechanisms produced by increased pore-pressure might be expected to correlate with injections wells and consequently implosive events with steam production wells. No such definitive correlation appears to exist (*Ross et al.*, 1996). Spatially-and temporally-coincident events can have very different mechanisms, events 17 and 24 are good examples (Figure 6.16, 6.17 and 6.18). In the southeast Geysers implosive and explosive events occurred in both areas of injection and production (*Kirkpatrick et al.*, 1996).

7.6.3 Constraining moment tensors

Only a few stations are required to constrain moment tensors well if three-component data are available (Section 6.6.3). A similar test in the Hengill-Grensdalur volcanic area, Iceland found moment tensors better constrained by polarity and amplitude observations from 10 stations than by only polarity observations from 30 *P*-wave polarity observations (*Miller*, 1996). This suggests that many of the earthquakes with only a few polarity and amplitude ratio observations in the present study may be better constrained than initially thought, *e.g.*, event 25; Figure 6.22. Inverting polarity and amplitude ratio data using the linear programming method provides a robust method for determining moment tensor solutions and is particularly applicable to areas were station coverage is sparse. Station coverage in the centre of the focal sphere could have been improved had instrument polarities of the UNT network been known (Figure 7.8).

7.7 Future work

Possibilities for future work arising from this study include:

- Further tomographic inversions for data from different years to assess changes in the

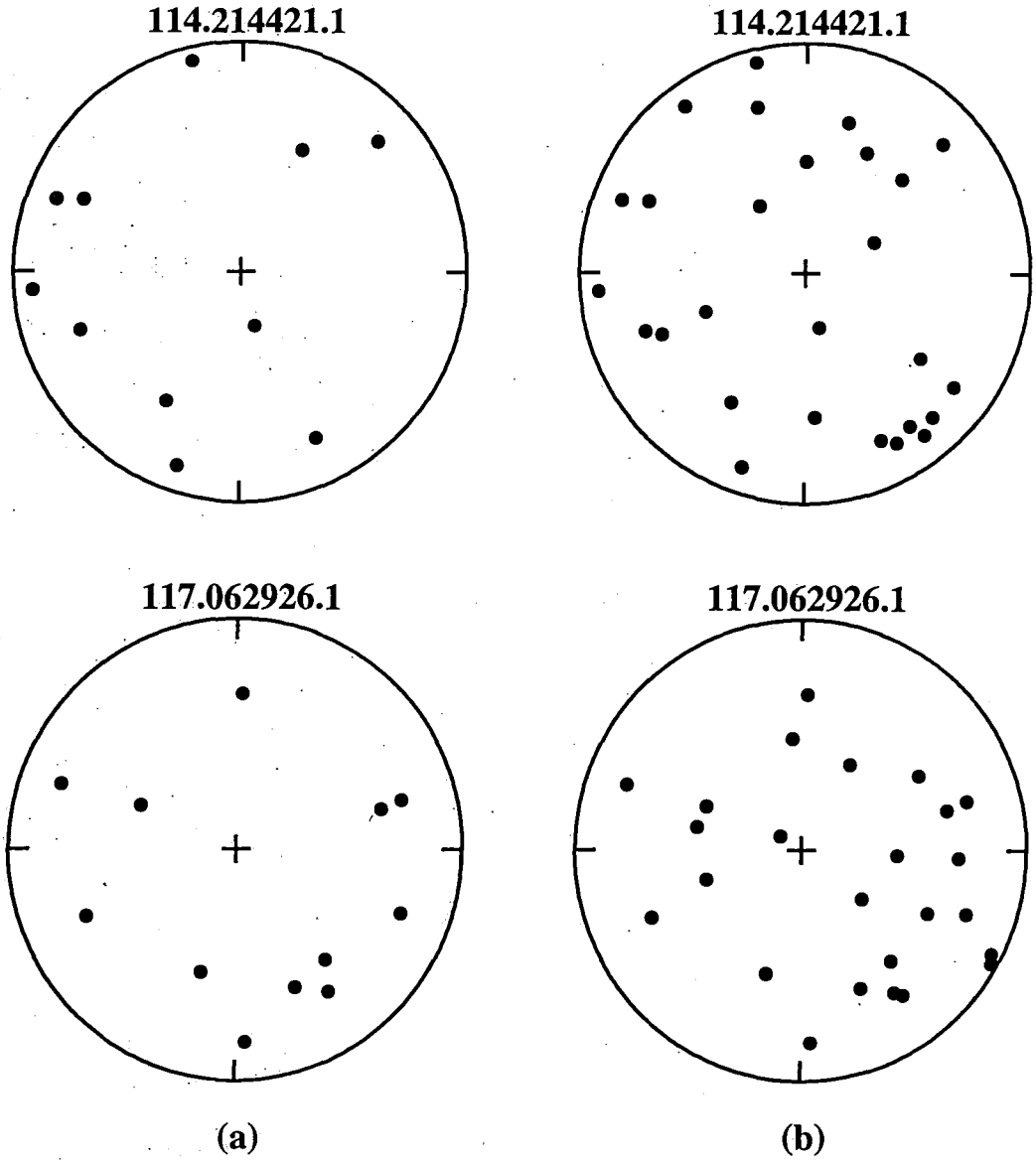

Figure 7.8. Focal sphere coverage for events 114.214421 and 117.062926.1. Solid dots indicate where polarity observations would map on the focal sphere for stations in (a) the temporary and CALNET networks, and (b) the temporary, CALNET and UNT networks.

reservoir.

- More focal mechanism solutions to add data points to the source-type plots.
- Master event relocations for earthquakes in the many seismic clusters.

- The recent release of extensive proprietary data on well locations, production and injection data enables in depth analysis of earthquake and production correlations.

- Calibrate changes in v_P/v_S with reductions in steam pressure and/or levels of liquid saturation within the exploited zone. Proprietary data on production, injection, reservoir conditions and well logs will greatly assist this.

- A more rigorous treatment of scalar moments so that moment magnitudes are determined directly.

- Formal assessment of the error budget in the focal mechanism solutions.

7.8 Conclusions

The principal conclusions are:

- Earthquakes are induced at the onset of production, continue during it and stop when production ceases.

- The number of induced earthquakes may be linearly related to either the volume of steam extracted, water injected or a combination of both.

- Three-dimensional wave-speed models of The Geysers geothermal area now provide highly accurate earthquake locations.

- Fluid deficient areas of the steam field can be imaged by v_P/v_S.

- Temporal depletion of liquid reserves in the steam reservoir can be remotely monitored by v_P/v_S.

- Non-DC earthquakes are induced at The Geysers geothermal.

- Explosive and implosive non-DC earthquakes occur in equal numbers producing an asymmetrical pattern on source-type plots about the positive and negative dipole loci suggesting the source process must involve the compensating flow of fluids.

References

Aki, K., A. Christoffersson and E. S. Husebye, Determination of the three-dimensional seismic structure of the lithosphere, *J. Geophys. Res.*, **82**, 2977-2986, 1977

Aki, K. and W. H. K. Lee, Determination of three-dimensional velocity anomalies under a seismic array using first P arrival times from local earthquakes, I, A homogeneous initial model, *J. Geophys. Res.*, **81**, 4381-4399, 1976

Aki, K. and P. G. Richards, *Quantitative Seismology, vol 1*, Freeman, New York, 557 pp., 1980.

Allis, R. G., Mechanism for induced seismicity at The Geysers geothermal reservoir, California, *Geophys. Res. Lett.*, **9**, 629-632, 1982

Apperson, K. D., Stress fields of the overriding plate at convergent margins and beneath active volcanic arcs, *Science*, **254**, 670-678, 1991

Arnott, S. K. and G. R. Foulger, The Krafla spreading segment, Iceland 1. Three-dimensional crustal structure and the spatial and temporal distribution of local earthquakes, *J. Geophys. Res.*, **99**, 23801-23825, 1994a.

Arnott, S. K., and G. R. Foulger, The Krafla spreading segment, Iceland 2. The accretionary stress cycle and non-shear earthquake focal mechanisms, *J. Geophys. Res.*, **99**, 23827-23842, 1994b.

Arnott, S. K. *A Seismic Study of the Krafla Volcanic System, Iceland*, Ph.D. Thesis, pp 283, University of Durham, England, 1990.

Atwater, T., Implications of plate tectonics for the Cenozoic tectonic evolution of western north America, *Geol. Soc. Am. Bull.*, **81**, 3513-3536, 1970

Barker, B. J., M. S. Gulati, M. A. Bryan and K. L. Riedel, Geysers reservoir performance, in Stone, C., ed., *Geothermal Resources Council Special Report,* **17**, 167-177, 1992

Batini, F., R. Console and G. Luongo, Seismological study of Larderello-Travale Geothermal area, *Geothermics*, **14**, 255-272, 1985

Benz, H. M., G. Zandt and D. H. Oppenheimer, Lithospheric structure of northern California from teleseismic images of the upper mantle, *J. Geophys. Res.*, **97**, 4791-4807, 1992

Blakely, R. J. and W. D. Stanley, The Geysers magma chamber, California: constraints from gravity data, density measurements, and well information, *Geothermal Resources Council Transactions*, **17**, 227-233, 1993

Castillo, D. A. and W. L. Ellsworth, Seismotectonics of the San Andreas fault system between Point Arena and Cape Mendocino in northern California; Implications for the development and evolution of a young transform, *J. Geophys. Res.*, **98**, 6543-6560, 199

Chapman, R. H., Gravity map of The Geysers area, California, *California Division of Mines and Geology Special Report*, **19**, 148-149, 1966

Chapman, R. H., Geophysical study of the Clear Lake region, California, *California Division of Mines and Geology Special Report*, **116**, 1-23, 1975b

Chatterjee, S. N., A. M. Pitt, and H. M. Iyer, v_P/v_S ratios in the Yellowstone National Park region, Wyoming, *J. Vol C. Geotherm. Res.*, **26**, 213-230, 1985

Clarke, S. H., Geology of the Eel River Basin and adjacent region: Implications for late Cenozoic tectonics of the southern Cascadia subduction zone and Mendocino triple junction, *AAPG Bull.*, **76**, 199-224, 1992

Cockerham, R. S., Evidence for a 180-km-long subducted slab beneath northern California, *Bull. Seismol. Soc. Am.*, **74**, 569-576, 1984

Crosson, R. S., Crustal structure modelling of earthquake data 1. Simultaneous least squares estimation of hypocentre and velocity parameters, *J. Geophys. Res.*, **81**, 3036-2046, 1976

Dahlheim, H. -A., P. M. Davis and U. Achauer, Teleseismic investigation of the east African rift, Kenya, *J. Afr. Earth Sci.*, **8**, 461-470, 1989

Davis, P. M., E. C. Parker and J. R. Evans, Teleseismic deep sounding of the velocity structure beneath the Rio Grande rift, in *New Mexico Geological Survey Guidebook*, 35th Field Conference, New Mexico Geological Survey, Socorro, New Mexico, 29-38, 1984

Dawson, P. B., J. R. Evans and H. M. Iyer, Teleseismic tomography of the compressional-wave velocity structure beneath the Long Valley region, California, *J. Geophys. Res.*, **95**, 11,021-11050, 1990

Denlinger, R. P. and R. L. Kovach, Seismic reflection investigations at Castle Rock Springs in The Geysers geothermal area, in *U.S. Geological Survey Professional paper 1141*, 117-128, 1981

Denlinger, R. P., Seismicity induced by steam production at The Geysers steam field in northern California (abstract), *EOS Trans. AGU*, **61**, 1051, 1980

Denlinger, R. P. and C. G. Bufe, Reservoir conditions related to induced seismicity at The Geysers steam reservoir, northern California, *Bull. Seismol. Soc. Am.*, **72**, 1317-1327, 1982

Dueker, K., E. Humphreys and G. Biasi, Teleseismic imaging of the western United States upper mantle structure using the simultaneous iterative reconstruction technique, in *Seismic Tomography*, edited by H. M. Iyer and K. Hirahara, 265-298, 1993

Eberhart-Phillips, D. M., Three-dimensional velocity structure in Northern California Coast ranges from inversion of local earthquake arrival-times, *Bull. Seis. Soc. Am.*, **76**, 1025-52, 1986.

Eberhart-Phillips, D., Investigations of crustal structure and active tectonic processes in

the Coast ranges, central California, *Ph.D. Thesis*, Stanford University, Stanford, California, 1989

Eberhart-Phillips, D., Local earthquake tomography: earthquake source regions, in *Seismic Tomography*, edited by H. M. Iyer and K. Hirahara, 613-643, 1993

Eberhart-Phillips, D. and D. H. Oppenheimer, Induced seismicity in The Geysers geothermal area, California, *J. Geophys. Res.*, **89**, 1191-1207, 1984

Einarsson, P., *S*-wave shadows in the Krafla caldera in northeast Iceland, evidence for a magma chamber in the crust, *Bull. Volcanol.*, **41**, 1-9, 1978

Ellsworth, W.L., Three-dimensional structure of the crust and mantle beneath the Island of Hawaii, Ph.D. Thesis, Massachusetts Institute of Technology, Cambridge, MA, 1977

Enedy, S. L., K. L., Enedy and J. Maney, Reservoir response to injection in the southwest Geysers, *Geothermal Resources Council Special Report*, **17**, 211-219, 1992

Evans, J. R., D. Eberhart-Phillips and C. H. Thurber, Users manual for *SIMULPS12* for imaging v_P and v_P/v_S: A derivative of the "Thurber" tomographic inversion *SIMUL3* for local earthquakes and explosions, *U. S. Geol. Surv. Open File Rep.*, 80-1060, 1-50, 1994

Evans, J. R., B. R. Julian, G. R. Foulger and A. Ross, Shear-wave splitting from local earthquakes at The Geysers Geothermal Field, California, *Geophys. Res. Lett.*, **22**, 501-504, 1995

Foulger, G. R. and D. R. Toomey, Structure and evolution of the Hengill-Grensdalur central volcano complex, Iceland: Geology, geophysics and seismic tomography, *J. Geophys. Res.*, **94**, 17,511-17,522, 1989

Foulger, G. R. and S. K. Arnott, Local tomography: volcanoes and the accretionary plate boundary in Iceland, in *Seismic Tomography*, edited by H. M. Iyer and K. Hirahara, 644-672, 1993

Foulger, G. R., A. D. Miller, B. R. Julian and J. R. Evans, Three-dimensional v_P and v_P/v_S structure of the Hengill Triple Junction and geothermal area, Iceland, and the repeatability of tomographic inversion, *Geophys. Res. Lett.*, **22**, 1309-1312, 1995

Foulger, G. R., C. C. Grant, A. Ross and B. R. Julian, Changes in structure at an exploited geothermal reservoir, California, in press, *Geophys. Res. Lett.*, 1996

Foulger, G. R. and R. E. Long, Anomalous focal mechanisms: Tensile crack formation on an accreting plate boundary, *Nature*, 310, 43-45, 1984.

Frazier, C. W., Discrete time solution of plane *P-SV* waves in a plane layered medium, *Geophysics*, **35**, 197-219, 1970

Furlong, K. P., W. D. Hugo and G. Zandt., Geometry and evolution of the San Andreas fault zone in northern California, *J. Geophys. Res.*, **94**, 3100-3110, 1989

Furlong, K. P., Thermal-rheologic evolution of the upper mantle and the development of

the San Andreas fault system, *Tectonophysics*, **223**, 149-164, 1993

Goyal, K. P., Injection recovery factors in various areas of the southeast Geysers, *Geothermics*, **24**, 167-186, 1995

Gunderson, R. P., Porosity of reservoir greywacke at The Geysers, in Stone, C., ed., *Geothermal Resources Council Special Report,* **17**, 89-93, 1992

Harris, R. A., H. M. Iyer and P. B. Dawson, Imaging the Juan de Fuca plate beneath southern Oregon using teleseismic *P*-wave residuals, *J. Geophys. Res.*, **96**, 19,879-19,889, 1991

Hawley, B. W., G. Zandt and R. B. Smith, Simultaneous inversion for hypocentres and lateral velocity variations: an iterative solution with a layered model, *J. Geophys. Res.*, **86**, 7073-7076, 1981

Hearn, B. C., J. M. Donnelly and F. E. Goff, Geology and chronology of the Clear Lake Volcanics, California, *U.N. symposium on development and use of geothermal resources*, San Francisco, Proceedings, **1**, 423-428, 1976b

Hearn, B. C., J. M. Donnelly-Nolan and F. E. Goff, The Clear Lake volcanics: Tectonic setting and magma sources, in *U.S. Professional Paper 1141, Research in The Geysers-Clear Lake Geothermal Area, Northern California*, 25-45, 1981

Hill, D. P., J. P. Eaton and L. M. Jones, Seismicity, 1980-86, *U.S. Geological Survey Professional Paper,* 1515, in The San Andreas fault system, California (ed. R. E. Wallace), 115-151, 1990

Hirahara, K., Three-dimensional seismic structure beneath southwest Japan: the subducting Philippine Sea plate, *Tectonophysics*, **79**, 1-44, 1981

Hubbert, M. K. and W. W. Rubey, Role of fluid pressure in mechanics of overthrust faulting, *Geol. Soc. Am. Bull.*, **70**, 115-166, 1959

Hudson, J. A., R. G. Pearce and R. M. Rogers, Source type plot for inversion of the moment tensor, *J. Geophys. Res.*, **94**, 765-774, 1989

Hulen, J. B. and D. L. Nielson, Interim report on geology of The Geysers felsite, northwestern California, *Geothermal Resources Council Transactions*, **17**, 249-258, 1993

Isherwood, W. F., Gravity and magnetic studies of The Geysers - Clear Lake geothermal region, California, *Second United Nations Symposium on Development and Use of Geothermal Resources, San Francisco, CA, Proceedings*, **2**, 1-65-1073, 1975b

Isherwood, W. F., Gravity and magnetic studies of The Geysers-Clear Lake geothermal region, *U.N. symposium on development and use of geothermal resources*, San Francisco, Proceedings, **2**, 1065-1073, 1976

Isherwood, W. F., Geophysical overview of The Geysers: in *U.S. Professional Paper 1141, Research in The Geysers-Clear Lake Geothermal Area, Northern California*, 83-96, 1981

Ito, H., J. De Vilbiss, and A. Nur, Compressional and shear waves in saturated rock during water-steam transition, *J. Geophys. Res.*, **84**, 4731-4735, 1979

Iyer, H. M. and R. B. Dawson, Imaging volcanoes using teleseismic tomography, in *Seismic Tomography*, edited by H. M. Iyer and K. Hirahara, 466-492, 1993

Iyer, H. M., D. H. Oppenheimer, T Hitchcock, J. N. Roloff and J. M. Coakley, Large *P*-wave delays in The Geysers-Clear Lake geothermal area, *U.S. Professional Paper 1141, Research in The Geysers-Clear Lake Geothermal Area*, Northern California, 97-116, 1981

Jachens, R. C. and A. Griscom, Three-dimensional geometry of the Gorda plate beneath northern California, *J. Geophys. Res.*, **88**, 9375-9392, 1983

Julian, B. R., A. D. Miller and G. R. Foulger, Non-shear focal mechanisms of earthquakes at The Geysers, California, and Hengill, Iceland, geothermal areas, *Geothermal Resources Council Transactions*, **17**, 123-128, 1993

Julian, B. R., Analysing seismic-source mechanisms by linear-programming methods, *Geophys. J. R. astr. Soc.*, **84**, 431-443, 1986

Julian, B. R. and G. R. Foulger, Earthquake mechanisms from linear-programming of seismic-wave amplitude ratios, *Bull. Seismol. Soc. Am.*, **86**, 972-980, 1996

Julian, B. R., A. Ross, G. R. Foulger and J. R. Evans, Three-dimensional seismic image of a geothermal reservoir: The Geysers, California, *Geophysical Res. Lett.*, **23**, 685-688, 1996

Julian, B. R. and G. R. Foulger, Preliminary report on 1991 microearthquake survey at The Geysers geothermal area, California, unpublished manuscript, 4 pp, 1992a

Julian, B. R. and G. R. Foulger, Preliminary report on 1991 microearthquake survey at the Hengill-Grensdalur geothermal area, Iceland, unpublished manuscript, 4 pp, 1992b

Julian, B. R. and D. Gubbins, Three-dimensional seismic ray-tracing, *J. Geophys.*, **43**, 95-113, 1977

Kennedy, B. M. and A. H. Truesdale, Active degassing in the NW Geysers High-temperature reservoir, *Geothermal Resources Council Transactions*, **18**, 325-330, 1994

Kerr, R. A., Geothermal tragedy of the commons, *Science*, **253**, 134-135, 1991

Kirkpatrick, A., J. E. Peterson and E. L. Majer, Microearthquake monitoring at the southeast Geysers using a high-resolution digital array, *Proc. 20th Workshop in Geotherm. Reservoir Engineering*, Stanford University, 79-89, 1995

Kirkpatrick, A., J. E. Peterson and E. L. Majer, Source mechanisms of microearthquakes at the southeast Geysers geothermal area, *California, Proc. 21st Workshop in Geotherm. Reservoir Engineering*, Stanford University, 1996

Kissling, E., Geotomography with local earthquake data, *Rev. Geophys.*, **26**, 659-698, 1988.

Kissling, E., W.L. Ellsworth, D. M. Eberhart-Phillips and U. Kradolfer, Initial reference models in local earthquake tomography, *J. Geophys. Res.*, **99**, 19,635-19,646, 1994

Knopoff, L. and M. J. Randall, The compensated linear vector dipole: a possible mechanism for deep earthquakes, *J. Geophys. Res.*, **75**, 4957-4963, 1970

Lange, A. L. and W. H. Westphal, Microearthquakes near The Geysers, Sonoma County, California, *J. Geophys. Res.*, **74**, 4377-4378, 1969

Lawson, C. L. and R. J. Hanson, (eds) Solving least squares problems, Prentice-Hall, Englewood Cliffs, New Jersey, 1974

Lees, J. M. and R. S. Crosson, Tomographic inversion for three-dimensional velocity structure at Mount St. Helens using earthquake data, *J. Geophys. Res.*, **94**, 5716-5728, 1989

Li, X.-D and T. Tanimoto, Waveform inversion of long period seismic data for structure, in *Seismic Tomography*, edited by H. M. Iyer and K. Hirahara, 64-91, 1993

Lin, C. H. and S. W. Roecker, Determination of earthquake hypocentres, focal mechanisms, and velocity structure in the Morgan Hill area through three-dimensional circular ray tracing, *EOS, Trans. Am. Geophys. Un.*, **71**, 1445, 1990

Lofgren, B. E., Monitoring crustal deformation in The Geysers-Clear Lake region, in *U.S. Geological Survey Professional Paper 1141, Research in The Geysers-Clear Lake Geothermal Area, Northern California*, 139 - 148, 1981

Ludwin, R. S., V. Cagnetti and C. G. Bufe, Comparison of seismicity in The Geysers geothermal area with the surrounding region, *Bull. Seismol. Soc. Am.*, **72**, 863-871, 1982

Ludwin, R. S. and C. G. Bufe, Continued seismic monitoring of The Geysers, California geothermal area, *U.S. Geolgical Survey Open File Report*, 80-1060, 50 pp., 1980

Majer, E. L. and T. V. McEvilly, Seismological investigations at The Geysers geothermal field, *Geophysics*, **44**, 246 - 268, 1979

Majer, R. J., T. V. McEvilly, F. Eastwood and L. Myer, Fracture detection using *P*- and *S*-wave VSPs at The Geysers, *Geophysics*, **53**, 76-84, 1988

Marks, S. M., R. S. Ludwin, K. B. Louie and C. G. Bufe, Seismic monitoring at The Geysers geothermal field, California, *U.S. Geolgical Survey Open File Report*, 78-798, 26 pp., 1978

Mavko, G. M., Velocity and attenuation in partially molten rocks, *J. Geophys. Res.*, **85**, 5173-5189, 1980

McLaughlin, R. J., Tectonic setting of pre-Tertiary rocks and its relation to geothermal resources in The Geysers-Clear Lake area, in *U.S. Professional Paper 1141, Research in The Geysers-Clear Lake Geothermal Area*, Northern California, 3-24, 1981

Menke, W. V., V. Levin and R. Sethi, Seismic attenuation in the crust at the min-Atlantic ridge plate boundary in south-west Iceland, *Geophys. J. Int..*, **122**, 175-182, 1995

Michelini, A. and T. V. McEvilly, Seismological studies at Parkfield. I. Simultaneous inversion for velocity structure and hypocentres using cubic B-splines parameterisation, *Bull. Seismol. Soc. Am.*, **81**, 524-552, 1991

Miller, A. D, Seismic structure and earthquake focal mechanism of the Hengill volcanic complex, SW Iceland, Ph.D. Thesis, pp208, University of Durham, England, 1996

Miller, A. D, G. R. Foulger and B. R. Julian, The Hengill-Grensdalur volcanic complex, S.W. Iceland: 2. Earthquake focal mechanisms, submitted to *J. Geophys. Res.*, 1996

Morelli, A., Teleseismic tomography: core-mantle boundary, in *Seismic Tomography*, edited by H. M. Iyer and K. Hirahara, 163-189, 1993

Nicholson, C. and D. W. Simpson, Changes in v_P/v_S with depth: implications for appropriate velocity models, improved earthquake locations, and material properties of the upper crust, *Bull. Seismol. Soc. Am.*, **75**, 1105-1123,1985

Nur, A. and G. Simmons, The effect of saturation on velocity in low porosity rocks, *Earth Planet. Sci. Lett.*, **7**, 183-193, 1969

O'Connell, Seismic velocity structure and microearthquake source properties at The Geysers, California, geothermal area, *Ph.D.* Thesis, University of California, Berkeley, California, 1986

O'Connell D. R. H. and Johnson L. R., Second-Order moment tensors of microquakes at The Geysers geothermal field, California, *Bull. Seismol. Soc. Am.*, **78,** 1674-1692, 1988

Oppenheimer, D. H., Extensional tectonics at The Geysers geothermal area, California, *J. Geophys. Res.*, **91**, 11,463-11,476, 1986

Oppenheimer, D. H. and J. P. Eaton, Moho orientation beneath central California from regional earthquake travel times, *J. Geophys. Res.*, **96**, 6,223-6,236, 1984

Oppenheimer, D. H. and K. E. Herkenhoff, Velocity-density properties of the lithosphere from three-dimensional modelling at The Geysers-Clear Lake region, California, *J. Geophys. Res.*, **86**, 6,057-6,065, 1981

Pavlis, G. L., Progressive inversion, Ph.D. Thesis, University of Washington, Seattle, Washington, 1982

Pavlis, G. L. and J. R. Brooker, The mixed discrete-continuous inverse problem: Application to the simultaneous determination of earthquake hypocentres and velocity structure, *J. Geophys. Res.*, **85**, 4801-4810, 1980

Rasmussin, J. and E. D. Humphreys, Tomographic image of the Juan de Fuca plate beneath Washington and western Oregon using teleseismic *P*-wave travel times, *Geophys. Res. Lett.*, **12**, 1417-1420, 1988

Romero, A. E., T. V. McEvilly, E. L. Majer and D. Vasco, Characterisation of the

geothermal system beneath the northwest Geysers steam field, California, from seismicity and velocity patterns, *Geothermics*, **24**, 471-487, 1995

Romero, A. E., A. Kirkpatrick, E. L. Majer and J. E. Peterson, Seismic monitoring at The Geysers geothermal field, *Geothermal Resources Council Trans*actions, **18**, 331-338, 1994

Romero, A. E, JR., T. V. McEvilly and E. L. Majer, Velocity structure of the Long Valley Caldera from the inversion of local earthquake *P* and *S* travel times, *J. Geophys. Res.*, **98**, 19,869-19,879, 1993

Ross, A., G. R. Foulger, and B. R. Julian, Non-double-couple earthquake mechanisms at The Geysers geotherm area, California, *Geophysical Res. Lett.*, **23**, 877-880, 1996

Schriener, A. and G. A. Suemnicht, Subsurface intrusive rocks at The Geysers geothermal area, California, in Silberman, M. C., C. W. Field and A. L. Berry, eds., Proceedings of Symposium on Mineral Deposition in the Pacific Northwest, U.S., *U.S. Geological Survey Open File Report 81-355*, 294-303, 1980

Silver, P. G. and T. H. Jordan, Optimal estimation of scalar seismic moment, *Geophys. J. R. astr. Soc.*, **70**, 755-787, 1982

Spencer, J. W. and A. M. Nur, The effects of pressure, temperature and pore water on velocities in westerly granite, *J. Geophys. Res.*, **81**, 889-904, 1976

Stanley, W. D. and R. J. Blakely, New geophysical models related to heat sources in The Geysers-Clear Lake region, California, in Stone, C., ed., *Geothermal Resources Council Transactions*, **17**, 267-272, 1993

Stanley, W. D. and R. J. Blakely, The Geysers-Clear Lake geothermal area, California: An updated geophysical perspective of heat sources, *Geothermics*, **24**, 187-221, 1995

Stanley, W. D., D. B. Jackson and B. C. Hearn, Preliminary results of geoelectrical investigations near Clear Lake, California, *U.S. Geological Survey Open-File Report*, 1-20, 1973

Stark, M. A., Imaging injected water in The Geysers reservoir using microearthqake data, *Geothermal Resources Council Transactions*, **14**, 1-8, 1990

Stark, M. A., Microearthquakes-A tool to track injected water in The Geysers reservoir, *Geothermal Resources Council Special Report,* **17**, 111-117, 1992

Stark, M. A. and S. D. Davis, Remotely triggered microearthquakes at The Geysers geothermal field, California, *Geophys. Res. Letts.*, **23,** 945-948, 1996

Stimac, J, F. Goff and B. C. Hearn, Petrologic considerations for hot dry rock geothermal site selection in the Clear Lake region, California, (abstract) *Proceedings of the 1992 Annual Geothermal Resources Council Meeting*, San Diego, CA, 1992

Thompson, R. C., Structural stratigraphy and intrusive rocks at The Geysers geothermal field, *Geothermal Resources Council Special Report,* **17**, 59-64, 1992

Thompson, R. C. and R. P. Gunderson, The orientation of steam-bearing fractures at The

Geysers geothermal field, *Geothermal Resources Council Special Report,* **17**, 65-68, 1992

Thurber, C. H., Earth structure and earthquake locations in the Coyote Lake area, central California, *Ph.D. Thesis*, pp 332 Massachusetts Institute of Technology, Cambridge, Massachusetts, 1981

Thurber, C. H., Earthquake locations and three-dimensional crustal structure in the Coyote Lake area, central California, *J. Geophys. Res.*, **88**, 8226-8236, 1983

Thurber, C. H., Seismic detection of the summit magma complex of Kilauea volcano, Hawaii, *Science*, **223**, 165-167, 1984

Thurber, C. H., Local earthquake tomography: velocities and v_P/v_S-theory, in *Seismic Tomography*, edited by H. M. Iyer and K. Hirahara, 563-583, 1993

Thurber, C. H. and S. R. Atre, Three-dimensional v_P/v_S variations along the Loma Prieta rupture zone, *Bull. Seismol. Soc. Am.*, **83**, 717-736, 1993

Thurber, C. H., S. R. Atre and D. Eberhart-Phillips, Three-dimensional v_P and v_P/v_S structure at Loma Prieta, California, from local earthquake tomography, *Geophys. Res. Lett.*, **22**, 3079-3082, 1995

Toksoz, M. N., C. H. Cheng and A. Timur, Velocities of seismic in porous rocks, *Geophysics*, **41**, 621-645, 1976

Truesdale, A. H., M. Walters, M. Kennedy and M. Lippmann, An integrated model for the origin of The Geysers geothermal field, *Geothermal Resources Council Transactions*, **17**, 273-280, 1993

Truesdale, A. H., Haizlip, W. T. Box, F. D'Amore, A geochemical overview of The Geysers geothermal reservoir, *Geothermal Resources Council Special Report*, **17**, 121-132, 1992

Um, J. and C. H. Thurber, A fast algorithm for two-point seismic ray tracing, *Bull. Seismol. Soc. Am.*, **77**, 786-792, 1987

Walck, M. C., Three-dimensional v_P/v_S variations for the Coso region, California, *J. Geophys. Res.*, **93**, 2047-2052,1988

Wallace, M. H. and T. C. Wallace, The paradox of the Loma Prieta earthquake: Why did rupture terminate at depth?, *J. Geophys. Res.*, **98**, 19,859-19,687, 1993

Walter, S. R., Intermediate-focus earthquakes associated with Gorda plate subduction in northern California, *Bull. Seismol. Soc. Am.*, **76**, 583-588, 1986

Walters, M. A., J. N. Sternfield, J. N. Haizlip, J. R. Drenick, A. F. Combs and J. Combs, A vapor-dominated reservoir at The Geysers, California,, *Geothermal Resources Council Special Report,* **17**, 121-132, 1992

Wessel, P. and W. H. F. Smith, Free software helps map and display data, *EOS Trans. Am. Geophys. Un.*, **72**, 441 445-446, 1991

White, D. E., L. J. P. Muffler and A. H. Truesdell, Vapor dominated hydrothermal systems

compared with hot-water systems, *Economic Geology*, **66**, 75-97, 1971

Williamson, K. H., Development of a reservoir model for The Geysers geothermal field, *Geothermal Resources Council Special Report,* **17**, 179-188, 1992

Zucca, J. J., L. J. Hutchings and P. W. Kasameyer, Seismic velocity and attenuation structure of the Geysers geothermal field, CA, *Geothermics*, **23**, 111-126, 1994

Zucca, J. J., L. J. Hutchings and P. W. Kasameyer, Seismic imaging for saturation conditions at The Geysers geothermal-field, California, *Geothermal Resources Council Transactions,* **17** 289-293, 1993

Additional references

Donnelly-Nolan, J. M., B. C. Hearn, G. H. Curtis and R. E. Drake, Geochronology and evolution of the Clear Lake volcanics, in *U.S. Professional Paper 1141, Research in The Geysers-Clear Lake Geothermal Area, Northern California,* 47-60, 1981

Evans, J. R. and J. J. Zucca, Active source, high resolution (NeHT) tomography: velocity and *Q*, in *Seismic Tomography*, edited by H. M. Iyer and K. Hirahara, 695-732, 1993

Foulger, G. R. and B. R. Julian, Non-double-couple earhquakes at the Hengill-Grensdalur Volcanic Complex, Iceland: Are they artefacts of crustal heteorgeneity?, *Bull. Seismol. Soc. Am.*, **83**, 38-52, 1993

Hamilton, R. M. and L. J. P. Muffler, Microearthquakes at The Geysers geothermal area, California, *J. Geophys. Res.*, **77**, 2081-2086, 1971

Stone, C. (ed.), Monograph on The Geysers geothermal field, *Geothermal Resources Council Special Report.*, **17**, 1992

Toomey, D. R. and G. R. Foulger, Application of tomographic inversion to local earthquake data from the Hengill-Grensdalur central volcano complex, Iceland, *J. Geophys. Res.*, **94**, 17,497-17,510, 1989

Appendix 1 Station co-ordinates of the permanent network stations

Station co-ordinates of seismometers in the four permanent networks with reference to the WGS84 ellipsoid. The permanent networks are UNT operated by UNOCAL, CALNET operated by the USGS and the northwest and southeast Geysers networks operated by CCPA and LBL respectively.

Table A1.1. CALNET

Station code	Latitude (°N)	Longitude (°W)	Height (m asl)	Sensor type
GACM	38:52.3642	-122:51.7969	969.01	vertical-only
GAXM	38:42.6444	-122:45.3666	363.00	vertical-only
GBGM	38:48.8343	-122:40.8265	1108.86	vertical-only
GBMM	39:08.5040	-122:29.7065	958.49	vertical-only
GCMM	38:48.3443	-122:45.3766	1269.94	vertical-only
GCRM	38:46.3843	-122:42.9866	702.93	vertical-only
GCSM	39:01.3639	-123:31.3380	679.49	vertical-only
GCVM	38:46.1742	-123:00.8970	134.21	vertical-only
GCWM	39:07.8439	-123:04.6174	1073.04	vertical-only
GDCM	38:46.0242	-123:14.3774	756.41	vertical-only
GDXM	38:48.4543	-122:47.6967	914.98	vertical-only
GGLM	38:53.7942	-122:46.6468	876.91	vertical-only
GGPM	38:45.8743	-122:50.7168	1038.05	vertical-only
GGPM	38:45.8743	-122:50.7168	1038.05	vertical-only
GGPM	38:45.8743	-122:50.7168	1038.05	vertical-only
GGPM	38:45.8743	-122:50.7168	1038.05	vertical-only
GGUM	38:51.3840	-123:29.9378	645.57	vertical-only
GHCM	38:36.3543	-123:11.8772	502.47	vertical-only
GHGM	39:07.6939	-122:49.5370	886.81	vertical-only
GHLM	39:02.4240	-123:01.1872	940.05	vertical-only
GHOM	39:02.6638	-123:32.4780	671.49	vertical-only
GHVM	39:05.0940	-122:44.1268	1019.75	vertical-only
GMCM	38:47.5542	-123:07.8672	410.30	vertical-only
GMKM	38:58.1641	-122:47.2868	889.88	vertical-only
GMMM	38:50.2842	-122:47.9967	946.97	vertical-only
GMOM	38:42.6043	-123:08.6572	786.36	vertical-only
GPMM	38:50.8442	-122:56.8470	767.10	vertical-only
GRTM	38:56.3142	-122:40.2466	602.78	vertical-only
GSGM	38:51.9942	-122:42.6666	1063.86	vertical-only
GSMM	38:46.1543	-122:46.9467	1000.99	vertical-only
GSNM	38:56.4240	-123:11.5674	854.26	vertical-only
GSSM	38:42.1143	-123:00.8770	266.25	vertical-only
GTSM	39:18.6938	-122:36.2168	1086.49	vertical-only

GWKM	39:03.1141	-122:29.5264	824.54	vertical-only
GWRM	39:12.4237	-123:18.0578	642.19	vertical-only
NFRM	38:31.3544	-123:09.7271	512.49	vertical-only
NHBM	38:35.3544	-122:54.6067	149.22	vertical-only
NMCM	38:35.4544	-122:54.8067	132.22	vertical-only
NMHM	38:40.1644	-122:37.9963	1294.91	vertical-only
NMHM	38:40.1644	-122:37.9963	1294.91	vertical-only
NMTM	38:48.3343	-122:26.8261	405.64	vertical-only
NMWM	38:33.0245	-122:43.4364	118.07	vertical-only
NPVM	38:38.5445	-122:25.6160	196.72	vertical-only
NSHM	38:31.1946	-122:36.4962	311.98	vertical-only

Table A1.2. UNT-network

Station code	Latitude (°N)	Longitude (°W)	Height (m asl)	Sensor type
ACR	38:50.2041	-122:45.6135	768.90	vertical-only
ANG	38:48.3042	-122:45.0946	1291.41	vertical-only
BUC	38:49.3882	-122:50.0986	858.75	vertical-only
CAP	38:50.7568	-122:48.5329	831.56	vertical-only
CLV	38:50.3097	-122:47.4157	962.09	vertical-only
DES	38:45.9461	-122:41.9170	518.91	vertical-only
DRK	38:47.2977	-122:48.1963	716.00	vertical-only
DVB	38:45.7462	-122:44.2891	854.92	3-component
DXR	38:49.3883	-122:46.3175	989.86	3-component
FNF	38:46.2450	-122:45.9316	794.82	3-component
FUM	38:47.5875	-122:47.2656	616.63	vertical-only
INJ	38:48.4863	-122:48.2754	734.53	3-component
LCK	38:49.1713	-122:44.4802	1137.01	vertical-only
MNS	38:46.5793	-122:42.9596	676.25	vertical-only
PFR	38:44.9278	-122:44.5117	961.95	vertical-only
SB4B	38:48.5610	-122:49.7780	327.88	vertical-only
SQK	38:49.4180	-122:48.5809	637.39	3-component
SSR	38:44.4100	-122:42.6494	1047.58	vertical-only
STY	38:48.7048	-122:46.9864	1019.84	vertical-only
TCH	38:46.9992	-122:44.1803	936.37	vertical-only
U14	38:47.1128	-122:46.3262	636.30	3-component
WRK	38:45.7748	-122:43.4133	963.76	3-component

Table A1.3. Northwest Geysers network

Station code	Latitude (°N)	Longitude (°W)	Height (m asl)	Sensor type
01	38:50.0742	-122:48.9568	705.98	3-component
02	38:50.4742	-122:49.0968	860.98	3-component
03	38:50.5442	-122:49.4268	797.98	3-component
04	38:49.9642	-122:49.8168	485.99	3-component
05	38:49.7142	-122:49.8168	599.00	3-component
06	38:49.5142	-122:49.3068	688.99	3-component
07	38:49.6942	-122:48.7668	610.98	3-component
08	38:50.2342	-122:48.2768	885.97	3-component
09	38:50.7442	-122:48.6968	889.97	3-component
10	38:50.8142	-122:49.5968	799.98	3-component
11	38:50.4542	-122:50.2068	593.99	3-component
12	38:49.7842	-122:51.0868	668.02	3-component
13	38:50.6142	-122:51.3268	509.01	3-component
14	38:50.8842	-122:50.8968	633.00	3-component
15	38:51.5142	-122:50.3868	952.99	3-component
16	38:51.6442	-122:49.7068	968.97	3-component

Table A1.4. Southeast Geysers network

Station code	Latitude (°N)	Longitude (°W)	Height (m asl)	Sensor type
01	38:46.0843	-122:41.9565	616.91	3-component
02	38:44.4043	-122:42.6565	1055.90	3-component
03	38:45.0443	-122:41.4665	822.91	3-component
04	38:46.5843	-122:42.9066	678.92	3-component
05	38:47.0043	-122:44.1866	950.93	3-component
06	38:46.2443	-122:45.9466	839.97	3-component
07	38:45.8143	-122:45.2366	870.96	3-component
08	38:45.7843	-122:43.4266	978.94	3-component
09	38:45.2443	-122:43.1965	980.94	3-component
10	38:45.3343	-122:44.0666	913.95	3-component
11	38:45.1643	-122:44.6666	1002.90	3-component
12	38:47.0343	-122:45.1366	975.95	3-component
13	38:46.3943	-122:44.2766	977.94	3-component

Appendix 2 Earthquake focal mechanisms at The Geysers

Focal mechanism solutions for 210 earthquakes determined by *Oppenheimer* (1986) plotted as lower-hemisphere, equal-area projections. Open circles are dilational arrivals and closed circles compressional arrivals. Great circles are nodal planes, one of which is the fault plane along which displacement occurred. The majority of first-motion data is satisfied by strike-slip, dip-slip or reverse-slip shear faults. A number of mechanisms display distributions of first-motion data which cannot be explained as a DC source and which may indicate non-DC mechanisms. These events are listed in Table A2.1:

Table A2.1. Earthquakes with non-DC polarity distributions

Earthquake number
7
24
38
45
46
50
51
62
63
65
73
75
86
98
102

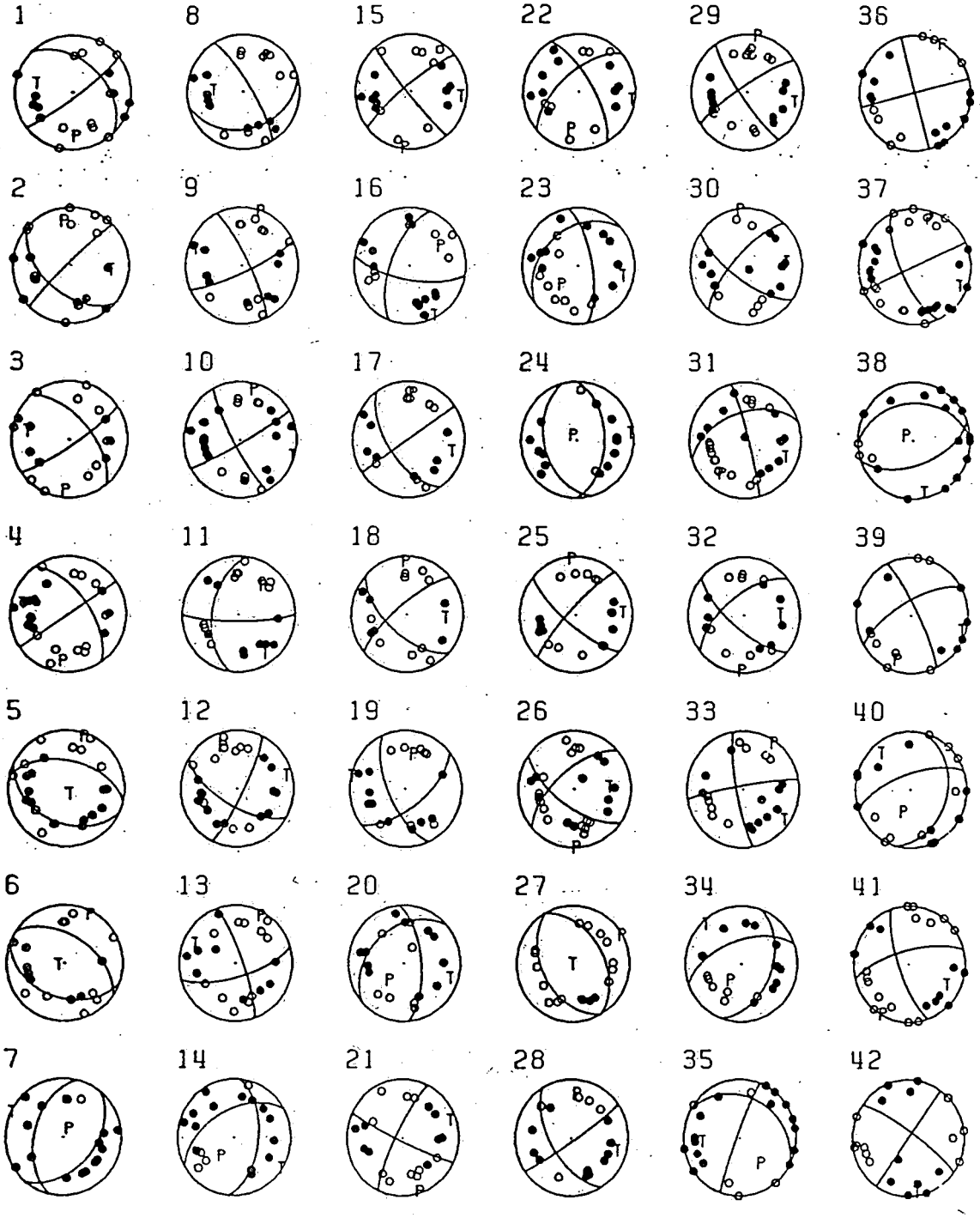
1
8
15
22
29
36
2
9
16
23
30
37
3
10
17
24
31
38
4
11
18
25
32
39
5
12
19
26
33
40
6
13
20
27
34
41
7
14
21
28
35
42

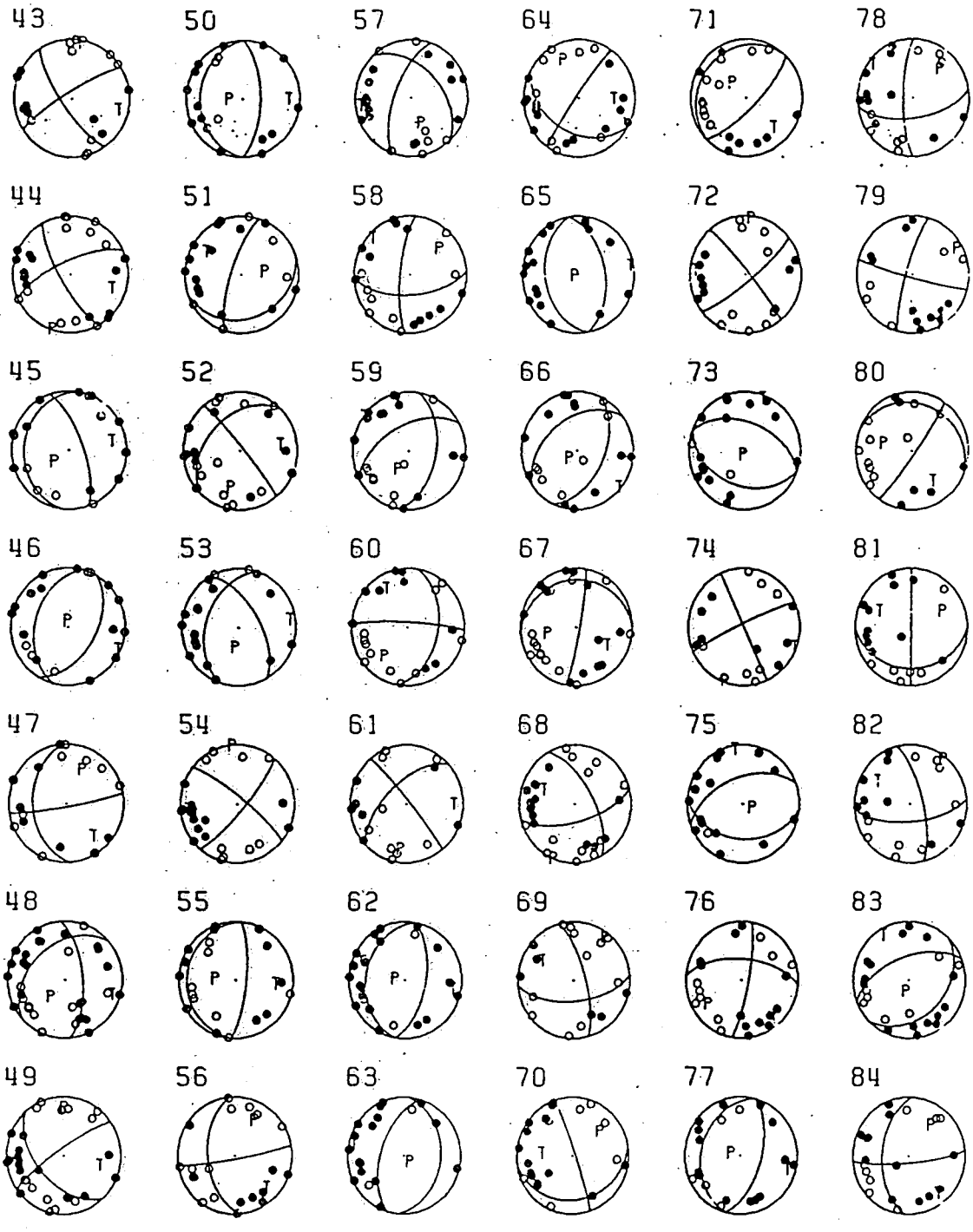
43
50
57
64
71
78
44
51
58
65
72
79
45
52
59
66
73
80
46
53
60
67
74
81
47
54
61
68
75
82
48
55
62
69
76
83
49
56
63
70
77
84

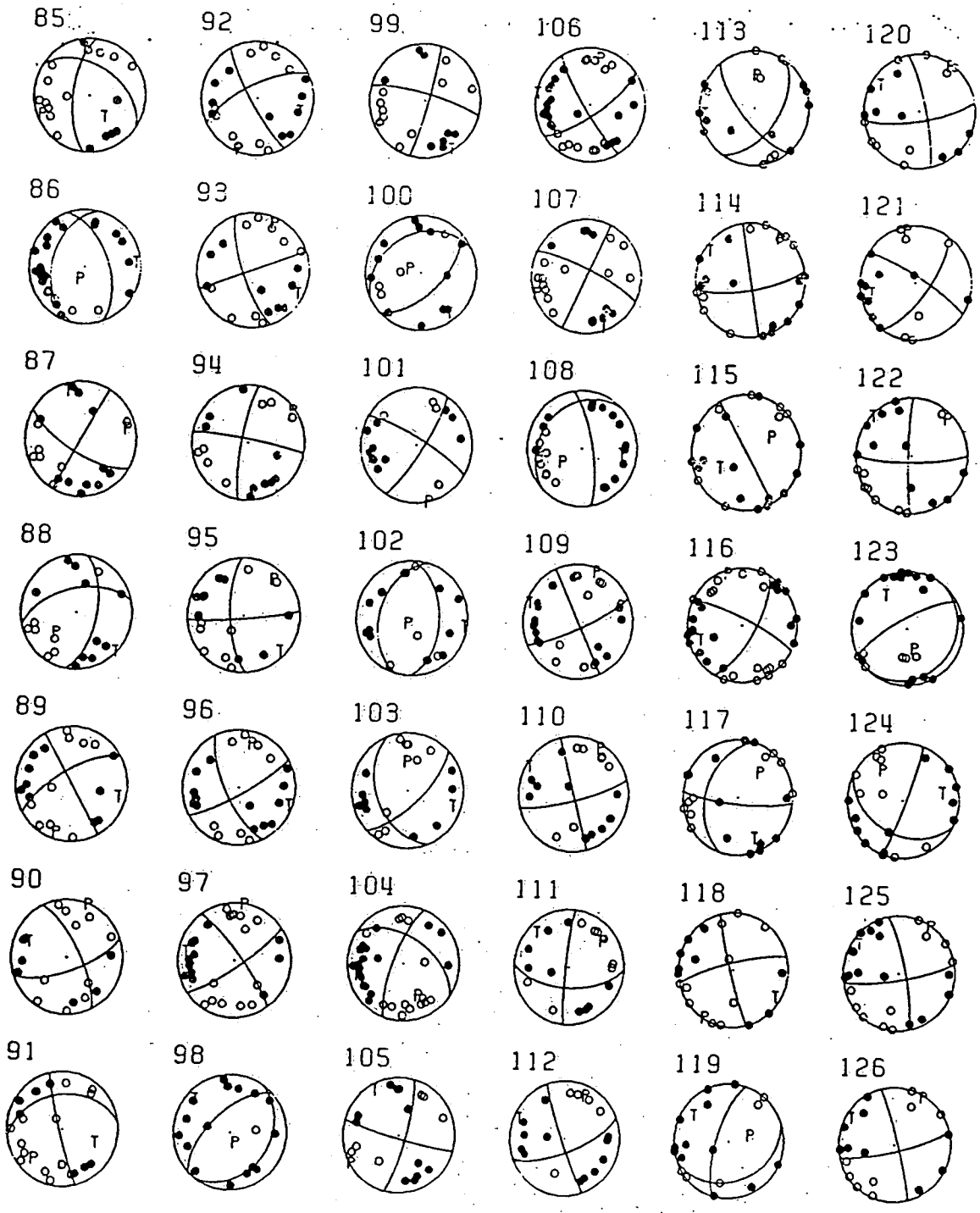
85
92
99
106
113
120
86
93
100
107
114
121
87
94
101
108
115
122
88
95
102
109
116
123
89
96
103
110
117
124
90
97
104
111
118
125
91
98
105
112
119
126

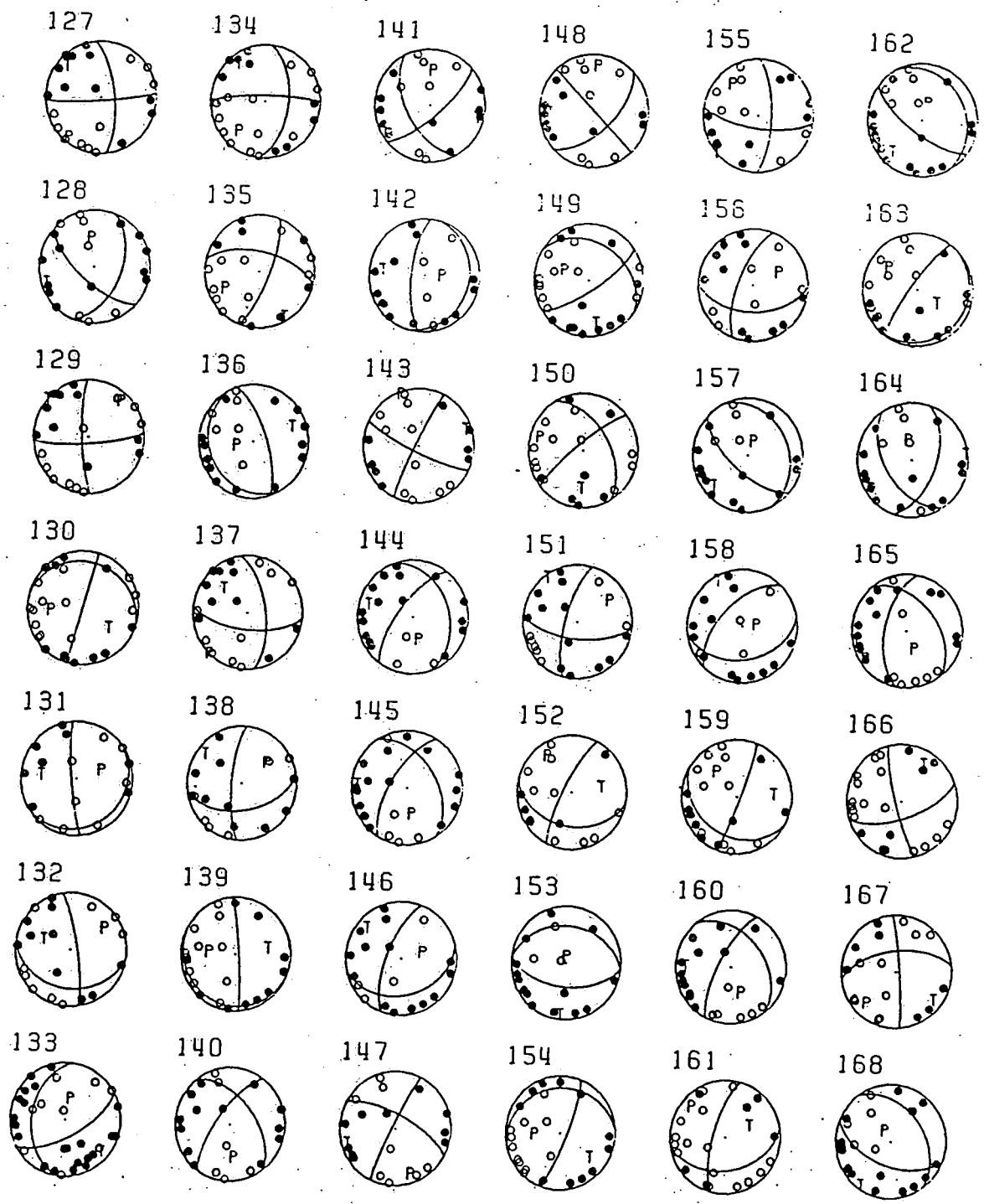
127
134
141
148
155
162
128
135
142
149
156
163
129
136
143
150
157
164
130
137
144
151
158
165
131
138
145
152
159
166
132
139
146
153
160
167
133
140
147
154
161
168

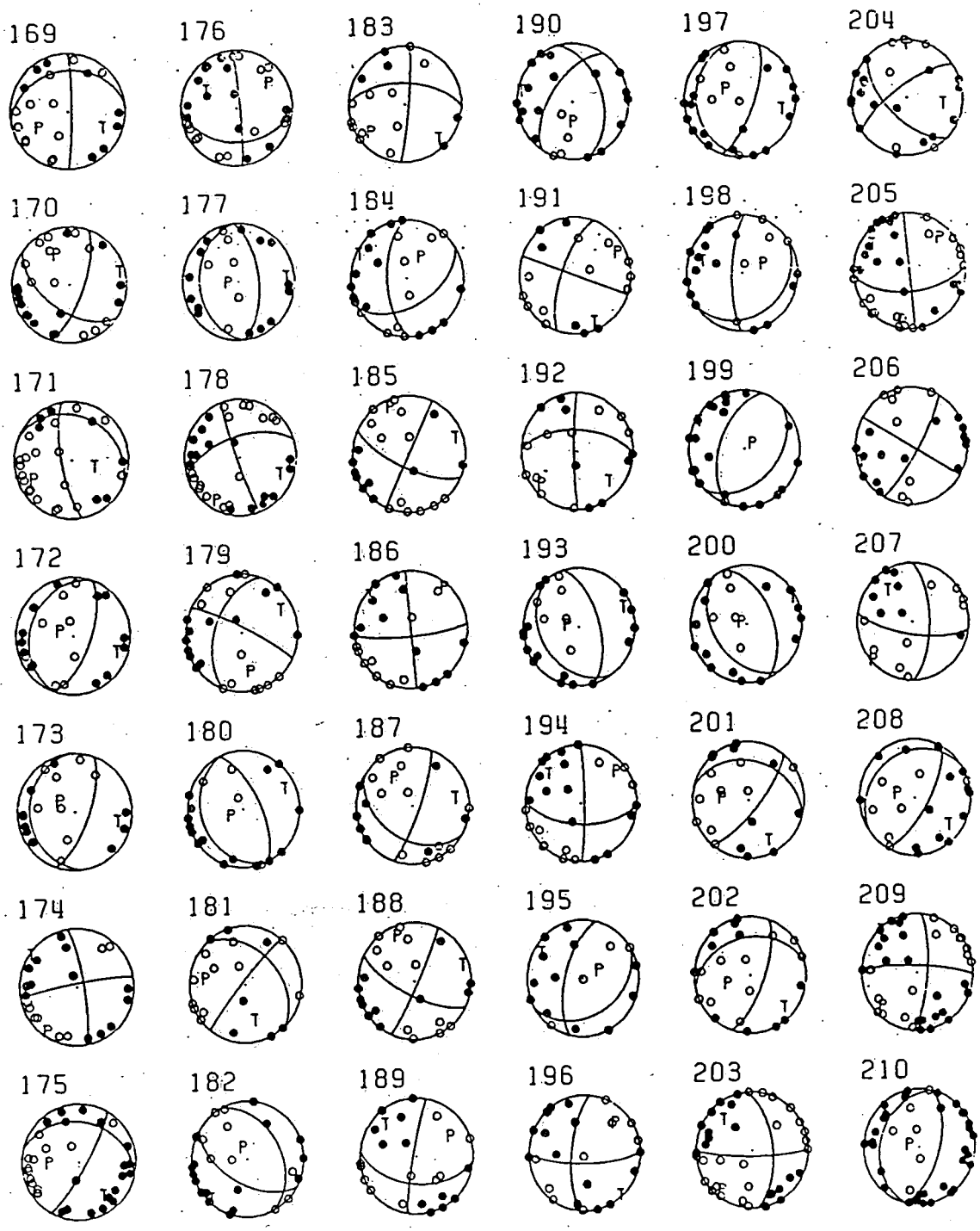
169
176
183
190
197
204
170
177
184
191
198
205
171
178
185
192
199
206
172
179
186
193
200
207
173
180
187
194
201
208
174
181
188
195
202
209
175
182
189
196
203
210

Appendix 3 Example seismograms

Example seismograms recorded at different stations for three well-recorded earthquakes. For each earthquake the vertical scaling is the same at all stations.

Event 115.143339.1

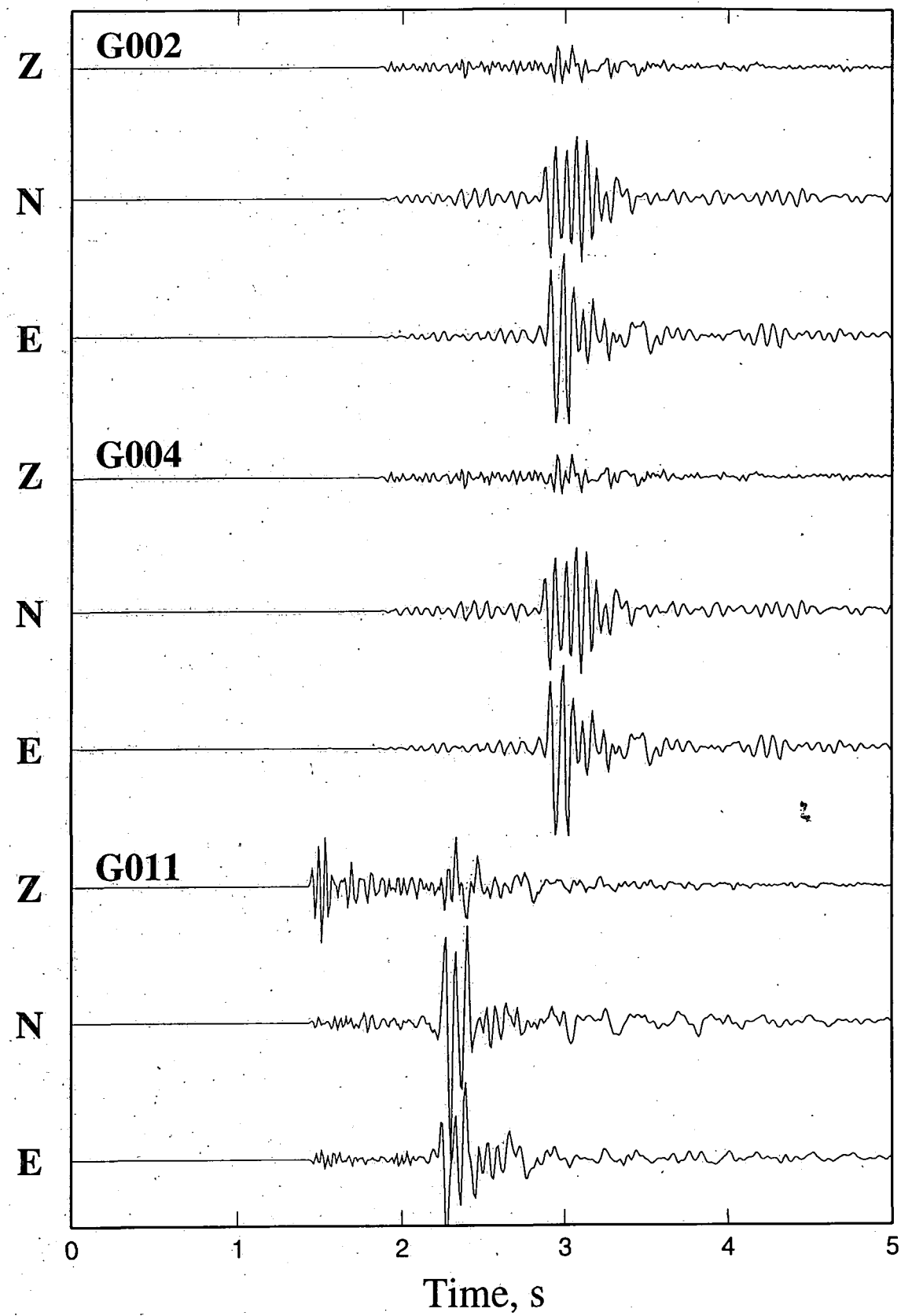

Event 118.033015.1

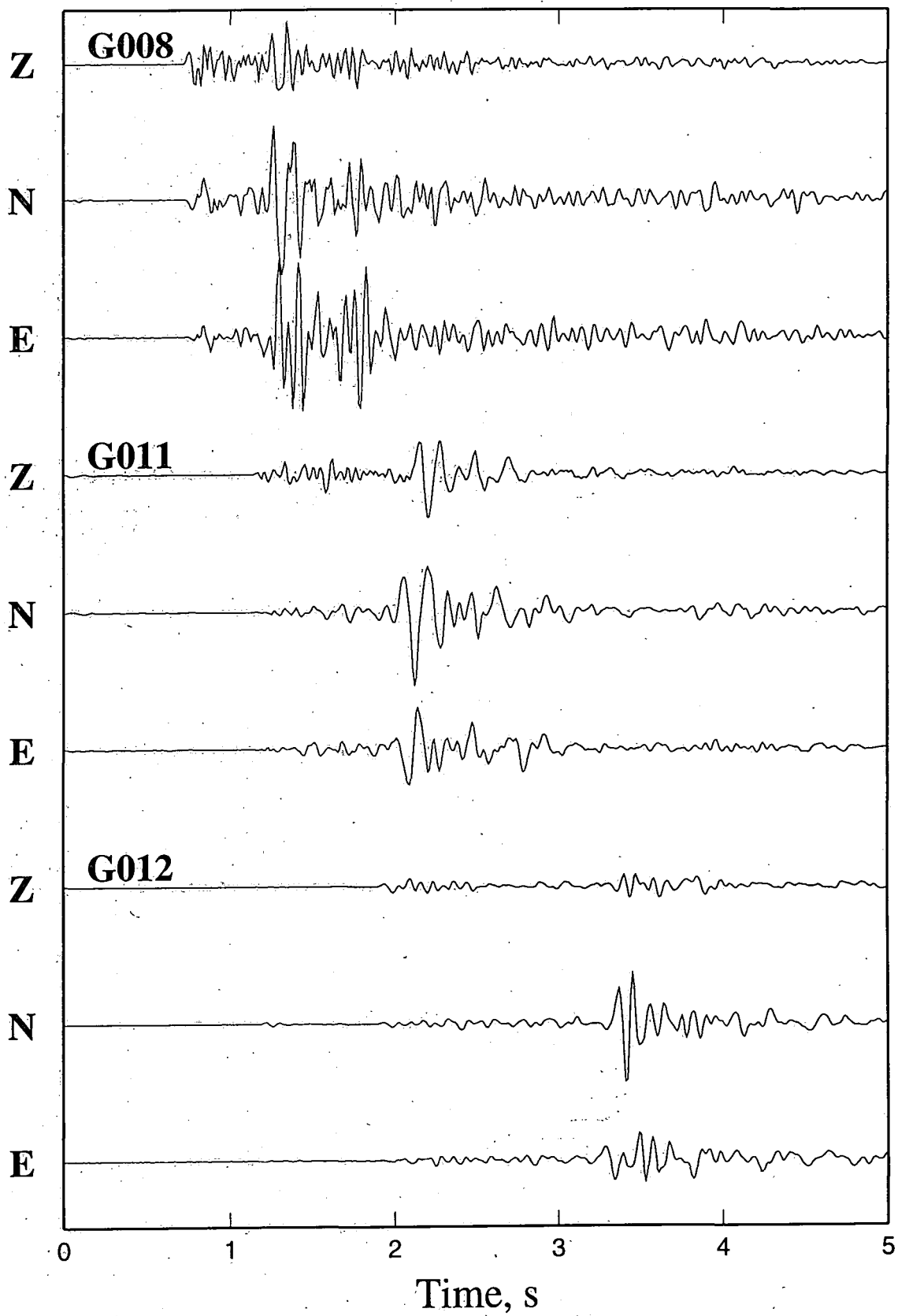

Event 120.013734.2

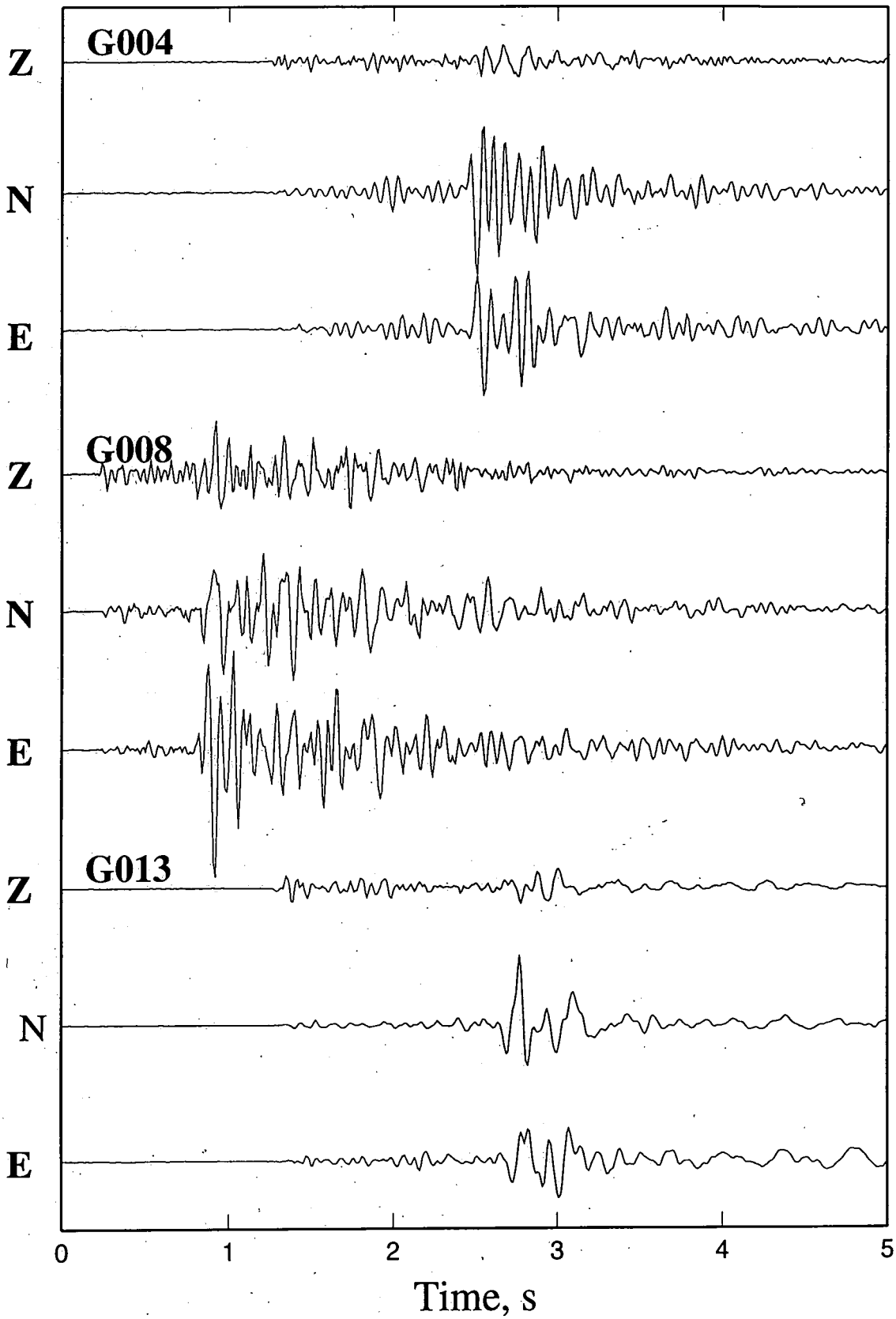

Appendix 4 Amalgamating earthquake data sets from different networks

A4.1 *match*

match compares origin times of earthquakes in the UNT permanent network with segment start times of earthquakes recorded on the temporary network, listing earthquakes recorded by both networks. A match is reported if the segment start time for an event recorded on the temporary network is within 30 s of the origin time of an event recorded by UNT.

match

```
#! /bin/sh
# Script VERSION 3: by A. C. Ross
# Shell script to match earthquakes recorded by both the temporary and UNT networks
# Times in earthquake catalogue files for each network are converted into seconds and the
# UNT catalogue is scanned for each temporary network catalogue time.
# A match is reported when the UNT time is within 30s of the temporary network time

awk '{print $1}' catalogue > iris
for file in iris catalog.uno
do
    awk '{  h = substr($1,1,2);
        m = substr($1,3,2);
        s = substr($1,5,2);
        print h m s, (h*3600+m*60+s)
    } ' $file > $file$$
done
rm iris

# Scan iris time in seconds for a given target UNOCAL time. The conditions of 2 'if' statements must be
# fulfilled for a match to be recorded. The first awk statement prints the UNOCAL time in hours, minutes
# and seconds, if a match is found the second awk statement prints the equivalent iris time. At the end of
# each loop regardless of whether a match has been successfully located or not the echo command will
# print the next line with UNOCAL time to be matched.

for time in `awk '{print $2}' catalog.uno$$`
do
```

```
    grep $time$ catalog.uno$$ | head -1 | awk '{printf "%s ",$1}'
    awk '((('$time'-$2) >= 0) && (('$time'-$2) <= 30)) {
        printf "%s ", $1}' iris$$
    echo
done
rm iris$$ catalog.uno$$
```

A4.2 *combine* and *combinelist*

The two shell scripts *combine* and *combinelist*, combine seismograms recorded on the UNT and temporary networks for earthquakes common to both. *combine* calls the Bourne shell scripts *match* and *combinelist*. If a match is found *combinelist* appends a list of UNT seismograms for that event to the list file of seismograms recorded by the temporary network.

combine

```
#! /bin/sh
# by A. C. Ross

# combine calls the match shell script to identify earthquakes common to both the UNT and temporary
# networks. This list is fed into the combinelist shell script which takes the UNT basename and generates
# a listfile.

combinelist $1 `match | awk 'NF==2'`
```

combinelist

```
#! /bin/sh
# by A. C. Ross
# combinelist generates a listfile, each line of which specifies one UNT seismogram. This list is appended
# to the appropriate listfile for seismograms recorded on the temporary network.

day=$1; shift
while test "$1" != ""
do
    mkahlist /db2/seismic/geysers91/unocal/g91$day/91$day$1.ah >> $2.1.list
    shift; shift
done
```

Appendix 5 *epick*

epick is an interactive picking program for displaying, measuring and modifying time measurements, amplitudes and other information from digital seismograms. Seismograms are stored in the Extended Data Representation (XDR) form of the Lamont AH-format (*adhoc*). These are accessed by *epick* via a user specified ASCII list file, each line of which specifies the name of an *adhoc* file to display followed by an integer indicating the seismograms position within this file. Most operations within *epick* are invoked by mouse-controlled menu commands but a set of special accelerators can be defined which duplicate these operations by single key strokes. The *epick* display consists of three, work-window components termed squash, display and pick windows (Figures A5.1 and A5.2).

Squash window: The squash window displays all seismograms recorded for a particular earthquake, which may run to several pages (Figure A5.1). In addition to the station name each sensor component is labelled. The method adopted differs for each network. The temporary network labels sensor components as 1, 2 and 3 to denote the vertical and two horizontal components while the UNT network uses z, n and e. The vertical-component CALNET seismic traces have a V label. If time measurements have been made for phase-arrivals then these will be indicated by a phase-code label (*P* or *S*). A seismogram is activated for more detailed examination by placing the cursor over it and depressing the mouse key.

Display window: Both the display and pick windows appear simultaneously (Figure A5.2). The display window shows the seismic trace selected from the squash window with an expanded vertical scale. A magnified subsection of this trace selected for display in the pick window is indicted by inverse video.

Pick window: The pick window shows the selected portion of the seismic trace. If the selected trace is the vertical component of a three-component sensor then the corresponding horizontal components will also appear (Figure A5.2). This is convenient when distinguishing between true *S*-phase arrivals and arrivals associated with converted *S*-to-*P* phases. Similarly if the first horizontal trace is selected in the squash window then the third component will also appear in the pick window and so on. Time measurements of phase-arrivals are indicated by solid, vertical black lines indicating the position of the arrival on each trace accompanied by a phase code label (*P* or *S*).

Most of the processing is completed in the pick window. The typical measurements made and information recorded are specified below;

- time-pick, time measurement for *P*- or *S*-phase arrival
- phase code label, *P* or *S*
- quality factor (0-4). Zero is good, four is poor
- arrival type, impulsive (i) or emergent (e)
- polarity, up (+) or down (-)
- amplitude, measured from first onset to first peak
- frequency, measured from first onset to first peak

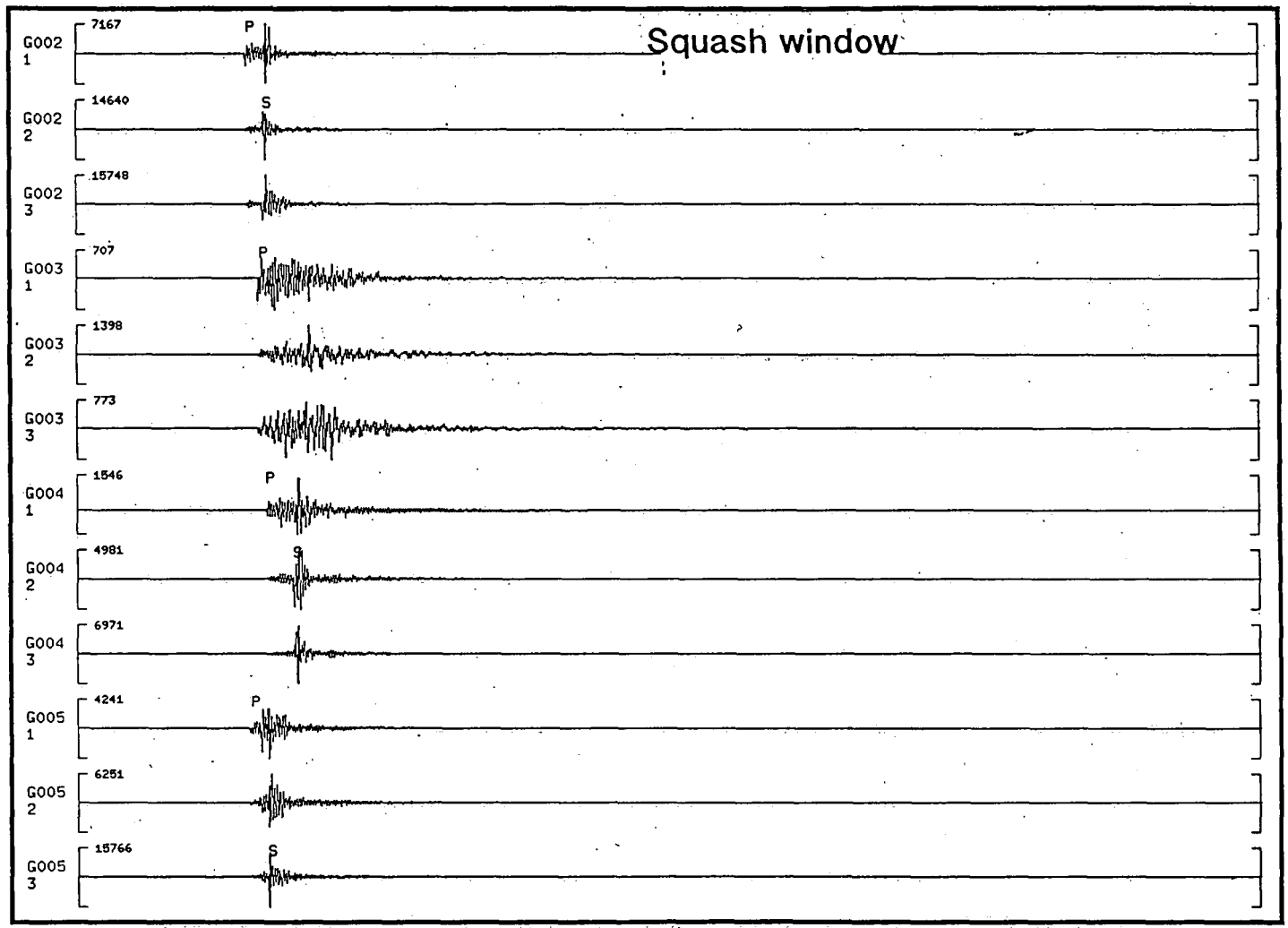

Figure A5.1. The Squash window shows pages of seismograms.

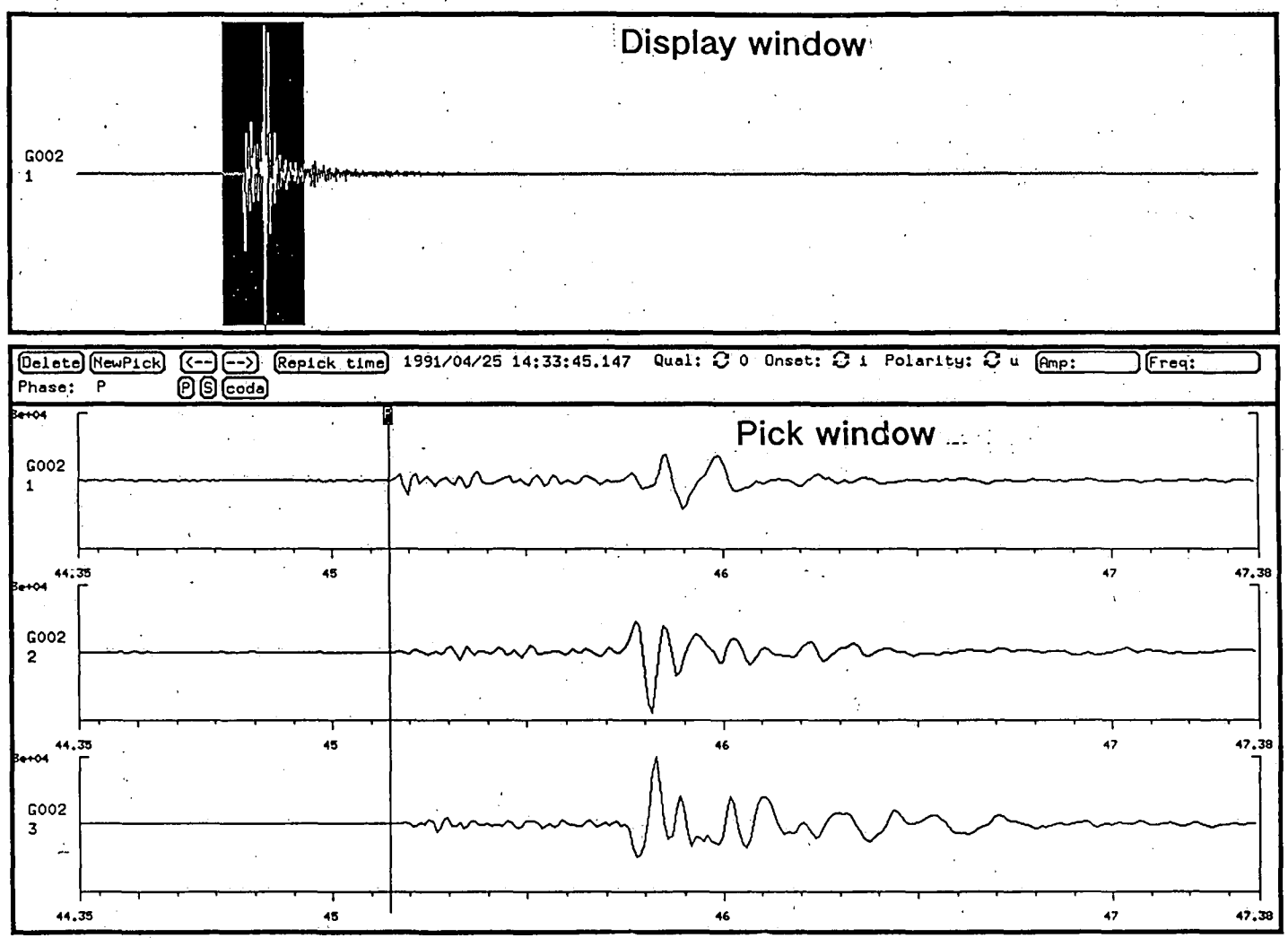

Figure A5.2. The display window shows the seismic trace selected from the squash window. A magnified subsection of this trace selected for display in the pick window is indicated by inverse video. The pick window is where each seismogram is processed.

Appendix 6 SIMULPS12-example input files

A6.1 *fort.1*: control file

Control file used in final inversion

```
185  0  0 1.0  4 1 0          neqs, nshot, nblast, wtsht, kout, kout2, kout3
10  1.0  0.020  0.01  -1.0  0.50  0.01  0.00  nitloc, wtsp, eigtol, rmscut, zmin, dxmax, rderr, ercof
5  0.10  0.03  1  2.0  2.0  99.00  0.50  hitct, dvpmax, dvpvsmax, idmp, vpdmp, vpvsdmp, stadmp, stepl
1  2  4  0.005 0 0.01  0      ires, i3d, nitmax, snrmct, ihomo, rmstop, ifixl
18.0  30.0  0.20  0.30  0.40    delt1, delt2, res1, res2, res3
9  2  0.5  0.5                 ndip, iskip, scale1, scale2
1.2  0.001 15 15                xfax, tlim, nitpb1, nitpb2
1  1  0                      iusep, iuses, invdel
```

A6.2 Description of paramenters

Parameter	Value	Description
neqs	386	Number of earthquakes
nshot	3	Number of shots
nblast	0	Number of blasts
wtsht	1.0	Weight given to shots (relative to earthquakes)
kout	4	Output control parameter
kout2	1	Output control parameter
kout3	0	Output control parameter
nitloc	10	Maximum number of iterations of event location routine
wtsp	1.0	Weight given to *S-P* times (relative to *P* times
eigtol	0.020	SVD cut-off in hypocentral adjustments
rmscut	0.01	RMS residual cutoff to terminate location iterations
zmin	0.0	Minimum earthquake depth
dxmax	0.50	Maximum horizontal hypocentral relocation per iteration
rderr	0.01	Estimated reading uncertainty
ercof	0.00	Used for hypocentral error calculations
hitct	1	DWS cutoff to remove node from inversion
dvpmax	0.10	Maximum v_p adjustment
dvpvsmax	0.03	Maximum v_p/v_s adjustment
idmp	1	Damping control parameter
vpdmp	5.0	v_p damping parameter
vpvsdmp	2.0	v_p/v_s damping parameter
stadmp	99.0	Station delay damping parameter
stepl	0.50	Raypath step length used in partial derivative calculatons
ires	1	Resolution output control parameter
i3d	2	Three-dimensional ray tracing control parameter
nitmax	4	Maximum number of iterations of the hypocentral relocation model adjustment loop
snrmct	0.005	Solution norm cutoff to terminate inversion
ihomo	1	Number of iterations to use ray-tracing in vertical planes
rmstop	0.01	RMS residual (for all events) to terminate inversion
ifixl	0	Number of iterations to fix hypocenters for
deltl	20.0	Raylength cut-off used to weight residuals
delt2	35.0	Raylength cut-off used to weight residuals

res1	0.10	Residual cut-off used for weighting
res2	0.25	Residual cut-off used for weighting
res3	0.30	Residual cut-off used for weighting
ndip	9	Number of planes searched during approximate ray-tracing (ART)
iskip	2	Number of planes near horizontal to skip during ART
scale1	0.5	Ray segment length
scale2	0.5	Controls number of paths tried during ray-tracing
xfax	1.2	Pseudo-bending control parameter
tlim	0.001	Travel-time difference cut-off to terminate pseudo-bending iterations
nitpb1	15	Maximum number of iterations during pseudo-bending
nitpb2	15	Maximum number of iterations during pseudo-bending
iusep	1	Flag to use *P* travel times (0=No; 1=Yes)
iuses	1	Flag to use *S-P* times (0=No; 1=Yes)
invdel	0	Flag to invert for station delays (0=NO; 1=Yes)

A6.3 *fort.2*: seismometer location input file

```
38 48.60 122 47.05  45.0          Centre of co-ordinate system and angle of rotation west of north
 48                               Number of stations
 G00138 45.89 122 50.74 1016 0.00 0.00  0  Station code, location and height above sea level
 G00238 47.25 122 48.99  893 0.00 0.00  0
 G00338 47.93 122 51.50  719 0.00 0.00  0
 G00438 45.53 122 45.17  932 0.00 0.00  0
 G00538 47.23 122 45.96  830 0.00 0.00  0
 G00638 47.83 122 42.84  759 0.00 0.00  0
 G00738 50.57 122 42.68  987 0.00 0.00  0
 G00838 49.47 122 48.63  670 0.00 0.00  0
 G00938 50.27 122 47.53  950 0.00 0.00  0
 G01038 51.82 122 48.13  735 0.00 0.00  0
 G01138 46.26 122 47.01 1009 0.00 0.00  0
 G01238 43.95 122 47.69  528 0.00 0.00  0
 G01338 50.67 122 53.97  741 0.00 0.00  0
 G01438 49.72 122 49.81  586 0.00 0.00  0
 G01538 49.63 122 45.11  911 0.00 0.00  0
 GACM38 52.36 122 51.80  969 0.00 0.00  0
 GAXM38 42.64 122 45.37  363 0.00 0.00  0
 GBGM38 48.83 122 40.83 1109 0.00 0.00  0
 GCMM38 48.34 122 45.38 1270 0.00 0.00  0
 GCRM38 46.38 122 42.99  703 0.00 0.00  0
 GDXM38 48.45 122 47.70  915 0.00 0.00  0
 GGLM38 53.79 122 46.65  876 0.00 0.00  0
 GGPM38 45.87 122 50.72 1038 0.00 0.00  0
 GMMM38 50.28 122 48.00  945 0.00 0.00  0
 GSGM38 51.99 122 42.66 1063 0.00 0.00  0
 GSMM38 46.15 122 46.95 1001 0.00 0.00  0
  ACR38 50.20 122 45.61  769 0.00 0.00  0
  ANG38 48.18 122 45.09 1291 0.00 0.00  0
  BUC38 49.39 122 50.10  859 0.00 0.00  0
  CAP38 50.76 122 48.53  832 0.00 0.00  0
  CLV38 50.31 122 47.42  962 0.00 0.00  0
  DES38 45.95 122 41.92  519 0.00 0.00  0
  DRK38 47.30 122 48.20  716 0.00 0.00  0
  DVB38 45.75 122 44.29  855 0.00 0.00  0
```

```
DXR38 49.39 122 46.32  990 0.00 0.00  0
FNF38 46.25 122 45.93  795 0.00 0.00  0
FUM38 47.59 122 47.27  617 0.00 0.00  0
INJ38 48.49 122 48.28  735 0.00 0.00  0
LCK38 49.17 122 44.48 1137 0.00 0.00  0
MNS38 46.58 122 42.96  676 0.00 0.00  0
PFR38 44.93 122 44.51  962 0.00 0.00  0
SB4B38 48.56 122 49.78  492 0.00 0.00  0
SQK38 49.42 122 48.58  637 0.00 0.00  0
SSR38 44.41 122 42.65 1048 0.00 0.00  0
STY38 48.70 122 46.99 1020 0.00 0.00  0
TCH38 47.00 122 44.18  936 0.00 0.00  0
U1438 47.11 122 46.33  636 0.00 0.00  0
WRK38 45.77 122 43.41  964 0.00 0.00  0
```

A6.4 *fort.3*: starting wave-speed models and nodal locations

Grid file used in the final stage of the graded inversion producing the wave-speed model presented in Chapter 5.

```
1.0 15 18 11                    finest nodal spacing, number of nodes in x, y, and z directions
-149.0 -10.0 -6.0 -4.0 -3.0  -2.0 -1.0 0.0 1.0 2.0 3.0 4.0 6.0 10.0 149.0          x-direction
-149.0 -10.0 -8.0 -6.0 -5.0 -4.0 -3.0 -2.0 -1.0 0.0 1.0 2.0 3.0 4.0 5.0 6.0 10.0 149.0   y-direction
-149.0 -2.0 -1.0 0.0 1.0 2.0 3.0 4.0 6.0 7.0 149.0                               z-direction
 2 2 2
 3 2 2
 4 2 2        Unmodelled velocity nodes in x,y and z-directions
 5 2 2        Nodes labelled 1-11 in z-direction refer to the v_P model
 6 2 2        Nodes labelled 12-22 in z-direction refer to the v_P/v_S model
 7 2 2
 8 2 2
 9 2 2
10 2 2
11 2 2
12 2 2
13 2 2
14 2 2
```

shortened for brevity

```
 3 17 21
 4 17 21
 5 17 21
 6 17 21
 7 17 21
 8 17 21
 9 17 21
10 17 21
11 17 21
12 17 21
13 17 21
14 17 21
 0 0 0
```

1.00 1.00 1.00 1.00 1.00 1.00 1.00 1.00 1.00 1.00 1.00 1.00 1.00 1.00 1.00 *v_P model*
1.00 1.00 1.00 1.00 1.00 1.00 1.00 1.00 1.00 1.00 1.00 1.00 1.00 1.00 1.00 *For each horizontal depth*
1.00 1.00 1.00 1.00 1.00 1.00 1.00 1.00 1.00 1.00 1.00 1.00 1.00 1.00 1.00 *section x increases across*
1.00 1.00 1.00 1.00 1.00 1.00 1.00 1.00 1.00 1.00 1.00 1.00 1.00 1.00 1.00 *increases across the page*
1.00 1.00 1.00 1.00 1.00 1.00 1.00 1.00 1.00 1.00 1.00 1.00 1.00 1.00 1.00 *and y increases down the*
1.00 1.00 1.00 1.00 1.00 1.00 1.00 1.00 1.00 1.00 1.00 1.00 1.00 1.00 1.00 *page*
1.00 1.00 1.00 1.00 1.00 1.00 1.00 1.00 1.00 1.00 1.00 1.00 1.00 1.00 1.00
1.00 1.00 1.00 1.00 1.00 1.00 1.00 1.00 1.00 1.00 1.00 1.00 1.00 1.00 1.00
1.00 1.00 1.00 1.00 1.00 1.00 1.00 1.00 1.00 1.00 1.00 1.00 1.00 1.00 1.00
1.00 1.00 1.00 1.00 1.00 1.00 1.00 1.00 1.00 1.00 1.00 1.00 1.00 1.00 1.00
1.00 1.00 1.00 1.00 1.00 1.00 1.00 1.00 1.00 1.00 1.00 1.00 1.00 1.00 1.00
1.00 1.00 1.00 1.00 1.00 1.00 1.00 1.00 1.00 1.00 1.00 1.00 1.00 1.00 1.00
1.00 1.00 1.00 1.00 1.00 1.00 1.00 1.00 1.00 1.00 1.00 1.00 1.00 1.00 1.00
1.00 1.00 1.00 1.00 1.00 1.00 1.00 1.00 1.00 1.00 1.00 1.00 1.00 1.00 1.00
1.00 1.00 1.00 1.00 1.00 1.00 1.00 1.00 1.00 1.00 1.00 1.00 1.00 1.00 1.00
1.00 1.00 1.00 1.00 1.00 1.00 1.00 1.00 1.00 1.00 1.00 1.00 1.00 1.00 1.00
1.00 1.00 1.00 1.00 1.00 1.00 1.00 1.00 1.00 1.00 1.00 1.00 1.00 1.00 1.00
2.47 2.47 2.47 2.47 2.47 2.47 2.47 2.47 2.47 2.47 2.47 2.47 2.47 2.47 2.47
2.47 2.47 2.47 2.47 2.47 2.47 2.47 2.47 2.47 2.47 2.47 2.47 2.47 2.47 2.47
2.47 2.47 2.47 2.47 2.47 2.47 2.47 2.47 2.47 2.47 2.47 2.47 2.47 2.47 2.47
2.47 2.47 2.47 2.47 2.47 2.47 2.47 2.47 2.47 2.47 2.47 2.47 2.47 2.47 2.47
2.47 2.47 2.47 2.47 2.47 2.47 2.47 2.47 2.47 2.47 2.47 2.47 2.47 2.47 2.47
2.47 2.47 2.47 2.47 2.47 2.47 2.47 2.47 2.47 2.47 2.47 2.47 2.47 2.47 2.47
2.47 2.47 2.47 2.47 2.47 2.47 2.47 2.47 2.47 2.47 2.47 2.47 2.47 2.47 2.47
2.47 2.47 2.47 2.47 2.47 2.47 2.47 2.47 2.47 2.47 2.47 2.47 2.47 2.47 2.47
2.47 2.47 2.47 2.47 2.47 2.47 2.47 2.47 2.47 2.47 2.47 2.47 2.47 2.47 2.47
2.47 2.47 2.47 2.47 2.47 2.47 2.47 2.47 2.47 2.47 2.47 2.47 2.47 2.47 2.47
2.47 2.47 2.47 2.47 2.47 2.47 2.47 2.47 2.47 2.47 2.47 2.47 2.47 2.47 2.47
2.47 2.47 2.47 2.47 2.47 2.47 2.47 2.47 2.47 2.47 2.47 2.47 2.47 2.47 2.47
2.47 2.47 2.47 2.47 2.47 2.47 2.47 2.47 2.47 2.47 2.47 2.47 2.47 2.47 2.47
2.47 2.47 2.47 2.47 2.47 2.47 2.47 2.47 2.47 2.47 2.47 2.47 2.47 2.47 2.47
2.47 2.47 2.47 2.47 2.47 2.47 2.47 2.47 2.47 2.47 2.47 2.47 2.47 2.47 2.47
2.47 2.47 2.47 2.47 2.47 2.47 2.47 2.47 2.47 2.47 2.47 2.47 2.47 2.47 2.47
3.52 3.52 3.52 3.52 3.52 3.52 3.52 3.52 3.52 3.52 3.52 3.52 3.52 3.52 3.52
3.52 3.41 3.61 3.72 3.77 3.82 3.90 3.99 4.02 4.05 3.95 3.85 3.72 3.61 3.52
3.52 3.35 3.50 3.62 3.67 3.71 3.69 3.68 3.78 3.88 3.85 3.81 3.67 3.60 3.52
3.52 3.28 3.24 3.51 3.59 3.67 3.75 3.82 4.02 4.22 4.00 3.77 3.59 3.60 3.52
3.52 3.23 3.27 3.44 3.42 3.40 3.63 3.87 4.01 4.16 4.03 3.90 3.60 3.60 3.52
3.52 3.19 3.31 3.37 3.25 3.13 3.52 3.91 4.00 4.09 4.05 4.02 3.60 3.60 3.52
3.52 3.15 3.33 3.21 3.04 2.88 3.27 3.66 3.82 3.98 3.99 4.00 3.61 3.60 3.52
3.52 3.12 3.36 3.04 2.84 2.64 3.02 3.41 3.63 3.86 3.92 3.99 3.62 3.59 3.52
3.52 2.89 3.12 3.40 3.15 2.90 3.32 3.73 3.74 3.75 3.90 4.05 3.56 3.58 3.52
3.52 2.66 2.88 3.76 3.46 3.17 3.62 4.06 3.85 3.64 3.88 4.12 3.51 3.57 3.52
3.52 2.90 3.08 3.58 3.55 3.51 3.69 3.88 3.79 3.71 3.77 3.84 3.53 3.56 3.52
3.52 3.13 3.29 3.41 3.63 3.85 3.77 3.69 3.73 3.78 3.67 3.56 3.55 3.56 3.52
3.52 3.20 3.35 3.50 3.51 3.51 3.49 3.47 3.46 3.44 3.48 3.52 3.54 3.55 3.52
3.52 3.27 3.40 3.60 3.38 3.17 3.21 3.25 3.17 3.10 3.29 3.48 3.53 3.54 3.52
3.52 3.33 3.45 3.65 3.55 3.44 3.42 3.40 3.35 3.29 3.39 3.48 3.52 3.53 3.52
3.52 3.40 3.50 3.70 3.71 3.72 3.63 3.54 3.52 3.49 3.49 3.49 3.52 3.52 3.52
3.52 3.60 3.59 3.58 3.58 3.58 3.57 3.56 3.56 3.55 3.52 3.50 3.51 3.48 3.52
3.52 3.52 3.52 3.52 3.52 3.52 3.52 3.52 3.52 3.52 3.52 3.52 3.52 3.52 3.52
4.33 4.33 4.33 4.33 4.33 4.33 4.33 4.33 4.33 4.33 4.33 4.33 4.33 4.33 4.33
4.33 4.13 4.39 4.54 4.59 4.64 4.78 4.92 4.95 4.98 4.78 4.58 4.59 4.37 4.33
4.33 4.08 4.27 4.44 4.39 4.34 4.43 4.53 4.72 4.91 4.74 4.57 4.53 4.33 4.33
4.33 4.03 3.95 4.17 4.25 4.34 4.57 4.79 4.95 5.10 4.79 4.48 3.99 4.27 4.33

4.33 3.98 4.01 4.20 4.26 4.33 4.55 4.78 4.79 4.82 4.67 4.54 4.11 4.26 4.33
4.33 3.92 4.08 4.22 4.26 4.31 4.54 4.76 4.64 4.53 4.56 4.59 4.22 4.25 4.33
4.33 3.85 4.10 4.24 4.36 4.47 4.74 5.00 4.73 4.46 4.66 4.86 4.30 4.23 4.33
4.33 3.78 4.12 4.26 4.45 4.64 4.95 5.25 4.82 4.39 4.75 5.12 4.38 4.21 4.33
4.33 3.59 3.75 4.50 4.43 4.36 4.75 5.14 4.71 4.27 4.59 4.91 4.27 4.21 4.33
4.33 3.40 3.39 4.75 4.42 4.08 4.55 5.03 4.59 4.15 4.42 4.70 4.16 4.21 4.33
4.33 3.67 3.70 4.54 4.35 4.17 4.40 4.62 4.40 4.17 4.27 4.36 4.30 4.19 4.33
4.33 3.94 4.01 4.32 4.29 4.26 4.24 4.22 4.21 4.20 4.11 4.02 4.45 4.17 4.33
4.33 4.04 4.17 4.65 4.53 4.41 4.27 4.14 4.26 4.39 4.21 4.03 4.41 4.17 4.33
4.33 4.14 4.32 4.98 4.76 4.55 4.30 4.06 4.32 4.58 4.30 4.03 4.37 4.17 4.33
4.33 4.25 4.45 5.04 5.02 5.00 4.67 4.36 4.44 4.52 4.32 4.12 4.33 4.17 4.33
4.33 4.35 4.58 5.11 5.28 5.44 5.04 4.65 4.55 4.46 4.34 4.22 4.29 4.17 4.33

Shortened for brevity

1.74 1.74 1.74 1.74 1.74 1.74 1.74 1.74 1.74 1.74 1.74 1.74 1.74 1.74 1.74 v_P/v_S *model*
1.74 1.74 1.74 1.74 1.74 1.74 1.74 1.74 1.74 1.74 1.74 1.74 1.74 1.74 1.74

1.74 1.76 1.82 1.76 1.75 1.75 1.72 1.68 1.74 1.80 1.80 1.80 1.74 1.74 1.74
1.74 1.75 1.78 1.77 1.78 1.79 1.75 1.72 1.74 1.75 1.79 1.82 1.77 1.75 1.74
1.74 1.74 1.74 1.78 1.81 1.84 1.79 1.75 1.73 1.71 1.77 1.84 1.80 1.76 1.74
1.74 1.74 1.74 1.76 1.78 1.81 1.77 1.74 1.72 1.70 1.75 1.79 1.78 1.75 1.74
1.74 1.74 1.74 1.74 1.76 1.78 1.75 1.73 1.71 1.68 1.72 1.75 1.76 1.74 1.74
1.74 1.74 1.74 1.75 1.76 1.77 1.75 1.74 1.73 1.71 1.73 1.75 1.76 1.74 1.74
1.74 1.74 1.74 1.75 1.75 1.76 1.75 1.75 1.75 1.74 1.75 1.75 1.76 1.74 1.74
1.74 1.74 1.74 1.75 1.76 1.76 1.75 1.75 1.74 1.74 1.74 1.75 1.75 1.74 1.74
1.74 1.74 1.74 1.76 1.76 1.76 1.75 1.74 1.74 1.74 1.74 1.74 1.74 1.74 1.74

Shortened for brevity

A6.5 *fort.4*: hypocentre and travel-time residuals

Example input hypocentre and travel time data for three earthquakes at The Geysers. The first line provides information on the date, time, latitude, longitude and depth of the earthquake bsl. The remainder gives the station code, an impulsive (i) or emergent (e) arrival, arrival phase and quality and the travel time residual. For *S*-waves the *S-P* travel time is given.

910401 23 1 53.35 38 50.17 122 46.37 1.46 0.00

G004iPu1 1.876G011ePd1 1.707G011_SP1 1.180G012ePd1 2.500G012_SP2 1.730 ACRiP_0 0.580

CAPiPd1 0.940 CLViP_0 0.640 LCKiPu1 0.980 FNFiP_2 1.630 FNF_SP1 1.120 STYiP_1 0.881

BUCiPd1 1.461 ANGiP_1 1.210 DXRiPu0 0.720 SQKiP_0 0.960

0

910401 2320 28.81 38 50.18 122 46.36 1.73 0.00

G004iPu1 1.893G011ePu1 1.663G011_SP1 1.240G012iPd2 2.496G012_SP2 1.730 ACRiP_0 0.627

CAPiPd0 0.987 CLViP_0 0.687 LCKiPu1 1.027 FNFiP_2 1.637 STYiP_2 0.917 ANGiP_2 1.257

DXRiPu0 0.757 SQKiP_1 0.987 SQK_SP2 0.690

0

910402 1720 17.67 38 48.22 122 45.24 1.33 0.00

U14iP_1 0.712 ACRiP_1 0.921 CAPiPd2 1.662 CLViP_2 1.252 LCKiPd1 0.821 FNFiP_1 0.902

FNF_SP2 0.630 STYiP_2 0.741 DVBeP_1 1.047 DVB_SP2 0.705 PFReP_2 1.352 SSR_P_0 1.772

MNSiP_1 1.072 WRKiP_1 1.232 DESeP_1 1.412 TCHeP_1 0.762 ANGiP_1 0.642 SQKiP_1 1.212

0

Appendix 7 Bourne-shell scripts used in data processing and presentation of results

A7.1 Calculating RMS travel-time residuals

The program *count.PS* locates earthquakes using the program *qloc3d* and calculates the total RMS travel-time residual for both *P*- and *S*-phases. The program requires an event file specified on the command line containing a list of earthquakes to be included in the calculation. An example of the output is given below.

Sum of P sq res=9.68346; No of phases=5658; RMS residual=0.0413698 s
Sum of *S* sq res=7.96735; No of phases=1426; RMS residual=0.0747476 s
Total rms residual=0.0580587 s

count.PS

```
#! /bin/sh
# Version 1: A. C. Ross, October 1995
# Locates an earthquake and calculates the RMS travel time residual for both P and S-phases.
# Locate each event and append the location, event label, phase type and travel-time residual to the file.
temp$$
infile=$1

for event in `cat infile`
do
    touch temp$$
    eloc3d $event | nawk 'NR==2 {print $2, $4, $6, "'$event'"}
                NR>5 {print $8, $10}' >> temp$$
done
# Calculate the RMS travel-time residual for P- and S-waves. Output the results into the file "info.3dmod"
nawk 'BEGIN {i=0; j=0; a=0; sump=0; sums=0; sima=0}
   NF==2 && $1=="P" {i++; sump+=$2**2}
   NF==2 && $1=="S" {j++; sums+=$2**2}
   NF==2 {a++; suma+=$2**2}
   END {print "Sum of P sq res="sump, "No of phases="i, "RMS residual="sqrt(sump/i) ;
    print "Sum of S sq res="sums, "No of phases="j, "RMS residual="sqrt(sums/j);
    print "Total RMS residual="sqrt(suma/a)
}' temp$$ > info.3dmod
rm temp$$
```

A7.2 Convert latitude and longitude into cartesian co-ordinates

SIMULPS12 uses a cartesian co-ordinate system to parameterize the model volume. For presentation purposes it was necessary to superimpose surface features such as faults, mountains, steam production area and seismic station locations onto the three-dimensional tomographic models produced (Figure 5.8). The program *convert.rots12* takes latitude and longitude values and converts these into a cartesian co-ordinate system, taking into account the model volumes 45° rotation west of north.

convert.rots12

```
#! /bin/sh
# Version 1 : A. C. Ross September 1993
# Rotates latitude and longitude co-ordinates into local co-ordinates i.e. 45 degrees west of north for
# modelled volume at The Geysers. convert.rots12 takes an input file specified on the command line with
# latitude and longitude co-ordinates
# cvangles ensures input latitude and longitude co-ordinates are in degrees
cvangles $* |
nawk '
    BEGIN {
        olt=38.81
        oln=-122.784
        yltkm=1.8502
        xlnkm=1.4476
    }
    {
        if ($1 == "SEGMENT")
            print $1
        else  {
            x=60*($2-oln)
            y=60*($1-olt)
            xnorm=x*xlnkm
            ynorm=y*yltkm
            # Rotate local co-ordinates into the new co-ordinate system. Give rotation angle in radians.
            x1=(xnorm*cos(0.7854) + ynorm*sin(0.7854))
            y1=(-1*(xnorm*sin(0.7854)) + ynorm*cos(0.7854))
            print x1, y1
        }
}'
```

A7.3 Colour contour cross-sections of wave-speed models

The program *new.plotcs* was written to generate colour contour cross-sections through v_P and v_P/v_S models such as those presented in Figures 5.9 and 5.11. The user can specify either a v_P or v_P/v_S model, the length and vertical dimensions of the cross-section, the scale the model is to be interpolated to and appropriate contours of the steam reservoir, felsite batholith and well resolved areas of the model. The program expects the input wave-speed model to have the format *x, y, z, model value*. *new.plotcs* is most commonly called by a second program to produce a series of cross-sectional diagrams such as presented in Figure 5.9.

new.plotcs

```
#! /bin/sh
# Version 1: A. C. Ross, October 1995
# Draw vertical colour plots of simul vP and vP/vS models

usage="Usage: $0 x1 y1 x2 y2 z-top z-bottom -Inode_spacing -M model [-Btickinfo]
 [-overlay] [-Xposition] [-Yposition] [-hypos hypo-file] [-Wwidth] [-title strin
g] xyzv.velocityfile"

case $# in
    0|1|2|3|4|5|6|7|8|9) echo $usage 1>&2; exit 1 ;;
esac

# Set defaults
title=""; fhypo=/dev/null ; ticks="a5f1/a2f1WSne"
overlay="" ; px=0.7 ; py=6 ; model=vp ; cscale=scale.perdiff

# Process command line
x1=$1; y1=$2; x2=$3; y2=$4; shift 4
z1=$1; z2=$2; shift 2

while test "$1" != ""
do
    case "$1" in
        -I*) node=`echo $1 | sed 's,-I,,'`; shift ;;
        -M*) model=$2; shift 2 ;;
        -B*) ticks=`echo $1 | sed 's,-B,,'`; shift ;;
```

```
        -o*) overlay=-O ; shift ;;
        -X*) px=`echo $1 | sed 's,-X,,'`; shift ;;
        -Y*) py=`echo $1 | sed 's,-Y,,'`; shift ;;
        -h*) fhypo=$2; shift 2 ;;
        -W*) W=$1; shift ;;
        -t*) title=$2; shift 2 ;;
        -*) echo $usage 1>&2 ; exit 1 ;;
        *) break ;;
    esac
done
velfile=$1; shift

# Get depth positions
nd=`echo $z1 $z2 $node | nawk '{ print (int($2-$1)/$3)+1 }'`
xwalk -x $z1 $z2 $nd > dep$$

# Get x,y positions of cross-section points
project -C$x1/$y1 -E$x2/$y2 -G$node |
nawk '
    BEGIN { n = '$node' }
    {
        if ($3/n - int($3/n) > 0.5) print $1, $2, n*(int($3/n)+1)
        else print $1, $2, n*int($3/n)
}' | uniq > xy$$
len=`tail -1 xy$$ | nawk '{print $3}'`


# Project hypocentres into plane of cross-section
project $fhypo -C$x1/$y1 -E$x2/$y2 -Fpz -V $W > hypos$$

# Create target-node file: "x, y, z, a", where a is length along cross-section
for depth in `cat dep$$`
do
    nawk '{ print $1, $2, '$depth', $3}' xy$$
done > targ$$
# Define colour scale to be used
if test "$model" = "vpvs"
then
```

```
        cscale=scale.vpvs
fi

echo "$x1 $y1 $x2 $y2" 1>&2

# Plot cross-section and interpolate the velocity model to the specified scale using the interpolation
# program csinterpolate and generate the colour image using the program grdimage

psbasemap -JX4.25/-1.0 -R0/$len/-1/4 -Ba2f1wsen -X$px -Y$py $overlay -K
sort +2 -n +1 -n +0 -n $velfile | csinterpolate -t targ$$ |
xyz2grd -Ggrd$$ -I$node -R
grdimage grd$$ -JX -R -C$cscale -X0 -Y0 -V -O -K

# Draw areas which are well resolved with spread = 4 contours
sort +2 -n +1 -n +0 -n ../spread/spreadfun."$model" |
nawk '
        {
        if ($4 == -1) $4 = 16
        print
}' | csinterpolate -t targ$$ |
xyz2grd -Ggrdspread$$ -I0.25 -R
grdcontour grdspread$$ -JX -R -Ccont4 -W6/255/255/255t15_25:1 -X0 -Y0 -V -O -K

# Plot hypocentres
psxy hypos$$ -JX -R -Sc0.05 -G0 -X0 -Y0 -O -K

# Get axis anotations correct, superimpose felsite batholith and reservoir contours
psbasemap -JX4.25/-1.0 -R-10/10/-1/4 -B"$ticks" -X0 -Y0 -O -K

if test "$x1" = "$x2"
then
        file="$x1"x
        label="x = $x1 km"
else
        file="$y1"y
        label="y = $y1 km"
fi
```

```
# Plot the top of the felsite and reservoir
psxy -JX -R -X0 -Y0 -W4/255/0/0 -M -O -K digit.local/felsite."$file"
psxy -JX -R -X0 -Y0 -W4/0/0/0t15_25:1 -M -O -K digit.local/felsite."$file"
psxy -JX -R -X0 -Y0 -M -W4/255/255/255 -O -K digit.local/reservoir."$file"

pslabel -JX -R -G255/255/255 -O -K << END
-9.25 3 12 0 4 5 $label
END

rm grd$$ grdspread$$ xy$$ dep$$ hypos$$ targ$$
```

Appendix 8 Final v_P and v_P/v_S models

Final v_P and v_P/v_S wave-speeds are plotted at their nodal position on horizontal slices through the three-dimensional model. Black lines: surface trace of major fault; grey lines: felsite batholith; black dashes lines: well resolved areas of the model; white triangles: mountains.

Depth = -1 km

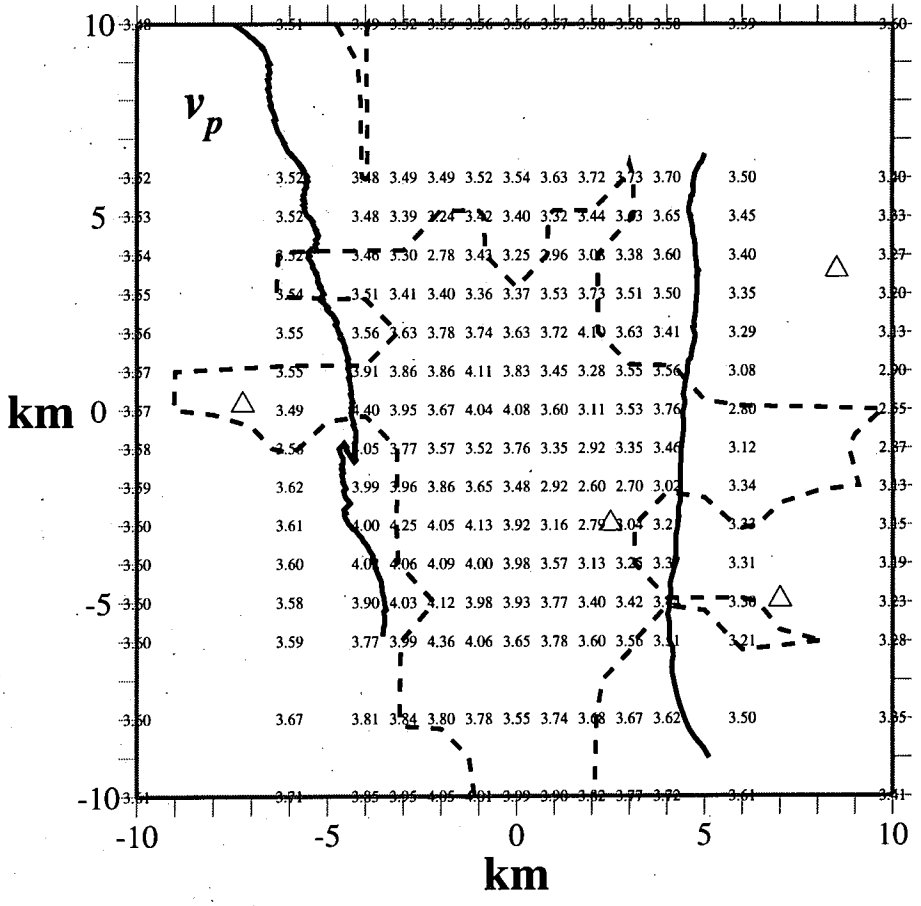

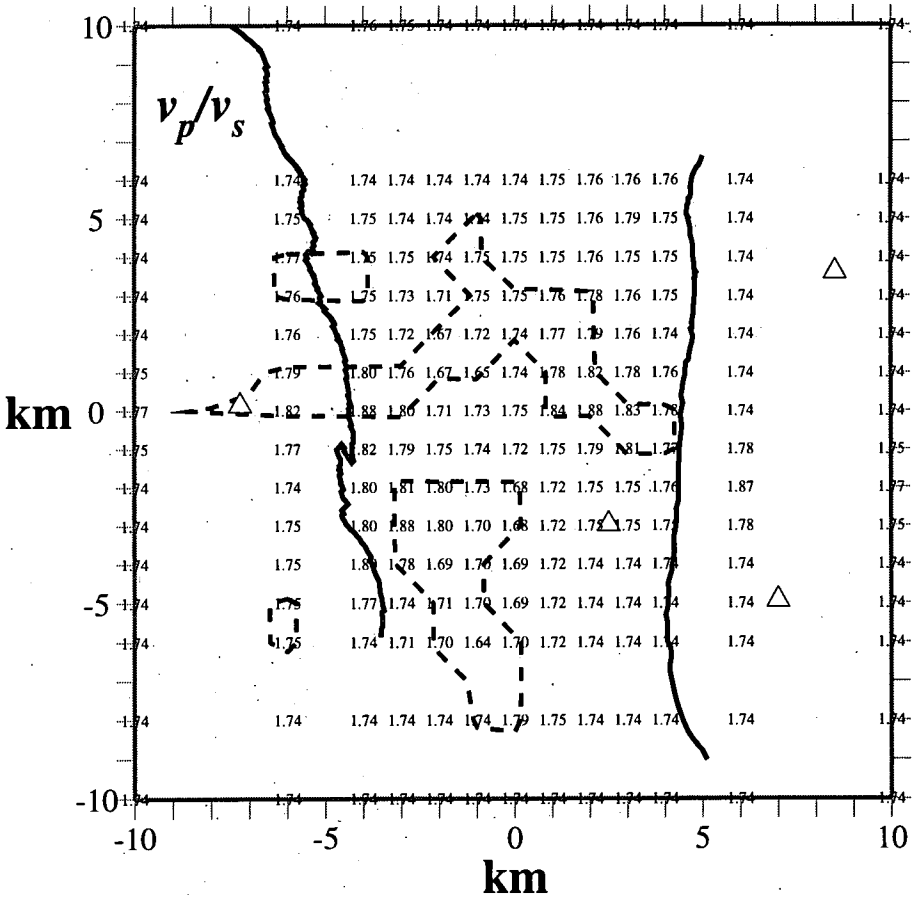

Depth = 0 km

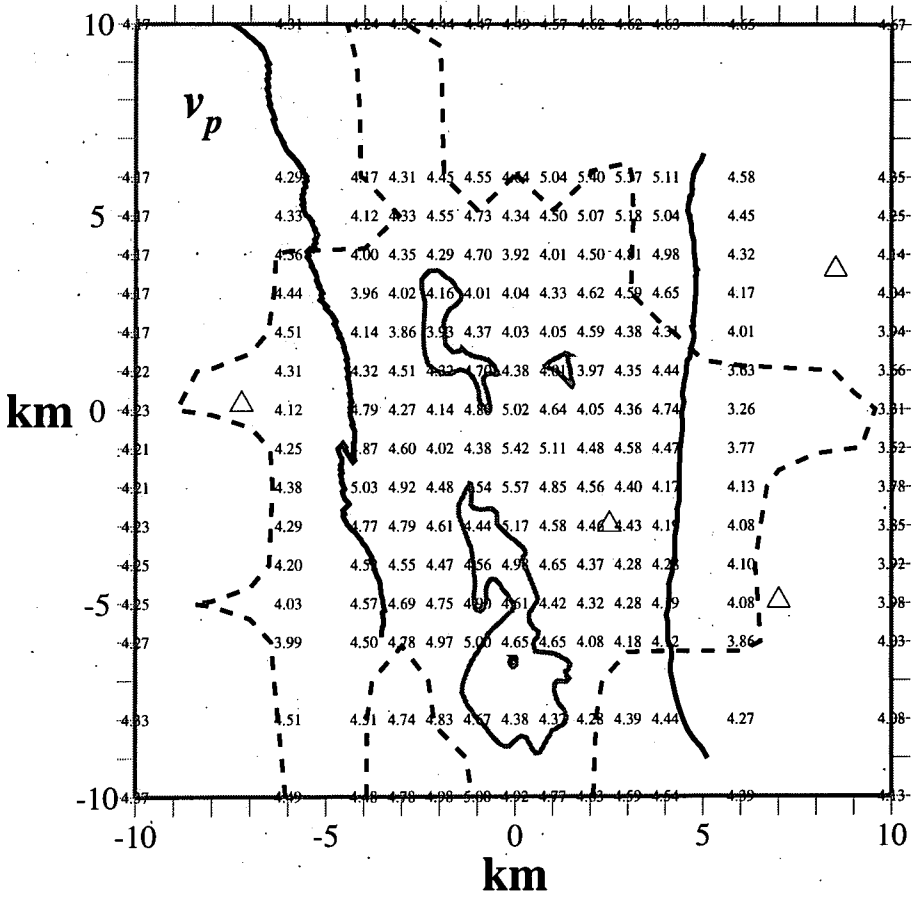

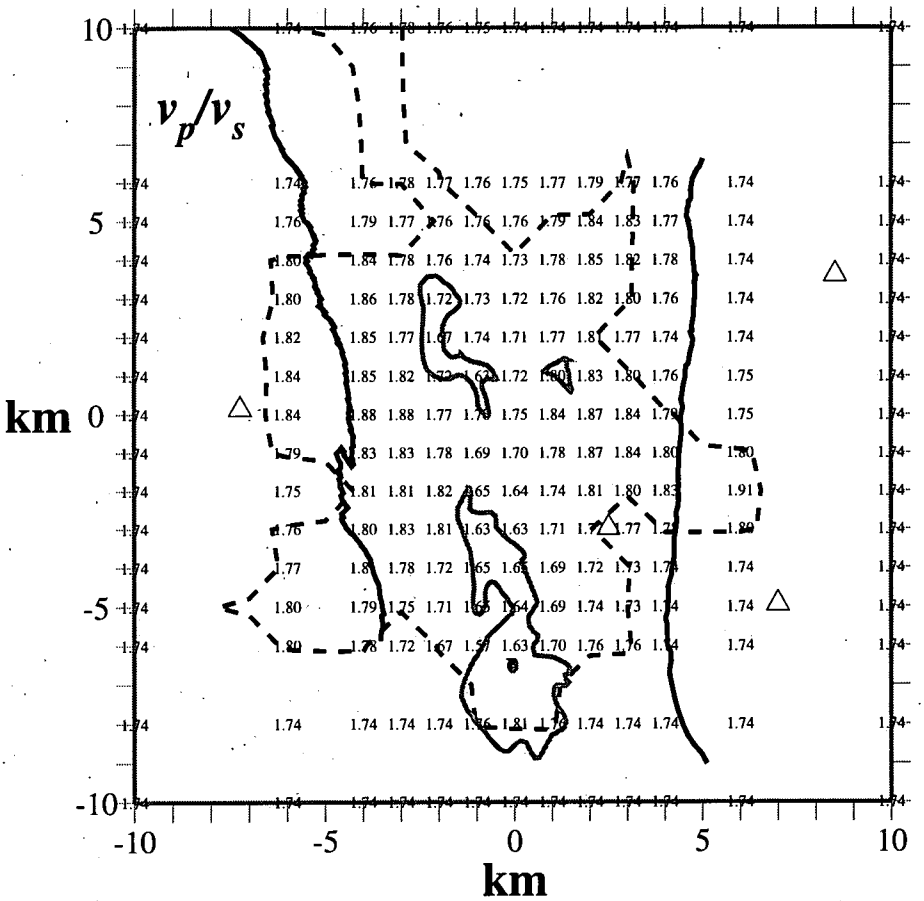

Depth = 1 km

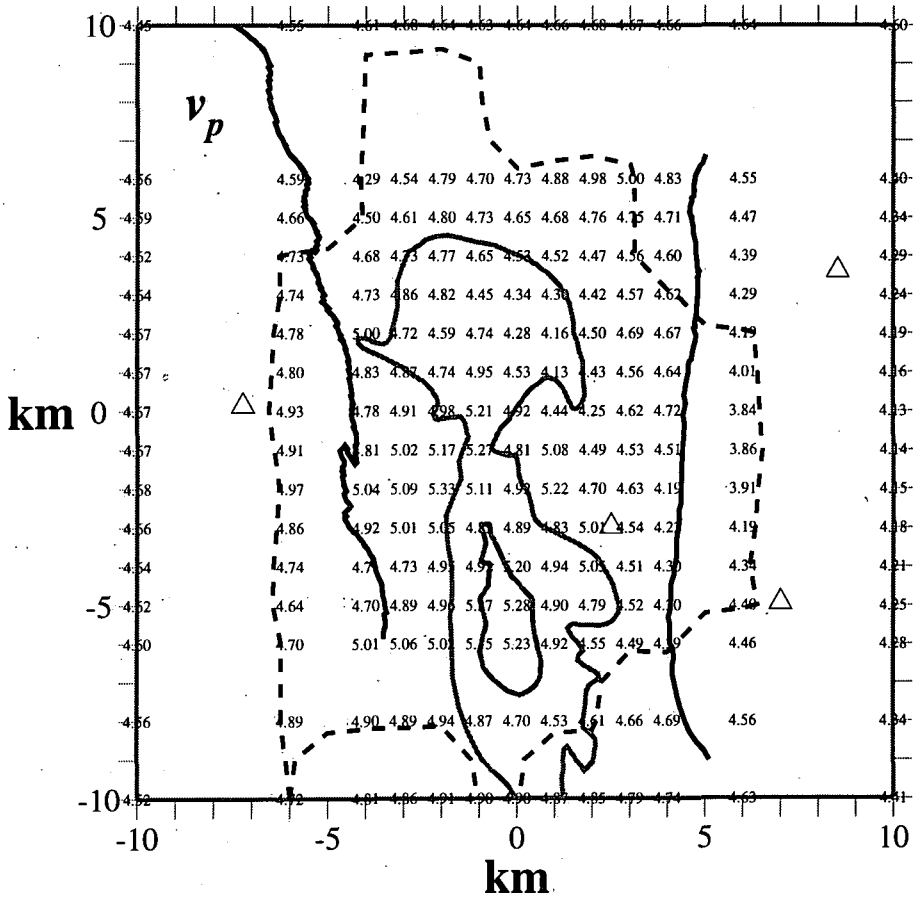

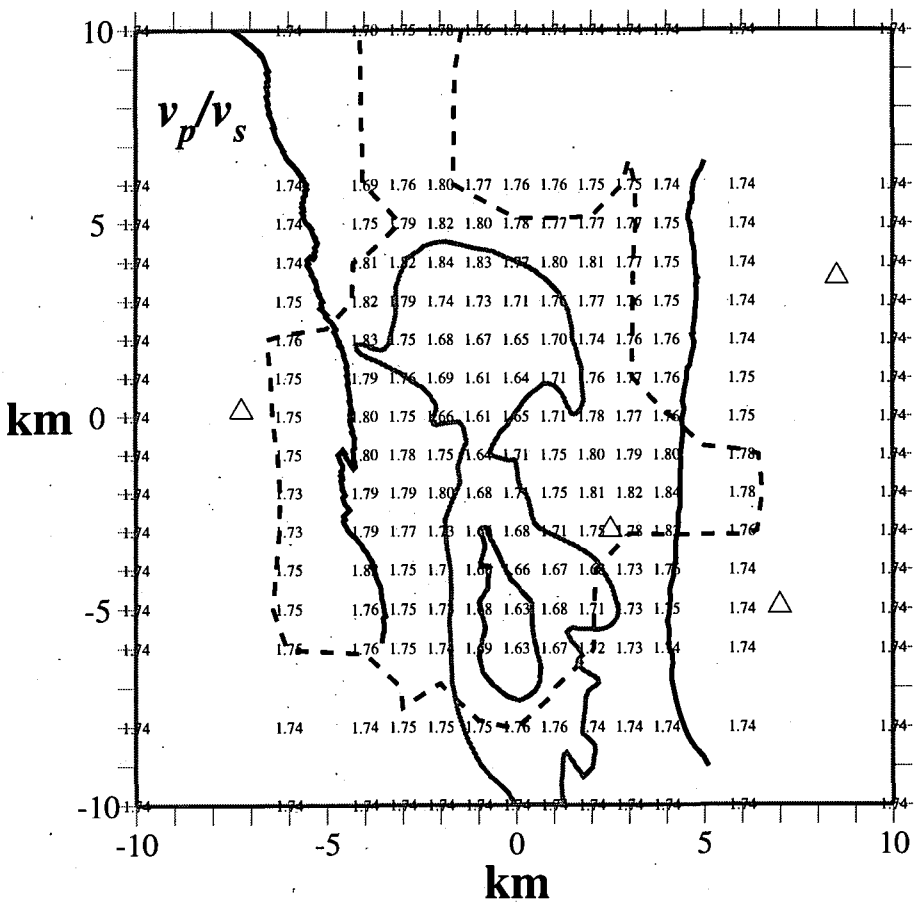

Depth = 2 km

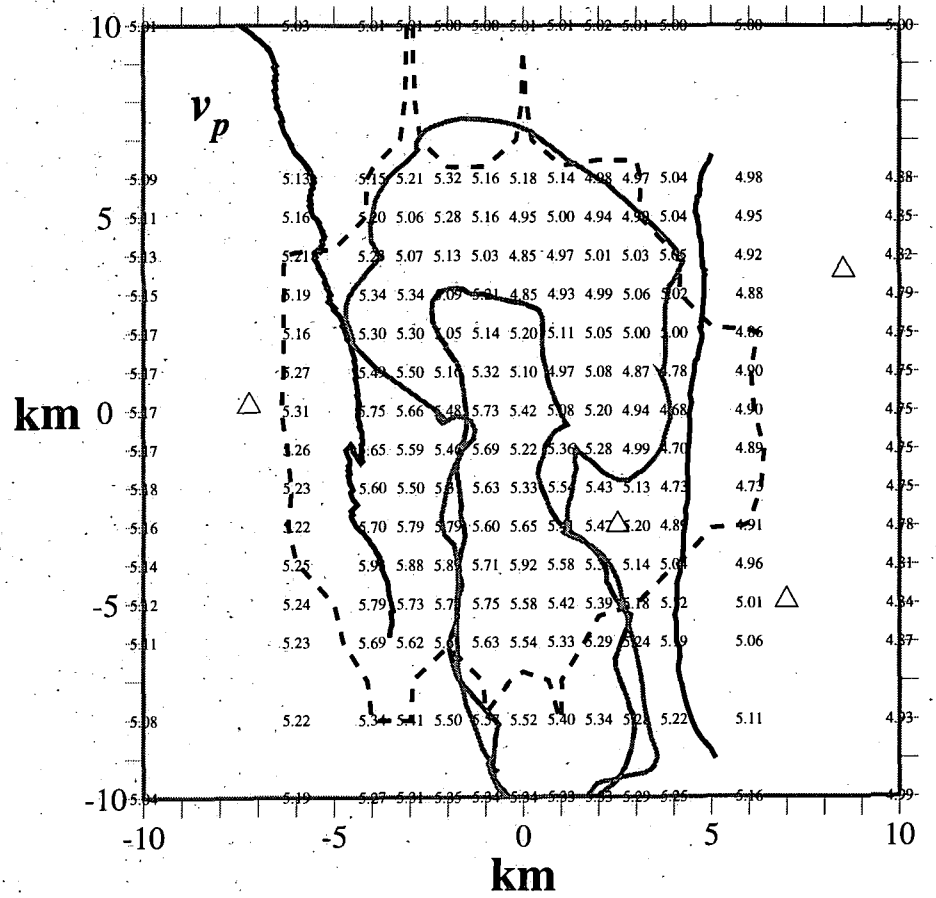

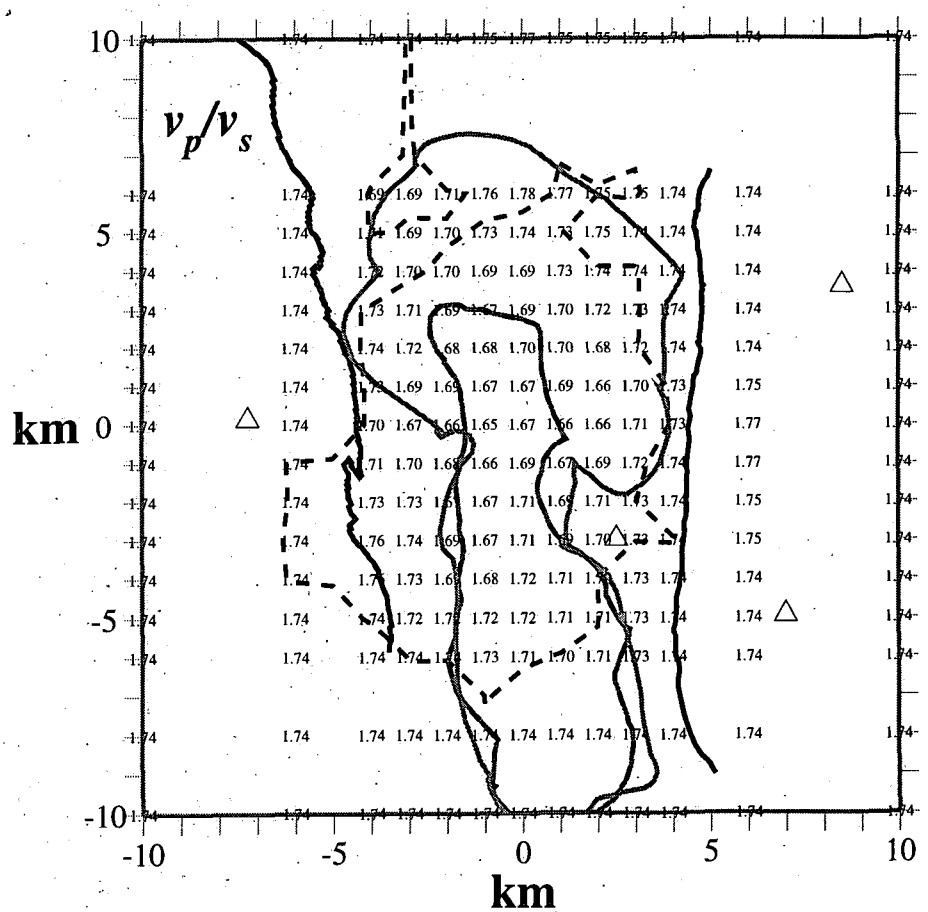

Depth = 3 km

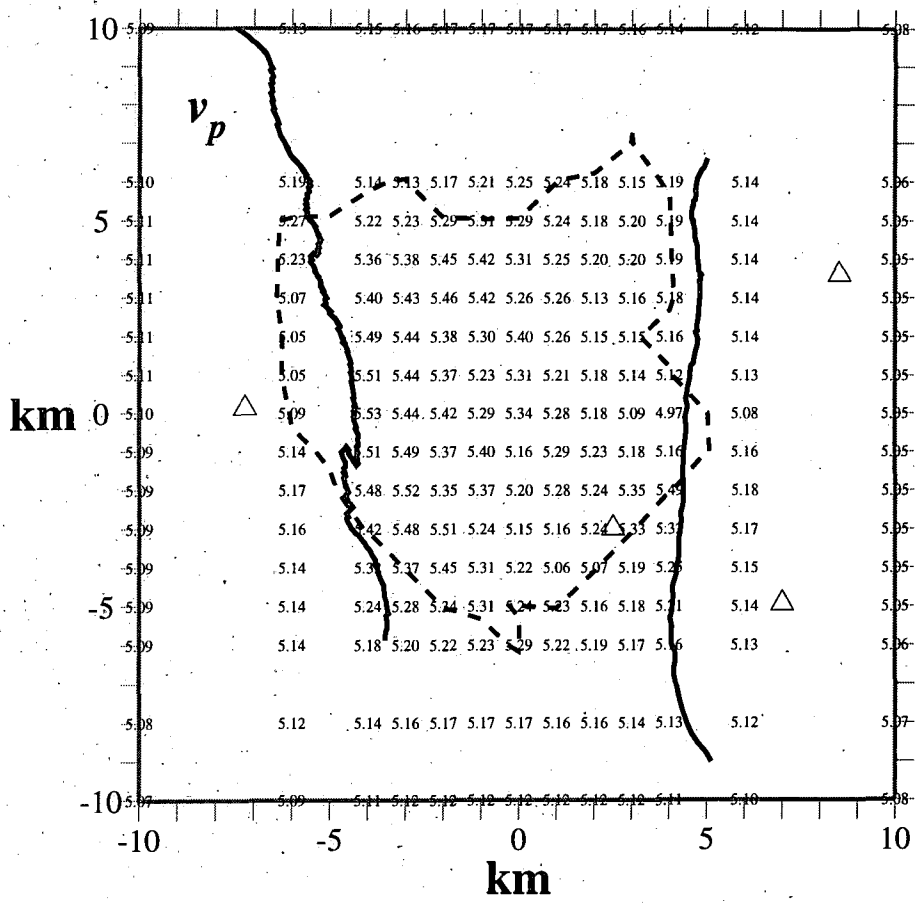

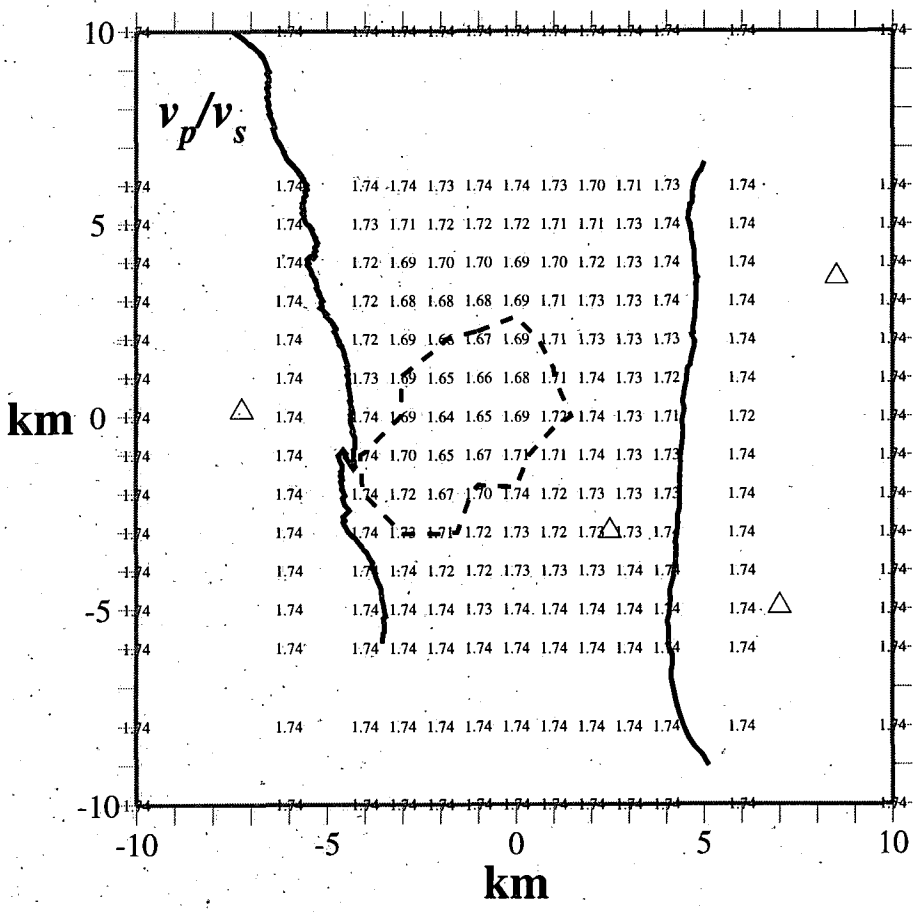

Depth = 4 km

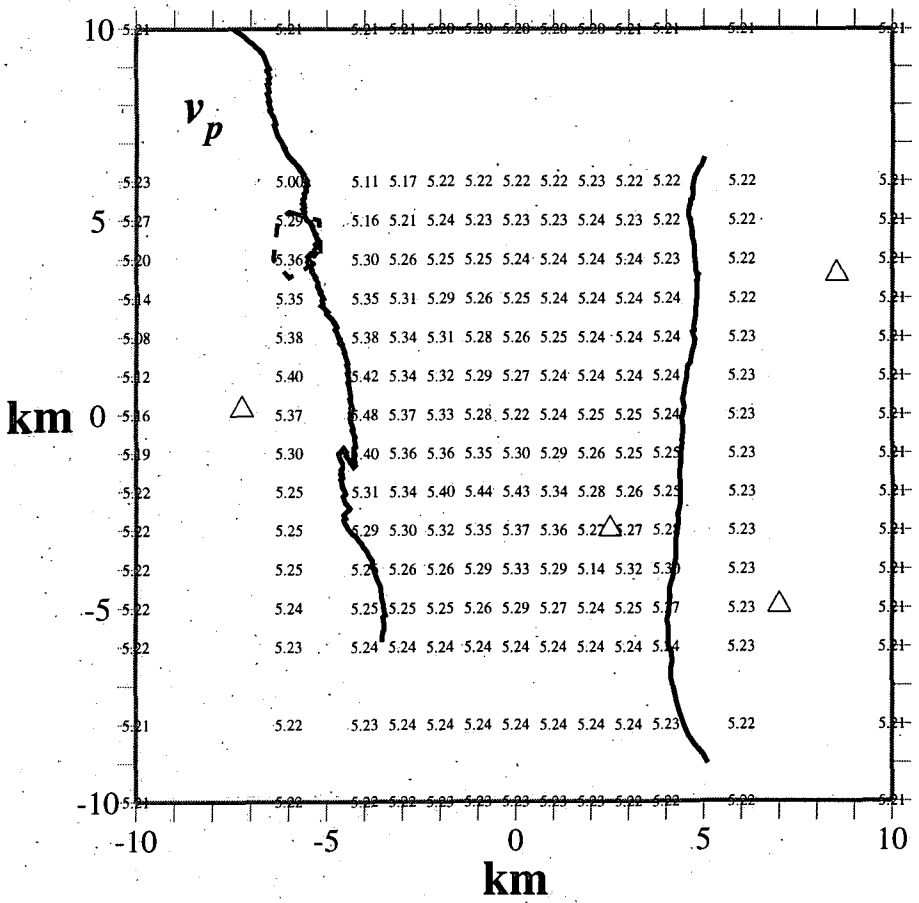

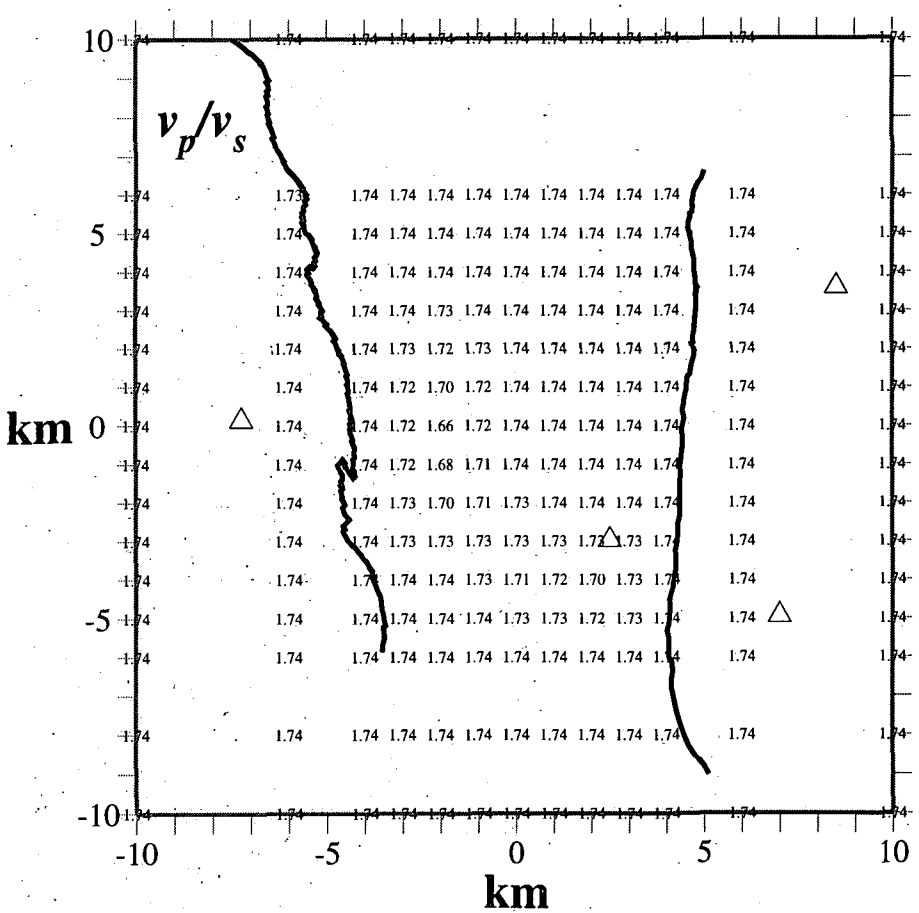

Appendix 9 Final earthquake locations

Final earthquake locations calculated using the three-dimensional wave-speed models. For each earthquake the final RMS travel-time residual are calculated using both the regional one-dimensional and three-dimensional wave speed models. The RMS travel-time residual is calculated using the three-dimensional wave-speed models and is given as a percentage of the RMS travel-time residual calculated using the regional model.

Event number	Latitude (°N)	Longnitude (°W)	Depth (km bsl)	1-d model RMS residual, s	3-d model RMS residual, s	% diff in RMS residual	Events used in tomography
091.230151.1	38:50.195	-122:46.348	1.534	0.093	0.059	63.81	*
091.232026.1	38:50.147	-122:46.358	1.734	0.069	0.049	72.12	*
092.172013.1	38:48.227	-122:45.196	1.459	0.077	0.025	32.27	*
094.004643.1	38:50.571	-122:47.402	1.811	0.046	0.053	113.70	
094.020043.1	38:50.371	-122:48.325	1.473	0.079	0.040	50.27	*
094.055513.1	38:47.523	-122:47.908	1.296	0.030	0.040	134.00	
094.075908.1	38:47.540	-122:47.711	1.015	0.106	0.088	82.41	*
094.080008.1	38:47.520	-122:47.749	1.118	0.042	0.021	49.18	*
094.154930.1	38:47.942	-122:47.940	3.813	0.086	0.023	26.44	*
094.223105.1	38:47.562	-122:44.765	1.433	0.049	0.019	38.13	*
094.224611.1	38:47.107	-122:45.542	0.522	0.056	0.025	44.09	*
095.041156.1	38:48.998	-122:50.052	0.356	0.062	0.039	63.91	*
095.203857.1	38:46.985	-122:46.456	1.571	0.089	0.040	45.40	
096.003948.1	38:48.708	-122:50.199	0.082	0.087	0.129	147.70	
096.195237.1	38:49.455	-122:49.925	1.083	0.082	0.070	85.82	
097.093540.1	38:49.095	-122:48.652	3.258	0.050	0.015	30.11	
098.081016.1	38:49.280	-122:50.141	0.989	0.024	0.010	42.41	*
098.093353.1	38:48.989	-122:50.560	1.364	0.068	0.028	40.90	*
098.132306.1	38:48.687	-122:47.757	1.463	0.104	0.057	54.57	*
098.142119.1	38:49.911	-122:47.282	1.047	0.060	0.033	54.43	*
098.172855.1	38:48.014	-122:44.439	1.923	0.056	0.018	32.07	*
098.194144.1	38:51.127	-122:47.618	2.450	0.059	0.046	78.02	*
099.051717.1	38:47.039	-122:43.118	1.630	0.055	0.033	60.18	*
099.071950.1	38:50.100	-122:52.529	2.232	0.075	0.011	14.87	*
099.082534.1	38:47.861	-122:43.694	4.892	0.059	0.037	63.07	*
099.085008.1	38:47.330	-122:44.812	0.919	0.033	0.033	97.81	*
099.103904.1	38:47.559	-122:46.870	1.844	0.061	0.019	31.80	*
099.172654.1	38:48.953	-122:49.719	0.617	0.079	0.033	41.42	*
099.193503.1	38:48.898	-122:49.513	0.897	0.089	0.086	96.27	*

100.040421.1	38:48.592	-122:49.797	0.630	0.054	0.038	70.99	*
100.063803.1	38:50.061	-122:50.279	1.663	0.078	0.033	42.74	
100.072139.1	38:49.948	-122:49.947	1.536	0.072	0.052	72.57	
100.072355.1	38:49.955	-122:50.029	1.553	0.106	0.115	109.10	
100.160056.1	38:45.893	-122:43.154	0.932	0.057	0.031	54.28	
101.021650.2	38:48.132	-122:46.067	1.082	0.086	0.070	81.19	*
101.073007.1	38:48.832	-122:48.740	2.949	0.049	0.027	55.74	*
101.131840.1	38:46.666	-122:43.227	1.874	0.052	0.027	50.84	*
101.154344.1	38:47.037	-122:45.031	0.769	0.047	0.028	58.89	*
101.184439.1	38:46.165	-122:44.721	1.875	0.052	0.025	49.10	*
102.000244.1	38:47.592	-122:44.710	1.999	0.077	0.025	32.53	*
102.074512.1	38:51.053	-122:47.511	2.421	0.059	0.047	79.00	*
102.155946.1	38:47.324	-122:48.208	3.376	0.041	0.026	64.35	*
103.031713.1	38:47.747	-122:44.105	1.544	0.077	0.042	54.84	*
103.065739.1	38:50.650	-122:44.130	2.680	0.069	0.062	90.14	*
103.105157.1	38:50.585	-122:44.068	2.313	0.079	0.047	59.84	*
103.200103.1	38:48.921	-122:50.036	0.126	0.109	0.082	75.10	*
103.214908.1	38:47.034	-122:43.425	1.826	0.119	0.042	34.87	
104.002347.1	38:47.198	-122:46.899	2.939	0.065	0.059	91.40	*
104.050547.1	38:46.940	-122:46.401	1.453	0.072	0.037	51.17	*
104.073739.1	38:47.135	-122:46.442	1.905	0.095	0.053	55.88	*
104.112505.1	38:45.998	-122:42.908	0.950	0.085	0.075	87.33	
105.011724.1	38:47.226	-122:45.027	3.973	0.067	0.033	49.77	*
105.025005.1	38:49.642	-122:45.388	1.131	0.061	0.026	43.04	*
105.092820.1	38:46.828	-122:43.444	1.889	0.074	0.066	89.32	
105.163806.1	38:49.511	-122:45.881	1.483	0.077	0.043	55.52	
105.172240.1	38:46.155	-122:42.971	0.635	0.091	0.070	77.28	*
105.175448.1	38:47.278	-122:43.080	1.721	0.060	0.052	86.28	*
106.005434.1	38:49.400	-122:50.043	1.115	0.080	0.069	85.67	*
106.012254.1	38:49.000	-122:46.871	1.970	0.048	0.026	53.89	
106.024835.1	38:48.176	-122:48.170	2.139	0.038	0.028	73.57	
106.033104.1	38:48.206	-122:46.093	1.352	0.072	0.032	44.85	*
106.061743.1	38:48.725	-122:48.197	2.157	0.059	0.022	37.48	*
106.073158.1	38:49.200	-122:50.174	0.980	0.056	0.025	44.59	*
106.080310.2	38:47.270	-122:45.223	1.220	0.036	0.033	91.85	
106.095059.1	38:48.992	-122:48.767	3.561	0.080	0.033	41.91	
106.095059.2	38:48.939	-122:48.810	3.575	0.058	0.036	61.77	
106.121658.1	38:48.270	-122:48.142	0.585	0.032	0.017	54.41	
106.121658.2	38:48.103	-122:48.278	0.504	0.033	0.026	77.12	
106.122309.1	38:47.362	-122:46.939	0.000	0.026	0.032	124.10	

106.122309.2	38:47.340	-122:46.877	0.169	0.036	0.029	80.21	
106.125935.1	38:48.675	-122:48.102	2.019	0.069	0.013	19.11	
106.125935.2	38:48.720	-122:48.192	1.732	0.105	0.020	18.71	
106.132857.1	38:49.574	-122:47.543	1.243	0.039	0.044	112.20	
106.132857.2	38:49.502	-122:47.721	0.410	0.159	0.145	91.03	
106.144627.2	38:49.245	-122:47.471	2.34	0.062	0.055	88.30	
106.144627.3	38:49.166	-122:47.478	2.208	0.029	0.014	49.02	
106.160051.1	38:47.399	-122:46.874	2.820	0.069	0.027	39.00	*
106.170850.1	38:47.617	-122:44.748	2.209	0.086	0.046	53.01	*
106.184035.1	38:47.562	-122:44.921	0.861	0.043	0.031	71.72	*
106.213412.1	38:48.620	-122:48.202	1.553	0.062	0.018	28.25	*
106.220554.1	38:49.346	-122:47.179	0.783	0.075	0.043	56.55	*
106.222740.1	38:48.792	-122:49.594	0.861	0.083	0.063	76.67	*
106.222945.1	38:49.267	-122:47.281	0.658	0.069	0.033	47.27	*
106.233408.1	38:46.439	-122:44.901	1.418	0.094	0.075	79.94	*
107.015827.2	38:49.506	-122:49.657	0.967	0.057	0.031	54.53	*
107.025528.1	38:48.051	-122:48.194	1.098	0.025	0.027	106.6	
107.043328.1	38:49.712	-122:48.204	1.157	0.078	0.035	44.71	*
107.045446.1	38:47.198	-122:45.279	0.713	0.054	0.034	63.99	
107.051947.1	38:47.562	-122:46.814	2.251	0.091	0.026	28.93	*
107.094626.1	38:47.217	-122:44.711	0.806	0.081	0.049	60.38	*
107.102853.1	38:49.451	-122:47.540	1.520	0.055	0.023	41.51	*
107.114322.1	38:52.094	-122:49.146	2.446	0.098	0.040	40.52	*
107.131231.1	38:49.947	-122:47.947	1.325	0.067	0.050	75.03	*
107.133652.1	38:48.686	-122:48.169	2.066	0.087	0.039	44.61	*
107.162307.2	38:49.341	-122:46.957	2.168	0.068	0.031	46.50	*
107.163420.2	38:46.216	-122:44.686	2.247	0.102	0.058	56.85	*
107.164134.1	38:49.191	-122:47.103	2.419	0.074	0.038	51.09	*
107.180043.1	38:46.213	-122:44.750	2.177	0.102	0.091	89.26	*
107.183013.2	38:49.073	-122:46.076	1.642	0.050	0.02	39.32	*
107.185943.1	38:47.377	-122:45.225	1.347	0.105	0.063	59.85	*
107.225324.1	38:48.730	-122:48.140	2.988	0.082	0.029	35.87	*
107.234524.2	38:49.606	-122:49.647	1.549	0.101	0.080	78.45	*
107.234734.1	38:49.683	-122:49.621	1.445	0.060	0.041	67.29	*
108.010924.1	38:49.434	-122:49.499	0.802	0.068	0.039	57.38	*
108.012358.1	38:48.137	-122:50.953	3.401	0.058	0.032	54.59	*
108.021016.1	38:47.812	-122:48.767	3.575	0.059	0.023	37.97	*
108.042441.1	38:49.031	-122:47.102	0.715	0.095	0.052	55.44	*
108.042714.1	38:48.915	-122:47.365	0.580	0.055	0.039	71.41	*
108.044458.1	38:47.912	-122:48.242	2.195	0.062	0.030	47.87	*
108.061652.1	38:48.167	-122:46.345	1.486	0.067	0.050	75.41	*

108.083429.1	38:47.377	-122:46.832	2.850	0.081	0.020	24.28	
108.092720.1	38:48.004	-122:48.718	4.001	0.051	0.021	41.77	*
108.103729.1	38:47.569	-122:47.977	1.268	0.048	0.024	49.68	*
108.121807.1	38:49.853	-122:47.955	1.280	0.092	0.033	35.46	*
108.125929.1	38:48.085	-122:49.357	0.821	0.041	0.036	89.11	
108.142340.1	38:49.258	-122:46.191	0.834	0.067	0.037	55.26	*
108.142502.1	38:49.233	-122:46.186	0.940	0.083	0.043	51.56	*
108.160746.1	38:48.797	-122:47.981	3.470	0.078	0.031	39.22	*
108.162130.1	38:49.309	-122:47.780	0.515	0.093	0.070	75.21	*
108.183323.1	38:47.464	-122:45.272	2.314	0.045	0.023	49.95	
108.183323.2	38:47.500	-122:45.316	2.426	0.046	0.019	42.63	
108.195823.1	38:49.070	-122:48.365	3.630	0.071	0.035	50.01	
108.195823.2	38:49.022	-122:48.420	3.248	0.039	0.030	74.85	
108.212940.1	38:48.810	-122:46.497	1.213	0.073	0.053	72.23	
108.212940.2	38:48.813	-122:46.401	1.688	0.059	0.039	65.97	
108.215852.1	38:49.478	-122:47.648	1.452	0.067	0.043	63.82	
108.215852.2	38:49.527	-122:47.605	1.227	0.070	0.024	34.68	
108.235853.1	38:50.219	-122:48.215	1.137	0.084	0.075	88.77	
108.235853.2	38:50.194	-122:48.178	0.915	0.043	0.021	48.00	
109.000116.1	38:48.564	-122:46.476	1.829	0.041	0.025	61.76	
109.000116.2	38:48.549	-122:46.438	1.794	0.041	0.037	89.08	
109.004250.1	38:48.020	-122:46.516	1.477	0.055	0.029	52.55	
109.004250.2	38:48.005	-122:46.568	1.237	0.043	0.034	78.23	
109.020058.1	38:48.285	-122:46.539	1.580	0.050	0.040	79.15	
109.044334.1	38:49.430	-122:47.411	1.789	0.107	0.096	90.01	
109.044334.2	38:49.403	-122:47.445	1.795	0.047	0.034	74.09	
109.054442.1	38:51.018	-122:49.091	1.888	0.096	0.019	19.69	
109.054442.2	38:50.917	-122:49.099	1.633	0.061	0.025	41.01	
109.070015.1	38:47.052	-122:45.270	0.428	0.052	0.030	58.29	
109.070015.2	38:47.012	-122:45.256	0.702	0.026	0.037	141.00	
109.094056.1	38:50.369	-122:48.885	1.597	0.082	0.066	80.40	
109.094056.2	38:50.355	-122:48.895	1.316	0.061	0.036	57.98	
109.120502.1	38:45.409	-122:43.505	2.983	0.044	0.014	33.11	*
109.132027.1	38:49.114	-122:50.233	0.604	0.015	0.014	92.33	*
109.142417.1	38:49.260	-122:48.352	3.179	0.047	0.021	44.56	*
109.143901.1	38:49.231	-122:47.498	2.262	0.024	0.010	40.26	*
109.144419.1	38:49.295	-122:48.333	3.054	0.048	0.025	52.15	*
109.183213.1	38:50.032	-122:49.661	2.030	0.020	0.018	86.60	*
109.190413.1	38:49.343	-122:49.299	1.480	0.026	0.020	73.87	*
109.194700.1	38:50.551	-122:46.122	1.683	0.031	0.013	42.21	*
109.232135.1	38:47.781	-122:45.021	1.921	0.015	0.036	233.90	
110.005936.1	38:48.452	-122:46.843	3.532	0.128	0.123	96.58	

110.005936.2	38:48.555	-122:46.888	3.378	0.034	0.016	46.31	
110.204504.1	38:49.519	-122:47.335	0.751	0.061	0.057	93.84	
110.204504.2	38:49.590	-122:47.252	0.517	0.043	0.057	130.40	
111.002359.1	38:46.995	-122:45.330	0.000	0.103	0.086	82.97	
111.002359.2	38:47.058	-122:45.234	0.723	0.045	0.030	67.10	
111.012558.1	38:47.606	-122:46.939	2.885	0.106	0.079	74.10	
111.012558.2	38:47.707	-122:46.949	2.878	0.059	0.014	23.28	
111.025530.1	38:48.259	-122:49.087	1.000	0.047	0.028	60.33	
111.025530.2	38:48.327	-122:49.160	0.545	0.050	0.049	98.63	
111.030149.1	38:48.765	-122:48.537	3.643	0.088	0.017	19.06	
111.030149.2	38:48.780	-122:48.565	3.704	0.057	0.030	51.97	
111.035226.2	38:47.368	-122:46.116	0.202	0.042	0.046	110.20	
111.035226.3	38:47.418	-122:45.972	0.000	0.058	0.026	44.35	
111.093646.1	38:47.953	-122:44.447	1.882	0.092	0.075	81.67	*
112.183823.1	38:49.013	-122:46.738	2.051	0.102	0.076	74.40	
112.183823.2	38:49.041	-122:46.778	1.988	0.049	0.025	50.73	
112.190610.1	38:49.556	-122:47.670	1.237	0.162	0.209	128.70	
112.190610.2	38:49.219	-122:47.540	0.463	0.055	0.081	146.90	
112.190714.1	38:48.330	-122:46.807	0.694	0.040	0.039	95.88	
112.190714.2	38:48.446	-122:46.729	0.006	0.099	0.061	61.45	
112.190937.2	38:49.237	-122:47.726	0.616	0.040	0.042	105.10	
112.190937.3	38:49.241	-122:47.646	0.483	0.035	0.013	37.80	
112.190937.1	38:47.300	-122:45.752	0.185	0.052	0.032	61.63	
112.190937.2	38:47.314	-122:45.787	0.305	0.044	0.023	52.43	
112.191150.4	38:47.047	-122:45.544	0.158	0.082	0.068	82.23	
112.191524.2	38:47.982	-122:44.885	1.091	0.061	0.040	65.88	
112.192656.2	38:48.877	-122:49.917	0.559	0.043	0.045	105.30	
112.204619.1	38:49.226	-122:46.765	2.052	0.082	0.042	50.78	
112.204619.2	38:49.248	-122:46.799	1.540	0.050	0.023	46.08	
112.205228.1	38:48.386	-122:46.961	1.642	0.076	0.035	45.49	
112.205228.2	38:48.406	-122:46.881	1.473	0.049	0.026	52.78	
112.211245.1	38:48.922	-122:47.534	0.266	0.058	0.068	116.00	
112.211245.2	38:49.028	-122:47.484	0.622	0.058	0.067	113.90	
113.021008.1	38:48.763	-122:48.340	2.050	0.111	0.105	94.24	
113.021008.2	38:48.730	-122:48.327	1.808	0.061	0.016	25.61	
113.033735.1	38:49.180	-122:47.634	3.872	0.053	0.028	53.28	
113.033735.2	38:49.102	-122:47.546	3.292	0.051	0.024	47.14	
113.044738.1	38:46.413	-122:46.247	2.772	0.092	0.030	32.96	*
113.063533.2	38:48.410	-122:45.430	1.394	0.056	0.050	89.99	
113.065243.2	38:49.089	-122:48.383	3.259	0.055	0.031	55.77	
113.193101.2	38:46.759	-122:43.580	1.257	0.046	0.039	84.96	
113.203615.1	38:47.446	-122:46.680	2.365	0.067	0.049	73.05	

113.203615.2	38:47.398	-122:46.706	2.633	0.078	0.029	36.74	
113.210118.1	38:48.611	-122:48.324	1.503	0.074	0.037	50.34	
113.210118.2	38:48.702	-122:48.365	1.675	0.081	0.037	45.89	
114.015820.1	38:47.557	-122:45.133	2.159	0.088	0.054	61.43	*
114.021729.1	38:51.498	-122:47.810	1.291	0.050	0.122	246.1	
114.094346.1	38:47.356	-122:46.596	2.271	0.065	0.040	61.25	*
114.102307.1	38:49.160	-122:49.588	0.996	0.063	0.052	82.72	
114.112308.1	38:49.177	-122:48.694	3.428	0.102	0.023	23.12	*
114.115429.2	38:50.061	-122:49.545	1.968	0.098	0.074	74.64	*
114.124939.1	38:48.648	-122:46.838	1.843	0.050	0.027	53.80	*
114.141635.1	38:50.319	-122:49.474	2.269	0.081	0.069	85.05	*
114.141808.1	38:48.200	-122:48.747	0.784	0.046	0.036	77.69	*
114.212724.1	38:49.721	-122:49.290	1.294	0.067	0.035	51.47	*
114.214421.1	38:47.872	-122:46.084	2.418	0.073	0.023	31.03	*
115.003727.1	38:46.213	-122:44.702	2.267	0.064	0.052	80.64	
115.003727.2	38:46.281	-122:44.704	2.121	0.063	0.034	54.64	
115.022239.1	38:46.233	-122:44.704	2.233	0.071	0.059	83.70	*
115.022452.1	38:46.203	-122:44.684	2.305	0.062	0.020	32.09	*
115.045418.1	38:46.699	-122:43.441	1.198	0.048	0.034	72.14	*
115.062846.1	38:49.417	-122:47.550	1.609	0.067	0.028	42.50	*
115.085212.2	38:49.206	-122:48.363	3.421	0.081	0.030	36.79	*
115.100049.1	38:48.082	-122:46.339	1.472	0.098	0.072	73.71	*
115.110449.1	38:47.329	-122:46.743	2.783	0.091	0.028	30.56	
115.125055.1	38:47.333	-122:45.101	1.186	0.049	0.030	60.67	*
115.134541.1	38:47.776	-122:44.969	1.547	0.072	0.060	83.82	*
115.142606.1	38:48.210	-122:48.192	1.691	0.084	0.065	77.75	*
115.142606.2	38:48.206	-122:48.197	1.836	0.063	0.030	48.23	*
115.143339.1	38:48.214	-122:48.130	1.977	0.089	0.026	28.86	*
115.150203.1	38:47.182	-122:46.181	0.163	0.046	0.045	96.67	*
115.155752.1	38:47.172	-122:46.384	2.103	0.070	0.022	31.59	*
115.160329.1	38:49.186	-122:48.370	3.324	0.099	0.023	23.28	*
115.161502.1	38:50.150	-122:49.602	1.967	0.040	0.024	59.88	*
115.180654.1	38:47.433	-122:46.620	0.263	0.049	0.038	77.85	*
115.192505.1	38:49.163	-122:48.316	3.396	0.114	0.033	28.88	*
115.214304.1	38:48.209	-122:48.570	0.482	0.064	0.047	73.68	*
115.225530.1	38:47.389	-122:46.885	4.075	0.086	0.050	58.72	*
116.031113.1	38:47.235	-122:46.416	1.826	0.083	0.040	48.18	*
116.040529.1	38:48.106	-122:48.231	3.949	0.071	0.047	65.34	*
116.050252.1	38:47.630	-122:44.887	1.515	0.058	0.023	39.23	*
116.052923.1	38:48.053	-122:48.371	3.918	0.085	0.026	30.70	*
116.063101.1	38:47.320	-122:46.516	2.130	0.057	0.016	28.07	*
116.100326.1	38:49.084	-122:48.736	3.325	0.108	0.023	21.28	

116.100326.2	38:49.169	-122:48.720	3.103	0.066	0.041	61.87	
116.114418.1	38:48.752	-122:46.506	1.988	0.065	0.053	82.06	
116.114418.2	38:48.735	-122:46.448	1.983	0.052	0.035	67.00	*
116.120620.1	38:47.625	-122:46.872	2.033	0.076	0.017	22.63	*
116.123207.1	38:49.415	-122:50.256	0.589	0.081	0.083	102.10	
116.153747.1	38:49.515	-122:47.136	1.428	0.063	0.026	41.70	*
116.171258.1	38:49.102	-122:48.749	3.316	0.041	0.012	29.83	*
116.201219.1	38:49.402	-122:46.726	1.090	0.190	0.190	100.10	
116.220821.1	38:45.597	-122:43.696	1.174	0.083	0.065	77.88	*
117.004516.1	38:48.222	-122:48.397	0.970	0.042	0.037	88.02	
117.011824.1	38:47.217	-122:45.137	1.816	0.057	0.022	37.98	*
117.062926.1	38:49.147	-122:48.252	3.512	0.104	0.025	24.20	*
117.102704.1	38:49.646	-122:48.538	1.008	0.084	0.052	61.07	*
117.111310.1	38:46.856	-122:44.514	0.280	0.085	0.050	58.98	*
117.132033.1	38:49.254	-122:47.598	1.650	0.058	0.040	68.27	*
117.144000.1	38:52.500	-122:48.790	2.956	0.101	0.038	38.10	*
117.150450.1	38:49.358	-122:46.929	1.869	0.056	0.042	75.28	*
117.153329.1	38:48.242	-122:48.643	1.517	0.083	0.050	60.61	*
117.154718.1	38:48.185	-122:48.624	1.554	0.051	0.034	67.75	*
117.154906.1	38:47.228	-122:46.485	1.105	0.060	0.031	50.94	*
117.184401.1	38:50.397	-122:49.106	0.533	0.089	0.074	82.29	
118.020136.1	38:50.045	-122:49.639	2.374	0.059	0.019	33.11	*
118.020914.1	38:49.333	-122:46.807	2.125	0.072	0.047	65.14	*
118.033015.1	38:48.232	-122:48.638	0.680	0.066	0.057	85.02	*
118.033015.2	38:47.178	-122:46.393	2.552	0.072	0.021	29.03	*
118.051552.1	38:47.396	-122:46.555	2.052	0.063	0.017	26.36	*
118.062541.1	38:49.971	-122:48.595	1.750	0.092	0.064	69.58	*
118.154843.1	38:45.962	-122:42.346	5.249	0.052	0.055	104.30	
118.154843.2	38:46.210	-122:41.787	4.253	0.060	0.051	85.64	
118.160954.2	38:47.323	-122:54.671	5.692	0.085	0.066	78.19	*
118.171534.1	38:49.210	-122:48.502	3.542	0.122	0.030	24.69	*
118.183234.1	38:48.343	-122:46.798	3.772	0.059	0.035	58.43	*
118.213911.1	38:48.727	-122:48.292	1.911	0.075	0.027	35.57	*
119.021240.1	38:46.284	-122:44.671	1.877	0.084	0.046	54.09	*
119.023146.1	38:47.421	-122:46.739	2.287	0.071	0.025	35.79	*
119.061323.1	38:49.154	-122:47.375	1.926	0.068	0.018	26.62	*
119.063749.1	38:50.357	-122:46.461	1.522	0.052	0.035	67.59	*
119.115615.1	38:48.847	-122:49.922	0.964	0.074	0.064	86.07	*
119.124754.1	38:49.641	-122:47.681	1.776	0.062	0.028	45.23	*
119.152525.1	38:49.003	-122:49.004	0.331	0.076	0.039	51.85	*
119.221128.1	38:48.310	-122:46.941	1.463	0.047	0.040	84.40	*
120.013734.1	38:49.090	-122:48.697	3.100	0.096	0.044	45.66	*

120.021319.1	38:48.009	-122:48.415	2.170	0.073	0.030	41.57	*
120.023443.2	38:50.243	-122:49.281	1.500	0.054	0.039	71.38	*
120.075101.1	38:47.639	-122:46.853	2.330	0.068	0.016	23.15	*
120.095348.1	38:45.329	-122:43.039	1.098	0.066	0.058	87.96	*
120.151019.1	38:47.567	-122:45.196	2.365	0.054	0.035	65.27	*
120.194215.1	38:47.396	-122:46.553	2.281	0.069	0.019	27.53	*
120.195132.2	38:47.156	-122:46.496	1.908	0.070	0.028	39.58	
120.225016.1	38:48.719	-122:49.153	0.402	0.061	0.044	72.22	*
121.002440.1	38:49.109	-122:48.728	3.187	0.065	0.021	32.42	*
121.013136.1	38:45.582	-122:43.568	0.701	0.044	0.033	75.80	*
121.022005.1	38:48.544	-122:46.298	2.732	0.056	0.031	56.25	*
121.054750.1	38:47.278	-122:46.940	3.440	0.068	0.022	32.33	*
121.055952.1	38:47.924	-122:56.438	5.469	0.041	0.029	70.92	
121.065532.1	38:48.083	-122:48.411	0.169	0.059	0.053	89.41	*
121.082410.1	38:48.869	-122:48.400	3.715	0.044	0.020	44.14	*
121.111438.1	38:48.922	-122:47.112	0.844	0.048	0.037	77.51	*
121.141656.1	38:47.794	-122:44.962	2.031	0.053	0.026	48.28	*
121.142747.1	38:47.313	-122:46.856	0.362	0.034	0.029	85.31	*

Geophysical Research Letters

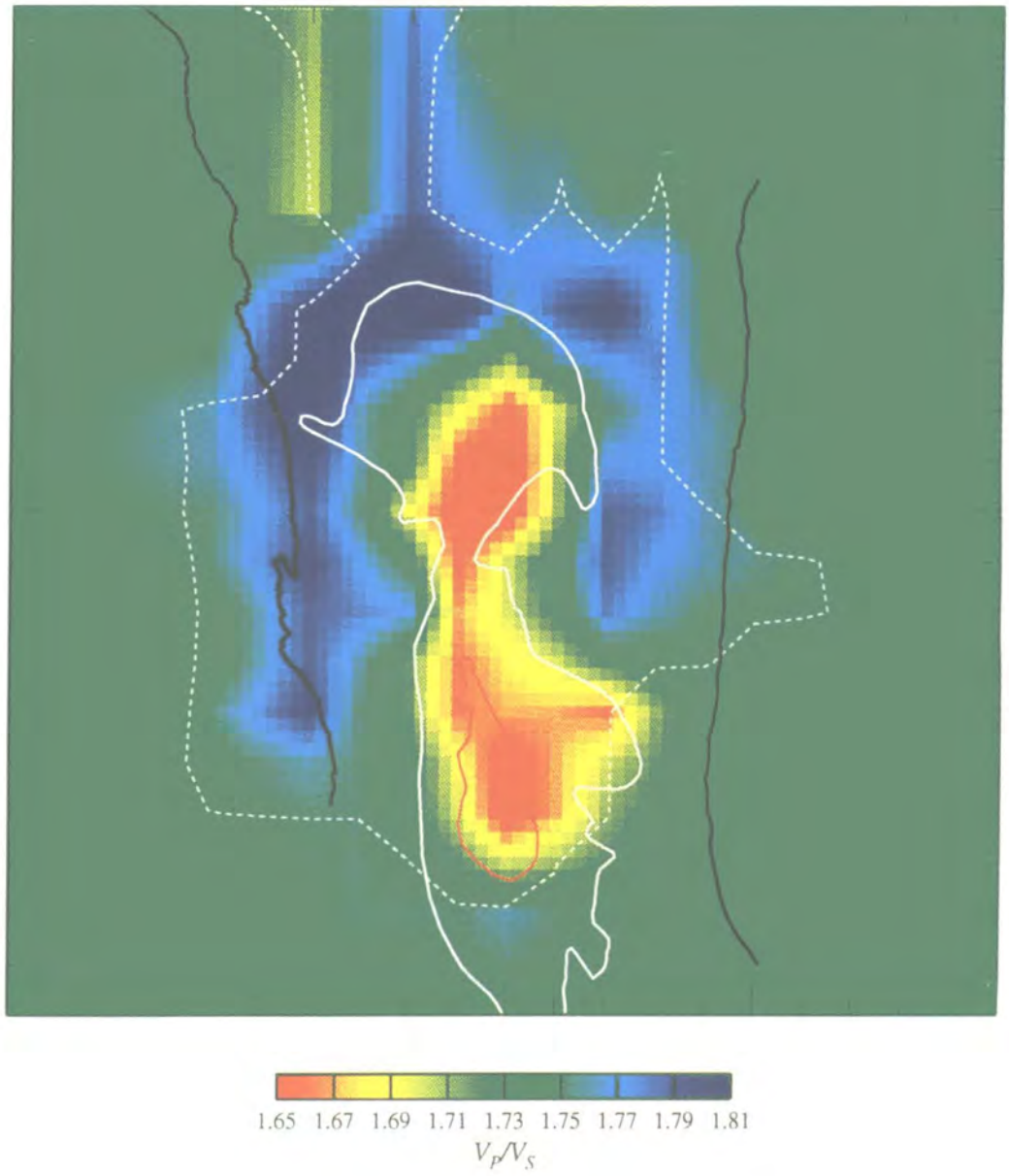

ARCH 15, 1996

Volume 23 Number 6

AMERICAN GEOPHYSICAL UNION

GEOPHYSICAL RESEARCH LETTERS, VOL. 23, NO. 6, PAGES 685-688, MARCH 15, 1996

Three-dimensional seismic image of a geothermal reservoir: The Geysers, California

B. R. Julian
U. S. Geological Survey, Menlo Park California

A. Ross[1] and G. R. Foulger[1]
Department of Geological Sciences, University of Durham, UK

J. R. Evans
U. S. Geological Survey, Menlo Park California

Abstract. Three-dimensional seismic travel-time tomography of The Geysers geothermal area, in the coast ranges of northern California, shows a strong (–9%) anomaly in V_P/V_S, the ratio of the compressional and shear wave speeds, that is not evident in V_P alone and corresponds closely to the most intensively exploited part of the geothermal reservoir. This anomaly probably indicates low pore pressure and relatively dry conditions, caused partly by boiling of pore water as steam is extracted. Steam pressure decreases over the last decade have probably caused seismologically measurable changes in wave speeds. Tomographic measurement of V_P/V_S is a promising technique both for identifying geothermal resources and for monitoring them during exploitation.

Introduction

The Geysers is the world's largest producer of geothermal electricity. Large-scale steam production and electricity generation began about 1970, accelerated in the early 1980s, and peaked in 1987 at about 3.5×10^3 kg s^{-1} and 2000 MW. Since the late 1980s production has decreased by about 10%/yr [*Barker et al.*, 1992] because of a drop in steam pressure as pore water has boiled away. This unanticipated decline emphasizes the need for methods of measuring conditions within geothermal reservoirs. Here we use local-earthquake travel-time tomography to obtain three-dimensional images of seismic-wave speeds at The Geysers, and find that the ratio of the wave speeds, V_P/V_S, is relatively insensitive to lithology but quite sensitive to the compressibility of the pore fluid, and thus its state of saturation.

The Geysers reservoir (Figure 1) occupies metamorphosed marine sedimentary and igneous rocks of the Franciscan Complex and the upper portion of a "felsite" batholith [*Thompson*, 1992]. It underlies an area of about 75 km^2 and extends from near the surface to at least 3 km below sea level. The heat source is unknown, but surface gravity and teleseismic travel-time anomalies near Mt. Hannah are consistent with a body of partial melt at mid-crustal depths [*Iyer et al.*, 1981]. The reservoir temperature is about 240°C and the pre-production pressure was about 3.5 MPa (35 bars) [*Barker et al.*, 1992]. Temperatures up to 350°C and anomalous isotope ratios in the northwestern part of the field may indicate a young, perhaps partly molten and degassing, pluton there [*Walters et al.*, 1992].

The geothermal area is very active seismically, generating about 140 earthquakes per month with $M_L > 1.2$. Although pre-production earthquake rates are uncertain [*Ludwin and Bufe*, 1980], it is clear that most of the current seismicity is induced, by both steam extraction and liquid injection [*Stark*, 1990]. The most active zone is within the reservoir, and activity has increased and spread laterally along with exploitation.

Data

We use these microearthquakes to study the structure of the geothermal reservoir, applying tomographic inversion techniques to 4032 *P*- and 944 *S*-wave arrival times from 185 earthquakes recorded on dense local seismometer networks to derive three-dimensional models of the compressional-wave speed V_P and the compressional : shear wave-speed ratio V_P/V_S. The study volume is 20 × 20 km in surface area and ranges in depth from -1 km to 6 km. The data were recorded in April 1991 by 32 stations of the permanent seismometer networks of the UNOCAL Corporation and the U. S. Geological Survey (USGS) and by 15 portable PASSCAL instruments (Figure 1). Arrival times were measured from digitized seismograms using an interactive graphical computer program, and are accurate to about 0.01 s for *P* waves and 0.02 s for *S* waves. All *S*-wave measurements are from horizontal-component seismograms. All the earthquakes in the geothermal area are shallower than about 4 km (Figure 2).

Inversion Method

The arrival times were inverted using the computer program *SIMULPS12* [*Evans et al.*, 1994], which solves simultaneously for earthquake locations and crustal structure (V_P and optionally V_P/V_S) by the iterative damped-least-squares method. At each iteration step, ray paths and earthquake locations are fully updated. The program *VELEST* [*Kissling et al.*, 1994] provided a one-dimensional V_P model used as the starting point for the inversion. The initial estimate of 1.74 for the ratio V_P/V_S is the median of 126 values obtained from Wadati diagrams for events with five or more S–P time measurements. We derived three-dimensional

[1]Also at U. S. Geological Survey, Menlo Park, Calif.

Paper number 95GL03321
0094-8534/96/95GL-03321$03.00

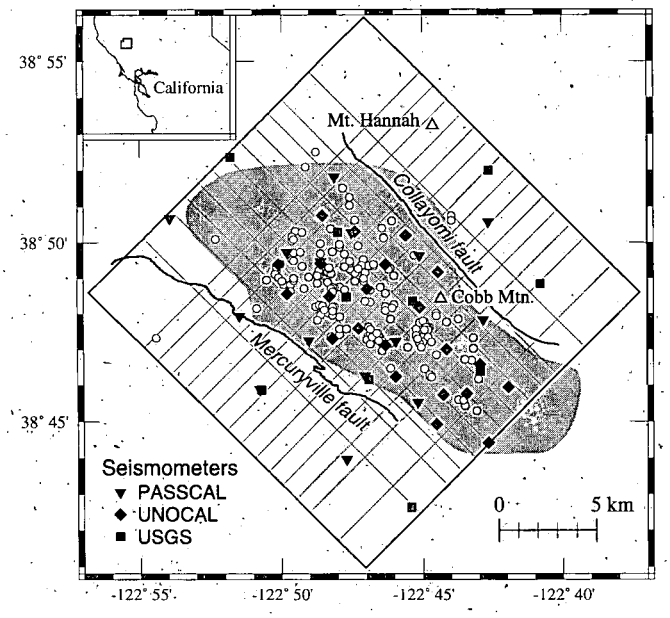

Figure 1. Map of The Geysers geothermal area, showing seismometer locations. Gray shading: geothermal field (*e.g. Thompson*, 1992). Large square: surface projection of the volume studied, with grid lines in gray. Crosses: epicenters of earthquakes used.

models in a series of "graded" inversions, in which a relatively coarse initial grid (63 nodes, 10-km horizontal spacing) is made progressively finer during successive inversions. The final grid has 1232 nodes with 1-km spacing. The final model gives a 70% reduction in variance, with RMS residuals of 0.022 s for P waves and 0.048 s for S waves. To assess the resolution of the results, we evaluate at each node a *spread* function, which measures the distance over which wave speeds are averaged [*Foulger et al.*, 1995]. In the main, the region shallower than 3 km is best resolved (Figures 3 & 4).

Results

The compressional-wave speed V_P varies horizontally by ±8.6% (RMS deviation) in the well resolved region above 3 km (Figure 3). The V_P model agrees broadly with those obtained in an early tomographic study of the coast ranges based on sparse USGS network data [*Eberhart-Phillips*, 1986] and a recent higher-resolution study of the central and northwest Geysers based on data from the UNOCAL network [*Zucca et al.*, 1993]. The regions of low V_P at Cobb Mtn. and northeast of the Collayomi fault are attributable to rocks of the Great Valley sequence and the Clear Lake volcanics [*Hearn et al.*, 1981]. V_P is systematically about 10% lower in the northwestern than in the central part of the reservoir at all well resolved depths. This anomaly is too large to be the effect of high temperature on the elasticity of minerals (about 3% for a 100°C change) and most of it must reflect variations in lithology or in the compressibility of the pore fluid.

Compared with V_P, variations in the wave-speed ratio V_P/V_S (Figure 4) are weaker (< ±3% RMS deviation) and have a simpler distribution. By far the strongest V_P/V_S anomaly (about −9%) coincides closely with the most intensively exploited part of the reservoir at depths of −1 to 2 km. At sea level this anomaly consists of two separate parts, as does the reservoir. The anomaly does not extend as far to either the northwest or the southeast as the reservoir. In the southeast, this discrepancy may be an artifact of limited resolution, but in the northwest the difference is real. A high-V_P/V_S "halo" surrounds the reservoir at depths down to 1 km, but this may be an artifact of limited resolution and high values may actually extend to greater distances.

Discussion

Table 1 gives theoretical estimates of the V_P/V_S anomalies that would be caused by differences in pore-fluid phase, temperature, and pore pressure, for rocks with porosities of zero and 0.02, the approximate value in the reservoir. For zero porosity, the V_P/V_S ratio equals that of the rock matrix, and the effects of pressure and temperature are much too small to contribute significantly to the observed anomaly. At finite porosities, the compressibility of the pore fluid strongly affects V_P/V_S. The largest effect is caused by the contrast between liquid and vapor, although the dependence of the vapor's compressibility on temperature and pressure is also significant.

The V_P/V_S anomaly is probably caused mostly by vapor domination. The reservoir was vapor-rich in its natural state, whereas the surrounding rocks are not, so the reservoir probably had a large V_P/V_S anomaly before exploitation began. This conclusion is supported by the results of a one-dimensional seismic study of the production area in 1984 [*O'Connell*, 1986], which found low V_P/V_S values at depths from 0 to 2 km. The magnitude of the anomaly in 1991 (−9%) could be explained entirely by the difference between water vapor in the reservoir and liquid water in the surrounding rocks, on the basis of the sensitivities in Table 1.

Production probably has increased the magnitude of the anomaly and changed its spatial variation, both by boiling away interstitial liquid and by decreasing steam pressure. Between 1968 and 1988, borehole pressures decreased by as much as 2.0 MPa in places, and they vary spatially by more than 1.0 MPa [*Barker et al.*, 1992], which could cause V_P/V_S variations of 6.6% or more. The two largest pressure minima coincide with the two V_P/V_S minima found at depths of 0 and 1 km from tomography.

High temperatures in the northwest Geysers can not explain high V_P/V_S there, because the temperature effect is smallest at high temperature and low pressure, so that the lower sensitivities from Table 1 apply.

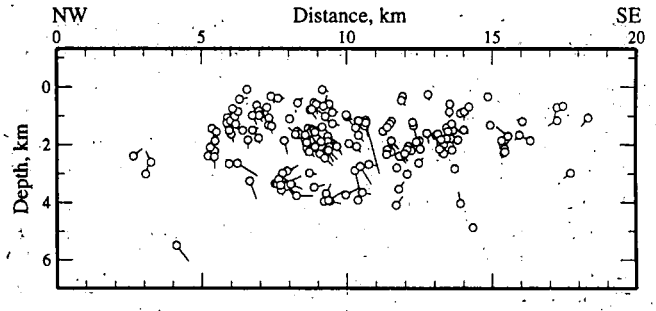

Figure 2. Northwest-southeast cross-section showing locations of earthquakes used. Lines connect locations determined using three-dimensional crustal model (circles) and one-dimensional starting model. Earthquakes are virtually absent below 4 km in the geothermal field.

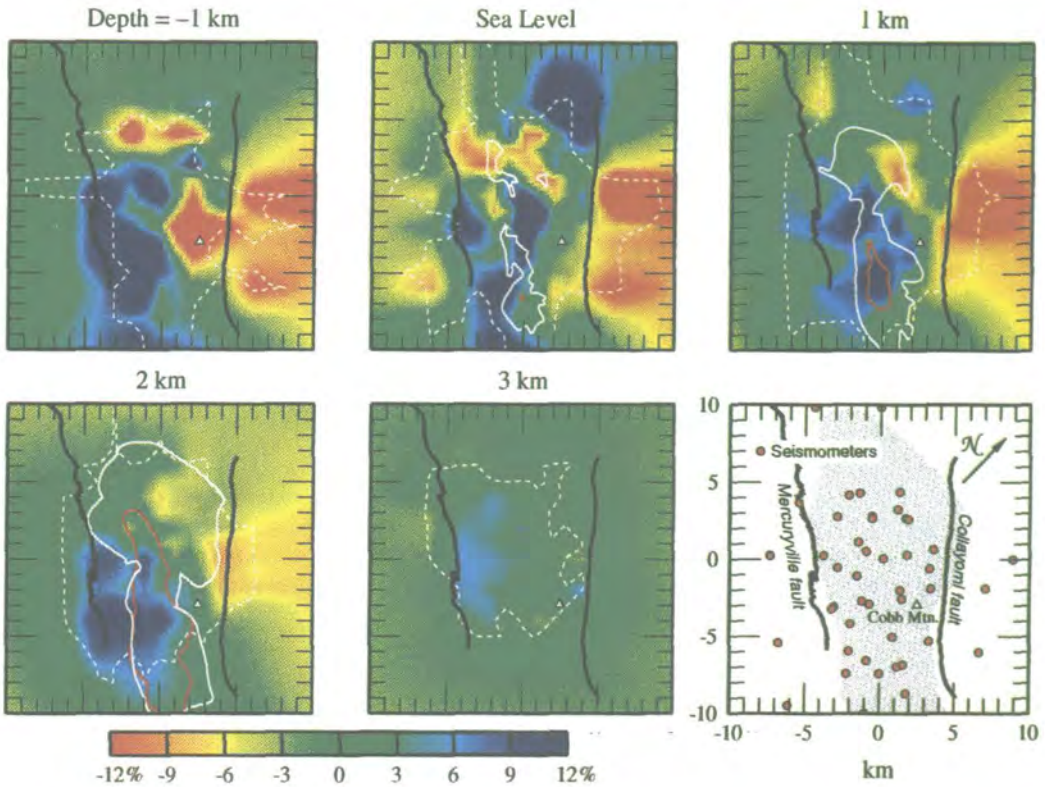

Figure 3. Maps showing variation of compressional-wave speed V_P from mean values at different depths (values to the left of maps). Areas within dashed white lines are well resolved (*spread* < 4 km). Solid white lines: boundary of steam reservoir. Red lines: boundary of felsite batholith. Gray shading (bottom right): surface projection of steam-production zone. V_P is low in the high-temperature northwest Geysers.

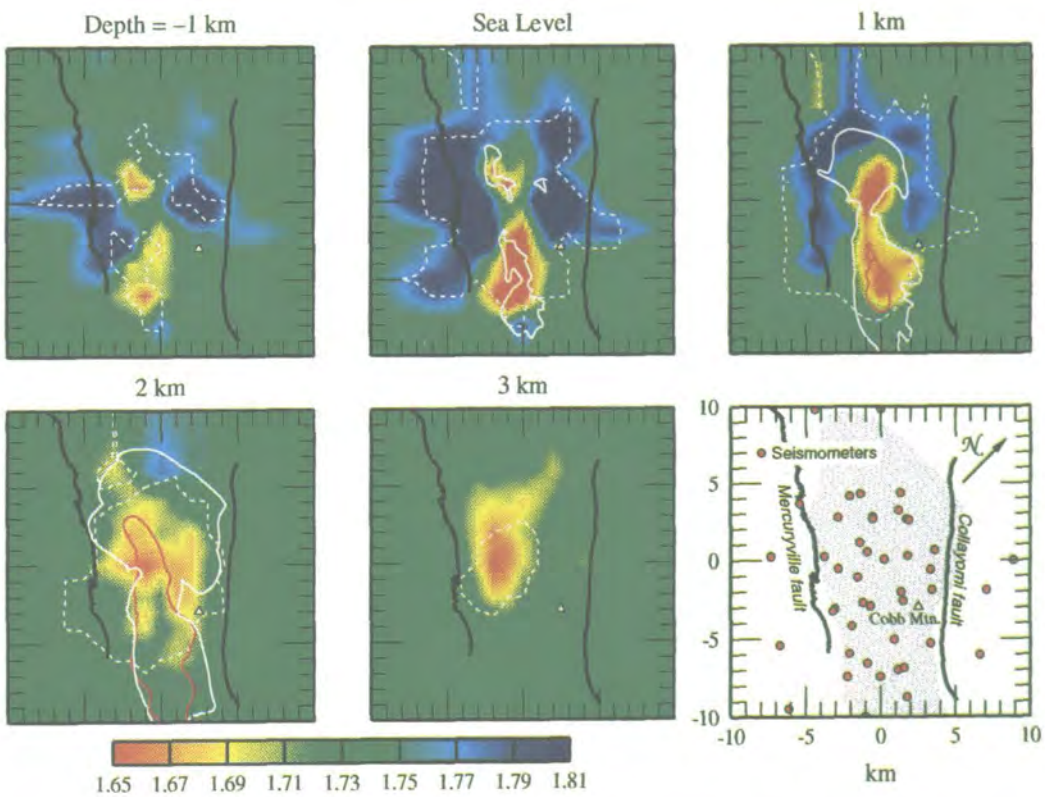

Figure 4. Same as Figure 3, for wave-speed ratio V_P/V_S. The value of V_P/V_S varies from 1.64 to 1.81 (average 1.74), corresponding to Poisson's ratios from 0.20 to 0.28.

Table 1. Theoretical V_P/V_S Anomalies

Cause	Porosity	
	0	0.02
Liquid –> Vapor	0	–14%
ΔT = +10°C (Liquid)	–0.06%	–1.70%
ΔT = +10°C (Vapor)	–0.06%	+0.10% to +0.68%
ΔP = –1 MPa (Liquid)	+0.004%	–0.20%
ΔP = –1 MPa (Vapor)	+0.004%	–6.6% to –10%

From $V_P/V_S = \left[K/\mu + 4/3\right]^{1/2}$ and the elastic moduli of water [*Keenan et al.*, 1969] and isotropic aggregates of rock-forming minerals [*Anderson and Liebermann*, 1969]. The macroscopic bulk modulus K is related to those of the fluid and the rock matrix, K_f and K_m, and the porosity ϕ by $1/K = \phi/K_f + (1-\phi)/K_m$. Both K_m and the macroscopic rigidity modulus μ are taken proportional to the corresponding moduli of quartz, and independent of the pore-fluid properties. Pressure changes in the matrix are assumed equal and opposite to those in the fluid. The ranges of values for the vapor phase correspond to conditions in the reservoir (P = 2.0 to 3.6 MPa; T = 240 to 350°C).

Although the pore fluid's properties affect the V_P/V_S ratio primarily by changing V_P, the anomaly is not clear in the V_P field alone (Figure 3). The reservoir must differ systematically from its surroundings in a way that increases both V_P and V_S and largely counters the effect of undersaturation. Lithologic variations associated with the "felsite" pluton and a metamorphic aureole above it [*Hulen and Nielson*, 1993], as well as hydrothermal alteration, may contribute to this effect.

Temporal variations in V_P/V_S, caused by decreases in both liquid saturation and pressure, probably are large enough to measure seismologically. If, as expected, the compressional-wave speed V_P is changing most rapidly, then analysis of P-phase data from existing single-component seismometer networks can provide valuable information on the state of the geothermal reservoir and its response to exploitation.

Acknowledgments. We thank M. Stark, S. Davis, and many others from the UNOCAL Corporation for assistance. F. Palmieri, the Abril trusts, C. Chapman, E. Frandsen, the Gauer Estate Vineyard, J. Aidlin, G. and M. Gouvea, and the Coldwater Creek Operator Corporation gave permission to operate instruments on their lands. This work was supported by a G. K. Gilbert Fellowship from the USGS, a NERC Grant and equipment Loan, and a loan of IRIS/PASSCAL equipment. A. R. is supported by a Ph.D. scholarship from the Dept. of Education for Northern Ireland. W. Ellsworth and R. Fournier gave helpful reviews.

References

Anderson, O. L., and R. C. Liebermann, Elastic constants of oxide compounds used to estimate the properties of the Earth's interior, in *The Application of Modern Physics to the Earth and Planetary Interiors*, edited by S. K. Runcorn, pp. 425-448, Wiley–Interscience, London, 1969.

Barker, B. J., M. S. Gulati, M. A. Bryan, K. L. Riedel, Geysers reservoir performance, in *Monograph on The Geysers Geothermal Field*, C. Stone, Ed., *Geotherm. Res. Council Special Rept., 17*, 167-177, 1992.

Eberhart-Phillips, D., Three-dimensional velocity structure in the northern California coast ranges from inversion of local earthquake arrival times, *Bull. Seismol. Soc. Am., 76*, 1025-1052, 1986.

Evans, J. R., D. Eberhart-Phillips, and C. H. Thurber, User's manual for SIMULPS12 for imaging v_p and v_p/v_s, a derivative of the Thurber tomographic inversion SIMUL3 for local earthquakes and explosions, *U. S. Geol. Surv. Open-File Rept., 94-431*, 142 pp., 1994.

Foulger, G. R., A. D. Miller, B. R. Julian, J. R. Evans, Three-dimensional v_p and v_p/v_s structure of the Hengill triple junction and geothermal area, Iceland, and the repeatability of tomographic inversion, *Geophys. Res. Lett., 22*, 1309-1312, 1995.

Hearn, B. C. Jr., J. M. Donnelly-Nolan, F. E. Goff, The Clear Lake volcanics: Tectonic setting and magma sources, in *Research in The Geysers-Clear Lake Geothermal Area, Northern California*, R. J. McLaughlin and J. M. Donnelly-Nolan, Eds., *U. S. Geol. Surv. Prof. Pap., 1141*, 25-45, 1981.

Hulen, J. B., and D. L. Nielson, Interim report on geology of The Geysers felsite, northwestern California, *Geotherm. Res. Council Trans., 17*, 249-258, 1993.

Iyer, H. M., D. H. Oppenheimer, T. Hitchcock, J. N. Roloff, J. M. Coakley, Large teleseismic P-wave delays in The Geysers-Clear Lake geothermal area, in *Research in The Geysers-Clear Lake Geothermal Area, Northern California*, R. J. McLaughlin and J. M. Donnelly-Nolan, Eds., *U. S. Geol. Surv. Prof. Pap., 1141*, 97-116, 1981.

Keenan, J. H., F. G. Keyes, P. G. Hill, J. G. Moore, *Steam Tables - Thermodynamic Properties of Water including Vapor, Liquid, and Solid Phases*, 162 pp., John Wiley & Sons, New York, 1969.

Kissling, E., W. L. Ellsworth, D. Eberhart-Phillips, U. Kradolfer, Initial reference models in local earthquake tomography, *J. Geophys. Res., 99*, 19635-19646, 1994.

Ludwin, R. S., and C. G. Bufe, Continued seismic monitoring of The Geysers, California, geothermal area, *U. S. Geol. Surv. Open-File Rept., 80-1060*, 50 pp., 1980.

O'Connell, D. R., Seismic velocity structure and microearthquake properties at The Geysers, California geothermal area, Ph. D. thesis, Univ. of Calif., Berkeley, 1986.

Stark, M. A., Microearthquakes – a tool to track injected water in The Geysers reservoir, *Geotherm. Res. Council Trans., 14*, 1697-1704, 1990.

Thompson, R. C., Structural stratigraphy and intrusive rocks at The Geysers geothermal field, in *Monograph on The Geysers Geothermal Field*, C. Stone, Ed. *Geotherm. Res. Council Special Rept., 17*, 59-63, 1992.

Walters, M. A., J. R. Haizlip, J. N. Sternfeld, A. F. Drenick, J. Combs, A vapor-dominated high-temperature reservoir at The Geysers, California, in *Monograph on The Geysers Geothermal Field*, C. Stone, Ed., *Geotherm. Res. Council Special Rept., 17*, 77-87, 1992.

Zucca, J. J., L. J. Hutchings, P. W. Kasameyer, Seismic velocity and attenuation structure of the Geysers geothermal field, CA, *Geothermics*, 23, 111-126, 1993.

B. R. Julian, U. S. Geological Survey, 345 Middlefield Rd., MS 977, Menlo Park, CA 94025. (e-mail: julian@andreas.wr.usgs.gov)

A. Ross, Department of Geological Sciences, University of Durham, Durham DH1 3LE, U. K. (e-mail: Alwyn.Ross@durham.ac.uk)

G. R. Foulger, Department of Geological Sciences, University of Durham, Durham DH13LE, U. K. (e-mail: G.R.Foulger@durham.ac.uk)

J. R. Evans, U. S. Geological Survey, 345 Middlefield Rd., MS 977, Menlo Park, CA 94025. (e-mail: evans@andreas.wr.usgs.gov)

(Received June 13, 1995; accepted July 19, 1995.)

Volume 23 Number 6 March 15, 1996
GRLAJ23(6) 605-696(1996) ISSN 0094-8276

Geophysical Research Letters

REGULAR SECTION

(continued on inside back cover)

Cover. *Ratio of compressional and shear seismic-wave speeds, V_P/V_S, 1 km below sea level (2 km below the surface) at The Geysers geothermal area, northern California, as determined by local-earthquake seismic tomography. The red and yellow colors mark a strong (-9%) anomaly that corresponds closely to the heavily exploited part of the geothermal reservoir. This anomaly is attributed to high compressibility of pore fluid, caused by boiling of interstitial water to steam during exploitation. Dashed white line: limit of good tomographic resolution. Black lines: faults. Red line: boundary of "felsite" batholith at 1 km depth. Solid White line: boundary of steam reservoir at 1 km depth, as determined by drilling. (See paper by Julian et al., this issue.)*

VOLUME 23 NUMBER 6 PAGES 605-696 MARCH 15, 1996

GEOPHYSICAL RESEARCH LETTERS, VOL. 24, NO. 2, PAGES 135-137, JANUARY 15, 1997

Industrially induced changes in Earth structure at The Geysers geothermal area, California

G. R. Foulger, C. C. Grant and A. Ross
Dept. Geological Sciences, University of Durham, Durham, DH1 3LE, U.K.

B. R. Julian
Seismology Section, U. S. Geological Survey, Menlo Park, California

Abstract. Industrial exploitation is causing clearly-measurable changes in Earth structure at The Geysers geothermal area, California. Production at The Geysers peaked in the late 1980s at ~3.5 x 10^3 kg s^{-1} of steam and 1800 MW of electricity. It subsequently decreased by about 10% per year [*Barker et al.*, 1992] because of declining reservoir pressure. The steam reservoir coincides with a strong negative anomaly (~0.16, ~9%) in the compressional-to-shear seismic wave speed ratio v_P/v_S, consistent with the expected effects of low-pressure vapor-phase pore fluid [*Julian et al.*, 1996]. Between 1991 and 1994 this anomaly increased in amplitude by up to about 0.07 (~4%). This is consistent with the expected effects of continued pressure reduction and conversion of pore water to steam as a result of exploitation. These unique results show that v_P/v_S tomography can easily detect saturation changes caused by exploitation of reservoirs, and is a potentially valuable technique for monitoring environmental change. They also provide geophysical observational evidence that geothermal energy is not a renewable energy source.

Introduction

The Geysers geothermal reservoir occupies greywacke sandstones and a felsite batholith, and lies within the San Andreas shear zone [*Thompson*, 1992] (Figure 1). It's surface area is about 75 km^2 and it extends from about 0.3 km above sea level, down to at least 3 km below sea level Although the fluid emerging from wells at The Geysers is dry steam, the total amount of fluid extracted since 1960, when significant exploitation started, is too large to have been stored in the reservoir as vapor. It is thought that much of the reservoir fluid is stored as liquid water in the rock pores, which boils as steam is extracted [*Barker et al.*, 1992]. Since 1968, reservoir pressure has declined from ~3.5 MPa (ref. 1) to less than 2 MPa throughout an extensive volume, while the temperature has remained constant at about 240°C in the main reservoir [*Truesdell et al.*, 1992]. Steam production has declined by 10% yr^{-1} in recent years and power generation is now only about 65% of the installed capacity.

Paper number 96GL03152.
0094-8534/97/96GL-03152$05.00

Data and Tomographic Inversions

Steam extraction at The Geysers induces many small-magnitude earthquakes, widely distributed throughout the reservoir [*Eberhart-Phillips and Oppenheimer*, 1984; *Stark*, 1991]. These are monitored by a permanent seismic network operated by the UNOCAL Corporation, which comprises 22 stations, 7 of which have three-component sensors. We used compressional- (*P*) and shear-wave (*S*) arrival times from local earthquakes observed on this network to determine the three-dimensional distributions of *P*- and *S*-wave speeds (v_P and v_S) in and around the reservoir. The tomographic method used incorporates ray

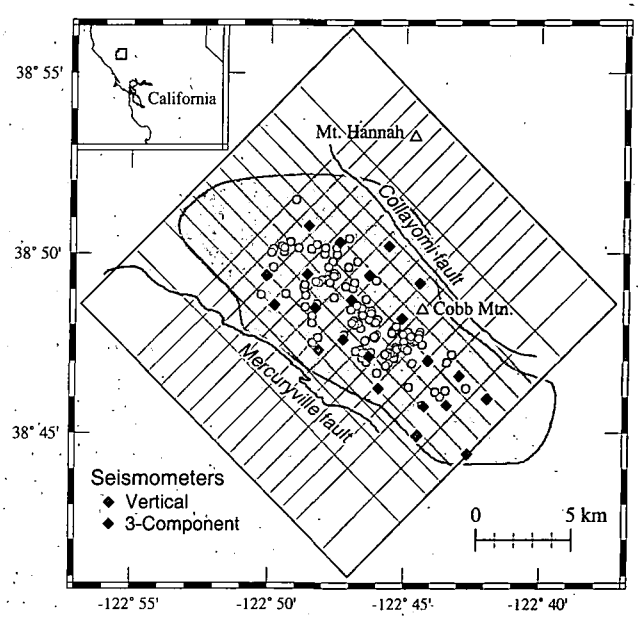

Figure 1. Map of The Geysers geothermal area. Gray zone: geothermal production are [*UNOCAL et al.*, 1991], diamonds: seismometers of the permanent UNOCAL network which were used in this study, circles: epicenters of earthquakes of the 1994 data set, large square: surface projection of the volume studied. Grid lines are shown in gray and intersect at nodes where seismic velocity is calculated. The grid extends from -1 to 4 km depth with 1-km node spacing, and has 1232 nodes. Heavy black lines: surface traces of the Collayomi and Mercuryville fault zones.

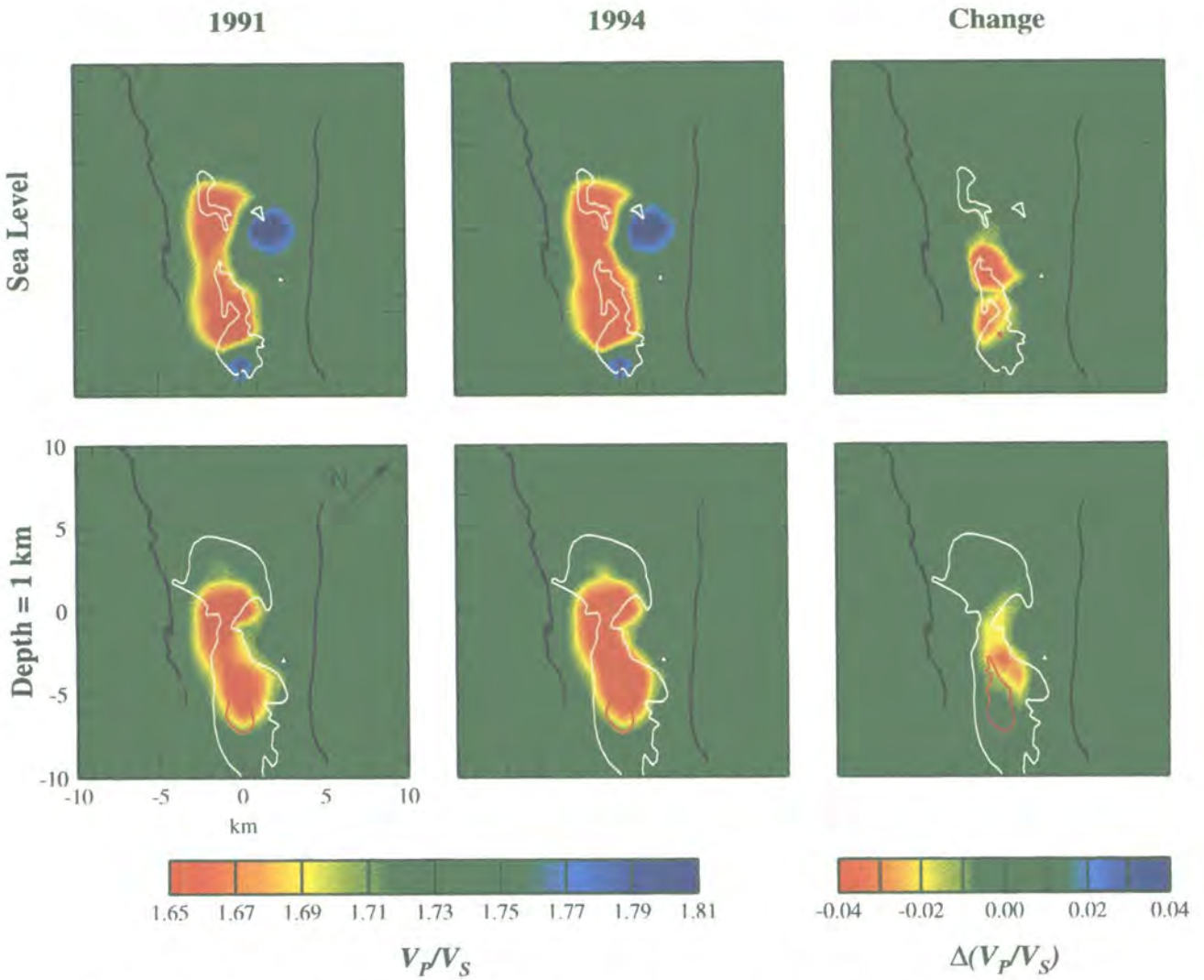

Figure 2. (a) Maps of wave-speed ratio v_P/v_S at two well-resolved depths for April 1991. Solid white line: boundary of the steam reservoir, black lines: surface traces of fault zones shown in Figure 1, (b) same as (a) except for December 1994, (c) same as (a) except showing change in v_P/v_S between 1991 and 1994.

bending and iteratively solves for earthquake locations and wave-speed structure, updating ray paths at each iteration step [*Thurber*, 1983; *Eberhart-Phillips*, 1986]. Separate inversions were performed using data from April 1991 and December 1994 and the results compared to reveal interim changes in the reservoir.

High-quality *P*- and *S*-wave arrival times were hand picked from digital seismograms to an accuracy of ~0.01 s for *P* and ~0.02 s for *S* waves. We measured *S*-wave arrival times at three-component stations only, and chose the earliest *S* wave wherever there was evidence of *S*-wave birefringence caused by material anisotropy. Both inversions imaged a volume extending from -1 to 4 km in depth (Figure 1). The 1991 data set includes 163 earthquakes, 2268 *P*- and 226 *S*-wave arrival times and the 1994 data set 146 earthquakes, 2522 *P*- and 656 *S*-wave arrival times. A one-dimensional starting model was obtained from an initial inversion of the 1991 data and a starting v_P/v_S ratio of 1.74 was obtained from Wadati diagrams [*Julian et al.*, 1996]. A series of inversions was performed with progressively decreasing nodal spacing for the 1991 data [*Julian et al.*, 1996] and a 75% reduction in arrival-time variance was achieved. The final RMS arrival-time residuals are 0.021 s for *P* waves and 0.036 s for *S* waves. For the 1994 data set, the starting model used was the three-dimensional model obtained using the 1991 data and the reduction in arrival-time variance was 77%. The final RMS arrival-time residuals for the 1994 data are 0.019 s for *P* waves and 0.055 s for *S* waves. The spread function, derivative weight sum [*Julian et al.*, 1996] and node resolutions confirm that the reservoir volume is well-resolved in the depth range 0 to over 2 km below sea level for both inversions.

Results

First order spatial variations in v_P and v_S are similar and reflect variations in lithology [*Julian et al.*, 1996]. In the reservoir, however, v_P/v_S shows a clear, coherent negative anomaly of about 0.16 (9%), which is strongest in the most heavily depleted volumes, northwest and southeast of the center of the reservoir (Figures 2a and b). In these places, pressure had dropped from an initial 3.5

MPa to as little as 1.4 MPa by the late 1980s [*Barker et al.*, 1992]. The 1991 and 1994 results are similar except in the center of the reservoir, where the anomaly became stronger by about 0.07 (4%) in the intervening 3.7 years (Figures 2a and b, Figure 2c). This change arises mainly from lowering of v_P 1991-1994, which indicates an increase in the rock compressibility.

In order to ensure that different inversion procedures did not cause spurious differences in the results, the two inversions were kept as similar as possible. The same node configurations and seismic stations were used. Damping values were optimized for each inversion, but differed only slightly between the two inversions, and tests showed that this made no significant difference to the results. The damping used was relatively strong, to minimize statistically insignificant differences in the results. We also inverted the 1994 data starting with a one-dimensional starting model and compared the results with an inversion of 1991 data that included additional stations from the U.S. Geological Survey CALNET network, and 15 temporary 3-component stations that we deployed. That latter inversion involved 185 earthquakes, 4032 *P*- and 944 *S*-wave arrivals, and produced a very well constrained v_P/v_S field that correlated excellently with the production area [*Julian et al.*, 1996]. This comparison showed an even higher-amplitude and spatially more extensive increase in the v_P/v_S anomaly than that revealed by the conservative results that we present here.

Interpretation and Conclusions

Julian et al. (1996) interpreted the negative v_P/v_S anomaly as a zone of low pressure that was also relatively dry as a consequence of boiling of the original liquid pore fluid as steam was extracted. Such a correlation between v_P/v_S and pore-fluid properties is expected on the basis of theory and laboratory experiments on porous rocks. These show that v_P/v_S is sensitive to the compressibility of the pore fluid, through its effect on v_P, and is relatively insensitive to the properties of the rock matrix [*Ito et al.*, 1979]. The change of the v_P/v_S anomaly is thus most likely a result of both decreasing pressure and depletion of the remaining pore water remaining between 1991 and 1994. This conclusion is supported by the fact that the zone of maximum change in v_P/v_S was, in the late 1980s, the site of a local pressure maximum, and the region of most rapid pressure decline. A temperature increase of about 25°C in a water-saturated reservoir could, in theory, also cause the observed change in v_P/v_S. However, the reservoir temperature remained constant 1991-1994 and certainly no cooling to such a large degree occurred [*Mitchell Stark*, personal communication, 1994].

The seismically-detected v_P/v_S change implies that pressure and/or liquid saturation decreased in the center of The Geysers reservoir between 1991 and 1994, a prediction that is consistent with the sparse published information based on well data. These unique results show that seismic tomography can be used to monitor the depletion of geothermal reservoirs and perhaps reservoirs of other kinds where gas and liquid exchange takes place. Further tomographic studies at The Geysers, for which extensive proprietary data on production, injection, and reservoir conditions exist, would be valuable for calibrating such a method. Because the compressional-wave speed v_P changes most, it might be possible to detect *changes* in pore-fluid properties using repeated tomographic inversions and *P*-phase data alone, despite the fact that identifying even a strong reservoir anomaly like that at The Geysers from *P*-wave data alone is difficult or impossible because it is masked by much stronger anomalies associated with lithological variations [*Julian et al.*, 1996]. If so, then data from commonly-existing single-component seismometer networks may provide valuable information on the state of geothermal reservoirs and their response to exploitation.

Acknowledgments. We thank M. Stark, W. Cumming and the UNOCAL Corporation for assistance in obtaining data and for many helpful discussions. Figure preparation was done using the GMT software [*Wessel and Smith*, 1991].

References

Barker, B.J., M.S. Gulati, M.A. Bryan and K.L. Riedel, Geysers reservoir performance, *Geotherm. Res. Council Special Rep.*, **17**, 167-177, 1992.

Eberhart-Phillips, D., Three-dimensional velocity structure in the northern California coast ranges from inversion of local earthquake arrival times, *Bull. Seismol. Soc. Am.*, **76**, 1025-1052, 1986.

Eberhart-Phillips, D., and D.H. Oppenheimer, Induced seismicity in The Geysers geothermal area, California, *J. Geophys. Res.*, **89**, 1191-1207, 1984.

Ito, H., J. De Vilbiss, and A. Nur, Compressional and shear waves in saturated rock during water-steam transition, *J. Geophys. Res.*, **84**, 4731-4735, 1979.

Julian, B. R., A. Ross, G.R. Foulger, and J.R. Evans, Three-dimensional image of reservoir depletion at The Geysers geothermal area, California, from v_P/v_S ratios, *Geophys. Res. Lett.*, **23**, 685-688, 1996.

Stark, M. A., Microearthquakes – A tool to track injected water in The Geysers reservoir, *Geotherm. Res. Council Special Rep.*, **17**, 111-117, 1991.

Thompson, R. C., Structural stratigraphy and intrusive rocks at The Geysers geothermal field, *Geotherm. Res. Council Special Rep.*, **17**, 59-63, 1992.

Thurber, C. H., Earthquake locations and three-dimensional crustal structure in the Coyote Lake area, central California, *J. Geophys. Res.*, **88**, 8226-8236, 1983.

Truesdell, A. H., J. R. Haizlip, W. T. Box, Jr., and F. D'Amore, A geochemical overview of The Geysers geothermal reservoir, *Geotherm. Res. Council Special Rep.*, **17**, 121-132, 1992.

UNOCAL, GGS, GEO, NCPA, SF and DWR, Map compiled through cooperative efforts, Pocket addition, *Geothermal Resources Council Monograph on The Geysers geothermal field, Special Rep.*, **17**, 1991.

Wessel, P. and W. H. F. Smith, Free software helps map and display data, *EOS Trans. AGU*, **72**, 441, 445-446, 1991.

G. R. Foulger, C. C. Grant and A. Ross, Dept. Geological Sciences, Univ. Durham, South Road, Durham, U.K. DH1 3LE and also at USGS, Menlo Park, CA 94025 (e-mail: alwyn.ross@durham.ac.uk, g.r.foulger@durham.ac.uk).

B.R. Julian, U.S. Geological Survey, MS 977, 345 Middlefield Road, Menlo Park, CA 94025. (e-mail: julian@andreas.wr.usgs.gov).

(Received June 16, 1996; revised September 23 1996; accepted October 2, 1996)

GEOPHYSICAL RESEARCH LETTERS, VOL. 22, NO. 4, PAGES 501-504, FEBRUARY 15, 1995

Shear-wave splitting from local earthquakes at The Geysers geothermal field, California

John R. Evans and Bruce R. Julian
U. S. Geological Survey, Menlo Park, California

G. R. Foulger and Alwyn Ross
Department of Geological Sciences, University of Durham, U. K.

Abstract. Shear-wave splitting from local microearthquakes recorded in The Geysers geothermal field shows that seismic anisotropy is distributed in a complex geographic pattern. At stations within about 2 km of northwest-striking regional faults, the fast polarization direction is parallel to those faults. The geothermal field, lying between two such faults, has both northwest and northeast fast polarization directions, often at the same station. This pattern suggests at least two causes of splitting: (1) extensive dilatancy anisotropy (EDA) and (2) fault-produced fractures or rock fabric. The observed anisotropy may derive from the upper 1.5 km of the crust, averaging 4% there; or it may be heterogeneously distributed throughout the upper 5 km. Fast polarization directions coincide with fracture directions inferred from borehole data for one of the youngest rock types in the region, a felsite pluton of about 1 Ma, and with injectate pathways inferred from microseismicity and geochemistry. Including in reservoir models a permeability anisotropy with a pattern similar to seismic anisotropy may help in optimizing fluid injection and steam recovery.

Introduction

The Geysers area is the largest commercially exploited vapor-dominated geothermal field in the world [*McLaughlin*, 1981]. It lies in McLaughlin's "central belt" of the Franciscan assemblage (late Jurassic to late Cretaceous melanges and broken formations of metamorphosed sandstone, argillite, basaltic rocks, chert, and exotic blocks). The area is complexly faulted by Franciscan thrust faults and Quaternary strike-slip and dip-slip faults, with extensive secondary ophiolite and serpentinite along many of these faults. Great Valley sequence rocks are present locally [*McLaughlin*, 1981]. The geothermal field is underlain by a ~1 Ma "felsite" pluton composed of at least three silicic to intermediate rock types [*Hulen and Nielson*, 1993]. The felsite appears to be responsible for atypically high porosity in the overlying rocks through (1) intrusion-induced tensional fracturing, (2) hydrothermal rock fracturing, and (3) mineral dissolution. The reservoir is mostly in Franciscan rocks and the upper 1 km of the felsite, both of which show extensive hydrothermal alteration. The felsite is approximately coeval with the Clear Lake Volcanics (<2.1 Ma), lying within and east of the geothermal field, and appears to be cogenetic with some of them.

In April, 1991, *Foulger et al.* [1993] operated a portable seismograph network in The Geysers region. Fifteen high-quality digital seismographs recorded continuously at 100 samples per second from 2-Hz three-component L-22™ geophones. Several thousand shallow microearthquakes (0.5 to 4 km below sea level), were recorded. Most were within the boundaries of the geothermal field.

Steam pressure has decreased rapidly since 1987 [*Beall*, 1993]. This decline has been mitigated by injecting water, with the greatest benefit derived at injection sites having high permeability, low steam pressure, and high reservoir superheat.

In this paper, we evaluate upper-crustal seismic anisotropy to infer permeability anisotropy. To the extent that seismic anisotropy reflects fracture orientation or other rock fabric, this information can help in designing optimal programs of injection to augment steam production. Most local earthquakes at The Geysers appear to be induced by production or injection [*Oppenheimer*, 1986; *Stark*, 1992]. Fracture data also will help in understanding earthquake induction and evaluating any hazard the earthquakes may pose.

Data and Method

We measured shear-wave splitting on 173 three-component records from 119 microearthquakes. These records are well within the "shear-wave window", with incidence angles less than the critical angle at the surface.

We inspected horizontal-plane particle-motion plots for linear *S* motion followed by elliptical or more complex motion [e.g., *Zhang and Schwartz*, 1994]. Records were first processed to remove the acausal effects of anti-alias filtering in the IRIS/PASSCAL recorders (J. Fowler, personal communication, 1993) and then resampled to 800 samples per second using the FFT algorithm (IRIS/PASSCAL records are rigorously unaliased). Both proved helpful in identifying and measuring the fast polarization direction, ϕ, and arrival times of the fast shear wave, t_{S1}, and the slow shear wave, t_{S2}.

We analysed all records with the PITSA software system [*Scherbaum and Johnson*, 1993], first using a horizontal-plane particle-motion plot to determine ϕ, then rotating the horizontal seismograms to this direction, and finally timing *S1* and *S2*. Each of these three measurements, ϕ, t_{S1}, t_{S2}, was characterized subjectively as "Excellent", "Good", or "Marginal". Examples of each grade of record are shown in Figure 1. About 69% of the records—an average of one per event—had a pick triple that was entirely at or above "Marginal", while 24% of the records were entirely "Excellent" or "Good". The vertical components of "Good" and "Excellent" records offer little evidence of an *S*-to-*P* converted precursor phase. (The lower example in Figure 1*a* has a noticeable vertical phase, but it lags *S2* by about 0.02 s.) In contrast, "Marginal" records, including those in Figure 1*c*, may be contaminated by precursor phases. We disregard the vertical components of all records, and emphasize "Good" and "Excellent" picks in the discussion that follows.

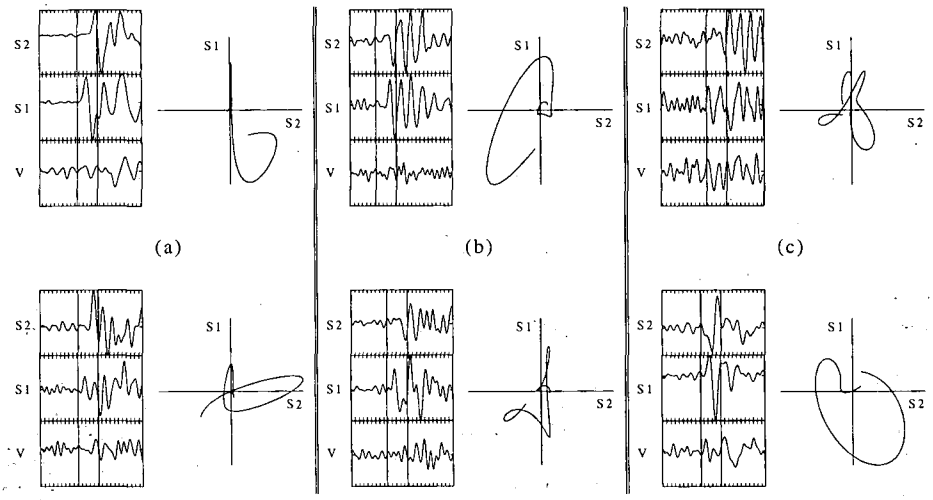

Figure 1. Seismogram examples, with horizontal components rotated to the measured *S1* direction. A 0.5-s window centered near *S1* is shown; relative amplitudes between components are correct. Horizontal particle-motion plots are for the 0.1-s subwindow between the vertical lines. (*a*) Examples of clear splitting (pick triple all "Excellent"). (*b*) Examples of "Good" records. (*c*) Examples of "Marginal" records.

Results

The similarities in Figures 1*a* and 1*b* between *S1* and *S2* waveforms is consistent with anisotropy but not in general with multiple-scattering models. However, systematic scattering effects cannot be ruled out as the source of observed particle motions. High-angle layering due to imbricate thrusts faults and their associated ultramafic rocks might produce multipathing and waveform complexity. A low-velocity surface layer can produce cruciform particle motions that could be misinterpreted as anisotropy [*Booth and Crampin*, 1985]. We proceed upon the assumption that these are anisotropy-induced split shear waves, at least in enough of the "Good" and "Excellent" records to permit meaningful interpretations.

Figure 2 is a map of observed ϕ. We noted no correspondence of ϕ with station-to-epicenter azimuth, so these are not simply measurements of S_V and S_H directions. The pattern of polarizations is complex, but northeast and northwest ϕ are most common (Figure 3). The principal compressive stress, σ_1, in this region lies between northeast [*Mount and Suppe*, 1992] and a more northerly azimuth near 15° (inferred from minimum compressive stress $\sigma_3 \approx 105°$ [*Oppenheimer*, 1986]). Hence, ϕ directions are not in simple agreement with the extensive dilatancy anisotropy (EDA) hypothesis of *Crampin* [1978], which predicts ϕ parallel to σ_1. (The EDA hypothesis is that wave-speed anisotropy in the crust is dominated by subvertical microcracks striking parallel to σ_1. Subvertical rays from local earthquakes are approximately in the plane of the cracks, yielding shear-wave splitting observable in horizontal particle motions.)

On the contrary, ϕ near the Mercuryville fault zone are mostly northwest—fault-parallel. The Mercuryville fault zone is a thrust with at least local Quaternary strike-slip motion

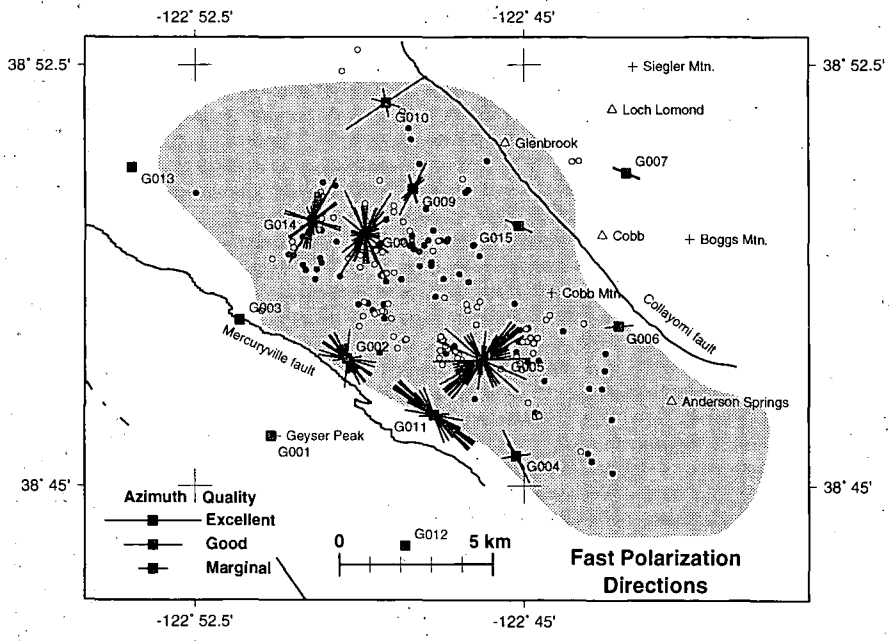

Figure 2. Map of stations used (squares) and observed *S1* polarization directions, ϕ. Shading: geothermal field; triangles: settlements; circles: earthquakes used here; dots: other earthquakes examined. Only data with reasonable estimates of both ϕ and delay time are shown, except at G006, G007, and G015, where either or both t_{S1} and t_{S2} is unreadable. Qualities "Excellent", "Good", and "Marginal" refer to ϕ. Figure made with the "GMT System" [*Wessel and Smith*, 1991].

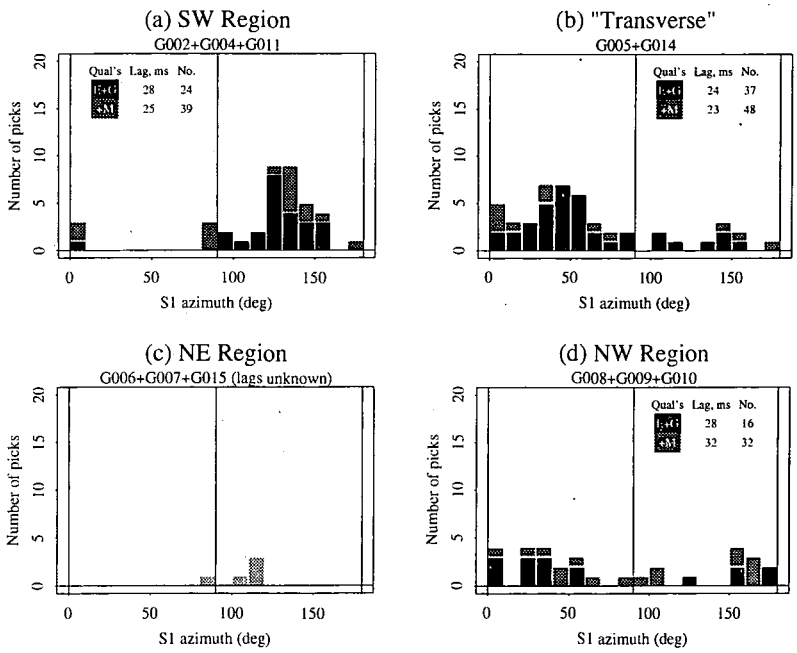

Figure 3. Histograms of ϕ for four groups of stations with similar directions. Groupings determined by examining individual-station histograms of this type. The median $t_{S2} - t_{S1}$ "lag" is given where known, with the number of data contributing. Same data selection as Figure 2. "E", "G", and "M": "Excellent", "Good", and "Marginal" data qualities.

[*McLaughlin*, 1981]. A few data of marginal quality suggest that stations G007 and G015 near the Collayomi fault zone, also have fault-parallel ϕ. The Collayomi fault zone is a regional right-lateral strike-slip fault with some local dip slip [*McLaughlin*, 1981].

In the geothermal field between these faults, two stations are dominated by northeast ϕ (Figure 3*b*) while others have mixed northeast and northwest ϕ (Figure 3*d*). We examined ϕ for different station-to-epicenter azimuths to isolate geographically the sources of these variations. No simple pattern emerged, other than that the few northwest ϕ at station G014 are all from events southeast of that station, near mixed-polarization station G008.

To determine the depths at which *S* traverses the dominant anisotropic medium, we plotted $t_{S2} - t_{S1}$ against event depth (Figure 4). We also plotted data by individual station and also made plots of just the highest quality picks. None of these plots suggested any correlation between lag and depth, with the possible exceptions of (1) events shallower than about 1 km below sea level and (2) the three best picks for G011 (among the asterisks in Figure 4). Both weakly suggest an increase of lag with depth, but there is scatter, even in the "Good" and better data, at least as large as any such signal.

The usual interpretation of this apparent depth independence would be that anisotropy at The Geysers is dominated by the shallowest ~1.5 km of rock. Following that inference, the median delay time of 26 ms (based on the 77 "Good" and better picks) and an average v_S of 2.4 km/s in the shallowest 1.5 km imply that the anisotropy averages 4%. However, the large scatter of lags suggests instead (1) large measurement errors or (2) strong, heterogeneous anisotropy throughout the sampled volume.

Discussion

We observe evidence of seismic wave-speed anisotropy in the splitting of *S* from shallow earthquakes at The Geysers. The measured ϕ make a pattern that is geographically complex but seems to correlate with distance from regional faults. The "Transverse" stations, particularly station G014, suggest an alternate correlation with distance from the center of the steam field or from the felsite. In other words, sites near the periphery of the steam field may be dominated by ϕ parallel to the boundary of the field. Additional stations near the northwest and southeast edges of the field are needed to distinguish between these alternatives.

The observed ϕ group, about in equal numbers, near northwest and northeast. Most stations are dominated by one or the other polarization direction, but several in the central part of the steam field are mixed. There is little correlation between event depth and $t_{S2} - t_{S1}$, and there is a great deal of scatter in these lags, implying shallow anisotropy, measurement inaccuracy, or heterogeneous anisotropy throughout the upper 5 km.

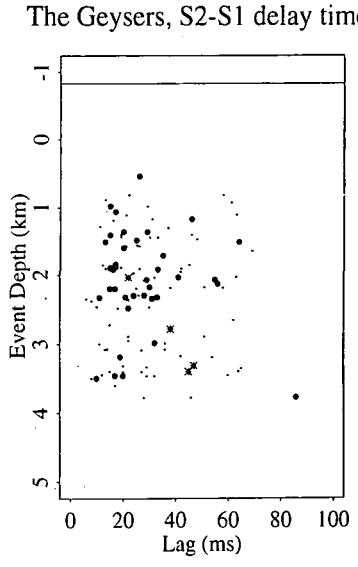

Figure 4. Earthquake depth below sea level *versus* $t_{S2} - t_{S1}$. Larger dots are "Good" or better data; stars: entirely "Excellent". Horizontal line: mean elevation of stations used.

These results are similar to those of *Zhang and Schwartz* [1994] for the Loma Prieta earthquake aftershock region along the San Andreas fault, 200 km south of The Geysers. There, most ϕ are parallel to the fault, while three stations show mixed northwest and northeast ϕ, and one station, the furthest from the fault, shows only northeast ϕ. Zhang and Schwartz interpreted the latter as indicating EDA, and the fault-parallel directions as indicative of fractures or other rock fabric related to the San Andreas fault system. They found no correlation with event characteristics for the mixed-polarization stations, and had no definitive explanation for this phenomenon.

We infer that ϕ near regional fault zones at The Geysers is controlled by fractures or other rock fabric resulting from fault-parallel shear. The other, northeast, group of ϕ is near that expected for EDA, and may be caused by that mechanism. Near the northwest and southeast ends of the steam field, northeast ϕ could also be caused by tangential fracturing at the periphery of an uplifted region formed over the intruded felsite—analogs of cone sheets. Mixed-polarization stations in the center of the steam field may sense both EDA and fault-shear effects.

Our results compare favorably with the borehole "steam-breakout" data of *Thompson and Gunderson* [1992] and with data from an oriented core sample studied by *Nielson et al.* [1991]. The former suggest that fractures in the young (~1 Ma) felsite pluton underlying much of The Geysers field are mostly oriented near northwest and northeast. These fractures presumably reflect Quaternary tectonism, including the San Andreas fault system. The Franciscan metagraywacke overlying most of the felsite and containing much of the geothermal reservoir has no apparent clustering of fracture azimuths in the steam-breakout data. One metagraywacke core examined by *Nielson et al.* [1991] had north-northeast oriented subvertical fractures while the other had low-angle fractures subparallel to bedding. This metagraywacke has been affected by previous stress regimes possibly overprinted only recently by the two modern fracture sets. If the felsite records recent fracturing and/or shearing, then the younger anisotropic features of the metagraywacke may be responsible for much of their seismic signature. Fractures that are open enough to cause seismic anisotropy also may dominate fluid flow patterns, so ϕ may be closely related to permeability anisotropy. To the degree that fault-parallel ϕ reflects rock fabric other than fractures, this fabric may block orthogonal flow and provide pathways for parallel flow. In either case, fluids are likely to flow parallel to ϕ. The strongly fault-parallel ϕ near the Mercuryville and Collayomi fault zones may be related to the bounding of the steam field at those fault zones.

Stark [1992] used microearthquake patterns and geochemical signatures of injectate in produced steam to infer injectate migration in the central part of field. Stark interpreted these patterns as evidence of injectate migration primarily down local steam-pressure gradients, although there is evidence of up-gradient flow in some areas. The microearthquake patterns instead suggest to us a predominance of northwest and northeast striking lineaments—a crosshatch. These are precisely the permeability-anisotropy directions we infer for this area from seismic anisotropy. Fractures or other rock fabric yield two dominant, orthogonal flow directions parallel to observed ϕ. Reservoir modeling may be improved by *a priori* inclusion of northwest and northeast permeability anisotropy in the geographic pattern suggested by Figure 2.

Since a heterogeneous distribution of anisotropy throughout the upper 5 km would explain both the scatter in $t_{S2} - t_{S1}$ and the mixed-polarization stations, we favor that explanation. Detailed mapping of anisotropy in three dimensions should be possible with a larger data set. A three-dimensional anisotropy map would be valuable for reservoir modeling, including the design of a reinjection program to extend the productive life of the reservoir.

Acknowledgements. This research is supported by the USGS Geothermal Program (JRE and BRJ) and a USGS G. K. Gilbert Fellowship (BRJ). AR is supported by a Ph.D. Studentship from the Department of Education, Northern Ireland. We wish to thank Zhi Zhang, Dennis Nielson, an anonymous GRL reviewer, John Vidale, and Bob Simpson for their helpful reviews of this manuscript. We also thank David Booth, Russ Evans, Xiangyang Li, Colin MacBeth, Aaron Martin, Bob Nadeau, John Orcutt, Wolfgang Rabbel, Martha Savage, and John Vidale for discussions and lessons in a technique new to all of us. A *caveat*: the first author, John Richard Evans of the U. S. Geological Survey, is not the same person as John Russell "Russ" Evans of the British Geological Survey, who has published many papers on seismic anisotropy.

References

Beall, J. J., The history of injection recovery in the Units 13 and 16 area of The Geysers steamfield [*sic*], *Trans. Geotherm. Resour. Counc.*, *17*, 211–214, 1993.

Booth, D. C., and S. Crampin, Shear-wave polarizations on a curved wavefront at an isotropic free-surface, *Geophys. J. R. Astron. Soc.*, *83*, 31–45, 1985.

Crampin, S., Seismic wave propagation through a cracked solid: polarization as a possible dilatancy diagnostic, *Geophys. J. R. Astron. Soc.*, *53*, 467–496, 1978.

Foulger, G. R., B. R. Julian, A. D. Miller, and A. Ross, Study of non-shear earthquake mechanisms in volcanic and geothermal areas, *Proc. First Workshop on Volc. Disaster Prevention*, Palo Alto, California, 8–12 March, 1993, 151–152, 1993.

Hulen, J. B., and D. L. Nielson, Interim report on geology of The Geysers felsite, northwestern California, *Trans. Geotherm. Resour. Counc.*, *17*, 249–258, 1993.

McLaughlin, R. J., Tectonic setting of pre-Tertiary rocks and its relation to geothermal resources in The Geysers-Clear Lake area, *U. S. Geol. Surv. Prof. Pap.*, *1141*, edited by R. J. McLaughlin and J. M. Donnelly-Nolan, 3–23, 1981.

Mount, V. S., and J. Suppe, Present-day stress orientations adjacent to active strike-slip faults: California and Sumatra, *J. Geophys. Res.*, *97*, 11,995–12,013, 1992.

Nielson, D. L., M. A. Walters, and J. B. Hulen, Fracturing in the northwest Geysers, Sonoma County, California, *Trans. Geotherm. Resour. Counc.*, *15*, 27–33, 1991.

Oppenheimer, D. H., Extensional tectonics at The Geysers geothermal area, California, *J. Geophys. Res.*, *91*, 11,463–11,476, 1986.

Scherbaum, F., and J. Johnson, *Programmable Interactive Toolbox for Seismological Analysis, PITSA, Version 4.0, 11-20-93*, Incorporated Research Institutions for Seismology, Data Management Center, Seattle, 1993.

Stark, M. A., Microearthquakes—A tool to track injected water in The Geysers reservoir, *Monograph on The Geysers Geothermal Field*, Special Report No. 17, edited by C. Stone, Geothermal Resource Council, Davis, California, 111–117, 1992.

Thompson, R. C., and R. P. Gunderson, The orientation of steam-bearing fractures at The Geysers geothermal field, *Monograph on The Geysers Geothermal Field, Special Report No. 17*, edited by C. Stone, Geothermal Resource Council, Davis, California, 65–68, 1992.

Wessel, P., and W. H. F. Smith, Free software helps map and display data, *Eos, Trans. AGU*, *72*, 441, 445–446, 1991.

Zhang, Z., and S. Y. Schwartz, Seismic anisotropy in the shallow crust of the Loma Prieta segment of the San Andreas fault system, *J. Geophys. Res.*, *99*, 9651–9661, 1994.

J. R. Evans and B. R. Julian, U. S. Geological Survey, 345 Middlefield Rd, MS-977, Menlo Park, CA 94025.

G. R. Foulger and A. Ross, Department of Geological Sciences, University of Durham, DH1 3LE, U. K.

(Received September 28, 1994; accepted November 16, 1994)

GEOPHYSICAL RESEARCH LETTERS, VOL. 23, NO. 8, PAGES 877-880, APRIL 15, 1996

Non-double-couple earthquake mechanisms at The Geysers geothermal area, California.

Alwyn Ross[1] and G. R. Foulger[1]
Dept. Geological Sciences, University of Durham, Durham, U.K.

Bruce R. Julian[2]
Branch of Seismology, U.S. Geological Survey, Menlo Park, California, U.S.A.

Abstract. Inverting *P*- and *S*-wave polarities and *P:SH* amplitude ratios using linear programming methods suggests that about 20% of earthquakes at The Geysers geothermal area have significantly non-double-couple focal mechanisms, with explosive volumetric components as large as 33% of the seismic moment. This conclusion contrasts with those of earlier studies, which interpreted data in terms of double couples. The non-double-couple mechanisms are consistent with combined shear and tensile faulting, possibly caused by industrial water injection. Implosive mechanisms, which might be expected because of rapid steam withdrawal, have not been found. Significant compensated-linear-vector-dipole (CLVD) components in some mechanisms may indicate rapid fluid flow accompanying crack opening.

Introduction

Non-double-couple (non-DC) earthquakes, whose seismic radiation is inconsistent with shear faulting, have recently been found at many volcanic and geothermal areas throughout the world [*Miller et al.*, 1995]. Surprisingly, however, most mechanisms published for earthquakes at the intensely seismically active Geysers geothermal area in northern California are of DC type [*e.g.*, *Oppenheimer*, 1986]. Almost all mechanisms have been derived solely from the polarities of *P*-wave first motions, which have limited information content and resolving power. *O'Connell and Johnson* [1988] obtained a non-DC mechanism for one of three earthquakes studied by inverting waveforms, but attributed this result to error. In this study, we obtain focal mechanisms of higher quality, using *P*- and *S*-wave amplitude data along with polarities, to determine whether non-DC earthquakes do in fact occur at The Geysers.

The Geysers is the most intensively exploited geothermal field in the world. The area experiences about 140 earthquakes of $M_L > 1.2$ per month, and events in recent years have local magnitudes up to 4.9 (UCB). Although the pre-production activity level is poorly known, it is clear that most of the earthquakes are induced by steam removal and water injection [*Stark*, 1990].

[1]Dept. Geological Sciences, University of Durham, South Road, Durham, U.K. DH1 3LE and also at USGS, Menlo Park, CA 94025 (e-mail: alwyn.ross@durham.ac.uk, g.r.foulger@durham.ac.uk).
[2]U.S. Geological Survey, MS 977, 345 Middlefield Road, Menlo Park, CA 94025. (e-mail: julian@andreas.wr.usgs.gov).

Paper number 96GL00590
0094-8534/96/96GL-00590$05.00

Data and Method

In April 1991 we deployed a temporary network of fifteen, three-component PASSCAL digital seismic stations with Mark Products model L22D 2-Hz sensors and REFTEK model 72A-02 data loggers in an array 15 km in diameter at The Geysers (Figure 1). We recorded continuously at a sampling rate of 100 sps and detected about 4000 local earthquakes. The network geometry provided good focal-sphere coverage for events in the central, most active part of the geothermal area. In addition, the UNOCAL Corporation operates 22 seismometers in the area and the U.S. Geological Survey (USGS) 18.

Seismic-wave amplitudes are strongly distorted by geometric spreading of rays, to which *P:S* amplitude ratios are relatively insensitive. We therefore used linear-programming methods [*Julian*, 1986; *Julian and Foulger*, 1995] to invert *P*- and *SH*-wave polarities and *P:SH* amplitude ratios and determine seismic moment tensors. We supplemented polarity and amplitude data recorded on the temporary network with polarity data from USGS stations. Data from the UNOCAL network contributed only to estimating earthquake locations, and not focal mechanisms, because the instrument polarities are unknown.

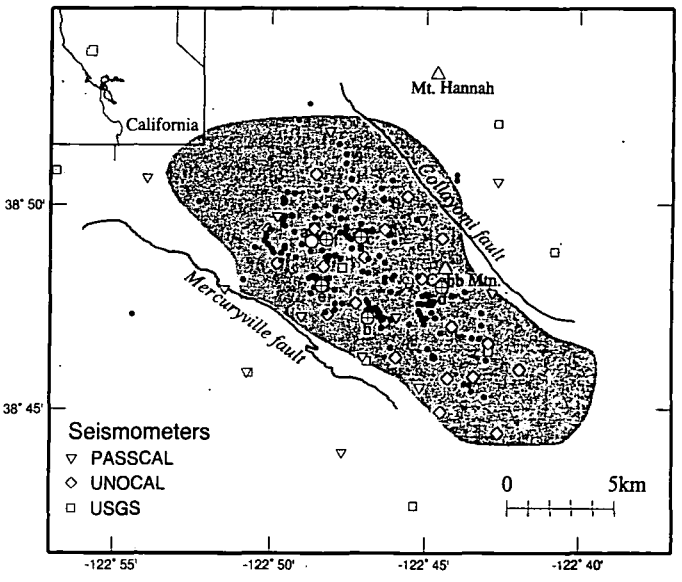

Figure 1. Map of The Geysers geothermal area, California, showing the steam production area (shaded), events used to derive the tomographic velocity structure (black dots) [*Julian et al.*, 1996] and events (a-f) for which focal mechanisms are shown in Figure 3. Seismic stations are also shown.

The seismograms recorded on the PASSCAL instruments were first processed to remove acausal effects of anti-alias filtering in the recorder (J. Fowler, personal communication, 1993) and then low-pass filtered (three-pole Butterworth response, 5 Hz corner frequency) to reduce the effects of wave scattering and attenuation. Rays were numerically traced [*Julian and Gubbins*, 1977] through high-quality velocity models of V_P and V_S [*Julian et al.*, 1996] as part of the process of determining hypocenter locations and mapping rays onto focal spheres. *P*-wave amplitudes were measured on vertical-component seismograms. *SH*-wave amplitudes were measured on transverse-component seismograms obtained by numerically rotating the digital seismograms. Amplitudes were measured from the first onset to the first peak, and only signals with similar rise times were used in ratios. We corrected amplitudes for the effect of the free surface and multiplied amplitudes by the cube of the wave speed at the focus to approximately eliminate systematic differences in P- and S-wave amplitudes (see *Aki and Richards* [1980], eqn. 4.91).

Wave attenuation affects compressional and shear waves differently, multiplying *P:S* amplitude ratios by

$$\exp\left(-\frac{\omega}{2}\left[\frac{t_p}{Q_p}-\frac{t_s}{Q_s}\right]\right).$$

where ω is angular frequency, Q_p and Q_s are the figures of merit for compressional and shear waves, and t_p and t_s are their travel times. We corrected for attenuation using $Q_p = 60$, a reasonable value for the reservoir [*Zucca et al.*, 1993] and a range of values for Q_s, which has not been measured at The Geysers. We present results for $Q_s = 84$ ($Q_s/Q_p = 1.4$, appropriate for attenuation by scattering from cracks and voids [*Menke et al.*, 1995]). A value as low as $Q_s = 27$ ($Q_s/Q_p = 0.45$, appropriate for attenuation by shear anelasticity), does not change the results enough to affect the conclusions of this paper.

Results

We studied focal mechanisms for 24 of the best-recorded earthquakes in detail. Hypocenter locations (Figures 1 and 2) were determined using up to 39 *P*- and 12 *S*-wave arrival times. The events were distributed throughout the deeper parts of the seismogenic volume because focal sphere coverage was best for those events (Table 1). Figure 3 shows solutions for six events and Table 2 gives the moment tensors.

The results for most of the earthquakes studied are close to DCs and, in terms of conventional shear-faulting interpretations, include strike-slip, thrust and normal orientations.

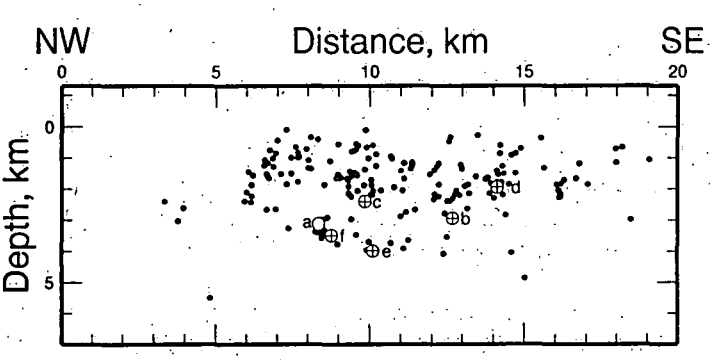

Figure 2. NW-SE cross-section showing hypocenters of the events illustrated in Figure 1. Symbols as in Figure 1.

Table 1. Origins and magnitudes of the earthquakes studied.

event	date, origin time	latitude longitude	depth bsl, km	moment mag M[1]
a	91/04/30 01:37:39.22	38.8183 -122.8116	3.10	1.77
b	91/4/14 00:23:50.30	38.7867 -122.7812	2.95	2.75
c	91/4/17 16:41:38.00	38.8199 -122.7850	2.40	2.02
d	91/4/21 09:36:49.29	38.7996 -122.7412	1.94	2.09
e	91/4/26 05:29:27.17	38.8001 -122.8060	3.99	1.88
f	91/4/27 06:29:31.08	38.8190 -122.8035	3.49	1.84

[1] $\log M_o = 1.5M + 16$ (M_o in N m)

Figure 3a shows a good example. Focal-mechanism solutions for the five earthquakes shown in Figure 3b-f depart strongly from DCs. These earthquakes all have areas of compression dominating the focal sphere, with one earthquake (event b) exhibiting no dilational arrivals. The explosive components comprise 20-33% of the total moment and indicate volume increases at the sources. Similar solutions are obtained if only *P*-wave polarities are used. Events b and f are particularly good examples.

The orientations of the principal axes of the moment tensors vary considerably, suggesting a locally heterogeneous stress field. In general, the P axes tend to be sub-horizontal and trend NW through NE. The T-axes tend to trend more east-west.

Discussion

In our limited data set about 20% of earthquakes at The Geysers have substantial non-DC components that include volume increases of up to 33%. Figure 4 shows a "source type plot" of the six events shown in Figure 3 [*Hudson et al.*, 1989]. About half of these lie between the DC and +Crack loci on the source type plot (earthquakes e, c and d) and thus may be explained by combined shear and tensile faulting. Earthquakes b and f lie between the +Crack and +CLVD loci and thus depart from the simple shear/tensile-fault model. They might be interpreted as opening cracks that are partially compensated by fluid flowing into the crack [*Julian*, 1983]. Such a process is likely in The Geysers, where earthquakes are induced by major changes in pore fluid pressure caused by the extraction of steam and reinjection of water.

Fluid injection would be expected to increase pore pressure, and thus to encourage crack opening and explosive mechanisms. *Stark* [1990] showed that some microearthquakes at The Geysers cluster around injection wells. The epicenters of events b, c and e are less than 600 m from injection wellheads, which supports the theory that they may be induced by local pressure increases caused by injection.

The removal of large volumes of steam at The Geysers has greatly decreased pore pressure, which might be expected to encourage events with implosive mechanisms. These were not well constrained in this study, though 1-2% of the best-constrained earthquakes of *Oppenheimer* [1986] are dominated by dilational arrivals [*Julian et al.*, 1993]. Implosive

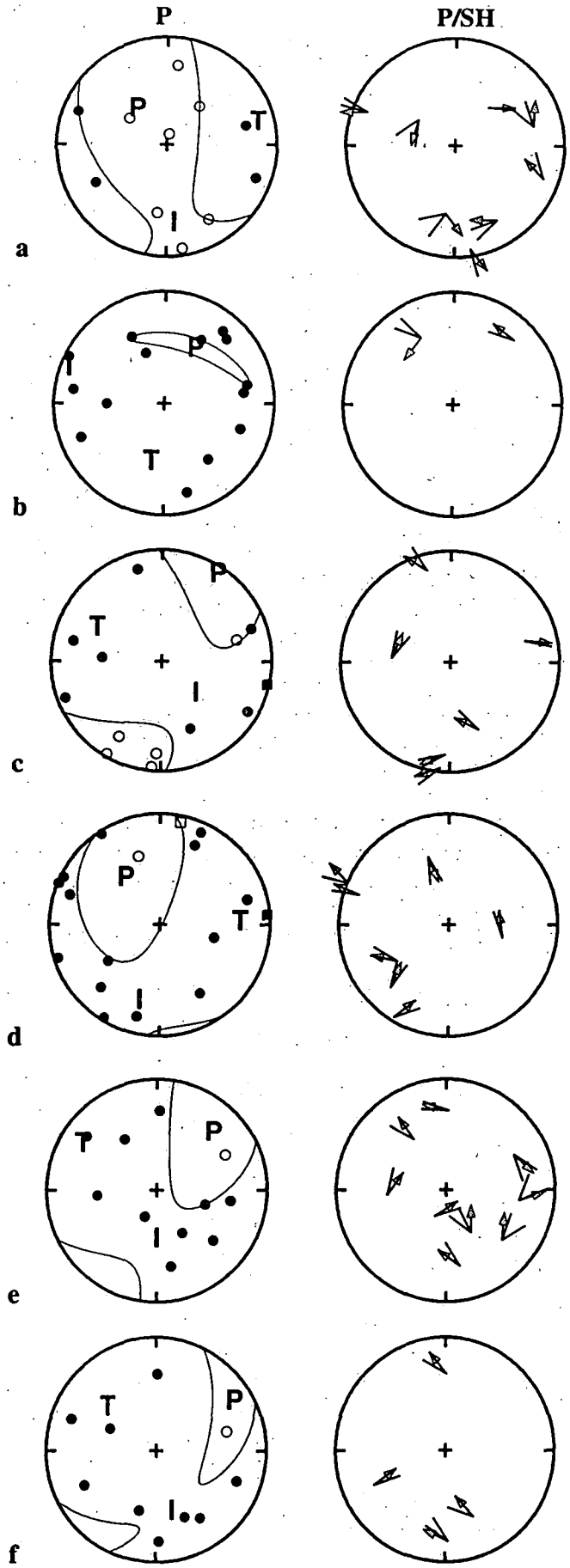

Table 2. Relative moment tensor components for events.

event	Relative moment tensor components					
	M_{xx}[1]	M_{xy}	M_{yy}	M_{xz}	M_{yz}	M_{zz}
a	-5.06	10.45	19.15	6.54	-13.43	-14.96
b	18.34	3.83	1.30	20.55	4.74	22.12
c	-1.17	-15.65	16.74	-5.23	13.03	14.27
d	-1.98	7.08	24.56	9.66	-19.34	-1.05
e	5.64	-19.96	18.36	-1.60	14.06	4.73
f	8.40	-10.88	8.69	-10.48	12.79	14.39

[1] Component coordinate system, x = north, y = east, and z = down.

earthquakes have been reported from the Krafla geothermal area, Iceland, but their first arrivals are less impulsive than those of explosive earthquakes there [*Arnott and Foulger*, 1994]. Earthquakes of this kind may be difficult to observe because cavity collapse may occur relatively slowly and excite seismic radiation inefficiently. Also, earthquakes induced by steam extraction may tend to be smaller and shallower than injection-induced earthquakes and thus poorly constrained by this study.

The observations presented here add to the mounting volume of evidence for non-DC earthquakes in geothermal areas. Future studies of earthquakes in geothermal areas should be designed to detect non-DC focal mechanisms, as this information may be key to understanding the processes of fluid movements in the reservoir. Furthermore, the importance of fluids in the nucleation of earthquakes and in the propagation of failure is becoming increasingly appreciated. A broader search for non-DC components in focal mechanisms thus has the potential to increase our understanding of earthquake processes in general.

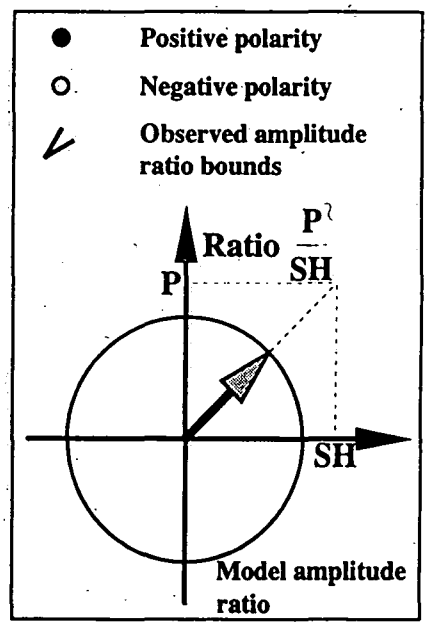

Figure 3. Focal mechanisms of six well-constrained earthquakes at The Geysers. Left: *P*-wave polarities; right: *P:SH*-wave amplitude ratios; open symbols: dilations; filled symbols: compressions; squares: lower-hemisphere observations plotted at their antipodal points. Theoretical amplitude ratios are represented as the directions of small arrows and pairs of lines indicate ranges compatible with the observations (see key). Upper focal hemispheres in equal-area projection.

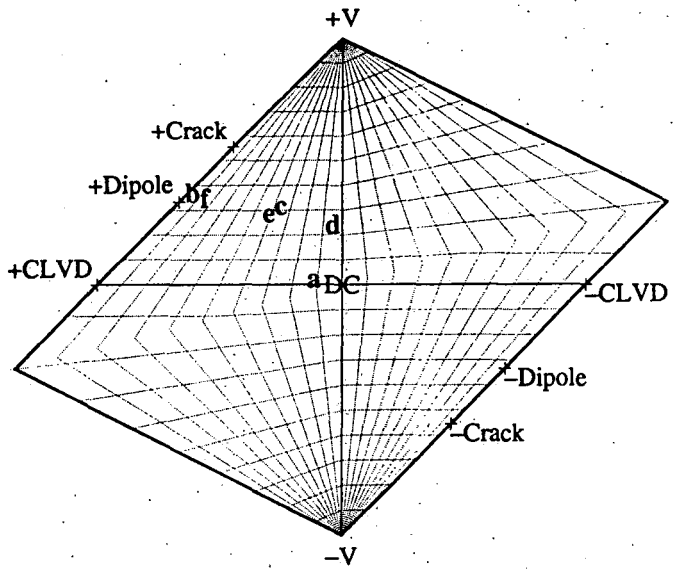

Figure 4. Equal-area "source type plot" [*Hudson et al.*, 1989] showing the earthquake mechanisms studied. The horizontal position shows the ratio of the CLVD component to the non-volumetric (CLVD+DC) component. The vertical position shows the volumetric component. Letters a-f correspond to earthquakes shown in Figures 1-3 and Tables 1 and 2. ±V: Isotropic volume changes; ±Dipole: Linear vector (force) dipoles; ±CLVD: Compensated linear vector dipoles; ±Crack: Opening and closing tensile cracks.

Conclusions

1. Study of a limited set of data suggests that about 20% of the earthquakes at The Geysers have substantial non-DC components.
2. Some earthquakes have explosive volumetric components of up to about 33%. Approximately half of these are consistent with combined shear and tensile faulting. The rest have significant CLVD components that may indicate fluid flow accompanying failure.
3. The non-DC events studied are probably caused by reinjection of water. Steam extraction might be expected to cause implosive earthquakes, but these are not well-constrained, and may be fundamentally more difficult to observe.

Acknowledgments. We thank M. Stark, S. Davis, W. Cumming and the UNOCAL Corporation for assistance and data. A. Miller and S. D. P. Williams assisted with software and helpful discussions. This work was supported by a USGS G. K. Gilbert Fellowship. NERC Grant GR9/134 and a loan of IRIS/PASSCAL equipment. A. R. was supported by a Ph.D scholarship from the Dept. of Education for Northern Ireland. Any use of trade names and trademarks in this publication is for descriptive purposes only, and does not constitute endorsement by the U.S. Government.

References

Aki, K, and P. G. Richards, *Quantitative Seismology*, vol 1, Freeman, New York, pp 557, 1980.

Arnott, S. K., and G. R. Foulger, The Krafla spreading segment, Iceland: 2. The accretionary stress cycle and non-shear earthquake focal mechanisms, *J. Geophys. Res.*, 99, 23827-23842, 1994.

Hudson, J. A., R. G. Pearce, and R. M. Rogers, Source type plot for inversion of the moment tensor, *J. Geophys. Res.*, 94, 765-774, 1989.

Julian, B. R., Evidence for dyke intrusion earthquake mechanisms near Long Valley Caldera, California, *Nature*, 303, 323-325, 1983.

Julian, B. R., Analysing seismic-source mechanisms by linear-programming methods, *Geophys. J. R. astr. Soc.*, 84, 431-443, 1986.

Julian, B. R., and G. R. Foulger, Moment tensors from linear inversion of body-wave amplitude ratios: Powerful constraints on earthquake mechanisms, submitted to *Bull. Seis. Soc. Am.*, 1995.

Julian, B. R., and D. Gubbins, Three-dimensional seismic-ray tracing, *J. Geophys.*, 43, 95-113, 1977.

Julian, B. R., A. D. Miller, and G. R. Foulger, Non-shear focal mechanisms of earthquakes at The Geysers, California, and Hengill, Iceland, geothermal areas, *Trans. Geotherm. Res. Council*, 17, 123-128, 1993.

Julian, B. R., A. Ross, and G. R. Foulger, Three-dimensional seismic image of a geothermal reservoir: The Geysers, California, in press, *Geophys. Res. Lett.*, 1996.

Menke, W., V. Levin and R. Sethi, Seismic attenuation in the crust at the mid-Atlantic plate boundary in south-west Iceland, *Geophys. J. Int.*, 122, 175-182, 1995.

Miller, A. D., G. R. Foulger, and B. J. Julian, Non-Double-Couple earthquakes II. Observations, submitted to *Rev. Geophys.*, 1995.

O'Connell, D. R. H., and L. R. Johnson, Second-order moment tensors of microearthquakes at The Geysers geothermal field, California, *Bull. Seis. Soc. Am.*, 78, 1674-1692, 1988.

Oppenheimer, D. H., Extensional tectonics at The Geysers geothermal area, California, *J. Geophys. Res.* 89, 1191-1207, 1986.

Stark, M. A., Microearthquakes- a tool to track injected water in The Geysers reservoir, *Trans. Geotherm. Res. Coun*, 14, 1697-1704, 1990.

Zucca, J.J., L.J. Hutchings and P.W. Kasameyer, Seismic velocity and attenuation structure of The Geysers geothermal field, CA., *Geothermics*, 23, 111-126, 1993.

(Received October 24, 1995; revised February 5, 1996; accepted February 12, 1996)